
Doctoral Thesis

# Dirac Plasmon Polaritons

*Author:*
Thomas Michael Jebb Sturges

*Supervisors:*
Dr. Eros Mariani
Prof. Bill Barnes

*A thesis submitted in fulfilment of the requirements for the degree of Doctor of Philosophy in Physics*

*in the*

Quantum Systems and Nanomaterials group
Department of Physics and Astronomy

June 2017

# Declaration of Authorship

This text entitled 'Dirac Plasmon Polaritons' is submitted by Thomas Michael Jebb Sturges to the University of Exeter as a thesis for the degree of Doctor of Philosophy in Physics, in July 2017.



I certify that all material in this thesis which is not my own work has been identified and that no material has previously been submitted and approved for the award of a degree by this or any other University.

Signed: _____

Date: _____

UNIVERSITY OF EXETER

# *Abstract*

College of Engineering, Mathematics and Physical Sciences
Department of Physics and Astronomy

Doctor of Philosophy in Physics

**Dirac Plasmon Polaritons**

by Thomas Michael Jebb Sturges

We study theoretically graphene-like plasmonic metamaterials, in particular a honeycomb structured array of identical metallic nanoparticles, and examine the collective plasmonic modes that arise due to the near-field dipolar coupling between the localised surface plasmons of each individual nanoparticle. An analysis of the band structure of these eigenmodes reveals a phenomenal tunability granted by the polarisation of the dipole moments associated with the localised surface plasmons. As a function of the dipole orientation we uncover a rich phase diagram of gapped and gapless phases, where remarkably every gapless phase is characterised by the existence of collective plasmons that behave as massless chiral Dirac particles, in analogy to electrons in graphene. We consider lattices beyond the perfect honeycomb structure in two ways. Firstly, we break the inversion symmetry which leads to collective plasmons described as massive chiral modes with an energy dependent Berry phase. Secondly, we break the three-fold rotational symmetry and investigate generic bipartite lattices. In this scenario we progressively shift one sublattice away from the original honeycomb arrangement and observe a sequence of topological phase transitions in the phase diagram, as well as the merging and annihilation of Dirac points in the dispersions. After examining the purely plasmonic response we wish to address the true eigenmodes responsible for transporting electromagnetic radiation. For this reason we examine plasmon polaritons that arise from the strong light-matter coupling between the collective plasmons in a honeycomb array of metallic nanoparticles and the fundamental photonic mode of an enclosing cavity. Here we identify that the Dirac point remains robust and fixed in momentum space, irrespective of the light-matter coupling strength. Moreover, we demonstrate a qualitative modification of the polariton properties through modulation of the photonic environment, including order-of-magnitude renormalisation of the group velocity and the intriguing ability to invert the chirality of Dirac polaritons.

# *Acknowledgements*

There are many to whom I am grateful. Firstly on a formal level, I would like to thank my host institution the University of Exeter and the various support staff who have aided with multiple queries. For financial support I acknowledge the College of Engineering, Mathematics and Physical Sciences for granting me a College Research Studentship, funded by the Engineering and Physical Sciences Research Council. I am also grateful for the hospitality of the Condensed Matter Physics Group at the University of Chalmers, as well as the organisers of the Frontiers of Condensed Matter 2015 and L'École de Physique des Houches. I would also like to sincerely thank Prof. Bill Barnes for providing me with the opportunity to undertake this PhD, and for the complete academic freedom to pursue my own interests.

I am indebted to Dr. Eros Mariani — who saved me from the brink of a career in engineering. It was a happy accident that I was placed under the guidance of Eros for my Master's project. However, because of his infectious enthusiasm and ability to explain deep ideas with sparkling clarity, I thoroughly enjoyed the research and was inspired to continue as a PhD student with him as my supervisor. The experience has been invaluable and I would like to express my deepest gratitude to Eros for the significant effort he has invested in preparing me for a career in scientific research.

A special mention needs to be made to each of my co-authors: Dr. Claire Woollacott, Prof. Guillaume Weick and Charlie-Ray Mann. Claire was a *de facto* supervisor as I transitioned from Master's student to PhD student, and has provided me with so much support and guidance over the years. Guillaume made significant contributions to my understanding of our research, and is a wonderfully ruthless editor of manuscripts. The newcomer PhD student Charlie has made critical contributions to the direction, and hopefully success, of our research. Thanks to all three of you!

I have enjoyed discussions and guidance from many of my colleagues. In particular I would like to acknowledge: Prof. Misha Portnoi — for advice on many issues such as career trajectories, Dr. Thomas Philbin — for helpful discussions about cavity QED, Dr. Ian Hooper — for IT support and discussions about numerics and simulations, Prof. Saverio Russo — group leader extraordinaire, Dr. Thomas Constant — for help with COMSOL, Prof. Gyaneshwar Srivastava — for help and guidance on many issues, and Dr. Alastair Humphrey — for showing me the lab and a real live nanoparticle! In addition I am very grateful to the other Mariani group members, Dr. Hai-Yao (Frank) Deng and Thomas McDermott, who have entertained many a question of mine.

To my friends and peers — Robin Churchill, Dr. Lachlan Marnham, Dr. Charles Downing, Dr. Vasil Saroka, Thomas Collier, Dr. Arseny Alexeev, Dr. Alex Pearce,

Ned Taylor and Natalie Whitehead — thank you for the laughs and comradeship. In particular I would like to thank Charles for his advice on issues scientific and otherwise, and who I have co-opted as a mentor of sorts.

I am thankful to Dr. Marcin Mucha Kruczynski and Dr. Steven Hepplestone for agreeing to examine this thesis, and to Prof. Gyaneshwar Srivastava for assuming the role of independent chair.

Most importantly, I say thank you to my amazing parents Karen & Bill, and my brother Iain. I have the best family one could wish for, and they have cheered me on, lifted my spirits, and kept me approximately sane throughout my PhD.

My final thank you goes to Karina, my best friend. I'm not sure I could have done it without you.

# Contents

# List of Figures

# Abbreviations

| | |
|---|---|
| **FDTD** | **F**inite-**D**ifference-**T**ime-**D**omain |
| **EELS** | **E**lectron **E**negry **L**oss **S**pectroscopy |
| **EM** | **E**lectro**M**agnetic |
| **SPP** | **S**urface **P**lasmon **P**olariton |
| **TM** | **T**ransverse **M**agnetic |
| **SP** | **S**urface **P**lasmon |
| **LSP** | **L**ocalised **S**urface **P**lasmon |
| **CD** | **C**oupled **D**ipole |
| **CP** | **C**ollective **P**lasmon |
| **SW** | **S**chrieffer-**W**olff |
| **CDP** | **C**onventional **D**irac **P**oint |
| **SDP** | **S**atellite **D**irac **P**oint |
| **TEM** | **T**ransverse **E**lectro**M**agnetic |

# Chapter 1

# Introduction

Much technological progress has been driven by advances in our understanding and ability to manipulate light. Even at the level of simple ray optics one can have an appreciation for the huge significance of devices such as microscopes and fiber optic cables. However, attempts to image features on the scale of the wavelength of light are fundamentally hindered by the diffraction limit [1]. Moving beyond traditional optics, this limit has been overcome with the use of plasmonic nanostructures [2, 3] such as metallic nanoparticles [4] which enable resolution right down to the molecular level [5]. This feat is due to a resonance effect: An external radiation source drives a collective oscillation of the valence electrons in a metallic nanoparticle which in turn experience an approximately harmonic restoring force from the ionic charge background, forming a localised surface plasmon resonance [6]. This generates a large optical field enhancement that is evanescently confined at the surface of the nanoparticle in a subwavelength region [7].

Individual nanoparticles have been extensively studied and successfully implemented in technologies such as surface enhanced Raman spectroscopy [5]. On the other hand, metamaterials — crafted arrays of functional components — have delivered fascinating new properties such as electromagnetic invisibility cloaking [8–10], perfect lensing [11, 12] and slow light [13]. Along these lines the focus is now shifting to plasmonic metamaterials consisting of ordered arrays of metallic nanoparticles, where interactions between the localised surface plasmons of each nanoparticle generate collective plasmonic modes that extend over the whole array [2, 3, 14–19]. Consequently the properties of these collective

plasmons crucially depend on the underlying lattice and its particular symmetries, which motivates the search for possible nanoparticle arrangements which may deliver unique and useful optical properties.

In fact there is a lattice which in the last decade has been elevated to a celebrity-like status, certainly within the condensed matter community. We are referring of course to the honeycomb structured lattice exhibited by graphene, a monolayer of carbon atoms arranged in a bipartite hexagonal lattice with three-fold rotational symmetry [20]. The hopping of electrons between carbon atoms within the honeycomb lattice leads to a band structure characterised by the presence of massless fermionic Dirac quasiparticles [21–24]. These pseudo-relativistic electrons possess an associated chirality which is responsible for many of the intriguing properties of graphene, such as a non-trivial Berry phase of $\pi$, the anomalous quantum Hall effect [22, 23], and the suppression of backscattering off smooth scatterers leading to very high mobilities in graphene samples [25, 26]. Importantly, the origin of all these phenomena is intrinsically linked to the symmetries of the system [27]. In essence, the effective massless Dirac Hamiltonian in graphene stems from the bipartite nature of the 2D lattice as well as from the time-reversal symmetric and parity-invariant nature of the system [28].

This fact has inspired the realisation of many artificial graphene systems [29] from cold atoms [30, 31] to photonic systems [32, 33]. As they share the same symmetries as real graphene, such artificial systems also boast relativistic Dirac quasiparticles that inherit many analogous phenomena. However, each different physical incarnation of the honeycomb lattice presents its own unique properties. In this thesis we are interested in the properties of collective plasmonic modes that exist in a honeycomb structured array of metallic nanoparticles, and their interaction with the photonic modes of an optical cavity. One can imagine how it might be interesting to recover some graphene-like properties in a plasmonic metamaterial, such as the suppression of backscattering off smooth inhomogeneities. Indeed we will discover that the collective plasmons behave as massless Dirac quasiparticles, but importantly with an extra degree of freedom encoded in their polarisation which provides a wide tunability of the bandstructure and eigenmodes. Naively one may expect that the presence of a photonic environment would not fundamentally alter the properties of the collective plasmons, however, we will unveil the intriguing ability to invert the chirality of Dirac polaritons simply by tuning the

coupling to a photonic environment that preserves the symmetries of the honeycomb lattice.

For this reason, in chapter 2 we begin with an introduction to the broader field of plasmonics as well as nanoparticle arrays in particular. We will discuss the effects of nanoparticle size, shape, arrangement and damping mechanisms on the optical properties, as well as explaining the regime in which we can model the interactions between localised surface plasmons as near-field dipolar. In addition we provide an introduction to polaritons and the strong-light matter coupling regime in general. Chapter 3 offers an introduction to graphene science and the technical concepts employed in the theoretical developments of later chapters. We will discuss the geometrical phase and related topics, as well as the electronic structure of graphene and phenomena linked to the chirality of Dirac quasiparticles.

In chapter 4 we study the collective plasmons that arise from the near-field dipolar interactions of the localised surface plasmons of individual nanoparticles arranged in a honeycomb lattice. We analyse the dispersion, Hamiltonian and eigenstates of the collective plasmons for an arbitrary polarisation of the dipole moments associated with the localised surface plasmons. When the dipole moments are orientated normal to the plane of the lattice the Hamiltonian maps to that of real graphene, and the dispersion exhibits Dirac cones with collective plasmons that behave as chiral massless Dirac bosons. In addition, due to the extra degree of freedom encoded in the polarisation the system has a highly tunable bandstructure. In fact we can even change its topology upon progressively tilting the polarisation, driving pairs of Dirac points to coalesce and annihilate resulting in a gapped phase. We identify a rich phase diagram that characterises the existence or absence of a gap in the dispersion as a function of the polarisation, and discover dispersions with several qualitative differences, including some that are translationally invariant in one direction and even flat bands. Moreover, we show that every gapless phase corresponds to dispersions with Dirac points. As the system is artificial there are several other possibilities to tune the physical properties, for example we show that breaking the inversion symmetry with inequivalent basis particles gives rise to gapped chiral modes with an energy dependent Berry phase.

The honeycomb structure is not the only bipartite, parity-invariant lattice. It belongs to the family of bipartite hexagonal lattices which all share these features, although the

honeycomb structure does boast an additional three-fold rotational symmetry. For this reason one might expect, as we show, that there is a wide class of bipartite hexagonal lattices which host Dirac-like collective plasmons, albeit with a modified band structure for each polarisation and a different distribution of gapped and gapless phases as a function of the polarisation. Indeed we show that a sequence of topological phase transitions occurs in the phase diagram while progressively shifting one sublattice with respect to the other.

These results suggest interesting possibilities in the design of ultra-thin metamaterials that effectively guide electromagnetic radiation via chiral Dirac modes, as well as the ability to precisely tune the bandstructure and eigenmodes. With an understanding of the collective plasmons in chapter 5 we will proceed to investigate the true eigenmodes responsible for transporting radiation in arrays of metallic nanoparticles, that arise from the interaction between the plasmonic modes and a photonic environment. Such light-matter interactions have been widely explored in the weak coupling regime where the semiclassical description of radiation is employed [2, 3, 14–19, 34]. However, it has long been known that a semiclassical description is unsatisfactory for describing the fundamental mechanisms of absorption in periodic systems where crystal momentum is conserved and the matter and light fields are strongly interacting [35, 36]. In this case a full quantum treatment is required, leading to new quasiparticles, termed polaritons, which are a coherent superposition of the light and matter fields. Specifically we will consider a honeycomb array of metallic nanoparticles embedded within a planar optical cavity and consider the interaction between collective plasmons and the fundamental cavity mode. We will verify that these plasmon polaritons are still described by a massless Dirac Hamiltonian, as expected from the symmetries of the matter system. However, we wish to emphasise that it is also the photonic states which can be tailored to give qualitatively distinct polaritonic properties for the same matter system. In this vein we will highlight a phenomenal tunability of the bandstructure and eigenstates that arises from modulation of the photonic states of the enclosing cavity, permitting order-of-magnitude renormalisation of the group velocity and the enthralling ability to invert the chirality of Dirac modes. These considerations suggest the ability to realise interesting transport properties of Dirac polaritons via modulation of a photonic environment that preserves the underlying symmetries of the system.

Lastly in chapter 6 we introduce preliminary results on pseudomagnetic gauge fields that

arise from suitably designed strains of the plasmonic metamaterial. We will see that the magnitude and even sign of the pseudomagnetic field can be altered by the orientation of the dipoles, implying a unique anisotropy whereby EM radiation of different polarisations would couple to collective plasmonic modes that experience significantly different pseudomagnetic fields. We then provide conclusions in chapter 7.

# Chapter 2

# Introduction to plasmonics

In the following we introduce foundational concepts in plasmonics relevant to the theoretical developments in this thesis, and review key results from the literature which place our work in context and provide insight into the experimental feasibility of our propositions.

Our research focuses on the properties of extended plasmonic and polaritonic modes supported by periodic arrays of metallic nanoparticles. Thus in section 2.1 we begin by discussing the optical properties of metals, introducing plasmons in bulk metals within the Drude model. These basic ideas are then extended to surface plasmon polaritons which can exist at the boundary between a metal and a dielectric. We decrease in dimensionality once more in section 2.2 to discuss localised surface plasmons in single metallic nanoparticles, and the effects of size, shape, and damping mechanisms. We arrive at our system of interest in section 2.3 where we examine the properties of collective plasmonic excitations that arise from interactions between nanoparticles in arrays. Later we wish to investigate the strong coupling between these collective plasmons and photons. Thus section 2.4 explains the formalism introduced by Hopfield for describing the strong-coupling regime between light and matter. We finish by summarising the chapter in section 2.5.

## 2.1 Plasmonics

Before describing nanoparticles we commence with a discussion of the basic optical properties of metals from the phenomenological view point of Maxwell's equations. We restrict ourselves to linear, isotropic and nonmagnetic media so as to present a clear and concise development of the models which lead to the notions of both bulk and surface plasmons. This will provide a backdrop to the introduction of localised surface plasmons in the subsequent section.

### 2.1.1 Electromagnetics

While they can be found in countless books, printed on t-shirts and engraved on monuments, it can't hurt to start a discussion involving electromagnetics by restating Maxwell's equations. The integral equations are shown in Figure 2.1 whilst the differential equations describing the four macroscopic fields **D**, **B**, **E** and **H** (electric displacement, magnetic induction, electric field and magnetic field) are

$$\nabla \cdot \mathbf{D} = \rho_{\text{ext}}, \tag{2.1}$$

$$\nabla \cdot \mathbf{B} = 0, \tag{2.2}$$

$$\nabla \times \mathbf{E} = -\frac{\partial \mathbf{B}}{\partial t}, \tag{2.3}$$

$$\nabla \times \mathbf{H} = \mathbf{J}_{\text{ext}} + \frac{\partial \mathbf{D}}{\partial t}, \tag{2.4}$$

where $\rho_{\text{ext}}$ and $\mathbf{J}_{\text{ext}}$ are the external charge and current densities.

The link between the electric (magnetic) field and the displacement (induction) field can be expressed as a constitutive relation, dependent on material properties. In a linear medium these fields are related by the identities

$$\mathbf{D} = \epsilon_0 \epsilon \mathbf{E}, \tag{2.5}$$

$$\mathbf{B} = \mu_0 \mu \mathbf{H}, \tag{2.6}$$

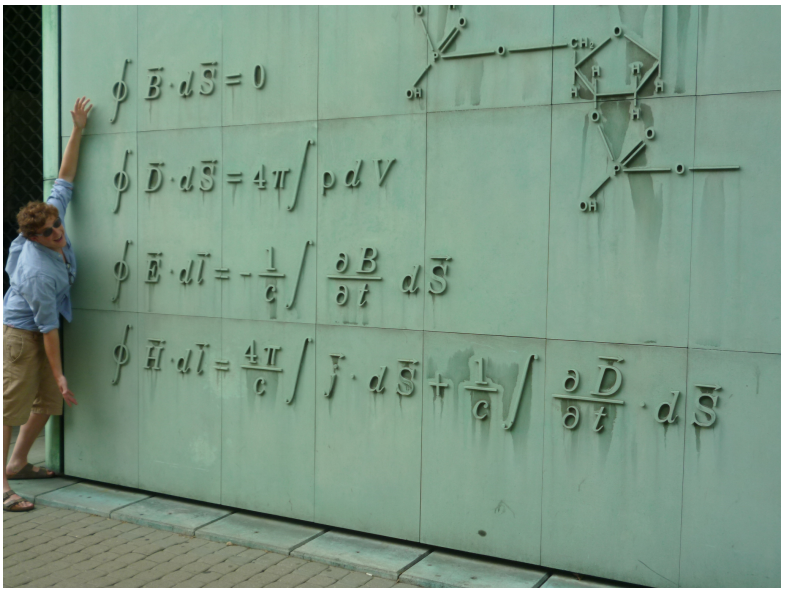


**Figure 2.1:** Maxwell's equations as featured on a monument in front of Warsaw University's Centre of New Technologies. Author included for scale.

where $\epsilon_0$ and $\mu_0$ are the permittivity and permeability of free space. We consider non-magnetic materials with a relative permeability $\mu = 1$. Moreover, we are interested in generalising the relative permittivity constant $\epsilon$ in equation 2.5 such that

$$\mathbf{D}(\mathbf{r}, t) = \epsilon_0 \int dt' d\mathbf{r}' \epsilon(\mathbf{r} - \mathbf{r}', t - t') \mathbf{E}(\mathbf{r}', t'), \tag{2.7}$$

which describes a linear homogeneous material with spatial and temporal dispersion. In the Fourier domain this becomes

$$\mathbf{D}(\mathbf{k}, \omega) = \epsilon_0 \epsilon(\mathbf{k}, \omega) \mathbf{E}(\mathbf{k}, \omega), \tag{2.8}$$

where $\epsilon(\mathbf{k}, \omega)$ is termed the dielectric function [3]. One can calculate an explicit expression for $\epsilon$ in terms of microscopic quantities within the free electron model, which we describe in the following section.

A general solution of Maxwell's equations can be constructed from a basis of plane waves $\mathbf{E}_0 \propto \mathrm{e}^{i(\mathbf{k}\cdot\mathbf{r} - \omega t)}$. By combining Maxwell's curl equations 2.3 and 2.4 these solutions can be seen to satisfy

$$\mathbf{k}(\mathbf{k} \cdot \mathbf{E}_0) - |\mathbf{k}|^2 \mathbf{E}_0 = -\epsilon(\mathbf{k}, \omega) \frac{\omega^2}{c^2} \mathbf{E}_0 .. \tag{2.9}$$

where we have used the identity $\epsilon_0\mu_0 = 1/c^2$. Note that equation 2.9 suggests that longitudinal waves ($\hat{\mathbf{k}} \cdot \hat{\mathbf{E}} = 1$) can only exist at the zeros of $\epsilon(\mathbf{k}, \omega)$. Later we will find that this occurs at the plasma frequency and corresponds to a bulk plasmon. Firstly however, we examine the dielectric function of the free electron gas.

### 2.1.2 Plasma model

The plasma model of a metal [37] assumes that a gas of free electrons exist within a fixed homogeneous ionic background. All interactions between electrons are effectively incorporated into a phenomenological effective electron mass $m$.

For frequencies below ultraviolet the characteristic dimensions of a metal such as the mean free path and unit cell are significantly smaller than the wavelength of light [3]. In these conditions the interaction of the metal with light is adequately described by a spatially local response, calculated in the long wavelength limit $\epsilon(0, \omega) = \epsilon(\omega)$ from the equation of motion for a single electron in a spatially homogeneous electric field:

$$m\left(\frac{d^2\mathbf{u}}{dt^2} + \gamma\frac{d\mathbf{u}}{dt}\right) = -e\mathbf{E}, \tag{2.10}$$

where $\mathbf{u}$ is the displacement of the electron and $\gamma = 1/\tau$ is a characteristic collision rate, with $\tau$ the relaxation time of the free electron gas. For noble metals at room temperature these values are typically on the order of $\gamma = 100\text{THz}$ and $\tau = 10^{-14}\text{s}$ [3]. Assuming a harmonic time dependence of $\mathbf{E}$ the solution of equation 2.10 gives us the polarisation density $\mathbf{P} = -ne\mathbf{u}$ as

$$\mathbf{P} = -\frac{ne^2}{m(\omega^2 + i\gamma\omega)}\mathbf{E}. \tag{2.11}$$

where $n$ and $e$ are the electron density and charge respectively. Upon equating the definition of the electric displacement field $\mathbf{D} = \epsilon_0\mathbf{E} + \mathbf{P}$ with the constitutive relation 2.5 we obtain the dielectric function

$$\epsilon(\omega) = 1 - \frac{\omega_\text{p}^2}{\omega^2 + i\gamma\omega}, \tag{2.12}$$

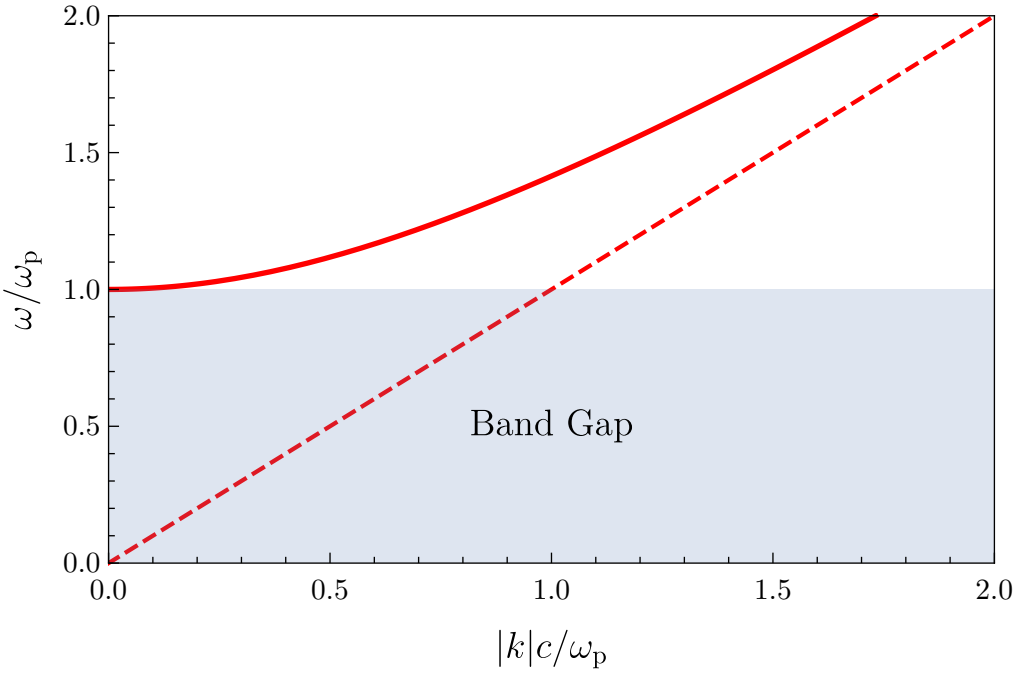


**Figure 2.2:** Dispersion of transverse EM modes within a metal described by the plasma model (solid line), corresponding to equation 2.14. The shaded region indicates where the propagation of travelling modes is forbidden, and the dashed line corresponds to the dispersion of light in vacuum.

where $\omega_p = \sqrt{ne^2/m\epsilon_0}$ is the plasma frequency. At large frequencies such that $\omega \gg \gamma$, damping can be neglected and one can approximate the dielectric function as

$$\epsilon(\omega) = 1 - \frac{\omega_p^2}{\omega^2}. \tag{2.13}$$

By inserting equation 2.13 into the wave equation 2.9 we obtain the dispersion of transverse waves ($\mathbf{k} \cdot \mathbf{E} = 0$) within the plasma model as

$$\omega = \omega_p \sqrt{1 + \left(\frac{c|\mathbf{k}|}{\omega_p}\right)^2}, \tag{2.14}$$

which is shown in Figure 2.2. We see the significance of the plasma frequency firstly as the cut-off frequency below which the propagation of transverse EM modes is forbidden in the plasma. Its significance in relation to longitudinal modes is discussed in the subsequent section.

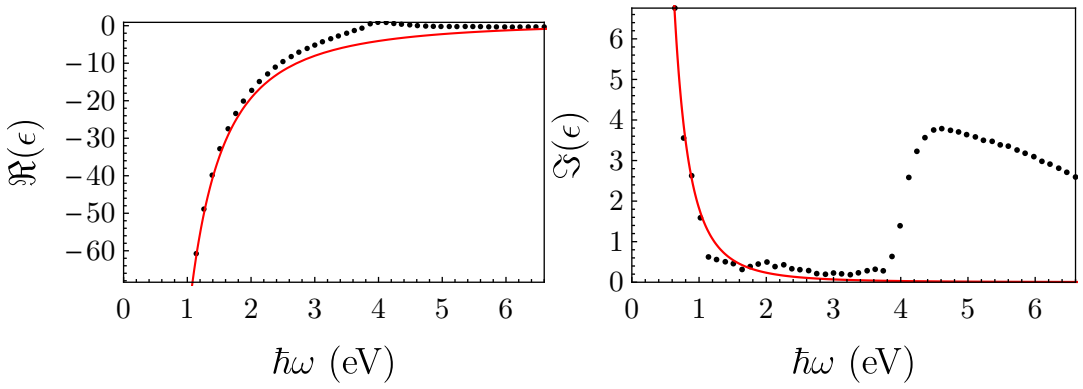


**Figure 2.3:** The plasma model of equation 2.12 (solid line) fitted to data for the real and imaginary components of $\epsilon$ (dots) of silver determined by Johnson and Christy [40]. The optimal fit parameters are $\omega_p = 8.94$eV and $\gamma = 22.8$meV. Based on figures from reference [3].

For frequencies less than $\omega_p$ the field falls off exponentially inside the metal as $e^{-z/\delta}$ where $\delta$ is termed the skin depth. In this regime the plasma model is valid so long as the mean free path of electrons $l$ is less than $\delta$. Typical values for noble metals at room temperature are $l \approx 10$nm and $\delta \approx 100$nm [3], so the model provides a reasonable description in this respect. However, interband transitions can cause a significant deviation from this simple description at visible frequencies [6]. Figure 2.3 shows experimental values of $\epsilon$ for silver fitted by a plasma (Drude) model, where one can clearly observe the sudden departure from a qualitative fit above the band edge threshold. Despite these drawbacks the Drude model is still commonly used, particularly in Finite-Difference-Time-Domain (FDTD) calculations where a phenomenological term $m\omega_0\mathbf{u}$ is introduced to equation 2.10 to model the damping caused by interband transitions [38, 39].

### 2.1.3 Volume plasmons

We have discussed some of the properties of electromagnetic excitations at frequencies above and below $\omega_p$. Now we consider the behaviour at the plasma frequency in the small damping limit (equation 2.13), which by inspection of the wave equation 2.9 corresponds to a longitudinal oscillation mode. The electric field is a pure depolarisation field

$$\mathbf{E} = -\frac{\mathbf{P}}{\epsilon_0} = \frac{ne\mathbf{u}}{\epsilon_0}, \tag{2.15}$$

which upon substitution into the equation of motion 2.10 gives

$$\frac{d^2\mathbf{u}}{dt^2} + \omega_{\mathrm{p}}^2\mathbf{u} = 0. \tag{2.16}$$

So we observe the significance of the plasma frequency also as the natural frequency of a free oscillation of the electron sea. The quanta of this longitudinal plasma oscillation is our first example of a plasmon, termed a volume plasmon [37]. As this is a longitudinal mode volume plasmons cannot couple directly to light and are typically excited by particle impact, as in Electron Enegry Loss Spectroscopy [41] (EELS) which is used to determine the plasma frequency of metals. Similarly due to a lack of radiative decay energy is predominantly lost through Landau damping [42–44]. Whilst this description is generally true for bulk metals, it is interesting to note that the photoexcitation of volume plasmons is possible in other geometries, for example high-energy volume plasmon modes in nanoshells [45] and volume plasmon polaritons in hyperbolic metamaterials [46, 47].

### 2.1.4 Surface plasmons

We have seen that for frequencies below the plasma frequency of a metal there is a photonic band gap, where the propagation of transverse EM modes is forbidden. However, propagating EM modes can exist at a metal-dielectric interface, where interactions between plasma oscillations (surface plasmons) and EM modes in the dielectric (photons) lead to a hybridised mode, called a surface plasmon polariton [2] (SPP). To better appreciate their properties, let us investigate the simplest geometry supporting a SPP.

We consider a system consisting of two half plane regions with homogeneous dielectric function

$$\epsilon(\omega, z) = \begin{cases} \epsilon_{\mathrm{M}}(\omega) & , z < 0 \\ \epsilon_{\mathrm{D}} & , z > 0 \end{cases}, \tag{2.17}$$

where $\epsilon_{\mathrm{D}}$ is the permittivity of the dielectric and $\epsilon_{\mathrm{M}}(\omega)$ is the dielectric function of the metal. We choose the propagation to be in the $x$-direction such that the electric field eigenmodes are $\mathbf{E}(x, y, z) = \mathbf{E}(z)\exp(i\beta x)$, where $\beta \equiv k_x$ is the propagation wavenumber. Our task now consists of solving the wave equation 2.9 in the absence of external stimuli $\nabla \cdot \mathbf{D} = 0$ in the two half planes, along with the interface boundary conditions

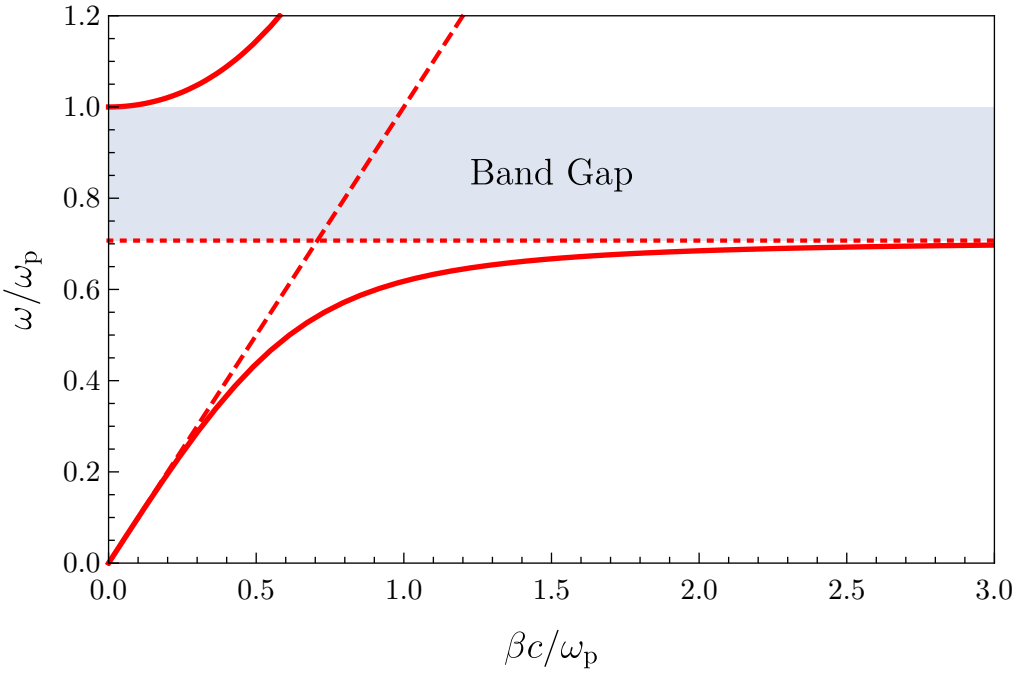


**Figure 2.4:** Dispersion of SPPs at the interface between a Drude metal and air (solid line). Also shown are the light line (dashed line), the surface plasmon frequency $\omega_{sp}$ (dotted line), and the band gap (shaded region).

which require continuity of $H_y$ and $\epsilon(z)E_z$ [48]. The well known details are relegated to Appendix A, where it is shown that SPPs only exist for transverse magnetic (TM) modes, and that for these modes to be confined to the surface we require the dielectric function to have an opposite sign in each of the half plane regions. The resulting dispersion equation is

$$\beta = \frac{\omega}{c}\sqrt{\frac{\epsilon_M(\omega)\epsilon_D}{\epsilon_M(\omega)+\epsilon_D}}, \tag{2.18}$$

which is plotted in Figure 2.4 for an interface between a Drude metal and air. Note that we have two distinct modes, each of which is a hybridisation of the original bare light and matter curves. These modes display an 'anti-crossing' at the original crossing point, and are separated by an energy gap. The curve that lies outside the light cone corresponds to the SPP mode evanescently confined to the surface with $\omega < \omega_p$, whereas the curve that lies within the light cone corresponds to the frequency regime $\omega > \omega_p$ where the material loses its metallic character and supports radiative modes. The SPP

mode tends towards the air light curve in the limit $\beta \to 0$, whereas in the opposite limit $\omega$ tends towards the value

$$\omega_{\mathrm{sp}} = \frac{\omega_{\mathrm{p}}}{\sqrt{1+\epsilon_{\mathrm{D}}}}, \tag{2.19}$$

known as the surface plasmon (SP) frequency. At the same time the group velocity tends to zero and the mode develops an electrostatic character, corroborated by the fact that this mode is also a solution of the Laplace equation [49].

Two notable consequences of the SPP dispersion are that firstly, as the lower branch lies outside the light cone, ideal SPPs on smooth surfaces are non-radiative and cannot be directly excited by light [2]. Techniques such as prism [50, 51], grating [52–54] and near-field [55, 56] coupling, as well as roughened or patterned metallic surfaces [57] must be used to overcome the momentum mismatch. Secondly, while there is a propagating mode at the interface, perpendicularly to the surface it is of a near-field nature and evanescently confined. This behaviour normal to the interface is characterised by the exponential decay length $\delta_{\mathrm{D}} = 1/k_z = \left[\beta^2 - \epsilon_{\mathrm{M}}(\omega/c)^2\right]^{-1}$, while the propagation has an attenuation length scale $L = [2\mathrm{Im}(\beta)]^{-1}$ [58]. Thus we see there is an inherent trade off between localisation and loss.

## 2.2 Localised surface plasmons

We have begun to see how the manipulation of material properties can drastically alter their electromagnetic response. Ever improving nanofabrication techniques have granted researchers the ability to control system features on a scale less than the wavelength of (visible) light itself, leading to the advent of metamaterials. This class of structures, with subwavelength constituents and patterning, have revealed some remarkable optical properties not found in nature such as electromagnetic invisibility cloaking [8–10], perfect lensing [11, 12] and slow light [13]. In this section we discuss the optical properties of individual metallic nanoparticles, before addressing the collective excitations that emerge in metamaterials consisting of arrays of such constituents in the following section.

The interaction of valence electrons with an external radiation source produces a non-propagating excitation in a metallic nanoparticle, termed a localised surface plasmon

(LSP). The LSP mode is evanescently confined to the surface of the nanoparticle, with a strong optical field enhancement in this subwavelength region [2, 3, 49]. This triumph over the diffraction limit has enabled resolution at the molecular level [5]. Such effects are pronounced at the LSP resonance frequency, which for gold and silver nanoparticles lies in the visible range, making nanoparticles particularly useful as the functional component in many products and sensors [59]. Moreover, LSPs can be excited by direct light illumination, in contrast to the volume and surface plasmons encountered so far.

In this section we will first analyse the eigenmodes of a spherical nanoparticle, as well as the response in presence of a quasistatic external electric field. It will be shown that in this regime, as well as in actuality for nanoparticles with dimensions less than 100nm under visible light illumination, the dominant mode is a dipolar excitation at the LSP resonance frequency. We then present an account of the effects of size, shape, material and dielectric environment on the LSP resonance. Following this we introduce an effective Hamiltonian, starting from the full electronic description and performing a decomposition into electronic centre of mass coordinates. This will form the noninteracting term of the Hamiltonians in subsequent chapters. Finally we discuss damping mechanisms for LSPs.

### 2.2.1 Eigenmodes of a spherical nanoparticle

We consider a metallic nanosphere of radius $\text{ר}$ embedded in a dielectric medium $\epsilon_{\mathrm{D}}$ as shown in Figure 2.5. Thus the full system can be described by the dielectric function

$$\epsilon(\omega, r) = \begin{cases} \epsilon_{\mathrm{M}}(\omega) & , r < \text{ר} \\ \epsilon_{\mathrm{D}} & , r \geq \text{ר} \end{cases} . \tag{2.20}$$

In the absence of external charges and fields, the electric potential eigenmodes are the well known solutions of the Laplace equation [49]

$$\Phi_l(r, \theta) = \begin{cases} A_l (r/\text{ר})^l P_l(\cos\theta) & , r < \text{ר} \\ B_l (\text{ר}/r)^{l+1} P_l(\cos\theta) & , r \geq \text{ר} \end{cases} , \tag{2.21}$$

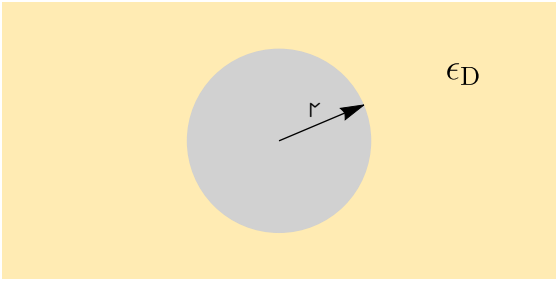


**Figure 2.5:** Schematic of a nanosphere of radius r embedded in a medium with dielectric constant $\epsilon_D$.

where $P_l$ is a Legendre polynomial of order $l$, $\theta$ is the polar angle from the $z$-axis, $A_l$ and $B_l$ are coefficients which require additional boundary conditions to specify, and unphysical solutions at $r \to 0$ and $r \to \infty$ have been neglected. Of course due to the spherical symmetry there are additional solutions for each choice of the $\hat{\mathbf{z}}$ direction. Continuity of the tangential electric field $E_\theta = -(1/r)(\partial\Phi_l/\partial\theta)$ is automatically satisfied whereas continuity of the normal component of the displacement field $D_r = -\epsilon(\partial\Phi_l/\partial r)$ designates the constraint

$$l\epsilon_M(\omega_l) + (l+1)\epsilon_D = 0, \tag{2.22}$$

which for a Drude metal leads directly to the LSP eigenfrequencies

$$\omega_l = \omega_p\sqrt{\frac{l}{l+(l+1)\epsilon_D}}, \tag{2.23}$$

where $\omega_M \equiv \omega_1$ is the Mie frequency [6]. It is seen in Figure 2.6 that as $l$ increases the mode becomes increasingly confined to the nanosphere surface, and the multipole solutions gradually approach the SP frequency $\omega_{sp}$ of a bulk metal-dielectric interface. However, the $l = 1$ solution is the only mode with a non-zero total dipole moment and thus the only mode that can couple to external radiation [49], in the limit of vanishing particle size with respect to the wavelength $\lambda$. Indeed for particles with radii up to tens of nanometers at visible wavelengths the optical response is strongly dominated by this $l = 1$ dipolar mode [6, 60]. Thus for $r \ll \lambda$ we can consider the effect of external radiation in the quasistatic limit, by considering a spatially homogeneous electric field $\mathbf{E}_0 = E_0\hat{\mathbf{z}}$ with a harmonic time dependence. The external field introduces the additional

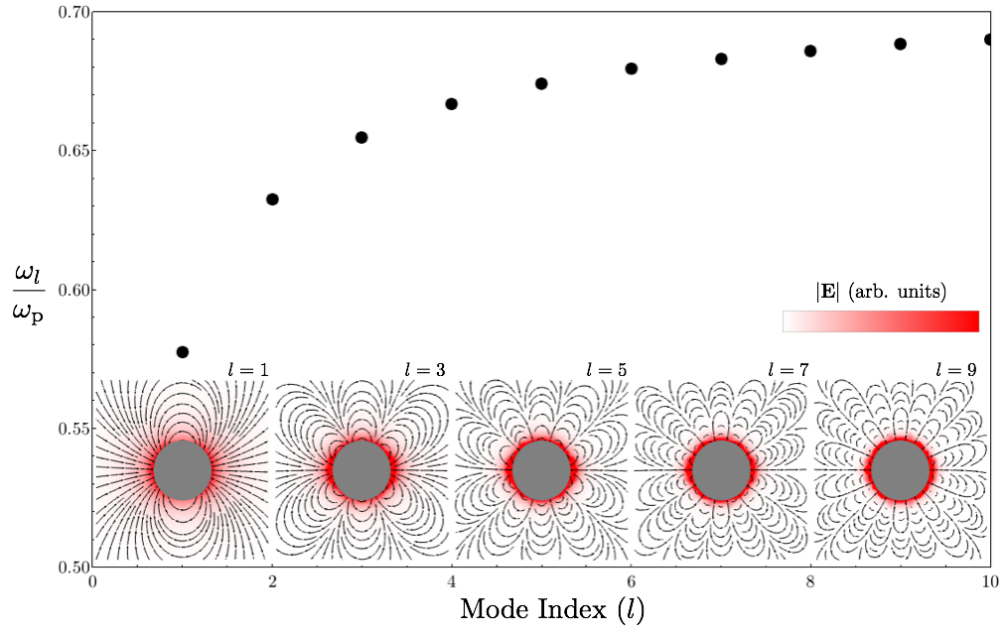


**Figure 2.6:** The eigenfrequency of the $l$th LSP mode of a nanoparticle in air (dots) is seen to tend towards the bulk SP frequency $\omega_{sp} \approx 0.71$. The insets show the electric field lines of various modes (given in each inset), as well as a visualisation of the field strength (color scale in arbitrary units).

boundary condition $\lim_{r\to\infty}(\Phi) = -E_0 z$ to the total electric potential $\Phi = \sum_l \Phi_l$, which gives the total electric field $\mathbf{E} = -\nabla\Phi$ as

$$\mathbf{E} = \begin{cases} \dfrac{3\epsilon_D}{\epsilon_M + 2\epsilon_D}\mathbf{E}_0 & , r < r \\ \mathbf{E}_0 + \dfrac{3\hat{\mathbf{r}}(\hat{\mathbf{r}}\cdot\mathbf{p}) - \mathbf{p}}{4\pi\epsilon_0\epsilon_D r^3} & , r \geq r \end{cases}. \tag{2.24}$$

Knowledge of the electric field eigenmodes of a nanosphere is useful for the development of interaction models used in later chapters. However, we must be wary of the realms of applicability of a quasistatic approximation and neglecting higher order multipoles. We will shortly collate studies on the effects of size, shape and material composition on the optical response of metallic nanoparticles.

### 2.2.2 Electronic centre-of-mass decomposition

We now seek to obtain an effective Hamiltonian for an individual spherical nanoparticle starting from a microscopic description. Although one can write down the exact Hamiltonian in terms of an ensemble of interacting ions and electrons, it is an impossible task to solve the corresponding Schrödinger equation and thus approximation schemes are

employed. The jellium model [61], whereby the complicated ionic structure is replaced by a constant background charge, has been used successfully to describe the properties of metallic nanoparticles [62–64], modelling the ionic background as a jellium sphere with sharp boundaries and a radius $\text{ר}$. By a trivial application of Gauss's law in integral form one finds the single-particle confining potential of valence electrons to be

$$U(r) = \frac{Ne^2}{8\pi\epsilon_0\epsilon_{\mathrm{D}}\text{ר}^3}(r^2 - 3\text{ר}^2)\Theta(\text{ר} - r) - \frac{Ne^2}{4\pi\epsilon_0\epsilon_{\mathrm{D}} r}\Theta(r - \text{ר}), \tag{2.25}$$

where $\Theta$ is the Heaviside step function and $N$ is the total number of valence electrons. Thus the Hamiltonian for the $N$ valence electrons is

$$H = \sum_i^N \left\{ \frac{p_i^2}{2m} + U(r_i) + \frac{e^2}{8\pi\epsilon_0} \sum_{j\neq i}^N \frac{1}{|\mathbf{r}_i - \mathbf{r}_j|} \right\}. \tag{2.26}$$

One can express this Hamiltonian in terms of the electronic centre of mass $\mathbf{h} = \sum_i \mathbf{r}_i/N$, its conjugated momentum $\mathbf{\Pi} = \sum_i \mathbf{p}_i$ and the relative coordinates in this frame: $\mathbf{r}'_i = \mathbf{r}_i - \mathbf{h}$ and $\mathbf{p}'_i = \mathbf{p}_i - \mathbf{\Pi}/N$. Assuming the displacement of the centre of mass $\mathbf{h}$ is small compared to the nanoparticle size, the single-particle potential $U(|\mathbf{r}'_i + \mathbf{h}|)$ can be expanded around $|\mathbf{h}| = 0$. Keeping terms up to second order in $\mathbf{h}$ within the harmonic part of the potential ($r' < \text{ר}$), and up to first order in the coulombic tail ($r' \geq \text{ר}$) transforms the Hamiltonian to

$$H = H_{\text{c.m.}} + H_{\text{rel}} + H_{\text{c}}. \tag{2.27}$$

The Hamiltonian of the centre-of-mass coordinates is

$$H_{\text{c.m}} = \frac{\mathbf{\Pi}^2}{2M} + \frac{1}{2}M\omega_0^2\mathbf{h}^2, \tag{2.28}$$

where $M = Nm$ is the total mass of the valence electrons and $\omega_0 = \omega_M\sqrt{1 - N_{\text{out}}/N}$ is the Mie frequency $\omega_M$ renormalised by a factor dependent on the number of valence electrons outside the jellium sphere, $N_{\text{out}} = N - \sum_{i=1}^N \Theta(\text{ר} - r_i)$. $H_{\text{rel}}$ is simply the Hamiltonian for the relative-coordinate system and of the exact same form as 2.26 with

the transformation $(\mathbf{p}, \mathbf{r}) \rightarrow (\mathbf{p}', \mathbf{r}')$. The coupling between the two coordinate systems to first order in $\mathbf{h}$ is given by $H_{\mathrm{c}}$ and is

$$H_{\mathrm{c}} = m_e \omega_M^2 \sum_i^N \mathbf{r}_i' \cdot \mathbf{h} \left\{ \Theta(\text{ר} - r_i') + \frac{\text{ר}^3}{r_i'^3} \Theta(r_i' - \text{ר}) \right\}. \tag{2.29}$$

This approximation scheme allows us to treat the localised surface plasmon as the oscillation of a collective coordinate associated with the centre of mass motion, damped by interactions with the relative-coordinate system.

As has been established by multiple photoabsorption experiments [65] the spectra of metallic nanoparticles typically display a 'giant dipole resonance' close to the classical Mie values for the dipole resonance frequency of a classical small metal sphere. Thus this resonance should be interpreted as being due to the collective motion of the delocalised valence electrons, with the external electromagnetic field coupling directly with the electronic centre-of-mass. In this way $H_{\mathrm{c.m.}}$, which is formally equivalent to the Hamiltonian of a point dipole, is the dominant term in the Hamiltonian for an LSP.

### 2.2.3 Effects of size, shape and material

Clearly the optical properties of nanoparticles depends on the dielectric environment, as seen explicitly in equation 2.23, as well as the material constituent of the nanoparticle via the plasma frequency. The effect of temperature on the absorption spectra is minimal for commercial electronics operating ranges [66, 67], as seen in Figure 2.7. However, it is the geometry of nanoparticles that is of interest, as one can fine tune the plasmonic properties by manipulating the size and shape of nanoparticles [60].

There are a wide range of nanofabrication techniques with varying levels of resolution and throughput [68]. With electron beam lithography it is possible to achieve sub-nanometer resolutions [69, 70], whilst few nanometer resolution is readily realisable [71]. There are a host of other methods such as the chemical synthesis of nanoparticles, including the use of DNA as a template to organise few nanometre nanoparticles into single chains with long-range order [72]. Consequently it is possible to precisely engineer the size, shape and arrangement of nanoparticles and thus the optical response.

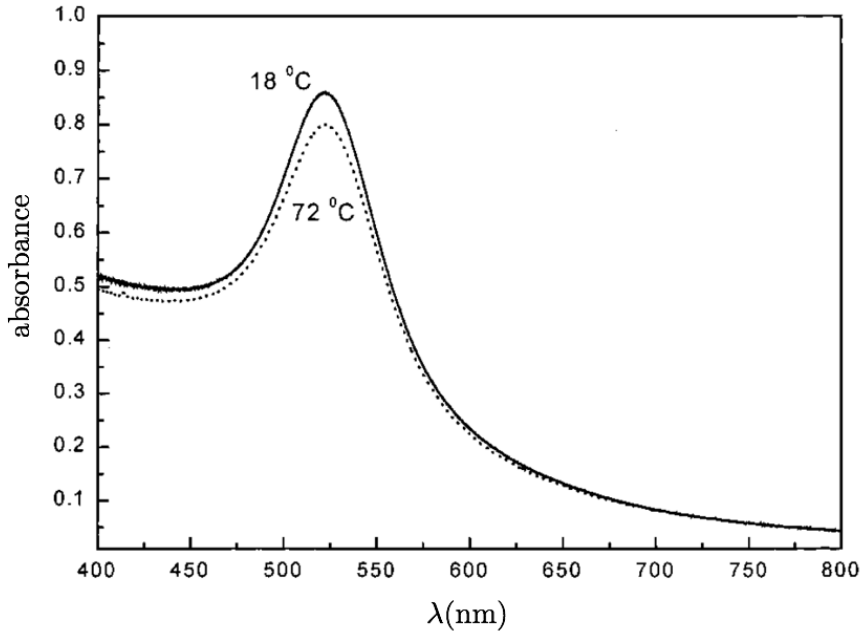


**Figure 2.7:** Temperature dependence of the absorption spectra for gold nanoparticles with radii of 22nm. The absorption spectra are measured at 18°C (solid line) and 72°C (dashed line) using spectrophotometry. Reprinted with permission from [66]. Copyright 1999 American Chemical Society.

Equation 2.23 suggests that the resonance frequency of metallic nanoparticles is size independent, however, spectroscopy measurements show that in reality this is not true. Whilst reports on the governing relationship between the size of nanoparticles and their spectra can be in conflict [73], as this scaling is dependent on other parameters of the particle and environment, in general an increase in particle size corresponds to a red-shift of the resonance peak [74], as seen in Figure 2.8. We can intuitively understand this shift as due to an increase in the separation of oppositely charged surfaces either side of the nanoparticle as its size increases, leading to a reduction in the restoring force and hence a decrease in the resonant frequency.

As well as the resonance peak, the width of the optical spectrum is also size-dependent, with two key mechanisms. Nanoparticles on the scale of ten nanometres have dimensions comparable to or less than the electron mean free path, leading to a modified scattering rate of the dielectric function 2.12 due to collisions with the nanoparticle surface, leading to a $1/r$ broadening of $\gamma$ as the particle size decreases. On the other hand as the particle size increases radiation damping, which scales like $r^3$, also causes a significant broadening. Accounting for these two key contributions, one typically models the scattering rate as [75]

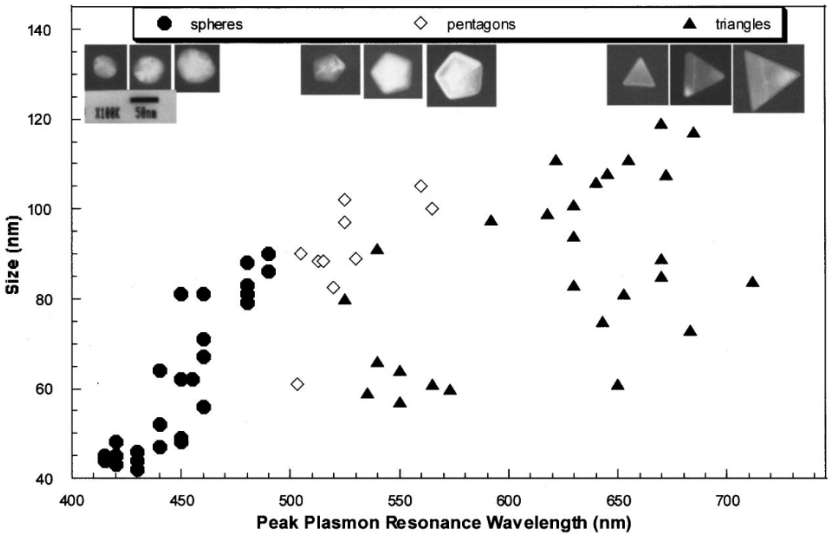


**Figure 2.8:** Plot of the peak plasmon resonance wavelength of individual nanoparticles as a function of their size, for three different shapes. Here size refers to: the diameter of spheres, the length between opposite corners of pentagons, and the length of a side of triangles. In each case there is a red-shift with increasing size, as well as a clear dependence on the shape itself. Reprinted from [74], with the permission of AIP Publishing.

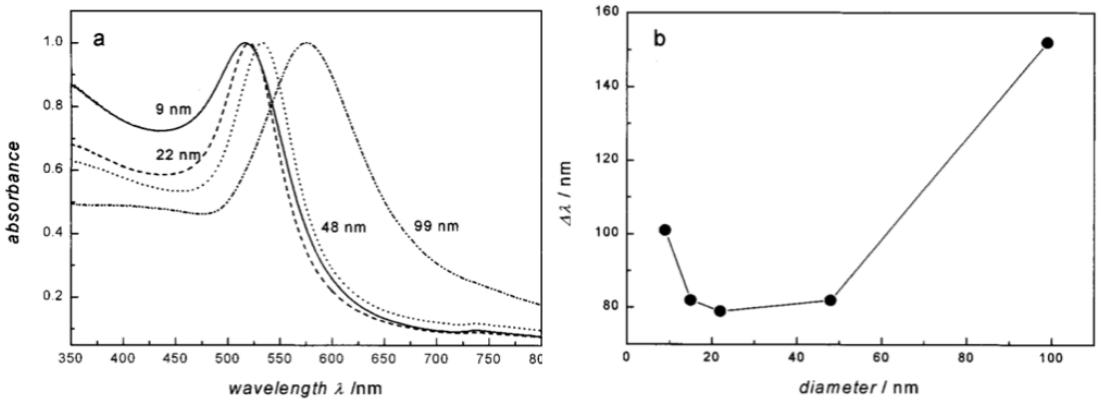


**Figure 2.9:** (a) Optical absorption spectra of spherical gold nanoparticles, normalised to the spectral peak maximum, for various diameters. (b) The bandwidth $\Delta\lambda$ of the spectra (full-width-half-maximum when fitted with a Lorentzian curve). Reprinted with permission from [66]. Copyright 1999 American Chemical Society.

$$\gamma = \gamma_0 + \frac{Av_F}{r} + \frac{2\omega_M^4 r^3}{3c^3}, \tag{2.30}$$

where $\gamma_0$ is the Ohmic damping rate, $v_F$ is the Fermi velocity of conduction electrons and $A$ is a geometrical factor [66, 76]. Thus for each nanoparticle and environment there is a dimensional sweet spot where the total broadening effects are minimal. In the example of Figure 2.9 with gold nanoparticles we can see this occurs at about $r = 10$nm.

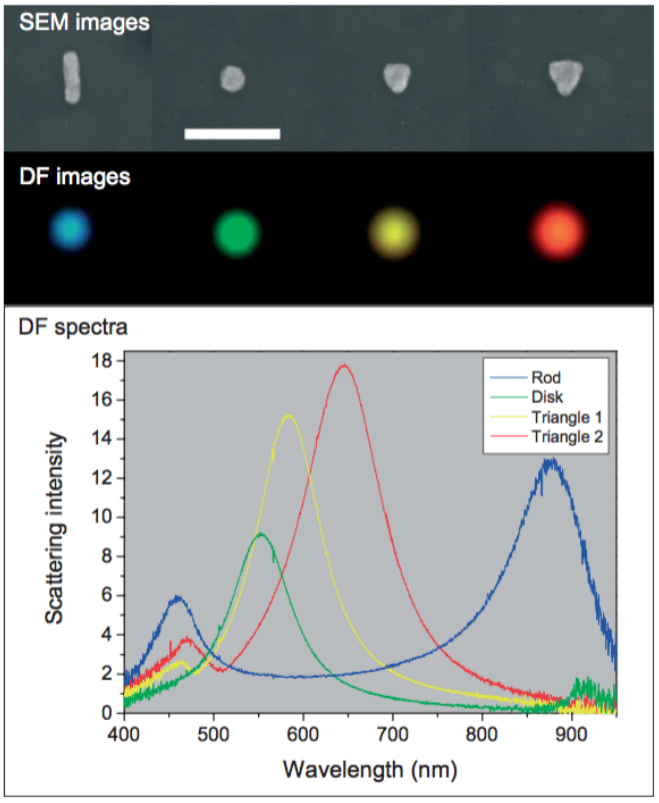


**Figure 2.10:** From left to right we see a 30nm thick nanoparticle rod, disk and two triangles, in scanning electron micrographs (top), dark-field images (middle), and dark-field spectra (bottom). The white scale bar is 300nm. Reprinted with permission from [77]. Copyright 2007 John Wiley & Sons.

The shape of a nanoparticle is also a key parameter in determining the optical response. In Figure 2.8 we see that the spectral peaks of different shapes are well separated in frequency. This effect is visually evident in Figure 2.10 where different shaped nanoparticles appear different colours in dark-field microscopy [77]. We also see that there are additional types of resonances in differently shaped nanoparticles. The nanorod has two discernible dipole resonances associated with the major and minor axis, which are red and blue shifted respectively. The triangular nanoparticles also display two resonances, in this case these correspond to a dominant dipole mode and a quadrupole mode at a smaller wavelength [78].

The multipolar characteristics of nanoparticles are pertinent to the reliability of models used throughout this thesis, which consider only the dipole response. Typically for nanospheres and similar geometries on the scale of a few tens of nanometers the electromagnetic response is overwhelmingly dipolar in nature [79, 80]. Even as the quadrupole mode becomes appreciable in nanoparticles on the scale of several tens of nanometres,

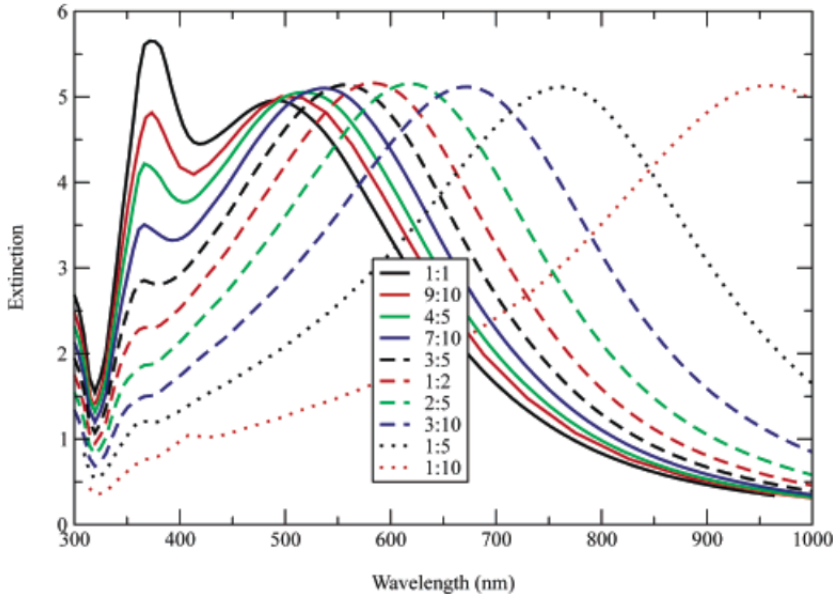


**Figure 2.11:** Exact electrodynamic calculation of the extinction spectra of oblate spheroids, all with the same equivalent volume, corresponding to a sphere radius of 80nm. In this figure the extinction is normalized to the area of a circle with radius equal to the semi-major axis. As the asymmetry is increased the dipole peak is red-shifted while the quadrupole mode shrinks in intensity. Reprinted with permission from [60]. Copyright 2003 American Chemical Society.

the dipolar mode is typically still dominant and well separated in frequency. Moreover, it is possible to introduce an asymmetry into the geometry so as to quench the quadrupole mode [60] as shown in Figure 2.11.

### 2.2.4 Damping mechanisms

The dephasing time $T_2 = 2\hbar/\Gamma$ of an LSP can be extracted from the homogeneous linewidth $\Gamma$ [3]. Attempts to deduce the linewidth of single nanoparticles from measurements on aggregates are limited by the inhomogeneous broadening introduced by sample variation and thus it can be preferable to conduct near-field measurements of individual nanoparticles [4]. Typical values for the dephasing time lie in the range $5\text{fs} \leq T_2 \leq 10\text{fs}$ [3] with various radiative and non-radiative decay mechanisms.

We have seen in Figure 2.9 that radiative damping becomes dominant for larger nanoparticles as the particle volume increases, whilst the contribution to $\Gamma$ is quite minimal for nanoparticles on the order of ten nanometres [81]. Instead the decay of plasmons into interband and intraband excitations introduces a significant dephasing factor [82]. Additionally for such small particles the electron mean free path becomes comparable to

the nanoparticles dimensions and surface scattering introduces the characteristic $1/r$ dependent broadening to the linewidth [73] as discussed previously.

For very small nanoparticles on the order of single or few nanometers Landau damping causes a significant linewidth broadening [6, 62, 63]. This effect can be understood in the context of section 2.2.2 where the Coulomb tail of the confining potential of a nanoparticle leads to a coupling $H_c$ between the centre of mass $H_{c.m.}$ and the electronic bath $H_{rel}$, inducing the decay of excitations of the centre-of-mass oscillation into particle-hole pairs in the electronic environment.

We have seen that the resonance peaks are strongly dependent on nanoparticle shape and this is equally true for damping timescales. For example, Sönnichsen et al. achieved a drastic reduction of the dephasing rate in gold nanorods [83] in contrast to nanospheres. In gold nanoparticles interband excitations become significant above a threshold of 1.8eV, so by increasing the aspect ratio of nanorods one redshifts the LSP resonance such that these effects are suppressed. This is in contrast to nanospheres where such a redshift can only be produced geometrically by an increase in volume, accompanied by an increase in radiative damping that negates any decrease to $\Gamma$.

## 2.3 Arrays of metallic nanoparticles

Dephasing times, as well as the majority of other optical properties are of course modified in the case of interactions between two or more nanoparticles. Now that we have delivered a basic description of the optical properties of individual nanoparticles we proceed to discuss the behaviour of collective excitations in arrays of interacting nanoparticles. We will see that interactions give rise to extended plasmonic modes with optical properties that are tunable not just by the individual constituents but by the lattice structure of the metamaterial and the microscopic interactions between LSPs. Understanding these modes is essential as they are the channel guiding electromagnetic radiation with strong lateral confinement over macroscopic distances.

In fact a significant deviation from the response of a single nanoparticle is seen for even just an interacting pair, where the plasmon resonance peak exhibits a red (blue) shift for polarisation parallel (perpendicular) to the separation axis [84]. One can visualise this

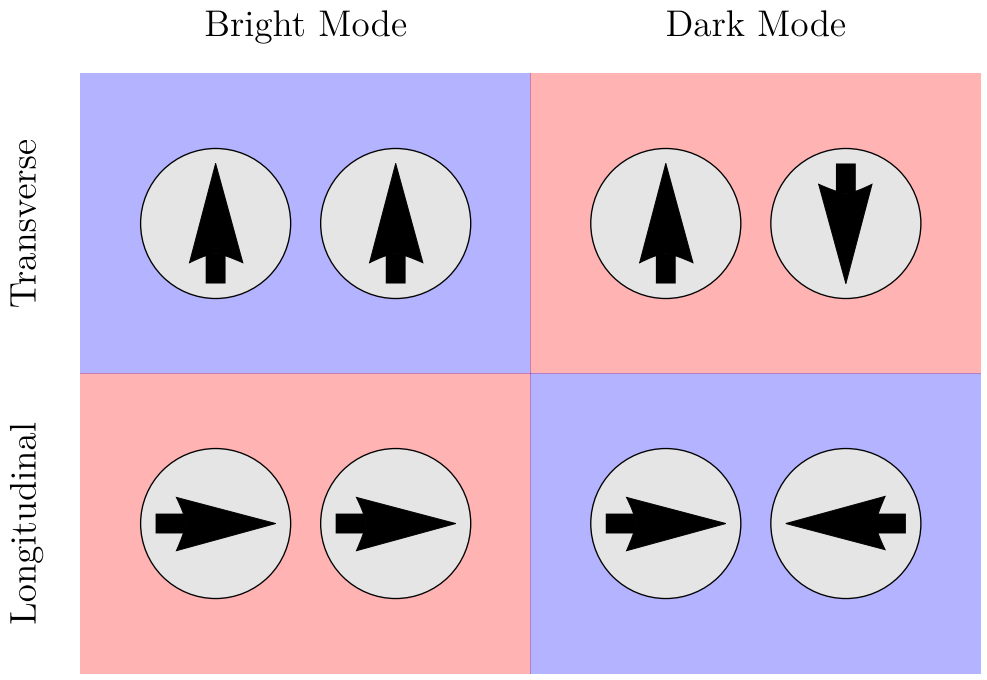


**Figure 2.12:** There are two sets of parallel and anti-parallel eigenmodes for an interacting nanoparticle dimer, those that are orientated perpendicular (transverse) and parallel (longitudinal) to the separation axis. Those with a net dipole moment are called bright modes, whereas the dark modes have no net dipole moment. The interaction also red or blue shifts the resonant frequency with respect to two non-interacting dipoles, as indicated by the colour of the enclosing boxes.

effect as shown in Figure 2.12, where the parallel polarisation is energetically favourable for the bright mode of two dipoles interacting quasi-statically.

In reality this situation is more complicated, with a competition between static, radiative and retardation effects. For an array of nanoparticles of radii $r$ and lattice constant $a$ excited by external radiation with wavelength $\lambda \gg r$ the optical response can be calculated in the Coupled Dipole (CD) approximation [17, 85]. This consists of obtaining a self consistent solution to the response of each particle at location $\mathbf{R}_i$ with dipole polarisation $\mathbf{p}_i = \alpha \mathbf{E}(\mathbf{R}_i)$ in the presence of the fields of the other $\mathcal{N} - 1$ particles [17, 85, 86]:

$$\mathbf{E}(\mathbf{R}_i) = \frac{1}{4\pi\epsilon_0\epsilon_\mathrm{D}} \sum_{j\neq i}^{\mathcal{N}-1} S_{ij} \tag{2.31}$$

where

$$S_{ij} = \underbrace{\mathrm{e}^{ikr_{ij}}}_{\text{retardation}} \left\{ \underbrace{\frac{k^2\hat{\mathbf{r}}_{ij} \times (\hat{\mathbf{r}}_{ij} \times \mathbf{p}_j)}{r_{ij}}}_{\text{radiative}} + \underbrace{\frac{[1 - ikr_{ij}]\overbrace{[3\hat{\mathbf{r}}_{ij}(\hat{\mathbf{r}}_{ij} \cdot \mathbf{p}_j) - \mathbf{p}_j]}^{\text{electrostatic}}}{r_{ij}^3}}_{\text{short-range}} \right\}, \tag{2.32}$$

$k = 2\pi/\lambda$, and $\mathbf{r}_{ij}$ denotes the interparticle separation vector between the $i$th and $j$th particle in an array. Good agreement between the CD approximation and more sophisticated electrodynamic calculations that include several multipoles is found for nanoparticles with a radius of 30nm and less [17], as well as for complementary experimental results [86]. We see that equation 2.32 captures short-range and electrostatic dipolar interactions ($1/r_{ij}^3$ terms), radiative dipolar coupling ($1/r_{ij}$ terms) as well as the effects of retardation (the factor $\mathrm{e}^{ikr}$). In Figure 2.13 we see the shift in the resonant frequency of the coupled array with decreasing lattice spacing, which blue shifts for the larger spacings where (retarded) radiative interactions are dominant, but red shifts for the smaller spacings where electrostatic interactions are dominant. Such long-range electrodynamic interactions only begin to become important for spacings greater than $\lambda/2\pi$ [17, 86] (i.e. $a \gtrsim 70$nm for visible frequencies), thus for closely packed arrays we can approximate equation 2.32 in the limit $a \ll \lambda$ as

$$\mathbf{E}(\mathbf{R}_i) = \sum_{j \neq i}^{\mathcal{N}'} \frac{1}{4\pi\epsilon_0\epsilon_{\mathrm{D}} r_{ij}^3} \left[3\hat{\mathbf{r}}_{ij}(\hat{\mathbf{r}}_{ij} \cdot \mathbf{p}_j) - \mathbf{p}_j\right], \tag{2.33}$$

where $\mathcal{N}'$ signifies a truncated sum up to terms where $kr_{ij} \ll 1$ holds. We note that for this approximation to hold we also require a minimal separation so that the nanoparticles experience a dipolar field from neighbouring particles, rather than the more complicated fields that exist close to the particle surface. Exact quasistatic calculations of linear chains of spherical nanoparticles have quantified this minimal separation to be $r \lesssim a/3$ [18]. The effects of retardation would cause the single band of the quasistatic dispersion to split into two anticrossing bands, as well as effecting the phases of each individual nanoparticle and thereby the distribution of constructive and destructive interference in the array. Whereas radiation losses results in a complex dispersion relation.

In modelling these electrostatic dipolar interactions one only needs to account for a few nearest neighbours to capture the important optical properties of arrays. For example,

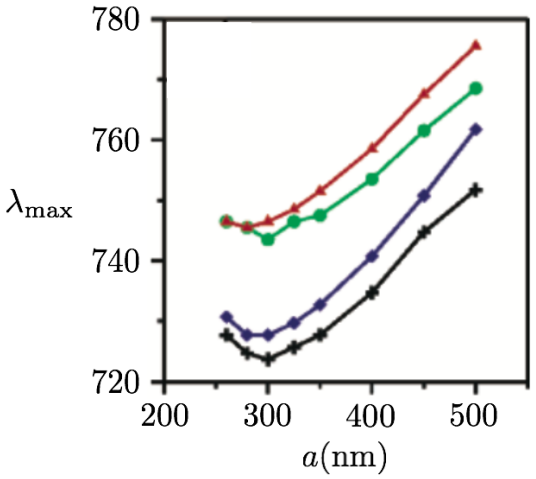


**Figure 2.13:** The peak resonant wavelength $\lambda_{max}$ of an array of nanoparticles, calculated in the Coupled Dipole approximation, for various lattice spacings $a$. For decreasing $a$ we see first a blue-shift for larger spacings where long-range electrodynamic interactions are the dominant contribution to the optical response. However, there is a turning point at about 300nm, below which there is a red-shift characteristic of electrostatic dipolar interactions. The calculations were performed for oblate spheroids with a principal axis of length 40nm and eccentricity 0.98, for hexagonal silver (black crosses), square silver (blue diamonds), hexagonal gold (green circles), and square silver (red squares) arrays. Adapted with permission from [86]. Copyright 2003 American Chemical Society.

measurements of closely spaced nanoparticle chains show a squeezing of the optical field with respect to a single nanoparticle, concentrated in interstitial sites [14]. As seen for two nanoparticles there is an energy split between parallel and perpendicular modes, which asymptotes with increasing chain length for only a few nanoparticles [16], as seen in Figure 2.14. In fact in section 4.2.7 we show that the qualitative features of the bandstructure and eigenstates of a honeycomb array are captured by considering only nearest-neighbour interactions. Thus remembering equation 2.28 for the Hamiltonian of an isolated nanoparticle, and referring to equation 2.33 we can see that the Hamiltonian of the near-field dipolar interactions between an array of metallic nanoparticles is

$$H = H_0 + H_{\text{int}}, \tag{2.34}$$

where

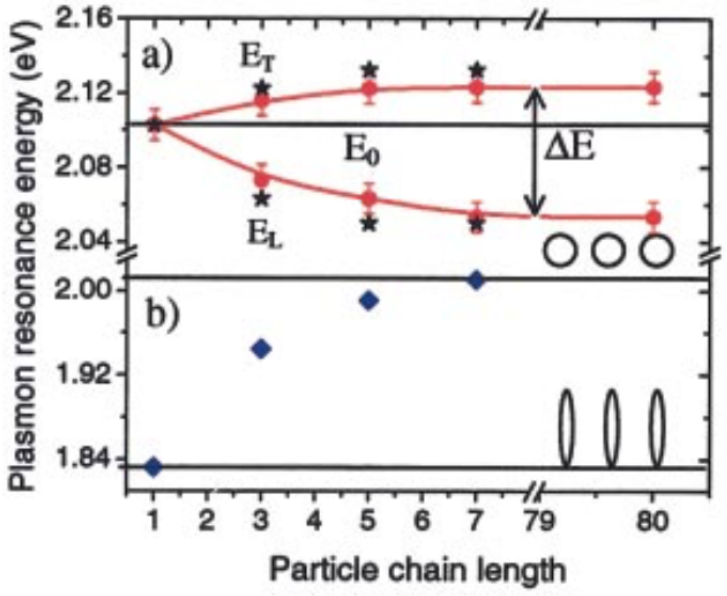


**Figure 2.14:** (a) Collective plasmon resonance energies for both longitudinal ($E_{\mathrm{L}}$) and transverse ($E_{\mathrm{T}}$) excitations for Au nanoparticle arrays of different lengths obtained via far-field spectroscopy (red circles) and FDTD simulations (black stars). (b) Simulation results for the collective plasmon resonance energies for transverse excitation of Au spheroids with aspect ratios 3:1 (blue diamonds). The resonances asymptote after only a few nanoparticles. Reprinted with permission from [16]. Copyright 2002 AIP Publishing LLC.

$$H_0 = \sum_{\mathbf{R}} \left[ \frac{\Pi^2(\mathbf{R})}{2M} + \frac{1}{2} M\omega_0^2 h^2(\mathbf{R}) \right], \qquad H_{\mathrm{int}} = \frac{N^2 e^2}{4\pi\epsilon_0\epsilon_{\mathrm{D}}} \sum_{\mathbf{R}} \sum_j \mathcal{C}_j, \tag{2.35}$$

and $\mathcal{C}_j = 1 - 3(\hat{\mathbf{p}} \cdot \hat{\mathbf{e}}_j)^2$ where $\mathbf{e}$ denotes the nearest $j$th nearest-neighbour vector. Here we have made the implicit assumption that all the dipoles are polarised in the same direction $\hat{\mathbf{p}}$, which is valid in the electrostatic limit as we discuss further in section 4.1 and appendix B.

So far we have discussed the collective plasmonic modes in arrays of metallic nanoparticles. In chapter 5 we will investigate their interaction with the photonic modes of a cavity, giving rise to new coupled light-matter modes termed plasmon polaritons which are the true eigenmodes responsible for transporting radiation. For this reason we now provide an introduction to the strong light-matter coupling regime and polaritons in general.

## 2.4 Polaritons

As has been evidenced throughout this chapter, it is the dielectric function of a material which performs the leading role in determining the optical response; and we have seen that we can significantly alter the properties of collective plasmons by tailoring the material environment. In reality these plasmonic modes do not exist in isolation, but interact with their photonic environment. Thus we can change the properties of plasmons through manipulation of the photon field.

In the so-called weak coupling regime between light and matter one treats the radiation field as a perturbation on the dynamics of the matter system, with the semiclassical theory of radiation providing an adequate description of the optical properties [87]. In this regime perhaps the most well-known example is the Purcell effect [88], whereby the spontaneous emission rate of an atom in a cavity is enhanced if the transition energy is in resonance with the cavity mode. On the other hand, if the interaction rate between light and matter excitations is faster than average dissipation rates, the perturbative weak coupling regime breaks down and one must describe interactions in the strong coupling regime.

The weak coupling regime has been extensively explored in metallic nanoparticle arrays [14–16, 18, 34]. However, it has long been known that the fundamental absorption processes in periodic systems require a full quantum-field-theoretic treatment of the strong-coupling regime [35, 36] which takes into account the conservation of crystal momentum between the photonic and matter excitations. The true eigenmodes are a coherent superposition of plasmons and photons, termed plasmon polaritons [89]. We briefly review the seminal work by Hopfield who, as well as Fano, first treated the strong coupling regime in the context of excitons in bulk solids. The applicability of this theoretical methodology to plasmonic systems is a key component of our own work in later chapters.

### 2.4.1 Hopfield and the strong coupling regime

In 1958 Hopfield published a treatment of the excitonic contribution to the dielectric function of an insulating crystal [35], showing that the interaction of photons and excitons leads to the formation of a hybrid mode. Termed a polariton, it is neither solely

photonic or excitonic in nature, but a coherent superposition of the two.

To elucidate the inadequacies of the semiclassical description consider a 3D array of identical atoms, each with a ground state $\phi_{\mathbf{R}}$ and excited state $\psi_{\mathbf{R}}$, where $\mathbf{R}$ are the atomic positions. The elementary excitations of the crystal $\Psi_{\mathbf{R}} = \psi_{\mathbf{R}} \prod_{\mathbf{R}' \neq \mathbf{R}} \phi_{\mathbf{R}'}$ with just one atom at $\mathbf{R}$ in an excited state don't have the required translational symmetry, but can be used to construct a Bloch state which is the zero-order excited state wavefunction

$$\Psi_{\mathbf{k}} = \frac{1}{\sqrt{\mathcal{N}}} \sum_{\mathbf{R}} \mathrm{e}^{i\mathbf{k}\cdot\mathbf{R}} \Psi_{\mathbf{R}}, \tag{2.36}$$

where $\mathcal{N}$ is the total number of atoms. Thus transitions to the ground state are proportional to the factor $\sum_{\mathbf{R}} \exp[i(\mathbf{k} - \mathbf{k}') \cdot \mathbf{R}]$ with emission of a photon with wavevector $\mathbf{k}'$. In the absence of Umklapp processes this dictates the conservation rule $\mathbf{k} = \mathbf{k}'$, so that each exciton is coupled to just one radiation mode. Due to the lack of a density of final states real transitions are forbidden, and instead energy is continuously exchanged between the excitonic and photonic modes. This suggests that we cannot think of absorption in a dielectric as simply a scattering process whereby a photon is absorbed by an exciton and subsequently re-emitted in an arbitrary direction, as would be the case for an isolated atom. Instead, the energy of an illuminating source is stored in these coherent hybrid modes of the crystal, and thus we require a description of the true eigenmodes of the light-matter interaction Hamiltonian of the crystal.

Excitons can be treated as approximate bosons in the limit $n_{\mathrm{exc}} a_0^3 \ll 1$, where $n_{\mathrm{exc}}$ is the density of excitons and $a_0$ is the Bohr radius [87]. In this case the full electronic Hamiltonian can be decomposed into a part that is quadratic in exciton creation and annihilation operators, formally mapping to a quantised polarisation field, plus higher order terms which can be treated as a perturbation [35]. We are not interested in excitons per se, so to elucidate the formalism applied to light-matter interactions in the strong coupling regime, let us consider the simpler and more general problem of quantising a polarisation field in interaction with the electromagnetic field. The Lagrangian density for this system is

$$\mathcal{L} = \underbrace{\frac{1}{8\pi}(\mathbf{E}^2 - c^2\mathbf{B}^2)}_{\text{light}} + \underbrace{\frac{1}{2\omega_0^2\beta}(\dot{\mathbf{P}}^2 - \omega_0^2\mathbf{P}^2)}_{\text{matter}} + \underbrace{(\mathbf{A}\cdot\dot{\mathbf{P}} + U\nabla\cdot\mathbf{P})}_{\text{interaction}}, \tag{2.37}$$

where $\omega_0$ is the natural frequency of the polarisation field and $U$ is the electromagnetic scalar potential. This Lagrangian describes the usual Maxwell equations plus an oscillating polarisation density with constitutive equation $\omega_0^{-2}\ddot{\mathbf{P}} + \mathbf{P} = \beta\mathbf{E}$ . We can switch to the Hamiltonian representation and expand in terms of the Fourier components of the fields $\mathbf{A}$ and $\mathbf{P}$ and their conjugate momenta. These fields represent a system of harmonic oscillators and so we introduce standard bosonic creation and annihilation operators that diagonalise the decoupled light and matter terms, expressing the interaction part in these operators also. We find the full Hamiltonian to be

$$H = \hbar\sum_{\mathbf{q}}\left(\underbrace{\omega_{\mathbf{q}}^{\text{ph}}c_{\mathbf{q}}^\dagger c_{\mathbf{q}}}_{\text{light}} + \underbrace{\omega_0 a_{\mathbf{q}}^\dagger a_{\mathbf{q}}}_{\text{matter}}\right) + H_{\text{int}}, \tag{2.38}$$

where $a_{\mathbf{q}}^\dagger$ and $c_{\mathbf{q}}^\dagger$ create quanta of the matter and light fields respectively, $\omega_{\mathbf{q}}^{\text{ph}} = c|\mathbf{q}|$ and the field operators in terms of the creation operators are

$$\mathbf{A} = \sum_{\mathbf{q}}\left(\frac{2\pi c\hbar}{\mathcal{V}|\mathbf{q}|}\right)^{1/2}\left(c_{\mathbf{q}}\mathrm{e}^{i\mathbf{q}\cdot\mathbf{R}} + c_{\mathbf{q}}^\dagger\mathrm{e}^{-i\mathbf{q}\cdot\mathbf{R}}\right), \tag{2.39}$$

$$\mathbf{P} = \sum_{\mathbf{q}}\left(\frac{\hbar\omega_0\beta}{2\mathcal{V}}\right)^{1/2}\left(a_{\mathbf{q}}\mathrm{e}^{i\mathbf{q}\cdot\mathbf{R}} + a_{\mathbf{q}}^\dagger\mathrm{e}^{-i\mathbf{q}\cdot\mathbf{R}}\right), \tag{2.40}$$

where $\mathcal{V}$ is the quantisation volume (which is compensated by the sum over all $\mathbf{R}$). The interaction Hamiltonian is

$$H_{\text{int}} = \hbar\omega_0\sum_{\mathbf{q}}\left[i\xi_{\mathbf{q}}\left(c_{\mathbf{q}}^\dagger a_{\mathbf{q}} + c_{-\mathbf{q}}a_{\mathbf{q}}\right) + \xi_{\mathbf{q}}^2\left(c_{\mathbf{q}}^\dagger c_{\mathbf{q}} + c_{-\mathbf{q}}c_{\mathbf{q}}\right)\right] + \text{H.c.}, \tag{2.41}$$

where $\xi_{\mathbf{q}} = \sqrt{\pi\omega_0\beta/\omega_{\mathbf{q}}^{\text{ph}}}$ parametrises the interaction strength. Note that we have suppressed the index representing the different possible polarisations. The Hamiltonian has translational invariance and different polarisations are decoupled so it is sufficient to choose a single polarisation. The eigenmodes of this coupled system, termed polaritons,

are a coherent superposition of light and matter excitations. Thus we introduce the operator

$$\gamma_{\mathbf{q}} = wa_{\mathbf{q}} + xc_{\mathbf{q}} + ya^{\dagger}_{-\mathbf{q}} + zc^{\dagger}_{-\mathbf{q}}, \tag{2.42}$$

which, if it is to be a normal-mode annihilation operator must obey the Heisenberg equation

$$\left[\gamma_{\mathbf{q}}, H\right] = \hbar\omega^{\mathrm{po}}_{\mathbf{q}}\gamma_{\mathbf{q}}, \tag{2.43}$$

where $\omega^{\mathrm{po}}_{\mathbf{q}}$ is the eigenfrequency dispersion of the polaritons. The eigenvalue equation 2.43 can be written in matrix form as

$$\begin{pmatrix} \omega^{\mathrm{ph}}_{\mathbf{q}}/\omega_0 + 2\xi^2_{\mathbf{q}} & -i\xi_{\mathbf{q}} & -2\xi^2_{\mathbf{q}} & -i\xi_{\mathbf{q}} \\ i\xi_{\mathbf{q}} & 1 & -i\xi_{\mathbf{q}} & 0 \\ 2\xi^2_{\mathbf{q}} & -i\xi_{\mathbf{q}} & -\omega^{\mathrm{ph}}_{\mathbf{q}}/\omega_0 - 2\xi^2_{\mathbf{q}} & -i\xi_{\mathbf{q}} \\ -i\xi_{\mathbf{q}} & 0 & i\xi_{\mathbf{q}} & -1 \end{pmatrix} \begin{pmatrix} w \\ x \\ y \\ z \end{pmatrix} = \frac{\omega^{\mathrm{po}}_{\mathbf{q}}}{\omega_0} \begin{pmatrix} w \\ x \\ y \\ z \end{pmatrix}, \tag{2.44}$$

which leads to the polaritonic dispersion

$$\omega^{\mathrm{po}}_{\mathbf{q}} = \frac{1}{\sqrt{2}} \left[ W^2_{\mathbf{q}} \pm \sqrt{W^4_{\mathbf{q}} - 4(\omega_0\omega^{\mathrm{ph}}_{\mathbf{q}})^2} \right]^{1/2}, \tag{2.45}$$

where

$$W^2_{\mathbf{q}} = \omega^2_0 + (\omega^{\mathrm{ph}}_{\mathbf{q}})^2 + 4\omega_0\omega^{\mathrm{ph}}_{\mathbf{q}}\xi^2_{\mathbf{q}}, \tag{2.46}$$

as shown in Figure 2.15. We see the prototypical polaritonic splitting and asymptotic tendency to bare light and matter curves and a band gap proportional to $\beta$. Note that in the polaritonic dispersion 2.45 we neglected the two negative energy solutions from the eigenvalue equation 2.44 as unphysical. We will continue to ignore such solutions for the rest of the thesis.

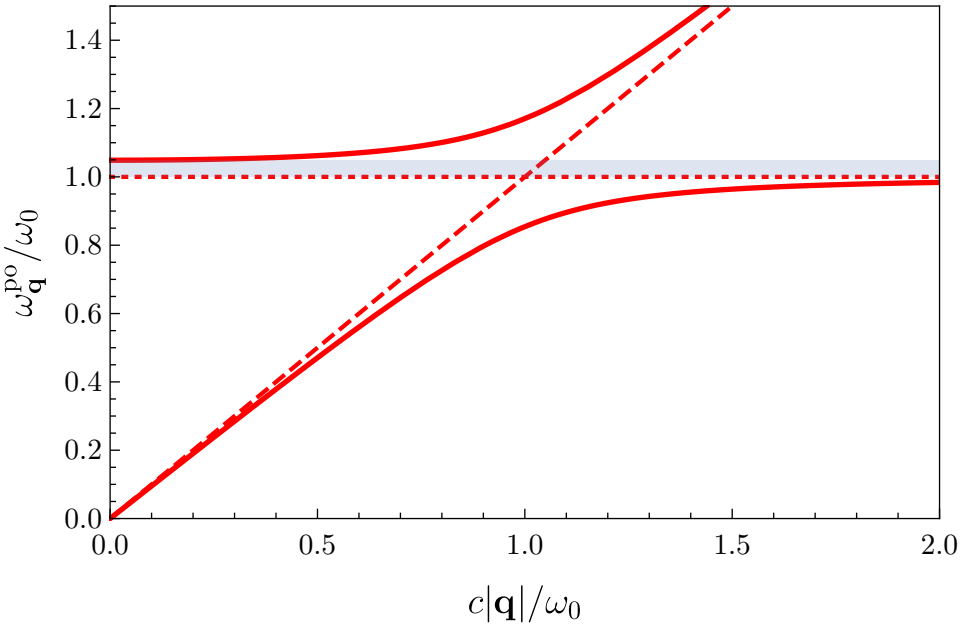


**Figure 2.15:** The polaritonic dispersion in an infinite dielectric medium (solid lines). Also shown are the light line (dashed line) and the resonant frequency of the polarisation field (dotted line). The shaded region corresponds to the band gap induced by the anti-crossing. In the figure $4\pi\beta = 0.1$.

## 2.5 Chapter Summary

The diffraction limit is a serious impediment to the resolution of microscopic structures. However, we have seen that metallic nanoparticles enable us to overcome this limit, as the electromagnetic fields associated to LSPs in nanoparticles are evanescently confined to the surface and significantly enhanced within subwavelength regions. LSP resonances can be excited by direct light illumination and typically lie in the visible spectrum. The exact frequency and bandwidth can be modulated by the size, shape, material and environment of the nanoparticle.

The situation becomes yet more interesting when we consider interactions between LSPs in arrays of nanoparticles, as this leads to new collective propagating plasmonic modes, the properties of which depend on the underlying lattice structure. Such metamaterials can exhibit a variety of novel optical phenomena not found in nature, such as electromagnetic invisibility cloaking, perfect lensing and slow light [8–13]. In the next section we will unveil some of the fascinating properties of graphene, which in combination with this section will explain our motivation in researching the plasmonic properties of a honeycomb array of metallic nanoparticles.

Throughout this chapter we have also given weight to the assumptions which underlie our models in later chapters. For example we have seen that for small enough nanoparticles, on the order of a few tens of nanometres, the optical response is predominantly dipolar. For closely spaced arrays the near-field interaction between neighbouring nanoparticles is dominant compared to long range radiative and retarded EM interactions, and one can consider just the instantaneous dipole-dipole interactions. That is so long as they are not too close (or indeed touching) so that the dipolar field approximation holds, valid for radii on the order $r \lesssim a/3$.

Before finishing this chapter we indicate how this thesis contributes to the current state of plasmonics and artificial Dirac materials. Research in optical metamaterials is shifting from three-dimensional structures to two-dimensional surfaces comprising of interacting plasmonic meta-atoms [90] and non-trivial plasmonic states, such as topological edge states, Majorana states and Jackiw-Rebbi midgap states [91, 92]. The focus is also largely tending towards quantum plasmonics, as it has been demonstrated that quantum behaviour such as entanglement is preserved in plasmons despite their macroscopic nature [93]. At the same time, artificial Dirac materials in various physical contexts have enabled the exploration of Dirac physics in new regimes [31, 94–97]. However, the emphasis in the literature is on tailoring the properties of Dirac materials via the symmetries of the matter system, and little attention is paid to the environment. The key contribution of this thesis is the emphasis and demonstration that one can fundamentally alter the properties of Dirac plasmon polaritons by manipulating just a photonic environment that preserves the underlying symmetries.

We have explained that out of the infinite possible arrangements of nanoparticles we choose to explore the honeycomb lattice structure synonymous with graphene. Now let us explain why.

# Chapter 3

# Introduction to graphene

In 2004 Novoselov et al. isolated graphene for the first time [20], sparking vast interest in the material. Graphene is a monolayer of carbon atoms arranged in a hexagonal bipartite lattice that forms a honeycomb structure. Being only one-atom-thick it is a truly two-dimensional material, a fact that is largely responsible for the unique electronic properties of graphene [24]. Previously it had been thought impossible for isolated graphene to exist, as it would be thermodynamically unstable; the thermal fluctuations of the constituent atoms becoming comparable to the interatomic spacing [98]. In stark contradiction to this prediction, it has been found to be stable under ambient conditions and of high crystal quality [22].

Even as much as half a century before its discovery it was well known that graphene (which can be considered a building block of graphite) would possess many remarkable electronic properties [21, 99, 100]. The behaviour of its electrons around the Fermi energy maps to those of high energy relativistic particles called 'massless Dirac fermions', and for this reason the electronic physics in graphene has been referred to as 'QED in a pencil trace' and studied by theorists as a $(2+1)$-dimensional QED analogue for several decades [101, 102].

The electronic properties of graphene arise primarily due to the symmetry and dimensionality of the material. This fact has motivated the investigation of many artificial graphene systems [29] from cold atoms [30, 31] to photonic arrays [32, 33]. We have seen in the previous chapter that the optical properties of nanoparticle arrays depend

crucially on the underlying lattice structure, and thus, it is expected that collective plasmonic excitations in honeycomb structured arrays of nanoparticles will inherit analogous properties of electrons in graphene. Firstly we will thus analyse the most remarkable aspects of the electronic properties of graphene itself. Our focus will be on the theoretical description of Dirac quasiparticles because we are not so much interested in graphene *per se*, but rather in the techniques and language used within the graphene community to describe this carbon incarnation of the honeycomb lattice.

Whilst we assume the reader has a familiarity with condensed matter theory, in the subsequent section 3.1 we wish to revise the topic of geometric phases, as key arguments in this thesis, such as the existence and stability of Dirac points, rely on some of these concepts. In section 3.2 we present the electronic structure of ideal monolayer graphene obtained in the tight-binding formalism. At energies close to the Fermi energy we discover that electrons in graphene behave like massless Dirac fermions with an associated chirality and non-trivial Berry phase. We will see consequences of these properties in section 3.3, such as a suppression of backscattering off smooth inhomogeneities leading to high mobilities, and a related exotic transport phenomenon called Klein tunneling where charge carriers in graphene can pass through arbitrarily tall and wide potential barriers with perfect transmission. Finally in section 3.4 we show the effects of strain in the lattice leading to artificial gauge fields.

## 3.1 Geometric phases and related concepts

In 1984 Michael Berry published a paper that changed our understanding of adiabatic evolutions of quantum states [103]. It was well understood [104] that in the adiabatic limit a state that evolves due to a slow variation of the system parameters would acquire a dynamical phase factor (the time integral of the energy) plus an additional phase factor, which (one thought) could be eliminated by a gauge transformation [105], due to the degree of freedom in choosing an arbitrary parameter-dependent phase factor of the eigenfunctions.

However, Berry showed that for evolutions corresponding to closed loops in the parameter space (i.e. returning to the original configuration) the additional phase factor, now known as the Berry phase, is gauge invariant modulo $2\pi$. Thus, the Berry phase has

physically observable effects. Additionally the Berry phase can be expressed solely as a line-integral (or surface integral) in the parameter space and does not depend explicitly on the dynamics of the system. For this reason it is also known as the geometric phase.

### 3.1.1 The geometric phase

Consider a system described by a Hamiltonian $H(\boldsymbol{\lambda})$ with a time dependence encoded in the parameters $\boldsymbol{\lambda} = \boldsymbol{\lambda}(t)$. We can construct an instantaneous basis from the eigenstates of the Hamiltonian

$$H(\boldsymbol{\lambda})|n, \boldsymbol{\lambda}\rangle = \epsilon_n(\boldsymbol{\lambda})|n, \boldsymbol{\lambda}\rangle. \tag{3.1}$$

However, this only defines $|n, \boldsymbol{\lambda}\rangle$ up to a phase factor. Thus, we are free to perform a gauge transformation $|n, \boldsymbol{\lambda}\rangle \rightarrow \mathrm{e}^{i\alpha(\boldsymbol{\lambda})}|n, \boldsymbol{\lambda}\rangle$ with the constraint that $\mathrm{e}^{i\alpha(\boldsymbol{\lambda})}$ be single valued to preserve orthonormality of the eigenfunctions. Thus, the general solution to the Schrödinger equation in this basis is

$$|\Psi(t)\rangle = \sum_n c_n(t)\mathrm{e}^{i\theta_n(t)}|n, \boldsymbol{\lambda}(t)\rangle, \tag{3.2}$$

where $\theta_n = -(1/\hbar)\int_0^t \epsilon_n(\boldsymbol{\lambda}(t'))dt'$ is a dynamical phase factor. We consider a system prepared in the state $|\Psi(0)\rangle = |n, \boldsymbol{\lambda}(0)\rangle$ and ask how it evolves. By substituting equation 3.2 into the Schrödinger equation we obtain an expression for the evolution of the coefficients as

$$\dot{c}_n = \underbrace{-c_n\langle n|\partial_t|n\rangle}_{\text{adiabatic}} \underbrace{- \sum_{m\neq n} c_m \frac{\langle n|\dot{H}|m\rangle}{\epsilon_m - \epsilon_n}\mathrm{e}^{i(\theta_m - \theta_n)}}_{\text{corrections}}, \tag{3.3}$$

where we have dropped the explicit label $\boldsymbol{\lambda}$ of the basis. Thus, in the adiabatic limit [106] the coefficients are given by $c_n(t) = c_n(0)\mathrm{e}^{i\gamma_n(t)}$ where

$$\gamma_n(t) = i\int_0^t \langle n, \boldsymbol{\lambda}(t')|\partial_{t'}|n, \boldsymbol{\lambda}(t')\rangle dt'. \tag{3.4}$$

The coefficients of the initial state $|n, \boldsymbol{\lambda}(0)\rangle$ are clearly $c_m(0) = \delta_{mn}$ and thus the state evolves adiabatically as

$$|\Psi(t)\rangle = \mathrm{e}^{i\gamma_n(t)}\mathrm{e}^{i\theta_n(t)}|n, \boldsymbol{\lambda}(0)\rangle. \tag{3.5}$$

Changing integration variables we can write the factor $\gamma_n$ as

$$\gamma_n = \int_\Gamma \boldsymbol{\mathcal{A}}_n \cdot d\boldsymbol{\lambda}, \tag{3.6}$$

which is a geometrical phase factor determined by an integral along the path $\Gamma$ mapped out in parameter space by $\boldsymbol{\lambda}(t')$ between $t' = 0$ and $t' = t$. The integrand

$$\boldsymbol{\mathcal{A}}_n = i\langle n|\nabla_{\boldsymbol{\lambda}}|n\rangle \tag{3.7}$$

is termed the Berry connection. Both $\boldsymbol{\mathcal{A}}_n$ and $\gamma_n$ depend on the gauge choice of the basis and these three factors transform as

$$|n, \boldsymbol{\lambda}\rangle \to \mathrm{e}^{i\alpha(\boldsymbol{\lambda})}|n, \boldsymbol{\lambda}\rangle, \tag{3.8}$$

$$\boldsymbol{\mathcal{A}}_n \to \boldsymbol{\mathcal{A}}_n - \nabla_{\boldsymbol{\lambda}}\alpha(\boldsymbol{\lambda}), \tag{3.9}$$

$$\gamma_n \to \gamma_n + \alpha(\boldsymbol{\lambda}(0)) - \alpha(\boldsymbol{\lambda}(t)). \tag{3.10}$$

Thus, it appears we can neglect the geometrical phase factor in our treatment as we can always choose $\alpha(\boldsymbol{\lambda})$ such that $\gamma_n \to 0$.

However, Berry made a crucial refinement to this argument with the consideration of cyclic evolutions such that the system traverses a closed path $\Gamma$ in parameter space with $\boldsymbol{\lambda}(T) = \boldsymbol{\lambda}(0)$. In this case if $\exp(i\alpha(\boldsymbol{\lambda}))$ is to be single valued $\alpha(\boldsymbol{\lambda}(0))$ and $\alpha(\boldsymbol{\lambda}(T))$ must be equivalent modulo $2\pi$. Thus, our choice of gauge is restricted such that the geometrical phase factor transforms as

$$m \in \mathbb{Z} : \gamma_n \to \gamma_n + 2\pi m. \tag{3.11}$$

The relevant factor $\exp(i\gamma_n)$ is unchanged and so we see that for closed paths the geometrical phase factor is gauge invariant if interpreted as a phase angle. Correspondingly we define the geometrical phase factor of a closed loop as the Berry phase, given by

$$\gamma_{B,n} = \oint_{\Gamma} \boldsymbol{\mathcal{A}}_n \cdot d\boldsymbol{\lambda}. \tag{3.12}$$

### 3.1.2 Berry curvature and Chern number

As the Berry phase is a gauge-invariant quantity it would be beneficial to have a gauge invariant way of computing it. In analogy with electromagnetism we define the Berry curvature as

$$\boldsymbol{\mathcal{B}} = \nabla \times \boldsymbol{\mathcal{A}}, \tag{3.13}$$

which formally resembles a real magnetic field, but in the parameter space. Here we have used 3D notation but the principles are generalisable to any dimensionality of $\boldsymbol{\lambda}$. We also drop the explicit label of the basis state $n$ from the Berry quantities. By virtue of Stokes' theorem we can express the line integral around a closed contour $\Gamma$ as an integral over any surface $S$ bounded by $\Gamma$, i.e.

$$\int_S \boldsymbol{\mathcal{B}} \cdot d\mathbf{S} := \oint_{\Gamma} \boldsymbol{\mathcal{A}}_n \cdot d\boldsymbol{\lambda}. \tag{3.14}$$

The notation ':=' implies the following. The LHS is an integral of the fully gauge invariant quantity $\boldsymbol{\mathcal{B}}$ and has a unique value, whereas the RHS is defined modulo $2\pi$.

Having obtained interesting results integrating the Berry connection along a closed contour, it is natural to investigate the result of integrating the Berry curvature over a closed surface. Consider the simple case of a sphere (or any surface that is homeomorphic to a sphere) in parameter space. We can subdivide the surface of the sphere into two regions $S1$ and $S2$ defined by a closed contour $\Gamma$ which traverses the two regions in opposite directions. Thus, from Stokes theorem the integral of the Berry curvature in each region is

$$\int_{S1} \boldsymbol{\mathcal{B}} \cdot d\mathbf{S} := \gamma_B, \qquad -\int_{S2} \boldsymbol{\mathcal{B}} \cdot d\mathbf{S} := \gamma_B, \tag{3.15}$$

and so subtracting these two quantities we find that

$$\oint_S \boldsymbol{\mathcal{B}} \cdot d\mathbf{S} := 0. \tag{3.16}$$

It follows that the integral of the Berry curvature over a closed surface is quantised in integer multiples of $2\pi$. By convention the corresponding integer is defined as the Chern number [107] given as

$$C = -\frac{1}{2\pi} \oint_S \boldsymbol{\mathcal{B}} \cdot d\mathbf{S}. \tag{3.17}$$

### 3.1.3 Berryology in the Brillouin zone

Having defined Berry quantities in a generic parameter space we wish to study their manifestation in Bloch bands. We now consider a Hamiltonian parametrised by a two-dimensional crystal wavevector $\mathbf{q} = (q_x, q_y)$ and consider the consequences of both time-inversion $\mathcal{T}$, space-inversion $\mathcal{I}$ and systems that are invariant under $\mathcal{IT}$. As $\mathbf{q}$ is periodic the Brillouin zone is a closed surface and we identify a topological invariant as the Chern number obtained from an integration of the Berry curvature over the whole Brillouin zone. As $\mathbf{q}$ is two-dimensional we can see that only the $z$ component of $\boldsymbol{\mathcal{B}}$ contributes to the Berry phase and Chern number, and so we refer to $\boldsymbol{\mathcal{B}}_z$ as the Chern density.

We can write the Berry curvature in the more useful form

$$\boldsymbol{\mathcal{B}}_i = i\epsilon_{ijk}\langle \partial_j n | \partial_k n \rangle, \tag{3.18}$$

where $|\partial_i n\rangle \equiv \partial_i |n\rangle$. In this representation we can verify that the effects of time-reversal ($\mathcal{T}$) and space-inversion ($\mathcal{I}$) on the Chern density and Chern number are

$$\mathcal{T}\boldsymbol{\mathcal{B}}_z(\mathbf{q}) = -\boldsymbol{\mathcal{B}}_z(-\mathbf{q}), \qquad \mathcal{T}C = -C, \tag{3.19}$$

$$\mathcal{I}\boldsymbol{\mathcal{B}}_z(\mathbf{q}) = \boldsymbol{\mathcal{B}}_z(-\mathbf{q}), \qquad \mathcal{I}C = C. \tag{3.20}$$

These results show that a system with time-reversal symmetry is topologically trivial, in the sense that it has a zero Chern number. At first glance it also suggests that a system with $\mathcal{IT}$ symmetry has an identically zero Chern density at every $\mathbf{q}$-point and thus a trivial Berry phase. However, let us see that this is not quite true.

### 3.1.4 Dirac points

Consider the operation of $\mathcal{IT}$ on the Berry phase. An arbitrary region $S$ in $\mathbf{q}$-space is invariant under $\mathcal{IT}$ and thus

$$\mathcal{IT}\gamma_B =: \int_S (\mathcal{IT}\boldsymbol{\mathcal{B}}_z)\mathrm{d}^2\mathbf{q}, \tag{3.21}$$

$$= -\int_S \boldsymbol{\mathcal{B}}_z \mathrm{d}^2\mathbf{q}, \tag{3.22}$$

$$:= -\gamma_B. \tag{3.23}$$

We see that as the Berry phase is only defined modulo $2\pi$, a system with $\mathcal{IT}$ symmetry does not (necessarily) have a trivial Berry phase of zero but instead an integer multiple of $\pi$

$$\gamma_B = n\pi. \tag{3.24}$$

This means that the Chern density must be a sum of Dirac delta functions

$$n_j \in \mathbb{Z} : \boldsymbol{\mathcal{B}}_z(\mathbf{q}) = \sum_j n_j \pi \delta(\mathbf{q} - \mathbf{K}_j), \tag{3.25}$$

with the delta functions acting as a source of Berry flux, either 0 or $\pi$. A point $\mathbf{K}_j$ that has a $\pi$ flux is called a Dirac point. Under smooth changes in the Hamiltonian the Berry curvature must change smoothly also. Thus, the only thing that can change is the location of Dirac points, unless they are brought into contact and annihilate in a topological transition [108, 109].

Note also that if the system possesses time-reversal symmetry (and thus a Chern number of zero) then there must be an even number of Dirac points. These two key points allow us to discuss the existence and stability of Dirac points in later chapters.

### 3.1.5 Berryology in a two-band model

We will largely be dealing with two-band models so let us introduce some general concepts. A two band Hamiltonian can be written (up to a global energy shift which does not alter the eigenstates) as

$$H(\mathbf{h}) = \boldsymbol{\sigma} \cdot \mathbf{h}, \tag{3.26}$$

where $\boldsymbol{\sigma} = (\sigma_x, \sigma_y, \sigma_z)$ is the vector of Pauli matrices and $\mathbf{h} = (h_x, h_y, h_z)$ is a vector of parameters. Before calculating the Berry phase let us introduce another useful representation of the Berry curvature by inserting a complete basis inside the inner product of equation 3.18 to obtain

$$\boldsymbol{\mathcal{B}}_n = -\mathrm{Im} \sum_{n' \neq n} \frac{\langle n|\nabla H|n'\rangle \times \langle n'|\nabla H|n\rangle}{(\epsilon_n - \epsilon_{n'})^2}. \tag{3.27}$$

The eigenvalues of the Hamiltonian are simply $\pm|\mathbf{h}|$ and we can write the eigenstates as

$$|+, \mathbf{h}\rangle = \begin{pmatrix} \cos(\theta_{\mathbf{h}}/2) \\ \mathrm{e}^{i\phi_{\mathbf{h}}} \sin(\theta_{\mathbf{h}}/2) \end{pmatrix}, \qquad |-, \mathbf{h}\rangle = \begin{pmatrix} \sin(\theta_{\mathbf{h}}/2) \\ -\mathrm{e}^{i\phi_{\mathbf{h}}} \cos(\theta_{\mathbf{h}}/2) \end{pmatrix}, \tag{3.28}$$

where $\theta_{\mathbf{h}}$ and $\phi_{\mathbf{h}}$ are the polar and azimuthal angle of $\mathbf{h}$ respectively. Evidently the gradient of the Hamiltonian with respect to its parameters is just the Pauli vector $\nabla_{\mathbf{h}} H = \boldsymbol{\sigma}$ and thus the Berry curvature 3.27 reads

$$\boldsymbol{\mathcal{B}}_{\pm} = -\mathrm{Im}\frac{\langle \pm|\boldsymbol{\sigma}|\mp\rangle \times \langle \mp|\boldsymbol{\sigma}|\pm\rangle}{4\mathbf{h}^2}. \tag{3.29}$$

Choosing the coordinate system with $\hat{\mathbf{z}}$ parallel to $\mathbf{h}$ the eigenvectors are $|+\rangle = (1,0)^T$ and $|-\rangle = (0,1)^T$ and so the matrix elements $\langle \pm|\boldsymbol{\sigma}|\mp\rangle$ can be calculated easily, leading to the Berry curvature

$$\boldsymbol{\mathcal{B}}_{\pm} = \pm\frac{1}{2}\frac{1}{\mathbf{h}^2}\hat{\mathbf{h}}. \tag{3.30}$$

Referring to equation 3.14 we see that one can interpret the Berry phase as the flux through the surface $\mathcal{S}$ of a monopole located at the origin of parameter space. As such it takes the simple form

$$\gamma_B^{\pm} = \pm\frac{1}{2}\Omega_{\Gamma}, \tag{3.31}$$

where $\Omega_{\Gamma}$ is the solid angle subtended by the surface $\mathcal{S}$ bounded by $\Gamma$. For clarity let us restate the procedure to calculate the Berry phase in an abridged form. Given a two-level Hamiltonian write it as $\boldsymbol{\sigma} \cdot \mathbf{h}$. Define the vector

$$\mathbf{V}_{\pm} = \pm\hat{\mathbf{h}}, \tag{3.32}$$

which is nothing more than the unit vector of Berry curvature for the eigenstate $|\pm\rangle$. A closed contour $\Gamma$ in $\mathbf{h}$ traces a closed contour $\tilde{\Gamma}$ in $\hat{\mathbf{h}}$ on the surface of a unit sphere. The Berry phase is then just the fraction of the sphere's surface area bounded by the contour $\tilde{\Gamma}$, multiplied by $\pm 2\pi$.

This makes the calculation of the Berry phase in a two-band model a simple and pleasingly visual experience, as we show in Figure 3.1. Now that we have revised these key concepts let us return to the real topic of this chapter and discuss the electronic properties of graphene.

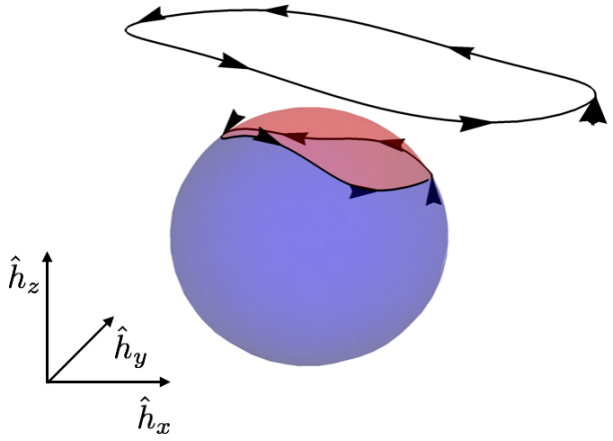


**Figure 3.1:** A visualisation of the calculation of the Berry phase. An arbitrary closed curve in $\mathbf{h}$ (larger black curve) corresponds to a closed curve in $\hat{\mathbf{h}}$ on the surface of a sphere. The Berry phase is directly proportional to the fraction of the sphere bounded by the curve (red area).

## 3.2 Electronic structure of graphene

The hexagonal bipartite lattice of graphene can be considered to comprise of two inequivalent sublattices [21]. Figure 3.2 shows the lattice structure and the first Brillouin zone in the reciprocal space. The electronic structure of a carbon atom is $1s^2 2s^2 2p^2$ with four valence electrons [110]. In graphene three of these electrons form strong covalent carbon-carbon bonds in the plane, leaving one remaining conduction electron, called a $\pi$-electron.

We will now explore the electronic properties of graphene in detail, by obtaining the band structure using a tight-binding calculation, and then focusing on the low-energy regime around the Fermi energy.

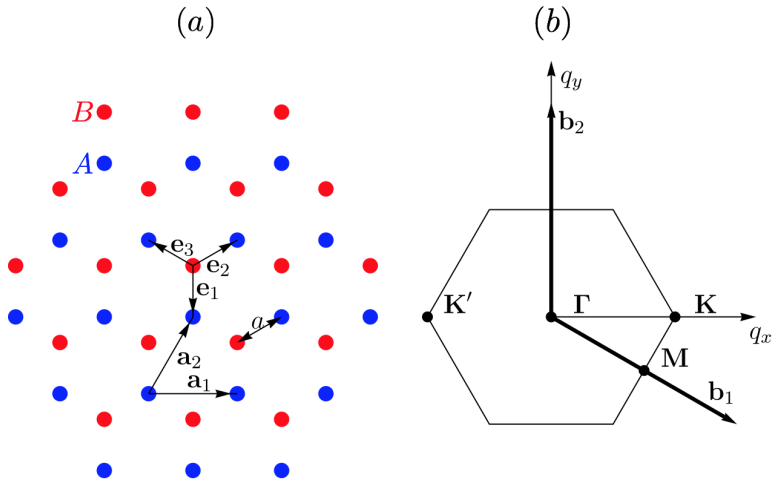


**Figure 3.2:** (a) The lattice structure of graphene, with lattice vectors $\mathbf{a}_1 = a(\sqrt{3}, 0)$ and $\mathbf{a}_2 = (a/2)(\sqrt{3}, 3)$. The nearest-neighbour vectors are defined as $\mathbf{e}_1 = a(0, -1)$, $\mathbf{e}_2 = (a/2)(\sqrt{3}, 1)$ and $\mathbf{e}_3 = (a/2)(-\sqrt{3}, 1)$. These link the inequivalent $A$ and $B$ lattice sites, represented by blue and red dots respectively in the figure. In graphene $a \approx 1.4$Å is the carbon-carbon distance. (b) The first Brillouin zone in reciprocal space defined by the primitive vectors $\mathbf{b}_1 = (2\pi/3a)(\sqrt{3}, -1)$ and $\mathbf{b}_2 = (4\pi/3a)(0, 1)$. Also shown are the topological points of high symmetry, $\mathbf{K} = (4\pi/3\sqrt{3}a)(1, 0)$, $\mathbf{K}' = -\mathbf{K}$, $\mathbf{\Gamma} = (0, 0)$ and $\mathbf{M} = (\pi/3a)(\sqrt{3}, -1)$.

### 3.2.1 Tight Binding Model of Graphene

The eigenfunctions of a crystal Hamiltonian $H$ can be represented in a basis of Bloch states constructed from atomic orbitals. The Bloch states are

$$\Phi_j(\mathbf{q}, \mathbf{r}) = \frac{1}{\sqrt{\mathcal{N}}} \sum_{\mathbf{R}} \mathrm{e}^{i\mathbf{q}\cdot\mathbf{R}} \varphi_j(\mathbf{r} - \mathbf{R}), \tag{3.33}$$

where $\mathbf{R}$ denotes the atomic positions, $\mathcal{N}$ is the number of unit cells and $\varphi_j$ is the atomic wavefunction in the state $j$, of which there are $n$ in the unit cell. The eigenfunctions in the crystal can thus be expressed as a linear combination of these Bloch states as

$$\Psi_i(\mathbf{q}, \mathbf{r}) = \sum_{j=1}^{n} u_{ij}(\mathbf{q}) \Phi_j(\mathbf{q}, \mathbf{r}), \tag{3.34}$$

where $u_{ij}$ are the expansion coefficients. In this representation, for the specific case of graphene we have

$$\Psi(\mathbf{q}, \mathbf{r}) = u_A(\mathbf{q}) \Phi_A(\mathbf{q}, \mathbf{r}) + u_B(\mathbf{q}) \Phi_B(\mathbf{q}, \mathbf{r}). \tag{3.35}$$

Substituting this eigenfunction into the stationary Schrödinger equation, multiplying by $\Phi_A^*$ and $\Phi_B^*$ respectively and integrating gives the system of equations [21]

$$\begin{pmatrix} H_{AA} & H_{AB} \\ H_{BA} & H_{BB} \end{pmatrix} \begin{pmatrix} u_A \\ u_B \end{pmatrix} = E \begin{pmatrix} u_A \\ u_B \end{pmatrix}, \tag{3.36}$$

where $H_{\mu\nu} = \langle \Phi_\mu | H | \Phi_\nu \rangle$, and we have assumed that $\langle \Phi_\mu | \Phi_\nu \rangle = \delta_{\mu\nu}$ as per the Slater-Koster scheme [111, 112]. Writing $H_{AA}$ more explicitly we have

$$H_{AA} = \frac{1}{\mathcal{N}} \sum_{\mathbf{R}_A} \langle \varphi_{\mathbf{R}_A} | H | \varphi_{\mathbf{R}_A} \rangle + \frac{1}{\mathcal{N}} \sum_{\mathbf{R}_A \neq \mathbf{R'}_A} \mathrm{e}^{i\mathbf{q}\cdot(\mathbf{R}_A - \mathbf{R'}_A)} \langle \varphi_{\mathbf{R'}_A} | H | \varphi_{\mathbf{R}_A} \rangle, \tag{3.37}$$

where $|\varphi_{\mathbf{R}}\rangle$ is defined via $\varphi_{\mathbf{R}}(\mathbf{r} - \mathbf{R}) = \langle \mathbf{r} | \varphi_{\mathbf{R}} \rangle$. Retaining only the dominant term when $\mathbf{R}_A = \mathbf{R'}_A$ we see that $H_{AA} = H_{BB} = \epsilon_{2p}$, which is just the orbital energy of the $2p$ level. Taking a nearest-neighbour approximation, $H_{AB}$ simplifies to a sum over the three nearest neighbours such that

$$H_{AB} = \frac{1}{\mathcal{N}} \sum_j \sum_{\mathbf{R}_B = \mathbf{R}_A + \mathbf{e}_j} \mathrm{e}^{-i\mathbf{q}\cdot\mathbf{e}_j} \langle \varphi_{\mathbf{R}_A} | H | \varphi_{\mathbf{R}_B} \rangle. \tag{3.38}$$

Identifying the transfer integral $t = \langle \varphi_{\mathbf{R}_A} | H | \varphi_{\mathbf{R}_B} \rangle \approx 2.8\text{eV}$ [24, 113] as the energy required for an electron to hop from one lattice site to its nearest neighbour, equivalent for all three, we can write equation 3.38 more simply as $H_{AB} = tf^*(\mathbf{q})$, where $f(\mathbf{q})$ is given explicitly using the nearest neighbour vectors as

$$f(\mathbf{q}) = \sum_j \mathrm{e}^{i\mathbf{q}\cdot\mathbf{e}_j} = \mathrm{e}^{iaq_y/2} \left[ \mathrm{e}^{-i3aq_y/2} + 2\cos\left(\sqrt{3}aq_x/2\right) \right]. \tag{3.39}$$

Similarly $H_{BA} = tf(\mathbf{q})$. Thus, we have all the terms $H_{\mu\nu}$ and can write (based on equation 3.36) the Hamiltonian as

$$H = \begin{pmatrix} 0 & tf^*(\mathbf{q}) \\ tf(\mathbf{q}) & 0 \end{pmatrix}, \tag{3.40}$$

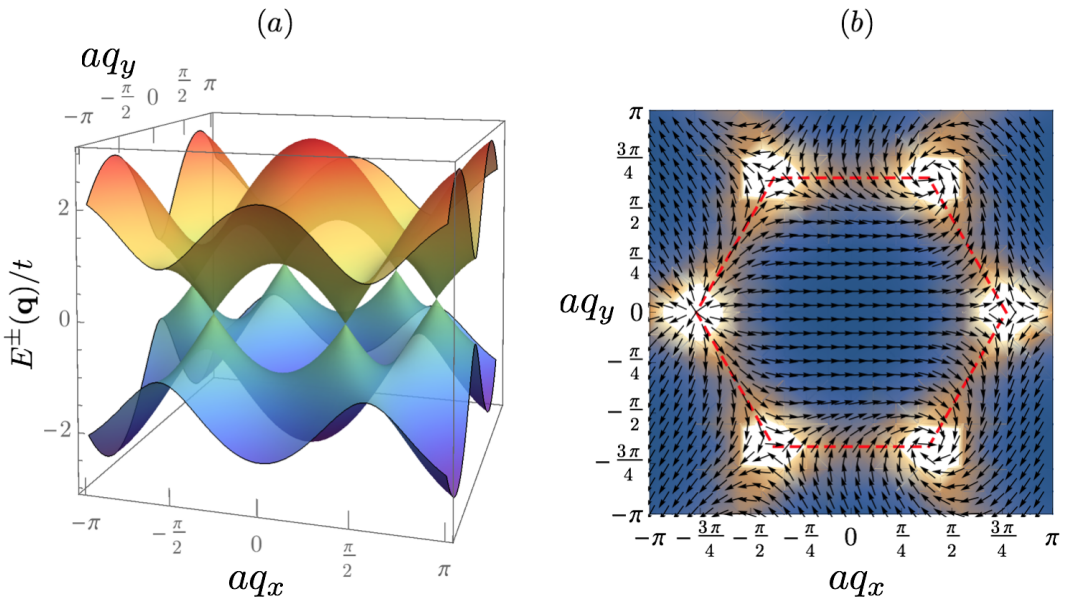


**Figure 3.3:** (a) The tight-binding band structure of graphene. (b) The direction (magnitude) of $\boldsymbol{\mathcal{B}}_+$ is represented by the black arrows (colour scale in arbitrary units). The arrows also correspond to the vector $\mathbf{V}_+$ of equation 3.32. The first Brillouin zone is indicated by the dashed red hexagon.

where we have set $\epsilon_{2p} = 0$ as it simply provides a global energy shift. Correspondingly the electronic band structure of graphene, as shown in Figure 3.3(a), is

$$E^{\pm}(\mathbf{q}) = \pm t|f(\mathbf{q})| \tag{3.41}$$

$$= \pm t\sqrt{1 + 4\left(\frac{\sqrt{3}q_x a}{2}\right)\cos\left(\frac{q_y a}{2}\right) + 4\cos^2\left(\frac{\sqrt{3}aq_x}{2}\right)}. \tag{3.42}$$

We see that graphene is a zero-gap semiconductor [114], with the conduction and valence bands meeting at zero energy, at two sets of inequivalent points in momentum space, corresponding to the topological points of high symmetry $\mathbf{K}$ and $\mathbf{K}'$ as defined in Figure 3.2(a).

The electronic properties of a system can not be determined uniquely from the band-structure, the nature of the eigenstates is crucial also, so in Figure 3.2(b) we plot from equation 3.30 the Berry curvature as a function of $\mathbf{q}$. To be clear, remember that we choose to parametrise an arbitrary two-band Hamiltonian by a vector $\mathbf{h}$, given in the basis of Pauli matrices. Thus, whilst $\boldsymbol{\mathcal{B}}_+$ is a function of $\mathbf{q}$, the arrows in Figure 3.2(b)

correspond to the Berry curvature in **h**-space, not **q**-space. By inspection we can see that the solid angle swept out by $\mathbf{V}_+$ when traversing a contour that encircles a $K$ or $K'$ point is $\pm 2\pi$, and we can identify these as Dirac points with a Berry phase of $\pi$. Let us now study these points further.

### 3.2.2 Massless Dirac fermions

In pristine graphene the Fermi energy $E_\mathrm{F}$ coincides exactly with the energy of the Dirac points, and for a realistic doping induced by environmental factors such as substrate doping the Fermi energy is still close to the conical points with $E_\mathrm{F} \ll t \approx 2.8\mathrm{eV}$ [24]. From Figure 3.3 we can see that the the bandstructure is approximately conical up to energies that are a significant fraction of $\pm 1\mathrm{eV}$. Therefore, to describe the electronic properties in the regime $E_\mathrm{F} \ll t$ we can expand the Hamiltonian (based on equation 3.40) around $\mathbf{q} = \tau\mathbf{K} + \mathbf{k}$ to first order in $\mathbf{k}$, where $\tau$ is a valley index, equal to $+1$ $(-1)$ for the $K$ $(K')$ valley. We see this is just a problem of expanding the function $f(\mathbf{q})$. Taking a series expansion of $\mathrm{e}^{i\mathbf{q}\cdot\mathbf{e}_j}$ to first order and noting that $\sum_{j=1}^{3} \mathrm{e}^{i\tau\mathbf{K}\cdot\mathbf{e}_j} = 0$ we have

$$f(\tau\mathbf{K} + \mathbf{k}) = \sum_{j=1}^{3} \mathrm{e}^{i\tau\mathbf{K}\cdot\mathbf{e}_j} \mathrm{e}^{i\mathbf{k}\cdot\mathbf{e}_j} \tag{3.43}$$

$$\approx -\tau \frac{3a}{2}(k_x + ik_y). \tag{3.44}$$

Thus, equation 3.43 leads directly to an expression for the approximate Hamiltonian that describes the low energy quasiparticles as

$$H_\tau = \tau\hbar v_F \left(k_x\sigma_x + \tau k_y\sigma_y\right) \tag{3.45}$$

where $v_F = \frac{3a|t|}{2} \approx c/300$ is the Fermi velocity. We can obtain a complete description of both valleys by constructing a block matrix

$$H = \hbar v_F \tau_z \otimes \boldsymbol{\sigma} \cdot \mathbf{k}, \tag{3.46}$$

which is given in the basis $\Psi = (\psi_{+,A}, \psi_{+,B}, \psi_{-,B}, \psi_{-,A})^T$ where $\psi_{\tau,s}$ denotes the component of the wavefunction in the $\tau$ valley and $s$ sublattice. Here $\tau_z$ denotes the Pauli matrix acting on the valley space. This Hamiltonian formally maps to the relativistic Dirac Hamiltonian which describes elementary spin-1/2 particles [24, 102]. The internal degree of freedom which is real spin for elementary massless Dirac fermions is given by the sublattice index in the case of graphene electrons. Thus, the spinors in graphene correspond to the distribution of probability density between the two sublattices $A$ and $B$.

The energy spectrum is seen to be conical and given by

$$E = \lambda \hbar v_F |\mathbf{k}|, \tag{3.47}$$

where the band index $\lambda = \pm 1$ corresponds to the upper and lower band respectively. Let us return to the Hamiltonian in each valley subspace $\Psi_- = (\psi_{+,A}, \psi_{+,B})$ and $\Psi_+ = (\psi_{-,B}, -\psi_{-,A})$, where we can write (based on equation 3.46) the Hamiltonian as

$$H_\tau = \hbar v_F \tau \boldsymbol{\sigma} \cdot \mathbf{k}. \tag{3.48}$$

This two level Hamiltonian is already written in the conventional form $\boldsymbol{\sigma} \cdot \mathbf{h}$ (equation 3.26), and the parameter space $\mathbf{h}$ is just $\mathbf{k}$ itself. As $\theta_\mathbf{k} = \pi/2$ the eigenvectors 3.28 are simply

$$|\lambda, \tau, \mathbf{k}\rangle = \frac{1}{\sqrt{2}}(1, \lambda\tau \exp[i\phi_\mathbf{k}]). \tag{3.49}$$

These eigenstates have a well defined chirality, in the sense that their representation in the Bloch sphere is simply $\mathbf{V}^\tau_\lambda(\mathbf{k}) = \lambda\tau\hat{\mathbf{k}}$. For massless particles chirality is the same as helicity $\eta_\mathbf{q}$, a term which originates in high-energy physics and is defined as the projection of a particle's spin onto its direction of motion [115]

$$\eta_\mathbf{q} = \frac{\boldsymbol{\sigma} \cdot \mathbf{q}}{|\mathbf{q}|}. \tag{3.50}$$

The helicity (or equivalently chirality) of a massless particle state is given by its eigenvalue $\eta = \pm 1$ when operated on by $\eta_{\mathbf{q}}$. Note that in the context of graphene $\boldsymbol{\sigma}$ does not represent the real spin of an electron but the sublattice pseudospin. Thus, by inspection of the Hamiltonian 3.48 we see that the chirality of the eigenstates 3.49 is $\eta = \lambda\tau$. In other words, in the $K$ valley the unit vector of Berry curvature $\mathbf{V}_{\pm}^{K}$ is constrained to align (anti-align) with the wavevector for the upper (lower) band, and vice versa for the $K'$ valley. Thus, we can immediately identify these states with an associated Berry phase of $\pi$.

## 3.3 Consequences of chirality

Many of the electronic properties of graphene can be understood as a result of chirality. Perhaps two of the most dramatic consequences are the suppression of backscattering off smooth potentials [25], and Klein tunneling [116] — the complete transmission (for certain angles of incidence) of graphene electrons through arbitrarily tall and wide barrier potentials.

### 3.3.1 Suppression of elastic backscattering

Consider an impurity potential $U(\mathbf{r})$ that varies smoothly on the scale of the lattice constant so as to suppress intervalley scattering. This allows us to work in a single valley subspace, and we choose the $K$ valley here. The potential modifies the Hamiltonian $H_0 = \hbar v_F \boldsymbol{\sigma}\cdot\mathbf{k}$ of graphene by the introduction of a diagonal term $V = U(\mathbf{r})\mathbb{1}$. The probability amplitude that such a potential causes a state $|\pm,\mathbf{k}\rangle$ to back scatter elastically into the state $|\pm,-\mathbf{k}\rangle$ is proportional to the matrix element $\langle\pm,-\mathbf{k}|T|\pm,\mathbf{k}\rangle$ of the corresponding $T$-matrix [117]

$$T = \sum_n T_n, \qquad T_n = V\left[(E - H_0)^{-1} V\right]^n. \tag{3.51}$$

Firstly we can easily see that if the potential is weak such that the $T$-matrix is well approximated by the zeroth order term $T_0 = V$, then the back scattering matrix element

is zero as the states $|+,\mathbf{k}\rangle$ and $|+,-\mathbf{k}\rangle$ (or $|-,\mathbf{k}\rangle$ and $|-,-\mathbf{k}\rangle$) are orthogonal. Moreover, as revealed by T. Ando et al. [25], by considering the full $T$-matrix and a little cunning manipulation of indices one can show that the back scattering matrix element disappears identically for any arbitrary potential $U(\mathbf{r})$. This remarkable result allows us to understand the high mobility and low resistivity in graphene as a direct consequence of chirality: Two states with anti-aligned wavevectors have anti-aligned 'pseudospins' $\mathbf{V}$ and thus are orthogonal states.

### 3.3.2 Klein tunneling

In this section we consider the transport of charge carriers through a step barrier potential (PNP junction). We will see some remarkable results which are the condensed matter analogue of the Klein 'paradox' for relativistic spin-1/2 elementary particles [116]. We consider the graphene Hamiltonian

$$H = \hbar v_F \boldsymbol{\sigma} \cdot \mathbf{k} + V(x), \tag{3.52}$$

where $V(x)$ is a barrier potential that we suppose to be smooth on the scale of the lattice constant (to suppress intervalley scattering) but sharp on the scale of the Fermi wavelength (so that we are justified in modelling the potential as a step barrier and matching wavefunctions at the discontinuities). We thus consider a potential that is translationally invariant in the $\hat{\mathbf{y}}$ direction given by

$$V(x) = \begin{cases} 0, & x < 0 \\ V_B, & 0 < x < D \\ 0, & x > D \end{cases}, \tag{3.53}$$

which segregates space into three distinct regions as shown in Figure 3.4. Consider the forward propagating (rightward bound) solution in any region. It is essentially the spinor $|\pm,\mathbf{k}\rangle$ of equation 3.49

$$\Phi^{\rightarrow}(V) = \mathrm{e}^{ik_x x}\mathrm{e}^{ik_y y}\begin{pmatrix} 1 \\ S\exp(i\phi_{\mathbf{k}}) \end{pmatrix}, \tag{3.54}$$

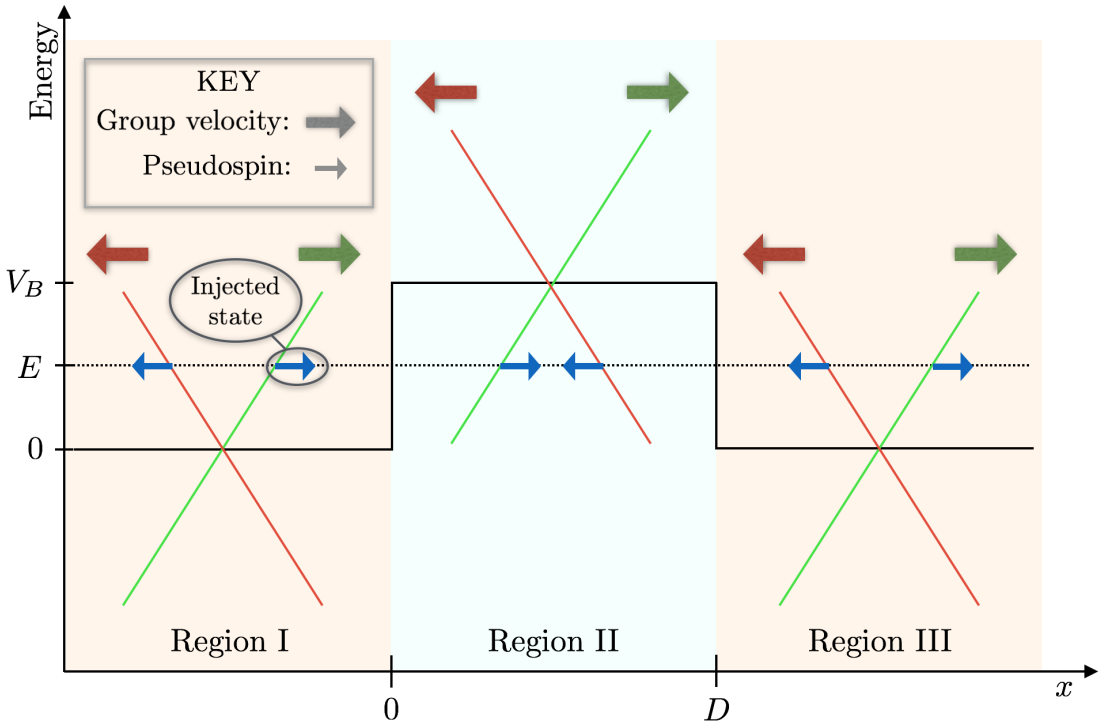


**Figure 3.4:** Schematic of Klein tunneling at normal incidence. The energy of the potential barrier and injected state are shown by the solid and dashed black lines respectively. The conical bandstructure (arbitrary scale) of graphene is superimposed in each region, with $k_x$ along the horizontal axis. The green (red) bands have positive (negative) group velocity as indicated by the large arrows. Also shown in the small blue arrows are the pseudospin vectors. The pseudospins of forward propagating states are antipodal (aka orthogonal) to the backward propagating states and so the injected state can only scatter into forward propagating states.

where $k_y$ is conserved across all regions due to the translational invariance, $k_x = \sqrt{(E-V)^2/\hbar^2 v_F^2 - k_y^2}$, $\phi_{\mathbf{k}} = \arctan(k_y/k_x)$ and $S(V) = \mathrm{sgn}(E-V)$. As the spectrum is isotropic the backward propagating solution $\Phi^{\leftarrow}$ is obtained easily from $\Phi^{\rightarrow}$ by the substitutions $k_x \to -k_x$, $k_y \to k_y$ and $\phi_{\mathbf{k}} \to \pi - \phi_{\mathbf{k}}$ and reads

$$\Phi^{\leftarrow}(V) = \mathrm{e}^{-ik_x x}\mathrm{e}^{ik_y y}\begin{pmatrix} 1 \\ -S\exp(-i\phi_{\mathbf{k}}) \end{pmatrix}. \tag{3.55}$$

If we specify the 'injected' state to be forward propagating in the region left of the barrier, the general solution is

$$\psi = \begin{cases} \Phi^{\rightarrow}(0) + r\Phi^{\leftarrow}(0), & x < 0 \\ A\Phi^{\rightarrow}(V_B) + B\Phi^{\leftarrow}(V_B), & 0 < x < D \\ t\Phi^{\rightarrow}(0), & x > D \end{cases} . \tag{3.56}$$

The coefficients $r$ (reflection), $t$ (transmission), $A$ and $B$ are obtained by equating the wavefunction in the three regions at the discontinuities in $V(x)$. From this it follows that the reflection coefficient is

$$r = \frac{2i \exp(i\phi_{\mathbf{k}}) \sin(k'_x D) \left(\sin\phi_{\mathbf{k}} - SS' \sin\phi_{\mathbf{k}'}\right)}{SS' \left[\exp(-ik'_x D)\cos(\phi_{\mathbf{k}} + \phi_{\mathbf{k}'}) + \exp(ik'_x D)\cos(\phi_{\mathbf{k}} - \phi_{\mathbf{k}'})\right] - 2i\sin(k'_x D)} \tag{3.57}$$

where the variables with (without) a prime symbol correspond to those inside (outside) the barrier region.

Figure 3.5 shows the transmission probability $T = 1 - |r|^2$ as a function of incidence angle. As can be seen from the figure and equation 3.57, at normal incidence the transmission is exactly unity irrespective of the barrier height or width. This counter intuitive result is directly analogous to the Klein paradox in QED, and is in stark contrast to the typical exponentially suppressed transmission associated with non-chiral electronic systems [106]. That it is directly related to chirality is highlighted in Figure 3.4 where we present a schematic of the pseudospin and bandstructure in each region. We see that a reflection is forbidden as this would violate the conservation of pseudospin, and hence there is only one (a forward propagating) channel into which a normally incident electron can scatter. There are also additional resonant values ($q'_x D = n\pi$) at which the transmission is unity, but most importantly we emphasise again that perfect transmission always persists for normal incidence.

Such intriguing chiral tunnelling phenomenon have important consequences for the electronic properties of graphene and device applications. The suppression of back scattering and high transmission amplitudes at several other scattering angles minimise the localisation effects expected from disorder, as well as help to explain the observed minimal conductivity of graphene even at vanishing charge carrier density [22, 118, 119]. We now

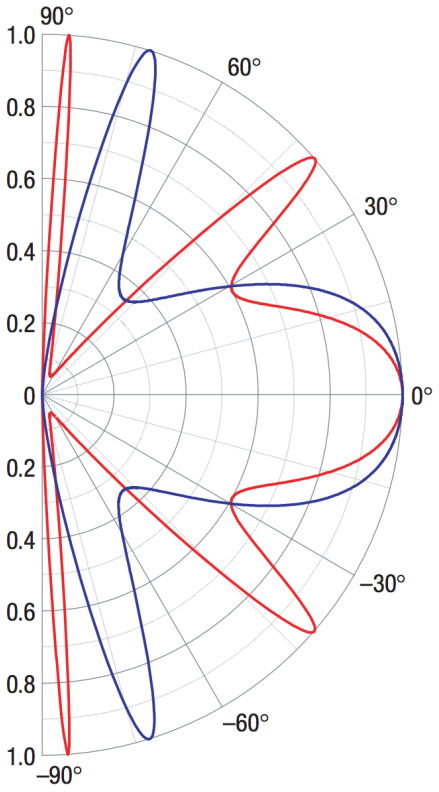


**Figure 3.5:** The transmission probability $T = 1 - |r|^2$ as a function of incidence angle $\phi_{\mathbf{k}}$, where $r$ is defined in equation 3.57. The red (blue) curve corresponds to a hole concentration of $1 \times 10^{12}\text{cm}^{-2}$ ($3 \times 10^{12}\text{cm}^{-2}$) and barrier height of 200meV (285meV) within region II (see Figure 3.4). Figure adapted with permission from [116]. Copyright 2006 Nature Publishing Group.

proceed to the final section of this introduction to explore the modification of graphene in the presence of strain induced pseudo-magnetic fields.

## 3.4 Pseudo-magnetic gauge fields

The electronic properties of graphene in presence of a real magnetic field display unique signatures [24], for example the half-integer quantum Hall effect [22] that is observable at room temperature [120]. The description of a magnetic field enters the Hamiltonian as a gauge field ($\mathbf{p} \to \mathbf{p} - e\mathbf{A}^{\mathrm{em}}$). Intriguingly the effects of intrinsic or mechanical deformation of a graphene membrane can also be expressed as a gauge field [118, 121], which suggests the possibility to realise magnetic phenomena in the absence of a magnetic field. Let us present the basic theory followed by a discussion of strain-induced Landau quantisation.

### 3.4.1 Modification of model due to strain

If a strain is imposed upon a graphene membrane, in general both the nearest neighbour lengths and orientations will be modified. Assuming the strain is smooth on the scale of the interparticle distances, the sublattice symmetry is unbroken and we are able to treat the system as a membrane within the theory of continuum mechanics [24]. We will restrict our investigations to in-plane deformations only. As usual the displacement vector is defined as $\mathbf{u}(\mathbf{R}) = \mathbf{R}'(\mathbf{R}) - \mathbf{R}$ where $\mathbf{R}$ and $\mathbf{R}'$ are the coordinates of the undeformed and deformed membrane respectively. The nearest neighbour coordinates of a particle at position $\mathbf{R}$ are transformed to

$$e'_\alpha = \left(\delta_{\alpha\beta} + \frac{\partial u_\alpha}{\partial x_\beta}\right) e_\beta, \tag{3.58}$$

to first order in $\mathbf{u}$, where Einstein summation is implied over the set $\{x, y\}$. Similarly the length becomes $|\mathbf{e}'|^2 = |\mathbf{e}|^2 + 2u_{\alpha\beta}e_\alpha e_\beta$ with the strain tensor defined to lowest-order in the strain as [122]

$$u_{\alpha\beta} = \frac{1}{2}\left(\frac{\partial u_\alpha}{\partial x_\beta} + \frac{\partial u_\beta}{\partial x_\alpha}\right). \tag{3.59}$$

Upon incorporating the modified nearest-neighbour vectors into the low energy graphene Hamiltonian 3.48 one realises that these alterations can be written as a gauge potential,

formally in much the same way as for a real magnetic field. As such, to first order in the strain tensor the Hamiltonian 3.48 becomes

$$H_\tau = \tau v_F \boldsymbol{\sigma} \cdot \boldsymbol{\pi}_\tau, \tag{3.60}$$

where $\boldsymbol{\pi}_\tau = \mathbf{p} - \tau e\mathbf{A}$ and the gauge potential is

$$\mathbf{A} = \frac{\hbar\beta}{ae} \begin{pmatrix} u_{xx} - u_{yy} \\ -2u_{xy} \end{pmatrix}, \tag{3.61}$$

with coefficients chosen so that $\mathbf{A}$ has the same units as a real magnetic vector potential, leading naturally to the definition of a 'pseudo-magnetic' field

$$B = \partial_x A_y - \partial_y A_x. \tag{3.62}$$

The factor $\beta \approx 2$ arises from the dependence of the hopping integral on inter-atomic distances and particulars of chemical bonding. We see that $\mathbf{A}$ has an opposite sign in each valley and thus mechanical deformations, unlike a real magnetic vector potential, do not globally violate time-reversal symmetry. However, formally similar gauge potentials produce physically similar effects. As an example we will now discuss the possibility to produce Landau quantisation in the absence of real magnetic fields.

### 3.4.2 Landau quantisation in zero magnetic field

Not all strains give rise to a non-vanishing pseudo-magnetic field. For example the simplest case of a uniform strain renders $\mathbf{A}$ a constant and hence $\mathbf{B}$ zero. It is perhaps not so surprising that a uniform finite $\mathbf{B}$ is realised by strains that possess the same triangular symmetry as the underlying lattice [123]. As an example one can employ a simple displacement vector of the form $\mathbf{u} \propto (2xy, x^2 - y^2)$, yielding the symmetric gauge $\mathbf{A} = (B/2)(-y, x)$. Under such a strain the energy spectrum now comprises of Landau levels which is made evident upon introduction of the bosonic operator $\gamma = (2eB\hbar)^{-\frac{1}{2}}(\pi_x - i\pi_y)$. The Hamiltonian 3.60 in the $K$ valley now reads

$$H = \hbar \begin{pmatrix} 0 & \omega_D \gamma \\ \omega_D \gamma^\dagger & 0 \end{pmatrix}, \tag{3.63}$$

where $\omega_D = v(2eB/\hbar)^{\frac{1}{2}}$. The Schrödinger equation for the eigenstates $\psi = (\psi_A, \psi_B)^{\mathrm{T}}$ and energy eigenvalues $E$ are

$$\gamma \psi_B = \epsilon \psi_A, \tag{3.64}$$

$$\gamma^\dagger \psi_A = \epsilon \psi_B, \tag{3.65}$$

where $\epsilon = E/\hbar\omega_D$. One can immediately identify the ground state as that with $\psi_A = 0$ so that the solution is completely polarised in pseudo-spin space, signifying that the state belongs entirely to the $B$ sublattice. For the $K'$ valley $\psi_A$ and $\psi_B$ switch places in equation 3.64 so that the ground state belongs entirely to the $A$ sublattice. By acting with $\gamma^\dagger$ upon 3.64 we obtain $\gamma^\dagger \gamma \psi_B = \epsilon^2 \psi_B$ and thus the energy spectrum is

$$E_n^{\pm} = \pm \hbar \omega_D \sqrt{n}, \tag{3.66}$$

where $n \in \mathbb{N}$. These discrete energy levels are exactly the same as the Landau levels one obtains from a real magnetic field. Unlike the spectrum of non-relativistic electrons here we have Landau levels that are not equally spaced in energy and a zero energy state shared equally by electrons and holes, yet completely polarised in pseudo-spin space as already discussed.

## 3.5 Chapter Summary

We have explored some of the remarkable electronic properties of graphene, such as the suppression of backscattering and Klein tunneling. Importantly the origin of these phenomena is not intrinsically linked to the statistics of the constituents, but rather to the symmetries of the honeycomb lattice itself. Therefore, it is not too great a leap of imagination to envisage that other physical systems that share the same symmetries as

graphene will reap similar rewards. In the next section we begin our investigation of a honeycomb structured array of metallic nanoparticles, and will unite our discussions of Dirac physics from this chapter and those of plasmonics from the preceding one.

# Chapter 4

# Dirac plasmons in bipartite lattices of metallic nanoparticles

Much of the research presented in this chapter forms the substance of a paper [124] published in the journal 2D Materials, on which I am first author. This work was carried out with my collaborators Claire Woollacott, Guillaume Weick and my supervisor Eros Mariani. The figures (and videos) are reproduced with permission from © IOP Publishing, all rights reserved.

In the previous two chapters which sampled the literature on both plasmonics and graphene science we have explained our motivation in studying a honeycomb structured lattice of metallic nanoparticles. We have seen that nanofabrication technologies enable one to precisely fabricate nanoparticle arrays [68] with near unlimited design possibilities for the constituents and arrangement. The optical properties of nanoparticle arrays depend crucially on the underlying lattice structure and the microscopic interactions between LSP resonances [60], and so we seek inspiration in choosing an interesting lattice out of the infinite possibilities. As is often the case, nature provides a candidate: the honeycomb structured array exhibited by graphene. Graphene has been shown to exhibit a myriad of fascinating electronic and transport phenomena [114], the majority of which are a direct consequence of the symmetries of the underlying lattice and not in any deep sense connected to the statistics of the constituents. This fact, along with the existence of other artificial graphene systems, suggests that collective plasmons in a

honeycomb array of nanoparticles should inherit many analogous properties to graphene, such as a non-trivial Berry phase of $\pi$ and the suppression of backscattering [116].

We begin in section 4.1 by presenting the general model of interacting metallic nanoparticles in the simpler context of a dimer and a linear chain. The subsequent section 4.2 is the bulk of this chapter and the corresponding published paper, where we study nanoparticle arrays with a perfect honeycomb structure, with and without inversion symmetry, as well as generic bipartite lattices. We explore the band structure of the CPs in section 4.2.5 and unveil a phenomenal tunability granted by the polarisation degree of freedom. Section 4.2.4 identifies a rich polarisation-space phase diagram that maps out those polarisations (i.e. the orientations of the dipole moments associated with the LSPs) which correspond to a gapped or gapless CP dispersion. Moreover, we show that all the gapless phases in the phase diagram are characterised by CPs behaving as massless chiral Dirac particles, in analogy with electrons in graphene. In section 4.2.6 we explore the effects of breaking the inversion symmetry, and find that in this case collective plasmons are described as gapped chiral Dirac modes with an energy-dependent Berry phase. We relax a further symmetry in section 4.3 by analysing generic bipartite hexagonal lattices of which the honeycomb structure is a special case. There we study the evolution of the phase diagram and unveil the emergence of a sequence of topological phase transitions when one hexagonal sublattice is progressively 'shifted' with respect to the other.

## 4.1 Model

Initially we will introduce and illustrate some of the approximations used to model an array of nanoparticles in the context of an interacting dimer of identical nanoparticles, as well as a linear chain. In this way we will be able to interpret some more complicated scenarios within simpler contexts, and understand which features arise due to the underlying lattice structure and those which originate in the polarisation degree of freedom. We will use a notation that is more verbose than required at this stage, so as to facilitate easy generalisation and understanding in the subsequent sections.

### 4.1.1 Model of a nanoparticle dimer

We have seen that for nanoparticles on the scale of a few tens of nanometers the electromagnetic response is overwhelmingly dipolar [6, 60, 65, 79, 80] and as per equation 2.28 the Hamiltonian for the LSP of a single isolated nanoparticle [62–64] located at $\mathbf{R}$ is

$$H_0(\mathbf{R}) = \frac{\mathbf{\Pi}^2(\mathbf{R})}{2M} + \frac{1}{2}M\omega_0^2\mathbf{h}^2(\mathbf{R}). \tag{4.1}$$

where $M = Nm$ is the mass of the $N$ valence electrons, and $\omega_0$ is the LSP natural frequency of oscillation. As discussed in chapter 2, $\omega_0$ typically lies in the visible spectrum with a magnitude on the order of 500THz. The LSP can be considered as a quantum bosonic mode with $\mathbf{h}$ and $\mathbf{\Pi}$ representing position and (conjugate) momentum operators of the electronic centre of mass [62, 63]. Equation 4.1 describes a quantum simple harmonic oscillator and can be rewritten in terms of creation ($a^\dagger_{\mathbf{R}}$) and annihilation ($a_{\mathbf{R}}$) operators as

$$H_0(\mathbf{R}) = \hbar\omega_0 a^\dagger_{\mathbf{R}} a_{\mathbf{R}}, \tag{4.2}$$

where

$$a_{\mathbf{R}} = \sqrt{\frac{M\omega_0}{2\hbar}}h(\mathbf{R}) + i\sqrt{\frac{1}{2\hbar M\omega_0}}\Pi(\mathbf{R}), \tag{4.3}$$

and $a^\dagger_{\mathbf{R}}$ annihilate and create LSPs in the nanoparticle at position $\mathbf{R}$, respectively. For completeness and reference the original operators in terms of creation and annihilation operators are

$$h(\mathbf{R}) = \sqrt{\frac{\hbar}{2M\omega_0}}(a_{\mathbf{R}} + a^\dagger_{\mathbf{R}}), \qquad \Pi(\mathbf{R}) = i\sqrt{\frac{\hbar M\omega_0}{2}}(a^\dagger_{\mathbf{R}} - a_{\mathbf{R}}). \tag{4.4}$$

The non-interacting part of the Hamiltonian for a dimer is thus simply a sum over equation 4.2 at the positions $\mathbf{R}_1$ and $\mathbf{R}_2$ of the two nanoparticles

$$H_0 = \sum_{n=1}^{2} H_0(\mathbf{R}_n) = \hbar\omega_0 \left( a^\dagger_{\mathbf{R}_1} a_{\mathbf{R}_1} + a^\dagger_{\mathbf{R}_2} a_{\mathbf{R}_2} \right). \tag{4.5}$$

As discussed in section 2.3 the interaction between the LSPs of two nanoparticles can be taken as a dipole-dipole interaction for nanoparticles with a radius $\text{ר}$ less than a few tens of nanometres [17, 86] and a minimal separation of $a \gtrsim 3\text{ר}$ [34]. For a small enough separation such that $a \ll c/\omega_0$ the near-field terms of the coupled dipole approximation are dominant. Thus, the interaction energy of the dimer is [48]

$$\mathcal{V}(\mathbf{R}_1, \mathbf{R}_2) = -\mathbf{p}_1 \cdot \mathbf{E}_2 = -\mathbf{p}_2 \cdot \mathbf{E}_1, \tag{4.6}$$

where $\mathbf{p}_n$ and $\mathbf{E}_n$ are the dipole moment and its electric field of the LSP at the nanoparticle position $\mathbf{R}_n$. Referring to equation 2.33 this is given by

$$\mathcal{V}(\mathbf{R}_1, \mathbf{R}_2) = \frac{1}{4\pi\epsilon_0\epsilon_\mathrm{D}|\mathbf{e}_{12}|^3} \left[ (\mathbf{p}_1 \cdot \mathbf{p}_2) - 3(\hat{\mathbf{e}}_{12} \cdot \mathbf{p}_1)(\hat{\mathbf{e}}_{12} \cdot \mathbf{p}_2) \right], \tag{4.7}$$

where $\mathbf{e}_{mn} = \mathbf{R}_m - \mathbf{R}_n$. In the following we assume that for an eigenmode of the dimer the dipole moments of the LSPs in each individual nanoparticle are polarised in the same direction $\hat{\mathbf{p}} = \hat{\mathbf{p}}_1 = \hat{\mathbf{p}}_2$. This assumption holds in the quasistatic regime where the wavelength of the eigenmode is much larger than the interparticle separation and we can neglect retardation effects. For a dimer of spherical nanoparticles the eigenmodes are aligned parallel or perpendicular to the separation axis $\hat{\mathbf{e}}_{12}$. To obtain a polarisation $\hat{\mathbf{p}}$ that is arbitrarily orientated one can use spheroidical nanoparticles (or other anisotropic nanoparticles) as discussed in detail in Appendix B. Therefore, in general the interaction energy 4.7 simplifies to

$$\mathcal{V}(\mathbf{R}_1, \mathbf{R}_2) = \frac{N^2 e^2}{4\pi\epsilon_0\epsilon_\mathrm{D}|\mathbf{e}_{12}|^3} \mathcal{C}_{12}(\hat{\mathbf{p}}) h(\mathbf{R}_1) h(\mathbf{R}_2), \qquad \mathcal{C}_{12}(\hat{\mathbf{p}}) = 1 - 3(\hat{\mathbf{e}}_{12} \cdot \hat{\mathbf{p}})^2, \tag{4.8}$$

where $\mathcal{C}_{mn}(\hat{\mathbf{p}})$ parametrises the interaction strength between dipoles located at $\mathbf{R}_m$ and $\mathbf{R}_n$, polarised in the direction $\hat{\mathbf{p}}$. We switch to the quantum representation of the

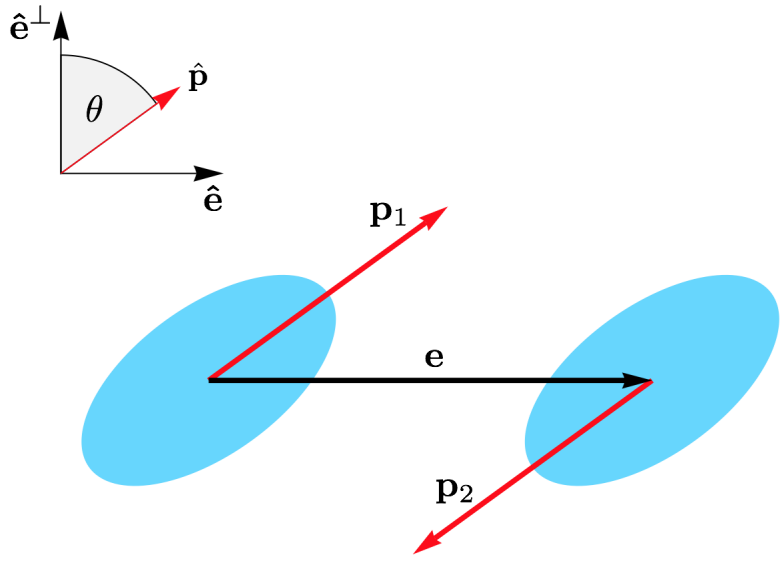


**Figure 4.1:** Schematic of an eigenmode of a dimer of anisotropic nanoparticles. The dipoles (red/gray arrows) are polarised along the direction $\hat{\mathbf{p}}$ (with angle $\theta$) determined by the orientated anisotropic nanoparticles (ovals). The nanoparticle centres are separated by the vector $\mathbf{e}$. The unit vector $\hat{\mathbf{e}}^{\perp}$ is the perpendicular unit vector to $\hat{\mathbf{e}}$.

interaction Hamiltonian $\mathcal{V}(\mathbf{R}_1, \mathbf{R}_2) \rightarrow H_{\text{int}}$ with substitution of the expressions 4.4 for $h(\mathbf{R}_n)$ such that $H_{\text{int}} \equiv H_{12}$ where

$$H_{\text{mn}} = \hbar\Omega_{mn}\mathcal{C}_{mn}(\hat{\mathbf{p}})(a_{\mathbf{R}_\text{m}} + a^{\dagger}_{\mathbf{R}_\text{m}})(a_{\mathbf{R}_\text{n}} + a^{\dagger}_{\mathbf{R}_\text{n}}), \qquad \mathcal{C}_{mn}(\hat{\mathbf{p}}) = 1 - 3(\hat{\mathbf{e}}_{mn} \cdot \hat{\mathbf{p}})^2, \tag{4.9}$$

where $\Omega_{mn} = Ne^2/(8\pi\epsilon_0\epsilon_D|\mathbf{e}_{mn}|^3 m\omega_0)$ is an interaction Hamiltonian between two identical nanoparticles. For spherical nanoparticles with a natural frequency $\omega_0$ corresponding to the Mie frequency of equation 2.23, the interaction strength $\Omega_{mn}$ can be written in terms of material parameters as

$$\Omega_{mn} = \omega_0 \left(\frac{\text{ר}}{|\mathbf{e}_{mn}|}\right)^3 \frac{1 + 2\epsilon_D}{6\epsilon_D}. \tag{4.10}$$

In the problem at hand $|\mathbf{e}_{12}| = a$ and we denote $\Omega \equiv \Omega_{12}$. Due to the rotational symmetry about $\hat{\mathbf{e}}$ we need only parametrise the polarisation by the angle $\theta$ from the normal to $\hat{\mathbf{e}}_{12}$ such that $\mathcal{C}(\theta) \equiv \mathcal{C}_{12}(\hat{\mathbf{p}}) = 1 - 3\sin^2\theta$ as shown in Figure 4.1. Note that by tilting the polarisation we can tune the interaction parameter $\mathcal{C}(\theta)$. It is easy to understand this physically if we take the limiting cases $\max[\mathcal{C}(\theta)] = \mathcal{C}(0) = 1$ where

the dipoles lie alongside one another (↑↑) and thus repel, and $\min[\mathcal{C}(\theta)] = \mathcal{C}(\pi/2) = -2$ where the dipoles are arranged head to tail (→→) and thus attract. Therefore, we have the interaction Hamiltonian

$$H_{\text{int}} = \hbar\Omega\mathcal{C}(\theta)(a_{\mathbf{R}_1} + a^\dagger_{\mathbf{R}_1})(a_{\mathbf{R}_2} + a^\dagger_{\mathbf{R}_2}). \tag{4.11}$$

The eigenfrequencies $\omega$ of the full Hamiltonian $H = H_0 + H_{\text{int}}$ can be obtained by introducing normal mode operators $\gamma_\tau$ which diagonalise the Hamiltonian as

$$H = \hbar\sum_\tau \omega_\tau \gamma^\dagger_\tau \gamma_\tau, \tag{4.12}$$

where we have labelled the indices as $\tau = \pm$ with hindsight. Clearly the new operators are a superposition of the original operators

$$\gamma_\tau = w_\tau a_{\mathbf{R}_1} + x_\tau a_{\mathbf{R}_2} + y_\tau a^\dagger_{\mathbf{R}_1} + z_\tau a^\dagger_{\mathbf{R}_2}, \tag{4.13}$$

and satisfy the equation $[\gamma_\tau, H] = \hbar\omega_\tau\gamma_\tau$ by definition. This leads immediately to the eigenvalue equation

$$\begin{pmatrix} \omega_0 & \Omega\mathcal{C}(\theta) & 0 & \Omega\mathcal{C}(\theta) \\ \Omega\mathcal{C}(\theta) & \omega_0 & \Omega\mathcal{C}(\theta) & 0 \\ 0 & -\Omega\mathcal{C}(\theta) & -\omega_0 & -\Omega\mathcal{C}(\theta) \\ -\Omega\mathcal{C}(\theta) & 0 & -\Omega\mathcal{C}(\theta) & -\omega_0 \end{pmatrix} \begin{pmatrix} w_\tau \\ x_\tau \\ y_\tau \\ z_\tau \end{pmatrix} = \omega_\tau \begin{pmatrix} w_\tau \\ x_\tau \\ y_\tau \\ z_\tau \end{pmatrix}. \tag{4.14}$$

The solutions are

$$\omega_\pm = \omega_0\sqrt{1 \pm 2\frac{\Omega}{\omega_0}|\mathcal{C}(\theta)|}, \tag{4.15}$$

which are plotted in Figure 4.2. As we see here, and as discussed without proof in section 2.3, for each polarisation angle $\theta$ there are two eigenmodes of a dimer. In the figure the black line corresponds to the dark mode, where the individual dipoles are anti-aligned and have no net dipole moment, whereas the red/gray line corresponds to the bright

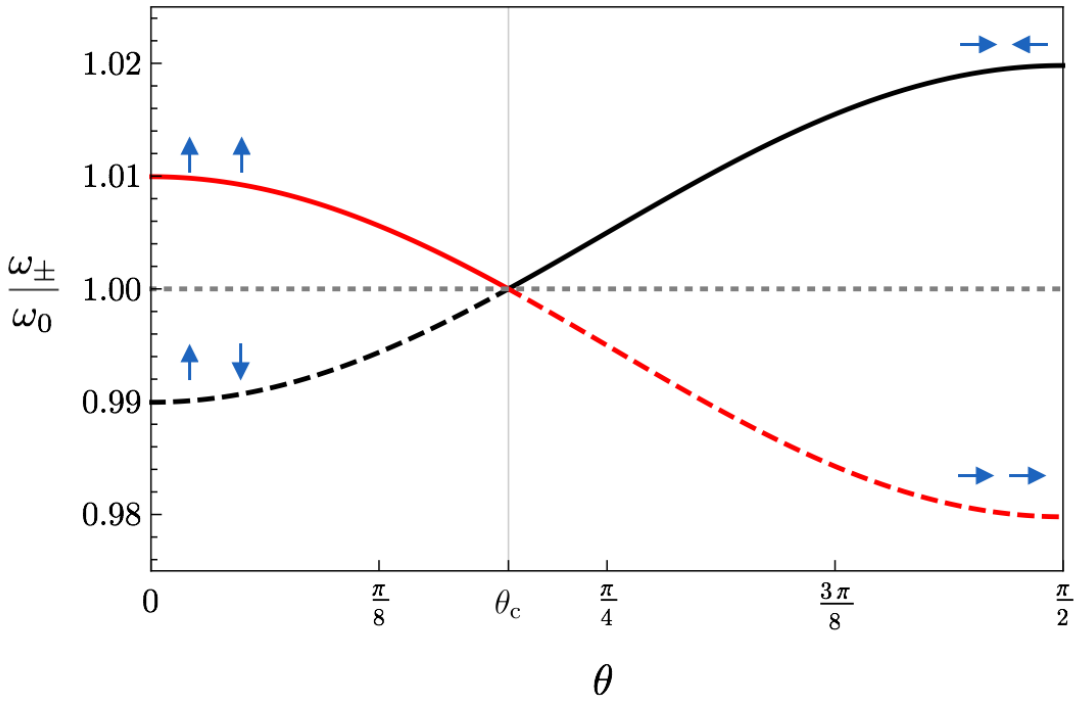


**Figure 4.2:** Eigenfrequencies of a dimer of identical nanoparticles as a function of polarisation angle $\theta$. Solid (dashed) curves represent the $+$ $(-)$ solutions, whereas red/gray (black) curves denote bright (dark) modes. At the critical angle $\theta_c = \arcsin(\sqrt{1/3})$ the interaction parameter $\mathcal{C}_{12}(\theta_c) = 0$ so the eigenfrequencies are those of two decoupled nanoparticles $\omega_+ = \omega_- = \omega_0$ (dashed gray line). Also shown are pairs of blue arrows, representing the polarisation of the dimer eigenmodes at the extrema $\theta = 0$ and $\theta = \pi/2$. Figure styling adapted from [125].

mode of aligned dipoles. The energy of the mode depends crucially on the polarisation angle $\theta$ and we see that the sign of the interaction energy for each mode switches at a critical angle $\theta_c = \arcsin(\sqrt{1/3})$. At this angle the interaction energy is exactly zero and the response is just that of two non-interacting dipoles.

### 4.1.2 Linear chain

Now that we have introduced the key quantities related to LSP interactions, we continue the exposition of our formalism by examining the simplest nanoparticle array, a monatomic linear chain as shown in Figure 4.3. The non-interacting part of the Hamiltonian is simply a sum of equation 4.2 over all lattice vectors $\mathbf{R}_m$

$$H_0 = \hbar\omega_0 \sum_m a^\dagger_{\mathbf{R}_m} a_{\mathbf{R}_m}. \tag{4.16}$$

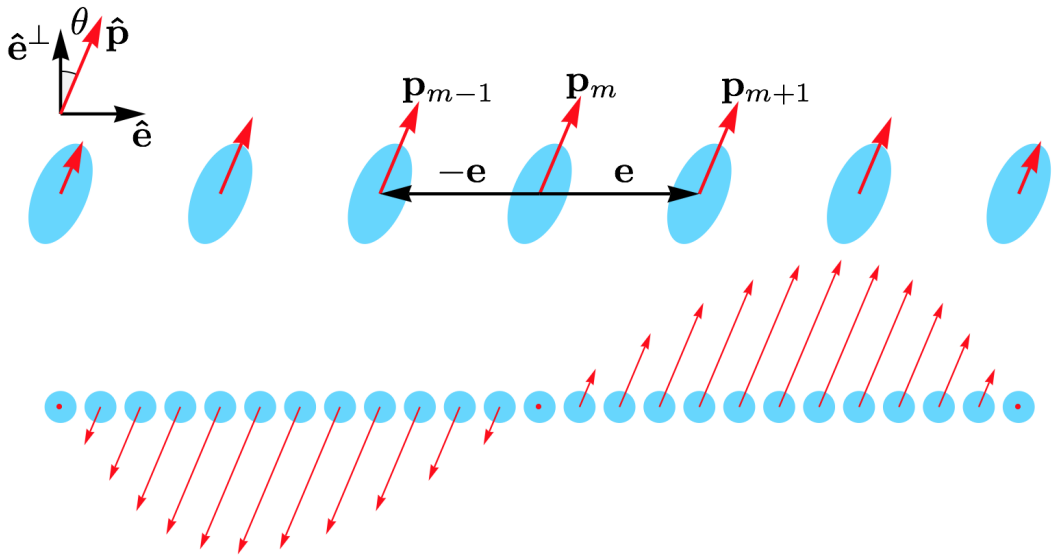


**Figure 4.3:** (Top) Schematic of the eigenmodes of (a section of) an infinite linear chain. The dipoles (red/gray arrows) are polarised in an arbitrary direction $\hat{\mathbf{p}}$ (with angle $\theta$) due to the orientated anisotropic nanoparticles (ovals). The nanoparticles are labelled as $m \in \mathbb{Z}$, ordered such that $m$ increases from left to right. A nanoparticle at position $\mathbf{R}_m$ has two nearest neighbours at $\mathbf{R}_{m-1}$ and $\mathbf{R}_{m+1}$. (Bottom) A zoom out of the same schematic, but with less detail.

We consider just nearest-neighbour interactions so that each nanoparticle located at $\mathbf{R}_m$ is interacting with another at $\mathbf{R}_{m+1}$ and $\mathbf{R}_{m-1}$, where $\mathbf{R}_{m\pm1} = \mathbf{R}_m \pm \mathbf{e}$ with $\mathbf{e}$ the nearest neighbour vector that points along the nanoparticle axis as indicated in Figure 4.3, whose magnitude is the lattice constant $a$. Thus, the interaction Hamiltonian $H_{\text{int}}$ is a sum of $H_{mn}$ (equation 4.9) over all $m \in \mathbb{Z}$ and $n \in \{m-1, m+1\}$. As the two nearest neighbour vectors have the same magnitude $a$ and are anti-aligned, it is easily verified that $\Omega_{m,m-1} = \Omega_{m,m+1} \equiv \Omega$ and $\mathcal{C}_{m,m-1}(\hat{\mathbf{p}}) = \mathcal{C}_{m,m+1}(\hat{\mathbf{p}}) \equiv \mathcal{C}(\theta)$. Thus, the interaction Hamiltonian reads

$$H_{\text{int}} = \sum_m \sum_n H_{\text{mn}} = \frac{\hbar\Omega}{2}\mathcal{C}(\theta) \sum_m a^\dagger_{\mathbf{R}_\text{m}} \left( a_{\mathbf{R}_{\text{m}-1}} + a^\dagger_{\mathbf{R}_{\text{m}-1}} + a_{\mathbf{R}_{\text{m}+1}} + a^\dagger_{\mathbf{R}_{\text{m}+1}} \right) + \text{H.c.}. \tag{4.17}$$

The bosonic operators 4.3 can be converted to momentum space by identifying their Fourier representation

$$a_{\mathbf{R}} = \frac{1}{\sqrt{\mathcal{N}}} \sum_{\mathbf{q}} \exp(i\mathbf{q}\cdot\mathbf{R}) a_{\mathbf{q}}, \tag{4.18}$$

where $\mathcal{N}$ is the number of nanoparticles. Using the identity $\sum_m^{\mathcal{N}} \exp(i\mathbf{q}\cdot\mathbf{R}_m) = \mathcal{N}\delta_{\mathbf{q},\mathbf{0}}$ this implies

$$a^\dagger_{\mathbf{R}_\mathrm{m}} a_{\mathbf{R}_\mathrm{m}+\mathbf{e}} = \frac{1}{\mathcal{N}} \sum_{\mathbf{q},\mathbf{k}} a^\dagger_{\mathbf{q}} a_{\mathbf{k}} \exp\left[i(\mathbf{k}-\mathbf{q})\cdot\mathbf{R}_m\right] \exp(i\mathbf{k}\cdot\mathbf{e}) \tag{4.19}$$

$$\implies \sum_m a^\dagger_{\mathbf{R}_\mathrm{m}} a_{\mathbf{R}_\mathrm{m}+\mathbf{e}} = \sum_{\mathbf{q}} a^\dagger_{\mathbf{q}} a_{\mathbf{q}} \exp(i\mathbf{q}\cdot\mathbf{e}), \tag{4.20}$$

and similarly for the other combinations of operators. Therefore, in momentum space the Hamiltonian $H = H_0 + H_\mathrm{int}$ is

$$H_0 = \hbar\omega_0 \sum_{\mathbf{q}} a^\dagger_{\mathbf{q}} a_{\mathbf{q}} + \frac{\hbar\Omega}{2} \sum_{\mathbf{q}} \left[ f_{\mathbf{q}}(\theta) a^\dagger_{\mathbf{q}} \left( a_{\mathbf{q}} + a^\dagger_{-\mathbf{q}} \right) + \mathrm{H.c.} \right], \tag{4.21}$$

where the function $\mathcal{C}(\theta)$ has been absorbed into the function $f_{\mathbf{q}}(\theta) = 2\mathcal{C}(\theta)\cos(\mathbf{q}\cdot\mathbf{e})$ which arises from the combination of exponential factors such as 4.20. We diagonalise the Hamiltonian in just the same way as in the previous subsection by introducing a normal mode operator $\gamma_{\mathbf{q}} = x_{\mathbf{q}} a_{\mathbf{q}} + y_{\mathbf{q}} a^\dagger_{-\mathbf{q}}$ which satisfies the equation $\left[\gamma_{\mathbf{q}}, H\right] = \hbar\omega_{\mathbf{q}}\gamma_{\mathbf{q}}$. This leads to the dispersion

$$\omega_{\mathbf{q}} = \omega_0 \sqrt{1 + 2\frac{\Omega}{\omega_0} f_{\mathbf{q}}}, \tag{4.22}$$

as shown in Figure 4.4. We note that the vector notation used here is unnecessary as we are dealing with a one dimensional system, but it will allow for an easy generalisation in later sections. We see that the bandwidth is modulated by the polarisation angle, indeed for $\Omega/\omega_0 \ll 1$ the dispersion has a bandwidth proportional to $4(\Omega/\omega_0)|\mathcal{C}(\theta)|$. Similarly as for the dimer there is a critical angle $\theta_\mathrm{c}$ where $\mathcal{C}(\theta_\mathrm{c}) = 0$, signifying that the dispersion is a flat band as the system is effectively a chain of decoupled nanoparticles with no possibility of propagating modes. In addition, unlike for the dimer which has two eigenfrequencies, note that because the linear chain is a monatomic system with translational invariance there is only one (wavevector-dependent) eigenfrequency.

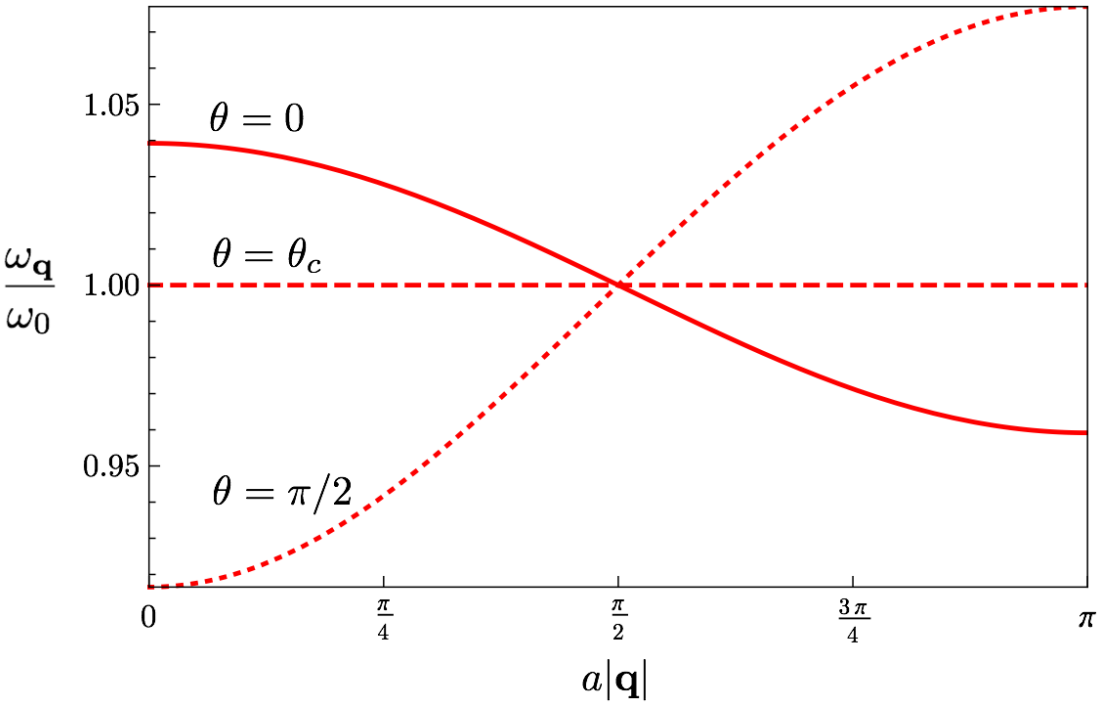


**Figure 4.4:** Dispersion of a linear chain of identical nanoparticles with polarisations $\theta = 0$ (solid line), $\theta = \theta_c$ (dashed line) and $\theta = \pi/2$ (dotted line). In the figure $\Omega/\omega_0 = 0.02$.

## 4.2 Perfect honeycomb lattice of identical nanoparticles

So far we have seen that the extra degree(s) of freedom encoded in the polarisation $\hat{\mathbf{p}}$ offer a wide tunability to plasmonic systems, allowing positive, negative and even zero interaction energies. In this section we unveil the tunable band structure of CPs in a honeycomb array of metallic nanoparticles, demonstrating a wide class of gapless phases that are characterised by collective plasmons that remarkably behave as massless chiral Dirac bosonic particles, in analogy to electrons in graphene. We will also see that for critical polarisations Dirac points merge and annihilate to form gapped phases, and that lifting the inversion symmetry gives rise to massive Dirac particles with an energy dependent Berry phase.

### 4.2.1 Model

We consider a bipartite hexagonal lattice with three-fold rotational symmetry as shown in Figure 4.5. This lattice, commonly referred to as the honeycomb array is (of course) exactly the same lattice as that of graphene. It can be considered as consisting of two

sublattices labelled $A$ and $B$ constructed by the vectors $\mathbf{R}_A \in \{m\mathbf{a}_1 + n\mathbf{a}_2 - \mathbf{e}\}$ and $\mathbf{R}_B \in \{m\mathbf{a}_1 + n\mathbf{a}_2 + \mathbf{e}\}$ respectively (for integer $m$ and $n$), where $\mathbf{a}_1 = a(\sqrt{3}, 0)$ and $\mathbf{a}_2 = (a/2)(\sqrt{3}, 3)$ are the lattice vectors of the hexagonal array, and $\mathbf{e} = a(0, -1)$ and $-\mathbf{e}$ are the positions of the basis particles. We consider a basis of identical nanoparticles that are distinguishable only by their position in the unit cell ($A$ or $B$). The non-interacting part of the Hamiltonian (as per equation 4.1) is thus

$$H_0 = \sum_{s=A,B} \sum_{\mathbf{R}_s} \left[ \frac{\Pi_s^2(\mathbf{R}_s)}{2M} + \frac{1}{2} M\omega_0^2 h_s^2(\mathbf{R}_s) \right], \tag{4.23}$$

which upon introduction of the bosonic operators

$$a_{\mathbf{R}_\mathrm{A}} | b_{\mathbf{R}_\mathrm{B}} = \sqrt{\frac{M\omega_0}{2\hbar}} h_A(\mathbf{R}_A) | h_B(\mathbf{R}_B) + i \sqrt{\frac{1}{2\hbar M\omega_0}} \Pi_A(\mathbf{R}_A) | \Pi_B(\mathbf{R}_B), \tag{4.24}$$

transforms to

$$H_0 = \hbar\omega_0 \sum_{\mathbf{R}_A} a^\dagger_{\mathbf{R}_\mathrm{A}} a_{\mathbf{R}_\mathrm{A}} + \hbar\omega_0 \sum_{\mathbf{R}_B} b^\dagger_{\mathbf{R}_\mathrm{B}} b_{\mathbf{R}_\mathrm{B}}. \tag{4.25}$$

This procedure should be very familiar from the linear chain example, with the difference that we have two operators to denote the geometrically inequivalent $A$ and $B$ basis particles, belonging to two inequivalent sublattices.

For the interaction Hamiltonian we consider just nearest neighbours, as we will show in section 4.2.7 that additional neighbours do not qualitatively alter the spectrum. Each nanoparticle interacts with three nearest neighbours belonging to a different sublattice, thus we need only sum over one sublattice and its three neighbours to capture all interactions. Using equation 4.8 we can immediately write this as

$$H_{\mathrm{int}} = \sum_{\mathbf{R}_B} \sum_{j=1}^{3} \mathcal{V}(\mathbf{R}_B, \mathbf{R}_B + \mathbf{e}_j) = \frac{N^2 e^2}{4\pi\epsilon_0 \epsilon_\mathrm{D} a^3} \sum_{\mathbf{R}_B} \sum_{j=1}^{3} \mathcal{C}_j(\hat{\mathbf{p}}) h_B(\mathbf{R}_B) h_A(\mathbf{R}_B + \mathbf{e}_j), \tag{4.26}$$

where the three nearest neighbours $\mathbf{e}_j = \mathcal{R}_j \mathbf{e}$ are related by the rotation operator $\mathcal{R}_j$ which rotates a vector by $2\pi(j-1)/3$ in the plane of the array. We parametrise the

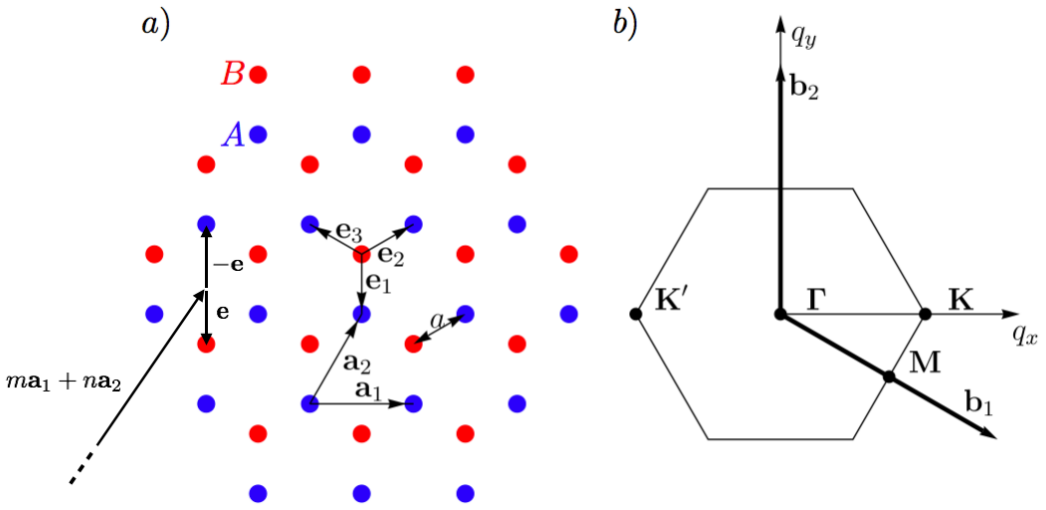


**Figure 4.5:** (a) The honeycomb structured lattice, with lattice vectors $\mathbf{a}_1 = a(\sqrt{3}, 0)$ and $\mathbf{a}_2 = (a/2)(\sqrt{3}, 3)$. The nearest-neighbour vectors are defined as $\mathbf{e}_1 = a(0, -1)$, $\mathbf{e}_2 = (a/2)(\sqrt{3}, 1)$ and $\mathbf{e}_3 = (a/2)(-\sqrt{3}, 1)$. These link the inequivalent $A$ and $B$ lattice sites, represented by blue and red dots respectively in the figure, located at the sublattice sites $\mathbf{R}_A = m\mathbf{a}_1 + n\mathbf{a}_2 - \mathbf{e}$ and $\mathbf{R}_B = m\mathbf{a}_1 + n\mathbf{a}_2 + \mathbf{e}$ respectively. Here $a$ is the nearest-neighbour separation distance. (b) The first Brillouin zone in reciprocal space defined by the primitive vectors $\mathbf{b}_1 = (2\pi/3a)(\sqrt{3}, -1)$ and $\mathbf{b}_2 = (4\pi/3a)(0, 1)$. Also shown are the topological points of high symmetry, $\mathbf{K} = (4\pi/3\sqrt{3}a)(1, 0)$, $\mathbf{K}' = -\mathbf{K}$, $\mathbf{\Gamma} = (0, 0)$ and $\mathbf{M} = (\pi/3a)(\sqrt{3}, -1)$.

polarisation vector $\hat{\mathbf{p}}$ in spherical coordinates, with the azimuthal angle $\phi$ measured from $\mathbf{e}_1$, so it reads

$$\hat{\mathbf{p}} = \sin\theta(\sin\phi\hat{\mathbf{x}} - \cos\phi\hat{\mathbf{y}}) + \cos\theta\hat{\mathbf{z}}. \tag{4.27}$$

Thus, the interaction parameter 4.9 is

$$\mathcal{C}_j(\theta, \phi) = 1 - 3(\hat{\mathbf{p}} \cdot \mathcal{R}_j\hat{\mathbf{e}})^2 = 1 - 3\sin^2\theta\cos^2\left(\phi - \frac{2\pi(j-1)}{3}\right). \tag{4.28}$$

Using the operators 4.24 to rewrite the interaction Hamiltonian in analogy to equation 4.9 gives

$$H_{\text{int}} = \hbar\Omega\sum_{\mathbf{R}_B}\sum_{j=1}^{3}\mathcal{C}_j(\theta, \phi)b^\dagger_{\mathbf{R}_\text{B}}\left(a_{\mathbf{R}_\text{B}+\mathbf{e}_\text{j}} + a^\dagger_{\mathbf{R}_\text{B}+\mathbf{e}_\text{j}}\right) + \text{H.c.} \tag{4.29}$$

where as per equation 4.10

$$\Omega = \omega_0 \left(\frac{\text{ר}}{a}\right)^3 \frac{1+2\epsilon_D}{6\epsilon_D}, \tag{4.30}$$

where ר is the radius of a nanoparticle (or a characteristic dimension for non-spherical particles, see appendix B for further details). Introducing the bosonic operators in momentum space via

$$a_{\mathbf{R}}|b_{\mathbf{R}} = \frac{1}{\sqrt{N}} \sum_{\mathbf{q}} \exp(i\mathbf{q}\cdot\mathbf{R}) a_{\mathbf{q}}|b_{\mathbf{q}} \tag{4.31}$$

transforms the Hamiltonian to

$$H = \hbar\omega_0 \sum_{\mathbf{q}} \left(a^\dagger_{\mathbf{q}} a_{\mathbf{q}} + b^\dagger_{\mathbf{q}} b_{\mathbf{q}}\right) + \hbar\Omega \sum_{\mathbf{q}} \left[f_{\mathbf{q}} b^\dagger_{\mathbf{q}} \left(a_{\mathbf{q}} + a^\dagger_{-\mathbf{q}}\right) + \text{H.c.}\right], \tag{4.32}$$

where the function

$$f_{\mathbf{q}} = \sum_{j=1}^{3} \mathcal{C}_j(\theta,\phi) \exp(i\mathbf{q}\cdot\mathbf{e}_j) \tag{4.33}$$

is a sum of three geometrical phase factors associated with each nearest neighbour, weighted by the polarisation dependent function $\mathcal{C}_j$. The function $f_{\mathbf{q}}$ plays a very similar role to the phase factor introduced for graphene (equation 3.39). However, remember that the functions $\mathcal{C}_j$ (equation 4.28) depend on the projection of the polarisation vector $\hat{\mathbf{p}}$ into the nearest-neighbour vector $\mathbf{e}_j$. Thus, whilst in graphene the hopping integral $t$ is identical for all three nearest-neighbours, in general for the plasmonic array the interaction energy between each nearest-neighbour is different, as they are modulated by $\mathcal{C}_j$. This introduces a rich tunability into the system that we will see shortly.

### 4.2.2 Exact diagonalisation

We describe the normal modes of the system in terms of the Bogoliubov operator

$$\beta^\tau_{\mathbf{q}} = w^\tau_{\mathbf{q}} a_{\mathbf{q}} + x^\tau_{\mathbf{q}} b_{\mathbf{q}} + y^\tau_{\mathbf{q}} a^\dagger_{-\mathbf{q}} + z^\tau_{\mathbf{q}} b^\dagger_{-\mathbf{q}}, \tag{4.34}$$

and impose that the Hamiltonian 4.32 is diagonal in this basis,

$$H = \hbar \sum_{\mathbf{q}} \sum_{\tau} \omega_{\mathbf{q}}^{\tau} \beta_{\mathbf{q}}^{\tau\dagger} \beta_{\mathbf{q}}^{\tau}, \tag{4.35}$$

with $\tau \in \{+, -\}$ the index denoting the two sets of inequivalent operators. The Heisenberg equation of motion $\left[\beta_{\mathbf{q}}^{\tau}, H\right] = \hbar\omega_{\mathbf{q}}^{\tau}\beta_{\mathbf{q}}^{\tau}$ leads immediately to an eigenvalue equation in momentum space, reminiscent of equation 4.14 for a nanoparticle dimer in real space

$$\begin{pmatrix} \omega_0 & \Omega f_{\mathbf{q}} & 0 & -\Omega f_{\mathbf{q}} \\ \Omega f_{\mathbf{q}}^* & \omega_0 & -\Omega f_{\mathbf{q}}^* & 0 \\ 0 & \Omega f_{\mathbf{q}} & -\omega_0 & -\Omega f_{\mathbf{q}} \\ \Omega f_{\mathbf{q}}^* & 0 & -\Omega f_{\mathbf{q}}^* & -\omega_0 \end{pmatrix} \begin{pmatrix} w_{\mathbf{q}}^{\tau} \\ x_{\mathbf{q}}^{\tau} \\ y_{\mathbf{q}}^{\tau} \\ z_{\mathbf{q}}^{\tau} \end{pmatrix} = \omega_{\mathbf{q}}^{\tau} \begin{pmatrix} w_{\mathbf{q}}^{\tau} \\ x_{\mathbf{q}}^{\tau} \\ y_{\mathbf{q}}^{\tau} \\ z_{\mathbf{q}}^{\tau} \end{pmatrix}. \tag{4.36}$$

From this we readily deduce the collective plasmonic dispersion

$$\omega_{\mathbf{q}}^{\tau} = \omega_0 \sqrt{1 + \tau 2 \frac{\Omega}{\omega_0} |f_{\mathbf{q}}|}, \tag{4.37}$$

and the coefficients of the coherent superposition

$$w_{\mathbf{q}}^{\tau} = \frac{\cosh\theta_{\mathbf{q}}^{\tau}}{\sqrt{2}} \frac{f_{\mathbf{q}}}{|f_{\mathbf{q}}|}, \quad x_{\mathbf{q}}^{\tau} = \tau \frac{\cosh\theta_{\mathbf{q}}^{\tau}}{\sqrt{2}}, \quad y_{\mathbf{q}}^{\tau} = -\frac{\sinh\theta_{\mathbf{q}}^{\tau}}{\sqrt{2}} \frac{f_{\mathbf{q}}}{|f_{\mathbf{q}}|}, \quad z_{\mathbf{q}}^{\tau} = -\tau \frac{\sinh\theta_{\mathbf{q}}^{\tau}}{\sqrt{2}}, \tag{4.38}$$

where

$$\cosh\theta_{\mathbf{q}}^{\tau} = \frac{1}{\sqrt{2}} \left( \frac{1 + \tau\Omega|f_{\mathbf{q}}|/\omega_0}{\sqrt{1 + \tau 2\Omega|f_{\mathbf{q}}|/\omega_0}} + 1 \right)^{1/2}, \tag{4.39}$$

$$\sinh\theta_{\mathbf{q}}^{\tau} = \frac{-\tau}{\sqrt{2}} \left( \frac{1 + \tau\Omega|f_{\mathbf{q}}|/\omega_0}{\sqrt{1 + \tau 2\Omega|f_{\mathbf{q}}|/\omega_0}} - 1 \right)^{1/2}. \tag{4.40}$$

As we have seen before, the polarisation degree of freedom $\hat{\mathbf{p}}$ gives a phenomenal tunability to a plasmonic spectrum and the honeycomb array is no exception. It is evident from

$f_{\mathbf{q}}$ that the dispersion of the two CP branches $\omega_{\mathbf{q}}^{\pm}$ depends crucially on the dipole orientation $(\theta, \phi)$. We will highlight this tunability by exploring several cases in subsequent sections.

Typically $\Omega \ll \omega_0$. As discussed in section 2.3 to model the interactions between neighbouring nanoparticles as near-field dipole-dipole interactions we require a minimal separation of $a \gtrsim 3r$ [18]. Thus, referring to equation 4.30, for nanoparticles in air or other materials with a dielectric function of order unity, the maximum value we can achieve is $\Omega/\omega_0 \approx 0.02 \ll 1$. As such the dispersion can be approximated as

$$\omega_{\mathbf{q}}^{\tau} = \omega_0 + \tau\Omega|f_{\mathbf{q}}|, \tag{4.41}$$

which reduces the hyperbolic functions to $\cosh\theta_{\mathbf{q}}^{\tau} \simeq 1$ and $\sinh\theta_{\mathbf{q}}^{\tau} \simeq 0$ so that the Bogoliubov operators in 4.35 take the simpler form

$$\beta_{\mathbf{q}}^{\tau} = \frac{1}{\sqrt{2}}\left(\frac{f_{\mathbf{q}}}{|f_{\mathbf{q}}|}a_{\mathbf{q}} + \tau b_{\mathbf{q}}\right). \tag{4.42}$$

We see that, as $y_{\mathbf{q}}^{\tau} = z_{\mathbf{q}}^{\tau} = 0$ for $\Omega \ll \omega_0$, we have halved the dimension of the Hamiltonian 4.32 in the original basis. This is evident upon incorporation of the expansions 4.42 into the Hamiltonian 4.37 which gives

$$H = \sum_{\mathbf{q}} \hat{\psi}_{\mathbf{q}}^{\dagger}\mathcal{H}_{\mathbf{q}}\hat{\psi}_{\mathbf{q}}, \tag{4.43}$$

where

$$\mathcal{H}_{\mathbf{q}} = \begin{pmatrix} \omega_0 & \Omega f_{\mathbf{q}}^{*} \\ \Omega f_{\mathbf{q}} & \omega_0 \end{pmatrix}, \tag{4.44}$$

is the Hamiltonian in the basis $\hat{\psi}_{\mathbf{q}} = (a_{\mathbf{q}}, b_{\mathbf{q}})$. Thus, we see that the non-resonant terms ($a_{\mathbf{q}}b_{\mathbf{q}}$ etc.) are negligible in the description of CPs in the honeycomb array of nanoparticles, and only produce corrections of order $(\Omega/\omega_0)^2$ to the spectrum.

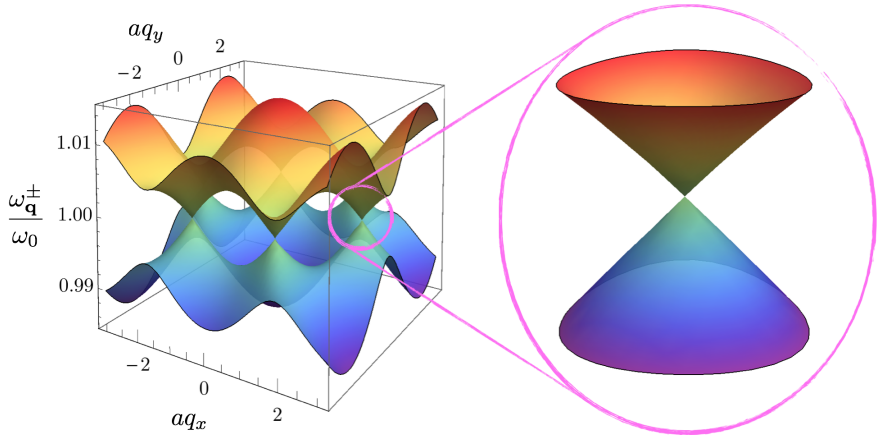


**Figure 4.6:** The CP dispersion 4.37 when the system is polarised normal to the plane ($\theta = 0$). Also shown is a zoom of the dispersion around the $K$ point. In the figure $\Omega/\omega_0 = 0.01$.

### 4.2.3 Dirac-like collective plasmons

It should be intuitively obvious that for $\theta = 0$ all the interaction parameters are equal, $\mathcal{C}_1 = \mathcal{C}_2 = \mathcal{C}_3 = 1$, as the dipoles are orientated normal to the plane and thus the projection onto all nearest neighbour vectors vanishes (see equation 4.28). This situation is directly analogous to the electronic tight-binding problem in graphene, where the hopping energy between all nearest neighbour carbon atoms is the same. In fact by comparing the dispersion from equation 4.37 for $\theta = 0$ (shown in Figure 4.6) to that of graphene we see a remarkable similarity. We observe an approximately conical spectrum for momenta around the corners of the Brillouin zone at a frequency $\omega_{\mathbf{q}}^{\tau} = \omega_0$ and thus wish to investigate the form of the Hamiltonian around these points.

There are two sets of inequivalent (not related by a reciprocal lattice vector) high symmetry points $K$ and $K'$, which we choose to take as $\pm\mathbf{K} = \frac{4\pi}{3\sqrt{3}a}(\pm 1, 0)$ in the first Brillouin zone. We expand the Hamiltonian around these points to first order in $\mathbf{k}$, where $\mathbf{q} = \pm\mathbf{K} + \mathbf{k}$ and $|\mathbf{k}| \ll |\mathbf{K}|$. The function $f_{\mathbf{q}}$ expands as $f_{\mathbf{q}} = -\frac{3a}{2}(\pm k_x + ik_y)$ which upon inspection of equation 4.41 shows that the dispersion is indeed conical,

$$\omega_{\mathbf{q}}^{\pm} = \omega_0 \pm v|\mathbf{k}|, \tag{4.45}$$

where $v = 3a\Omega/2$ is the group velocity. Around the $K$ point the Hamiltonian 4.44 can be represented in Pauli spin matrices as

$$\mathcal{H}_{\mathbf{q}}^{K} = \hbar \begin{pmatrix} \omega_0 & -v(k_x - ik_y) \\ -v(k_x + ik_y) & \omega_0 \end{pmatrix} = \hbar\omega_0 \mathbb{1} - \hbar v \boldsymbol{\sigma} \cdot \mathbf{k}, \tag{4.46}$$

where $\sigma_n$ is the $n$th Pauli spin matrix and $\boldsymbol{\sigma} = (\sigma_x, \sigma_y)$ is a vector of Pauli spin matrices. We denote the basis as $\hat{\boldsymbol{\psi}}_{\mathbf{k}}^{K} = (a_{\mathbf{k},\mathrm{K}}, b_{\mathbf{k},\mathrm{K}})$ to make it explicit that we're expanding around the $K$ point. Following exactly the same procedure around the $K'$ point gives $\mathcal{H}_{\mathbf{k}}^{K'} = \hbar\omega_0 \mathbb{1} + \hbar v(\sigma_x k_x - \sigma_y k_y)$, which although correct cannot be written as a function of $\boldsymbol{\sigma} \cdot \mathbf{k}$. For this reason (as we saw in the Chapter on graphene) one commonly adopts the basis $\hat{\boldsymbol{\psi}}_{\mathbf{k}}^{K'} = (b_{\mathbf{k},\mathrm{K}'}, a_{\mathbf{k},\mathrm{K}'})$ which transforms the Hamiltonian to

$$\mathcal{H}_{\mathbf{k}}^{K'} = \hbar\omega_0 \mathbb{1} + \hbar v \boldsymbol{\sigma} \cdot \mathbf{k}. \tag{4.47}$$

Whilst it is often convenient to work in these 'valley' subspaces the full Hamiltonian in the basis $\hat{\boldsymbol{\Psi}}_{\mathbf{k}} = (a_{\mathbf{k},\mathrm{K}}, b_{\mathbf{k},\mathrm{K}}, b_{\mathbf{k},\mathrm{K}'}, a_{\mathbf{k},\mathrm{K}'})$ of both valleys is

$$\mathcal{H}_{\mathbf{k}} = \hbar\omega_0 \mathbb{1} - \hbar v \tau_z \otimes \boldsymbol{\sigma} \cdot \mathbf{k} \tag{4.48}$$

which, up to a global energy shift of $\hbar\omega_0$ corresponds to a massless Dirac Hamiltonian for the CPs and demonstrates that the corresponding spinor eigenstates represent massless Dirac-like bosonic excitations and will present similar effects to those of electrons in graphene [21, 24]. This is one of the key results of the thesis and is interesting in and of itself, opening up many questions to be addressed on the nature of Dirac quasiparticles that (unlike electrons in graphene) are bosonic, have a finite lifetime, and can couple to electromagnetic modes to form polaritons. However, we have so far investigated just one polarisation and so we wish to explore the nature of the eigenmodes and dispersions throughout the entire polarisation ($\hat{\mathbf{p}}$) space. Recall that we can obtain a polarisation in an arbitrary direction by employing orientated anisotropic nanoparticles, such as spheroidical nanoparticles as discussed in appendix B. We now explore the rich and varied physics permitted by this additional degree of freedom.

### 4.2.4 The topology of polarisation-space and Dirac point merging

We have seen that the particular polarisation $\hat{\mathbf{p}} = (\theta, \phi) = (0, 0)$ corresponds to a dispersion with Dirac points. Following this we wish to determine if Dirac points exist in the dispersion for an arbitrary polarisation. A necessary but not sufficient condition is that the dispersion is gapless, and so initially we map out the 'gapless' regions in $\hat{\mathbf{p}}$-space, where every interior point corresponds to a gapless dispersion. Subsequently we will demonstrate that every gapless region also corresponds to dispersions with Dirac points.

It is obvious that 'touching points' (degeneracies in the dispersion which we don't immediately identify as Dirac) occur when $|f_{\mathbf{q}}(\theta, \phi)| = 0$, as a glance at the dispersion 4.37 reveals that in this case $\omega_{\mathbf{q}}^{+} = \omega_{\mathbf{q}}^{-} = \omega_0$. The requirement $|f_{\mathbf{q}}| = 0$ necessitates that the function

$$f_{\mathbf{q}} = \mathrm{e}^{iaq_y/2}\left(\mathcal{C}_1\mathrm{e}^{-i3aq_y/2} + \mathcal{C}_2\mathrm{e}^{i\sqrt{3}aq_x/2} + \mathcal{C}_3\mathrm{e}^{-i\sqrt{3}aq_x/2}\right) \tag{4.49}$$

also vanishes. Vanishing real and imaginary components gives the set of simultaneous equations

$$(\mathcal{C}_2 + \mathcal{C}_3)\cos(\sqrt{3}aq_x/2) = -\mathcal{C}_1\cos(3aq_y/2), \tag{4.50}$$

$$(\mathcal{C}_2 - \mathcal{C}_3)\sin(\sqrt{3}aq_x/2) = \mathcal{C}_1\sin(3aq_y/2). \tag{4.51}$$

Adding the square of both equations we arrive at the condition (for $\mathcal{C}_2\mathcal{C}_3 \neq 0$)

$$\sin^2\left(\frac{\sqrt{3}aq_x}{2}\right) = \frac{(\mathcal{C}_2 + \mathcal{C}_3)^2 - \mathcal{C}_1^2}{4\mathcal{C}_2\mathcal{C}_3}, \tag{4.52}$$

which clearly only has a solution when

$$0 \leq \frac{(\mathcal{C}_2 + \mathcal{C}_3)^2 - \mathcal{C}_1^2}{4\mathcal{C}_2\mathcal{C}_3} \leq 1. \tag{4.53}$$

This condition maps out the regions of $\hat{\mathbf{p}}$-space which are gapless (white regions) or gapped, as shown in Figure 4.7. We observe a rich phase diagram with several topologically disconnected 'pockets', in the sense that we can't smoothly deform a gapless region of $\hat{\mathbf{p}}$-space within one pocket into another without passing through a singularity (intersection tips of gapped regions). Now that we have a phase diagram which informs us whether or not a particular polarisation is gapless we can proceed to ask which regions or points correspond to dispersions characterised by Dirac points.

Referring to section 3.1.3, we observe that due to the parity-time ($\mathcal{IT}$) symmetry of the honeycomb array the Berry phase of an eigenstate for a particular polarisation must be 0 or $\pi$ for any region of $k$-space. $\mathcal{IT}$ symmetry also implies the Chern density is a sum of Dirac delta functions that are monopoles of Berry flux, otherwise known as Dirac points. As the system is always topologically trivial (a total Chern number of 0) and smooth under continuous changes in the polarisation, Dirac points can only appear or disappear in pairs by merging and 'annihilating' [108, 109]. It follows that if the dispersion contains Dirac points for any polarisation within a simply connected gapless region of $\hat{\mathbf{p}}$-space (a region with all points gapless and connected by a continuous path), then the dispersion must have Dirac points throughout that entire region. Thus, we can immediately identify the entire region that contains $(0, 0)$ as being characterised by dispersions with Dirac points.

However, we still need to verify the existence of at least one Dirac-like dispersion within each of the regions topologically disconnected from that containing $(0, 0)$. As the system possesses a 6-fold rotational symmetry in $\phi$ (2-fold in $\theta$) there are just two inequivalent pockets needing investigation. We choose the points $(i)$ and $(ii)$ in Figure 4.7 as well as another point $(iii)$ in the first region studied to test our assumptions.

The three points under study are $(i)$ $(\theta, \phi) = (\pi/2, \pi/2)$, $(ii)$ $(\theta, \phi) = (\pi/4, \pi)$ and $(iii)$ $(\theta, \phi) = (\pi/6, 0)$. Using equations 4.52 and 4.50 we obtain the degeneracy points $\pm\mathbf{K}_D$ for each polarisation and expand the function $f_{\mathbf{q}}$ to first order in the deviation $\mathbf{k}$ around each degeneracy point. We obtain

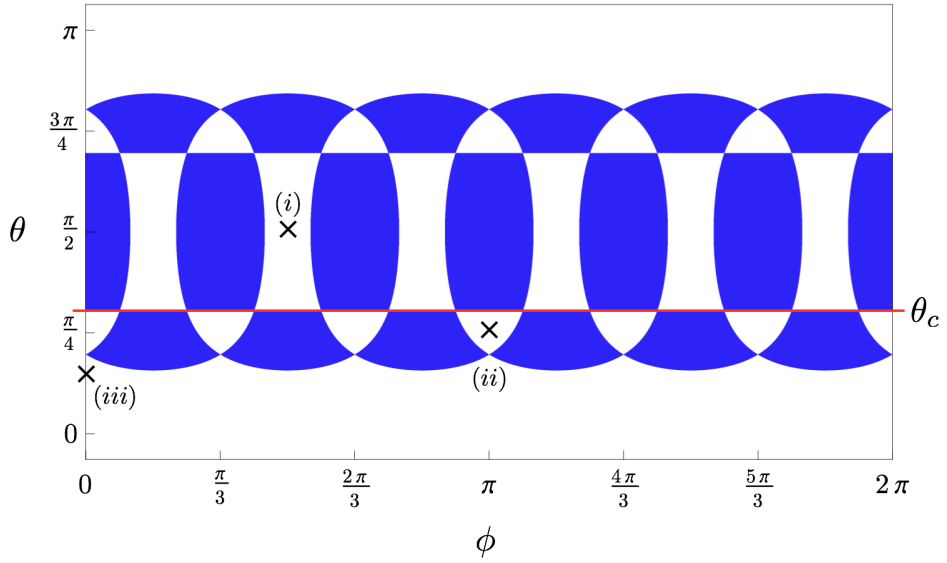


**Figure 4.7:** Phase diagram of $\hat{\mathbf{p}}$-space, parametrised by $\theta$ and $\phi$, showing which regions are gapless (white) or gapped (blue). The red solid line corresponds to the critical angle $\theta = \theta_c$ (equation 4.61) which demarcates a boundary between gapless and gapped phases. In the text we investigate the polarisations $(i)$, $(ii)$ and $(iii)$.

$$(i): \quad \pm\mathbf{K}_D^{(i)} = \frac{2}{\sqrt{3}a}\arccos(\frac{2}{5})(\pm 1, 0) \qquad f_{\mathbf{k}}^{(i)} = \frac{3a}{2}\left(\pm\frac{\sqrt{7}}{2}k_x - ik_y\right), \tag{4.54}$$

$$(ii): \quad \pm\mathbf{K}_D^{(ii)} = \frac{2}{\sqrt{3}a}\arccos(\frac{2}{5})(\pm 1, 0) \qquad f_{\mathbf{k}}^{(ii)} = \frac{3a}{4}\left(\mp\frac{\sqrt{7}}{2}k_x + ik_y\right), \tag{4.55}$$

$$(iii): \quad \pm\mathbf{K}_D^{(iii)} = \frac{2}{\sqrt{3}a}\arccos(-\frac{2}{13})(\pm 1, 0) \qquad f_{\mathbf{k}}^{(iii)} = \frac{-3a}{8}\left(\pm\frac{\sqrt{55}}{2}k_x + ik_y\right). \tag{4.56}$$

These expansions show that the CP dispersion 4.41 forms elliptical cones in the vicinity of the degenerate points. Moreover, by incorporating these expansions into equation 4.35 we find that in each case the Hamiltonian can be written as

$$\mathcal{H}^{(m)} = \hbar\omega_0\mathbb{1} + \frac{3\hbar a\Omega}{8}\boldsymbol{\sigma}\cdot\mathbf{h}^{(m)}, \tag{4.57}$$

where $h_x^{(m)} = \alpha_x^{(m)}k_x$, $h_y = \alpha_y^{(m)}k_y$, $h_z = 0$ and the dimensionless scale factors for the three cases are

$$\left(\alpha_x^{(i)}, \alpha_y^{(i)}\right) = \left(\pm 2\sqrt{7}, -4\right), \tag{4.58}$$

$$\left(\alpha_x^{(ii)}, \alpha_y^{(ii)}\right) = \left(\mp\sqrt{7}, 2\right), \tag{4.59}$$

$$\left(\alpha_x^{(iii)}, \alpha_y^{iii)}\right) = \left(\mp\sqrt{55}/2, -1\right). \tag{4.60}$$

We remind the reader of the discussions in section 3.1.5 for determining the Berry phase of an arbitrary two-band Hamiltonian. A Hamiltonian of the form $\boldsymbol{\sigma} \cdot \mathbf{h}$ has eigenstates whose Berry curvature $\mathcal{B}_\pm = \pm 1/(2\mathbf{h}^2)\hat{\mathbf{h}}$ formally resembles a magnetic monopole. Therefore, the Berry phase $\gamma_B^\pm = \int_S \boldsymbol{\mathcal{B}} \cdot d\mathbf{S}$ of a closed curve $\Gamma$ in $\mathbf{h}$ is simply half the solid angle of any surface $S$ bounded by $\Gamma$. Equivalently, we can consider the curve $\tilde{\Gamma}$ in $\hat{\mathbf{h}}$ traced out on the surface of a unit sphere due to the curve $\Gamma$ in $\mathbf{h}$. The Berry phase is then simply the fraction of the sphere's surface bounded by $\tilde{\Gamma}$ multiplied by $\pm 2\pi$. For each of the Hamiltonians $\mathcal{H}^{(m)}$ of equation 4.57, any closed contour in $\mathbf{k}$ traces out a closed contour in $\hat{\mathbf{h}}$ that is a unit circle in the $x$-$y$ plane that bounds exactly half the unit sphere. Therefore the Berry phase around each of the three degenerate points considered is $\pi$, and we identify these as Dirac points.

This completes the verification that the dispersion always contains Dirac points in all gapless regions of Figure 4.7. This is an important result. Firstly it demonstrates that the Dirac points of the graphene-like dispersion are robust in a wide window around $\theta = 0$. Secondly we have demonstrated the existence of Dirac Hamiltonians for a wide range of polarisations, which will possess dispersions with varied group velocities, intervalley separations, symmetries and other characteristics. This permits one to finely tune and design Dirac systems with certain desired properties. We will highlight the many distinct gapped and gapless dispersions in the next section.

Finally, we would like to investigate the form of the Hamiltonian at the boundary between gapless and gapped phases. A convenient choice of $\theta$ to examine is the symmetry line

$$\theta_c = \arcsin(\sqrt{2/3}), \tag{4.61}$$

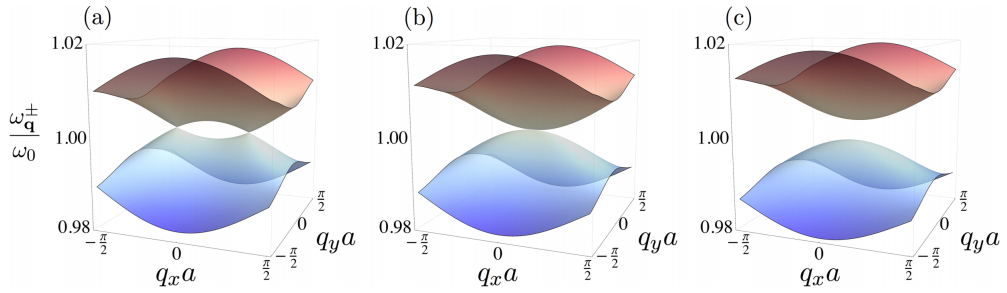


**Figure 4.8:** Collective plasmon dispersion for (*a*) $\delta\theta = -0.5$, (*b*) $\delta\theta = 0$, and (*c*) $\delta\theta = 0.5$, with $\phi = 0$ and $\Omega/\omega_0 = 0.01$. Reprinted with permission from [124]. Copyright 2015 IOP Publishing.

which is a boundary for all $\phi$ between the two phases (see Figure 4.9). In particular let us choose $\phi = 0$ for simplicity. In general the merging of Dirac points must occur at one of the four points $\mathbf{K}_0 = (m\mathbf{b}_1 + n\mathbf{b}_2)/2$ for $m, n \in \{0, 1\}$ [109], and in this case at $\mathbf{K}_0 = (0, 0)$. We expand the Hamiltonian 4.44 to lowest order in $\mathbf{k} = \mathbf{q} - \mathbf{K}_0$ and $\delta\theta = \theta - \theta_c$ to obtain

$$\mathcal{H} = \begin{pmatrix} \hbar\omega_0 & -g - \hbar^2 k_x^2/2m^* + iv\hbar k_y \\ -g - \hbar^2 k_x^2/2m^* - iv\hbar k_y & \hbar\omega_0 \end{pmatrix}, \tag{4.62}$$

where $m^* = 2\hbar/av$ is the effective mass along the $x$-direction, and $g = 3\sqrt{2}\hbar\Omega\delta\theta$ is the parameter which drives the topological phase transition. Referring to equation 4.62 and Figure 4.8 we observe that as we approach $\delta\theta = 0$ from negative values the spectrum consists of two Dirac points which converge towards one another and merge into a hybrid point at $\mathbf{K}_0$. Here, just at the transition, the spectrum is linear along $q_y$ and quadratic along $q_x$. As soon as $\delta\theta > 0$ there is a finite gap $2g$ and the Dirac points can be said to have annihilated.

This phenomenon is reminiscent of the Dirac point merging in graphene predicted to occur for large deformations of the lattice [108, 109]. However, whilst such deformations of the lattice have been realised for artificial graphene systems such as cold atoms in optical lattices [31] and microwave systems [126, 127], in real graphene the required mechanical deformations appear impossible to achieve. In contrast, for our proposal one need only modulate the polarisation, permitting the manipulation of Dirac points without changing the underlying lattice.

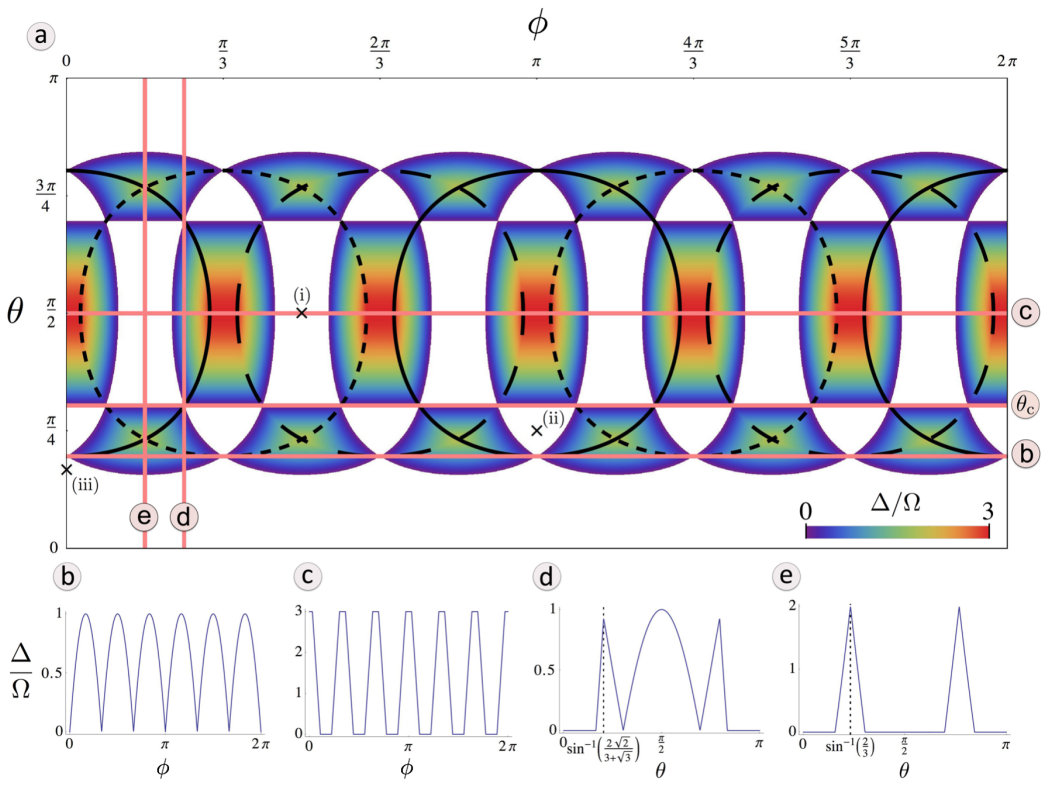


**Figure 4.9:** (a) Phase diagram of $\hat{\mathbf{p}}$-space for the perfect honeycomb lattice, showing at which polar and azimuthal angles ($\theta$ and $\phi$, respectively) a gap opens in the spectrum. White indicates a gapless region, while the size of the gap $\Delta$ is given by the colour bar (in units of $\Omega$). The black lines indicate where one of the interaction parameters $\mathcal{C}_j$ is zero ($\mathcal{C}_1 = 0$, $\mathcal{C}_2 = 0$ and $\mathcal{C}_3 = 0$ along the solid, dashed and dotted lines, respectively). The straight lines labelled (b), (c), (d), and (e) correspond to the cuts shown in the other panels, respectively at (b) $\theta = \arcsin(1/3)$, (c) $\theta = \pi/2$, (d) $\phi = \pi/4$ and (e) $\phi = \pi/6$. In the figure, $\Omega/\omega_0 = 0.01$. Reprinted with permission from [124]. Copyright 2015 IOP Publishing.

### 4.2.5 Highly tunable spectrum

Of course a dispersion containing Dirac points is not the only interesting or even desired characteristic. In this section we wish to discuss the phase diagram of Figure 4.7 and the tunability of the possible dispersions a little further. In fact in Figure 4.9 we show an embellished version of the phase diagram, including a colour scale that indicates the size of the gap, defined as the difference in energy between the minimum of the upper (+) and the maximum of the lower (−) band. For $\Omega/\omega_0 \ll 1$ this reduces to the simple expression $\Delta \simeq 2\Omega \min[f_{\mathbf{q}}]$.

Additionally, we overlay black curves which indicate the angles where one of the nearest-neighbour coupling strengths $\mathcal{C}_j$ defined in equation 4.28 equals zero. These render the system equivalent to a collection of non-interacting 1D chains with a dispersion that is

invariant along one direction. Interestingly these curves pass through the intersection of gapped and gapless regions, at which point the spectrum presents 'Dirac lines' as seen in Figure 4.10. There are also points in Figure 4.9 where two black curves intersect, signalling that the interaction of two nearest neighbours vanish and the system can effectively be described as isolated dimers, leading to flat bands with no wavevector dependence. To fully appreciate the tunability of the dispersions we invite the reader to watch the video in Figure C.1, where we observe the evolution of the bandstructure as we vary the polarisation along a continuous path in the phase diagram.

In Figures 4.10 and 4.11 we present a selection of different dispersions and the corresponding density of states (DOS), highlighting the wide variety of gapped and gapless regimes. Observe the singularities in the DOS which arise due to Lifshitz transitions and corresponding sudden changes in the topology of equipotential lines [128]. By varying the polarisation we can change their position in energy, and increase the coupling of light to the collective plasmonic modes at different frequencies. Figure 4.10(a) is the familiar graphene-like polarisation, with a DOS that varies linearly around $\omega_0$, and a characteristic vanishing DOS at the Dirac energy. Bearing a close resemblance is Figure 4.11($a$), corresponding to a critical polarisation of merged Dirac points. Here the DOS varies as a square root around $\omega_0$. The Figures 4.10(b) and 4.11(b) correspond to polarisations where one of the $\mathcal{C}_j$ vanishes, rendering the dispersion transitionally invariant in one direction, though gapped in Figure 4.11 and gapless in Figure 4.10. In all the figures we see ability to tune both the band gap and the bandwidth. In particular Figure 4.11 examines a polarisation where two of the $\mathcal{C}_j$ parameters are zero and the system is dispersionless.

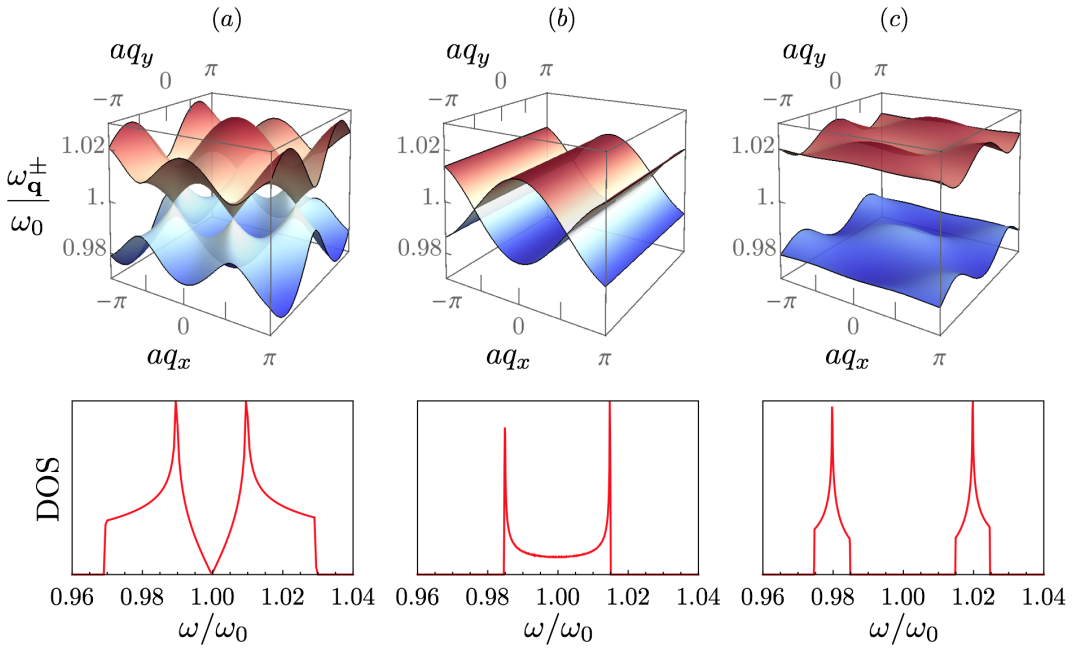


**Figure 4.10:** Collective plasmon dispersion for $(a)$ the out-of-plane polarisation $\theta = 0$, $(b)$ $\theta = \arcsin\sqrt{1/3}$, and $(c)$ an in-plane polarisation $\theta = \pi/2$. In the figure $\Omega/\omega_0 = 0.01$ and $\phi = 0$.

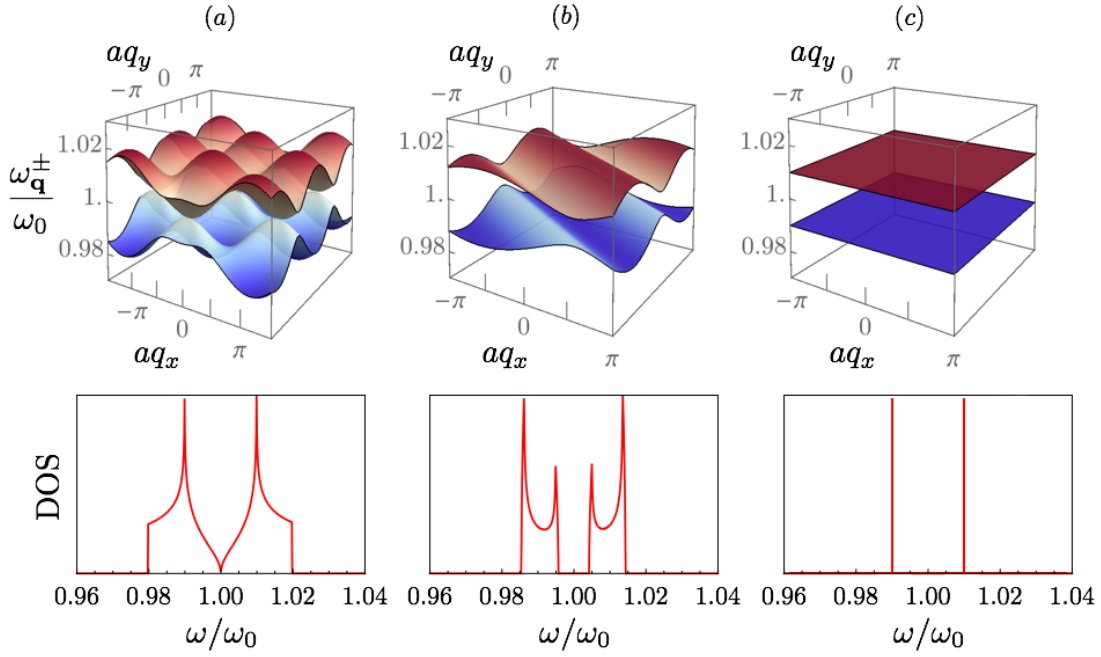


**Figure 4.11:** Collective plasmon dispersion for $(a)$ $(\theta, \phi) = (\arcsin\sqrt{2/3}, \pi/2)$, $(b)$ $(\theta, \phi) = (\arcsin\left[2/\sqrt{3(2+\sqrt{3})}\right], \pi/4)$, and $(c)$ $(\theta, \phi) = (\arcsin\sqrt{2/3}, \pi/2)$. Note that in $(a)$ we show a larger area in momentum space to make the hybrid points clearly visible. In the figure $\Omega/\omega_0 = 0.01$.

### 4.2.6 Inversion asymmetry and an energy dependent Berry phase

The ability to open a band gap in graphene is highly desirable if one wishes to exploit its exotic properties in electronics applications, however this has proven to be quite challenging in experiments [129, 130].

In our artificial graphene system opening a band gap should be quite trivial as it simply requires one to fabricate the two (geometrically inequivalent) sublattices such that they are physically inequivalent, breaking the inversion symmetry. For example this could be realised by fabricating the two sublattices out of different materials or as different sizes. We have seen that nanofabrication technologies afford a great degree of control over design parameters so one should be able to finely tune the band gap. We now investigate the effect of such an inversion asymmetry.

We consider a perfect honeycomb array with the $A$ and $B$ sublattices consisting of two different types of metallic nanoparticles, with inequivalent resonance frequencies $\omega_A$ and $\omega_B$ and radii $r_A$ and $r_B$. The analysis presented in section 4.2.2 applies here with minor changes, including an interaction coefficient that now reads

$$\Omega \to \tilde{\Omega} = \left(\frac{\omega_A \omega_B}{\omega_0^2}\right)^{1/2} \left(\frac{r_A r_B}{r^2}\right)^{3/2} \Omega. \tag{4.63}$$

It is convenient to express the two LSP frequencies as $\omega_A = \bar{\omega} + \delta$ and $\omega_B = \bar{\omega} - \delta$, where $\bar{\omega}$ is the average frequency, and $\delta$ the difference in magnitude between each LSP frequency and the mean value. As a result the CP dispersion now reads

$$\omega_{\mathbf{q}}^{\pm} = \sqrt{\bar{\omega}^2 + \delta^2 \pm 2\sqrt{\bar{\omega}^2\delta^2 + (\bar{\omega}^2 - \delta^2)\tilde{\Omega}^2 |f_{\mathbf{q}}|^2}}, \tag{4.64}$$

where $f_{\mathbf{q}}$ has the same definition as before in equation 4.33. As $\delta$ tends to zero it is easily seen that the dispersion tends towards equation 4.37 of identical sublattices (with the substitution $\bar{\omega} \to \omega_0$). In Figure 4.12 we plot the dispersion in equation 4.64 for $\theta = 0$ and several values of $\delta$. The extrema of the two bands are still dictated by $f_{\mathbf{q}}$ and so always occur at the $K$ and $K'$ points with a band gap of size $2\delta$ for any finite difference in the LSP frequencies. It is also clear that the bandwidth of the individual

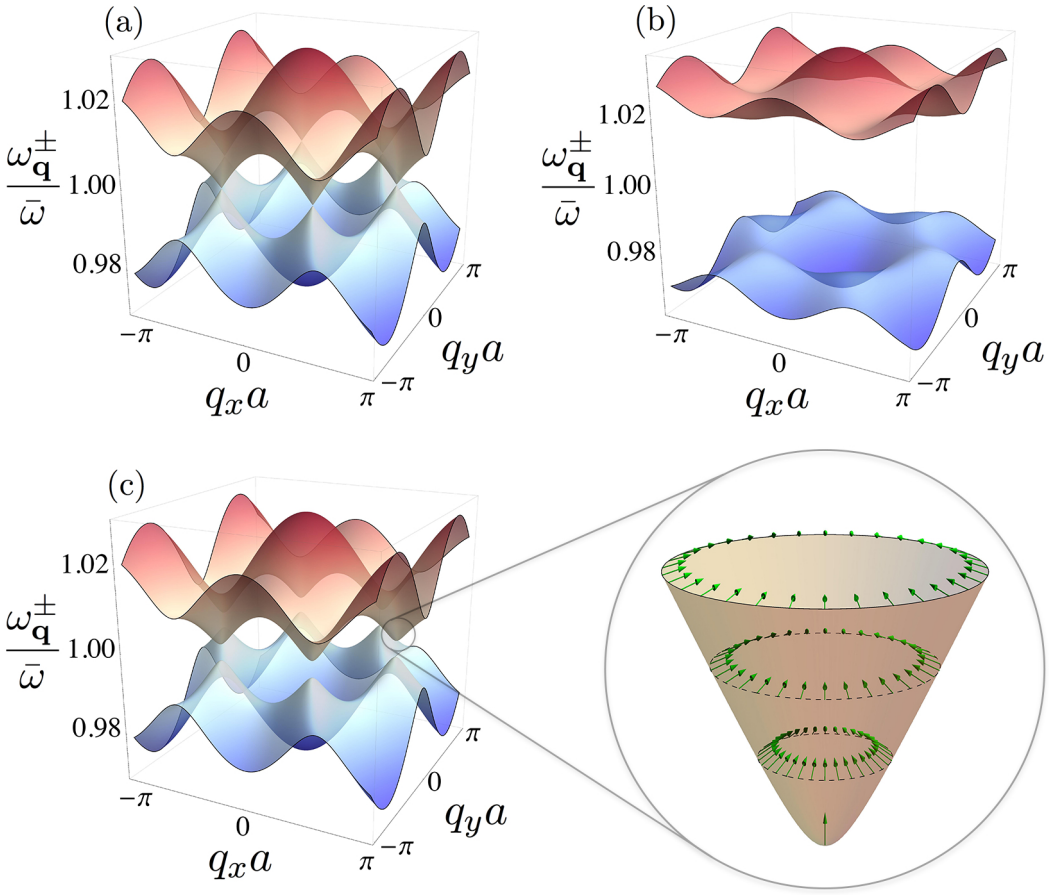


**Figure 4.12:** Collective plasmon dispersions from equation 4.64 with LSP polarisation normal to the plane ($\theta = 0$), for (a) $\delta/\bar{\omega} = 0$, (b) $\delta/\bar{\omega} = 0.002$ and (c) $\delta/\bar{\omega} = 0.02$. The zoom in panel (c) shows the upper collective plasmon branch in the vicinity of the $K$ point in the first Brillouin zone, while the arrows depict the unit vector $\mathbf{V}_{\mathbf{k}}^{\pm}$ defined in equation 4.66. In the figure, $\tilde{\Omega}/\bar{\omega} = 0.01$. Reprinted with permission from [124]. Copyright 2015 IOP Publishing.

bands decreases with increasing asymmetry. The effects of the symmetry breaking term $\delta$ are further explored in the video of Figure C.2.

In the vicinity of the Dirac points the system is described by a massive Dirac Hamiltonian

$$\mathcal{H}_{\mathbf{k}} = \hbar\bar{\omega}\mathbb{1} - \hbar\tau_z \otimes (\tilde{v}\boldsymbol{\sigma}\cdot\mathbf{k} - \delta\sigma_z)\,, \tag{4.65}$$

with eigenvalues $\omega_{\mathbf{k}}^{\pm} = \bar{\omega} \pm \sqrt{\tilde{v}^2|\mathbf{k}|^2 + \delta^2}$, where $\tilde{v} = 3a\tilde{\Omega}/2$. With increasing wavevector the Hamiltonian in each valley evolves continuously from a purely out-of-plane Zeeman term $\hbar\delta\sigma_z$ (when $\tilde{v}|\mathbf{k}| \ll \delta$) to a massless Dirac Hamiltonian $-\hbar\tilde{v}\boldsymbol{\sigma}\cdot\mathbf{k}$ (when $\tilde{v}|\mathbf{k}| \gg \delta$). As the quasiparticle Hamiltonian is formally that of an $s = 1/2$ (pseudospin) system we can represent the eigenstates of (say) the $K$ valley as vectors in the Bloch sphere

$$\mathbf{V}_{\mathbf{k}}^{\pm} = \pm \frac{1}{\sqrt{\tilde{v}^2|\mathbf{k}|^2 + \delta^2}} \begin{pmatrix} -\tilde{v}k_x \\ -\tilde{v}k_y \\ \delta \end{pmatrix}. \tag{4.66}$$

Several of these pseudospin vectors are plotted in the zoom of panel ($c$) in Figure 4.12, with the tails of the vectors positioned at the corresponding momenta and frequency eigenvalues. We see that the magnitude of the projection of $\mathbf{V}_{\mathbf{k}}^{\pm}$ into the equatorial plane of the Bloch sphere is zero at the band minimum and tends towards 1 with increasing energy. Thus, from inspection of Figure 4.12 we immediately ascertain that at the extrema of the bands the Berry phase $\gamma_B = 0$ (see section 3.1.5 and equation 3.31) and increases monotonically as a function of energy to the asymptotic value of $\pi$. More explicitly we find that the energy dependent Berry phase is given in the $K$ valley by

$$\gamma_B(\omega) = \pi \left(1 - \frac{\delta}{|\omega - \bar{\omega}|}\right) \tag{4.67}$$

defined for $\delta/|\omega - \bar{\omega}| \leq 1$. An equivalent analysis in the $K'$ valley yields an equal and opposite Berry phase. Such a tunable Berry phase suggests the possibility of interesting transport phenomena controlled by this pseudospin degree of freedom. For example, consider qualitatively the tunnelling of a quasiparticle state through a step potential barrier at normal incidence, injected in the upper band and transmitting into the lower band. Referring to the zoom of Figure 4.12(c) observe that for states in the immediate vicinity of the extrema of the bands there will be a vanishing transmission as the (equal and opposite) pseudospins will be antipodal. This is in contrast to the typical Klein tunnelling result of perfect transmission which we would observe for states with large momenta. Thus, we see that we should be able to tune the transmission probability to arbitrary values.

### 4.2.7 Interactions past nearest-neighbours

In the previous sections we have only incorporated the effects of nearest-neighbour interactions into our model. The dipole-dipole interaction falls off as an inverse cube law

and so next-nearest and further neighbours can noticeably change the bandstructure. However, as we shall see the important qualitative signatures remain intact.

Consider the graphene-like polarisation $\theta = 0$. We are by now familiar with the procedure for obtaining the Hamiltonian and can immediately identify the form of the Hamiltonian for an arbitrary set of '$n$th-nearest-neighbours'. Starting from a $B$ site, if the $n$th-nearest-neighbours belong to the $A$ sublattice then due to the 3-fold rotational symmetry of the honeycomb structure this inter-sublattice interaction generates off-diagonal terms in the Hamiltonian proportional to the factor

$$f_{mn}(\mathbf{q}) = \sum_{j=1}^{3} \exp\left(i\mathbf{e}^1_{mn} \cdot \mathcal{R}_j \mathbf{q}\right), \tag{4.68}$$

where

$$\mathbf{e}^s_{mn} = m\mathbf{a}_1 + n\mathbf{a}_2 + s\mathbf{e}. \tag{4.69}$$

Note that $\mathbf{e}^1_{nm}$ ($\mathbf{e}^0_{nm}$) is the vector between a $B$ site and an arbitrary $A$ site ($B$ site). If instead the $n$th-nearest-neighbours belong to the $B$ sublattice than the 6-fold rotational symmetry of the hexagonal lattice implies that this intra-sublattice interaction generates diagonal terms proportional to the factor

$$g_{mn}(\mathbf{q}) = \sum_{j=1}^{3} \cos\left(\mathbf{e}^0_{mn} \cdot \mathcal{R}_j \mathbf{q}\right). \tag{4.70}$$

From this it is straightforward to verify that for all $m$ and $n$ the zeroes of $f_{mn}$ occur at the high symmetry points $K$ and $K'$. In effect the Dirac point remains robust with the inclusion of an arbitrary number of nearest-neighbours. We note however that the function $g_{mn}$ provides a non-vanishing shift of the Dirac point in energy, but of course this factor is weighted by $|\mathbf{e}^0_{mn}|^{-3}$ that leads to a convergent shift for our two-dimensional model.

More explicitly, let us consider the effect of 2nd and 3rd nearest-neighbours for $\Omega \ll \omega_0$. We write the Hamiltonian including the $n$th-nearest-neighbours as

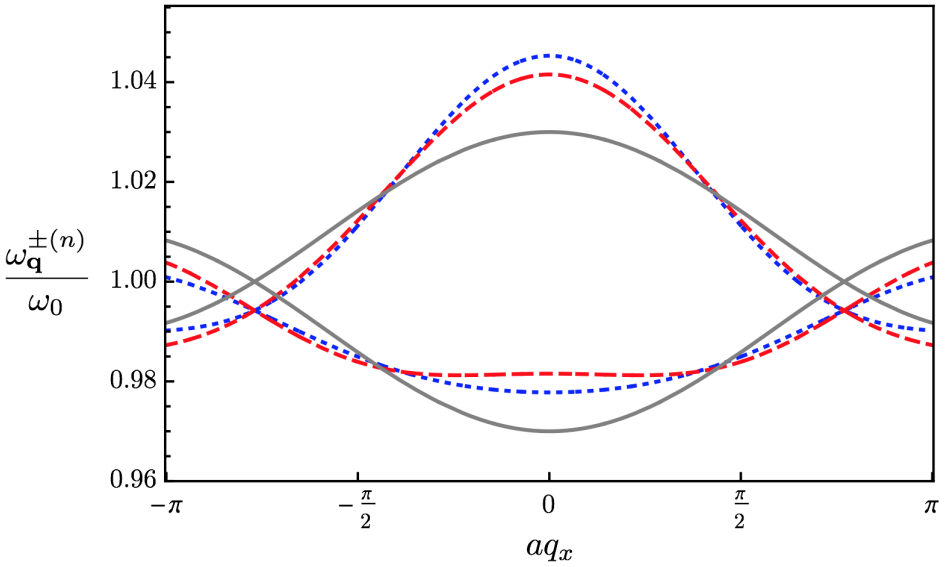


**Figure 4.13:** The collective plasmon dispersions along the $K'\Gamma K$ direction for $\theta = 0$, including the effects of nearest (solid gray lines), next-nearest (red dashed lines), and next-next-nearest (blue dotted lines) neighbours.

$$H^{(n)} = \sum_{m}^{n} H_m \tag{4.71}$$

where $H_1$ is the original nearest-neighbour Hamiltonian in equation 4.44 and

$$H_2 = \frac{2\hbar\Omega}{3\sqrt{3}} \begin{pmatrix} g_{\mathbf{q}} & 0 \\ 0 & g_{\mathbf{q}} \end{pmatrix}, \qquad H_3 = \frac{\hbar\Omega}{8} \begin{pmatrix} 0 & f_{2\mathbf{q}} \\ f_{2\mathbf{q}}^* & 0 \end{pmatrix}. \tag{4.72}$$

Here, $g_{\mathbf{q}} = \sum_{j=1}^{3} \mathcal{D}_j \cos(\mathbf{q} \cdot \mathbf{e}_j^{(2)})$ where $\mathcal{D}_j = 1 - 3\sin^2\theta \sin^2(\phi - 2\pi[j-1]/3)$ and the 2nd-nearest-neighbours are $\mathbf{e}_1^{(2)} = \mathbf{a}_1$, $\mathbf{e}_2^{(2)} = \mathbf{a}_2 - \mathbf{a}_1$ and $\mathbf{e}_3^{(2)} = -\mathbf{a}_2$. The dispersions $\omega_{\mathbf{q}}^{\pm(n)}$ corresponding to the Hamiltonians $H^{(n)}$ are

$$\omega_{\mathbf{q}}^{(2)} = \omega_{\mathbf{q}}^{\pm} + \frac{2\Omega}{3\sqrt{3}} g_{\mathbf{q}}, \tag{4.73}$$

$$\omega_{\mathbf{q}}^{(3)} = \omega_{\mathbf{q}}^{\pm(2)} \pm \left[ \sqrt{|f_{\mathbf{q}}|^2 + \frac{1}{4}\mathrm{Re}(f_{\mathbf{q}} f_{2\mathbf{q}}) + \frac{1}{64}|f_{2\mathbf{q}}|^2} - |f_{\mathbf{q}}| \right]. \tag{4.74}$$

The dispersions for $\theta = 0$ are plotted in Figure 4.13 where we see no dramatic qualitative changes, whilst the low-energy Hamiltonian expanded around the **K** point is

$$H_K = \hbar\left(\omega_0 - \frac{\Omega}{\sqrt{3}}\right)\mathbb{1} + \hbar v\mathbf{k}\cdot\left(\frac{\boldsymbol{\sigma}^*}{4} - \boldsymbol{\sigma}\right). \tag{4.75}$$

We see that the inclusion of 2nd and 3rd nearest neighbours produces a global energy shift and an asymmetry between the two bands. However most importantly, around the $K$ and $K'$ points the dispersion is only slightly modified: the Dirac points persist and the spectrum is still conical, albeit with a moderate trigonal warping. The inclusion of further sets of neighbours, which belong all to one sublattice or the other, will produce similar but progressively less important effects. Thus, we conclude that around the Dirac points the important physics is captured with the inclusion of nearest-neighbour interactions only.

## 4.3 Arbitrary bipartite hexagonal array

The existence of Dirac points is not a phenomenon in solid state physics unique to graphene or the honeycomb structure in general. The four-component wavefunction of the quasiparticles, along with the effective massless Dirac Hamiltonian in real and artificial graphene stem from the bipartite nature of the 2D lattice as well as from the time-reversal symmetric and parity-invariant nature of the system [28]. All bipartite hexagonal lattices share these properties, with the honeycomb structure boasting the additional invariance under rotation by integer multiples of $2\pi/3$. Therefore, we expect to find Dirac points in a wide range of these lattices.

For this reason we parameterise a generic bipartite hexagonal lattice as having exactly the same $A$ sublattice as the honeycomb structure, with the $B$ sublattice shifted rigidly by a vector $\boldsymbol{\ell}$ from the honeycomb arrangement, such that the new nearest-neighbour vectors become $\mathbf{e}'_j = \mathbf{e} - \boldsymbol{\ell}$, as shown in Figure 4.14. Due to the $\mathcal{IT}$ symmetry and zero total Chern number we can expect an even number of Dirac points (including zero) for a lattice with arbitrary $\boldsymbol{\ell}$. As we have already identified the dispersions for a wide range of polarisations as hosting Dirac points in the $\boldsymbol{\ell} = (0,0)$ lattice, any $\boldsymbol{\ell} \neq (0,0)$ obtained by a continuous variation of $\boldsymbol{\ell}$ will also preserve these Dirac points unless the resulting

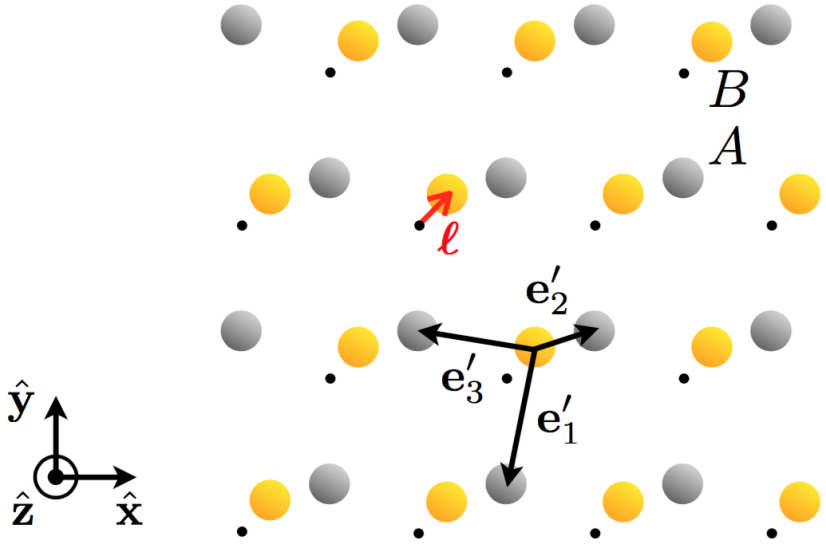


**Figure 4.14:** Generic hexagonal bipartite lattice, obtained by displacing the sublattice $B$ of the honeycomb structure by a vector $\boldsymbol{\ell}$. The black dots indicate the original position of the $B$ lattice sites, when $\boldsymbol{\ell} = (0, 0)$, as in Figure 4.5(a). Reprinted with permission from [124]. Copyright 2015 IOP Publishing.

deformation of the dispersion induces a phase transition such that the two inequivalent Dirac points merge and annihilate. The main questions to be addressed concern the verification of the existence of Dirac CPs in generic bipartite hexagonal lattices and mapping out those regions in $\boldsymbol{\ell}$-space that correspond to Dirac-like dispersions, as well as the fate of the phase diagram of Figure 4.7 while progressively distorting the original lattice.

The mathematical procedure to obtain the Hamiltonian and the band structure for CPs in the general bipartite hexagonal system is an extension of that presented previously. The replacement of the new nearest neighbour vectors $\mathbf{e} \to \mathbf{e}'_j$ in the interaction Hamiltonian 4.26 leads to the dispersion relation

$$\omega_{\mathbf{q}}^{\tau} = \omega_0 \sqrt{1 \pm 2\frac{\Omega}{\omega_0}|f'_{\mathbf{q}}|}, \tag{4.76}$$

where

$$f'_{\mathbf{q}} = \sum_{j=1}^{3} \mathcal{C}'_j(\theta, \phi) \exp(i\mathbf{q} \cdot \mathbf{e}'_j). \tag{4.77}$$

Here, $\mathcal{C}'_j = (a/|\mathbf{e}'_j|)^3(1-3\sin^2\theta\cos^2\phi_j)$ is a generalisation of $\mathcal{C}_j$ defined in equation 4.28, with $\phi_j = \phi + \arctan\left[(\mathbf{e}'_j\cdot\hat{\mathbf{x}})/(\mathbf{e}'_j\cdot\hat{\mathbf{y}})\right]$ the angle between $\mathbf{e}'_j$ and the projection of the LSP polarisation $\hat{\mathbf{p}}$ into the $x$-$y$ plane. Note that, as the three nearest neighbour vectors are not equivalent in general, we explicitly include the factor $(a/|\mathbf{e}'_j|)^3$ in $\mathcal{C}'_j$.

An equivalent analysis to that in section 4.2.4 yields a phase diagram for each lattice, identifying the domains of LSP polarisation that exhibit Dirac CP quasiparticles. From equation 4.77 we obtain the condition for gapless plasmonic dispersions at an arbitrary polarisation,

$$0 \leq \frac{(\mathcal{C}'^2_2+\mathcal{C}'^2_3)^2-\mathcal{C}'^2_1}{4\mathcal{C}'_2\mathcal{C}'_3} \leq 1. \tag{4.78}$$

Figure 4.15 shows the resulting phase diagram of gapped and gapless states as a function of $\hat{\mathbf{p}}(\theta,\phi)$ for five different lattices, where the cream and orange regions indicate gapless and gapped CP spectra, respectively. While diagram (a) of Figure 4.15 corresponds to the honeycomb lattice $\boldsymbol{\ell} = (0,0)$, diagrams (b)-(e) are obtained by progressively 'displacing' the $B$ sublattice in the $-\hat{\mathbf{y}}$ direction (see Figure 4.14). The phase diagram (b), obtained for $\boldsymbol{\ell} = (0,-0.0893a)$ is topologically equivalent to that of the honeycomb lattice (a). Despite the rather small displacement (less than 10% of $a$), the broken discrete rotational symmetry of the lattice induces an evident distortion of the phase diagram. For larger deformations, in diagrams (b) to (e) we observe that the topology of the phase diagram changes, as indicated by the arrows in the figure. For example, when going from $\boldsymbol{\ell} = (0,-0.0893a)$ to $\boldsymbol{\ell} = (0,-0.1433a)$ ((b) to (c)), a compact gapless domain splits into two disconnected pockets separated by a gapped phase. In contrast, when going from $\boldsymbol{\ell} = (0,-0.1433a)$ to $\boldsymbol{\ell} = (0,-0.1437a)$ ((c) to (d)), the topological phase transition occurs by annihilation of a gapless domain into a gapped one, which we see implies the annihilation of Dirac points in the graphene-like dispersion $\theta = 0$. Finally, when going from $\boldsymbol{\ell} = (0,-0.1437a)$ to $\boldsymbol{\ell} = (0,-0.1967a)$ ((d) to (e)), the transition occurs by the merging of three topologically disconnected gapless domains into one. Even larger deformations lead to a phase diagram that is mostly dominated by gapped phases. We note that the phase diagram always possesses a 2-fold rotational symmetry in $\phi$ as the polarisations $\hat{\mathbf{p}} = (\theta,\phi)$ and $\hat{\mathbf{p}} = (\theta,\phi+\pi)$ are equivalent.

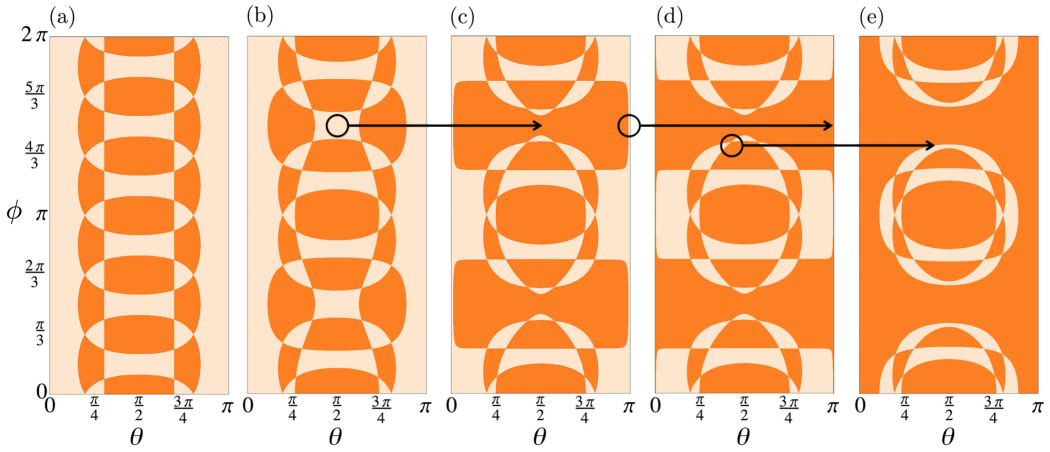


**Figure 4.15:** Phase diagrams showing the polarisation $\hat{\mathbf{p}} = (\theta, \phi)$ at which the CP spectrum is gapped or gapless (orange and cream regions, respectively) for different positions of the $B$ sublattice, parametrised by the vector $\boldsymbol{\ell}$ (see Figure 4.14). Panel (a) corresponds to $\boldsymbol{\ell} = (0, 0)$, i.e., a perfect honeycomb lattice, while in panels (b) $\boldsymbol{\ell} = (0, -0.0893a)$, (c) $\boldsymbol{\ell} = (0, -0.1433a)$, (d) $\boldsymbol{\ell} = (0, -0.1437a)$ and (e) $\boldsymbol{\ell} = (0, -0.1967a)$. The black arrows highlight (some of) the locations of topological phase transitions between panels. Reprinted with permission from [124]. Copyright 2015 IOP Publishing.

The five phase diagrams shown in Figure 4.15 are snapshots from the video of Figure C.3, which shows a large succession of phase diagrams corresponding to lattice deformations from $\boldsymbol{\ell} = (0, 0)$ to $\boldsymbol{\ell} = (0, -0.2a)$. As is clear from the video and can be inferred from panels (c) and (d) in Figure 4.15, the spectrum for the polarisation $\theta = 0$, for which the analogy between our CPs and electrons in graphene holds, is gapped for deformations larger than $\boldsymbol{\ell} \simeq (0, -0.1435a)$. Whilst we are not discussing elastic deformations of real graphene membranes it is insightful to note that the literature on strained graphene suggests that a ca. 20% change in one of the nearest-neighbour hopping lengths is needed to merge the two Dirac points and open a gap in the spectrum [108, 109, 131].

Figure 4.16 further illuminates the qualitatively distinct physical regimes realisable in different lattices for the same dipole polarisation. For $\theta = 0$, Figure 4.16(a) shows the CP band gap $\Delta$ in units of the coupling $\Omega$ as a function of the position of the $B$ sublattice (white regions indicate a gapless CP dispersion). For a perfect honeycomb array, the $B$ sublattice is located at the center of the triangle (black dot) defined by the three neighbouring nanoparticles in sublattice $A$ (depicted as blue circles in the figure). The grey areas indicate regions for which the interparticle distance is smaller than $3r$ and where the dipole-dipole approximation is expected to break down such that higher multipoles need to be taken into account. Also note that as we have only included the effects of nearest-neighbours, this model becomes less viable as we approach the dotted

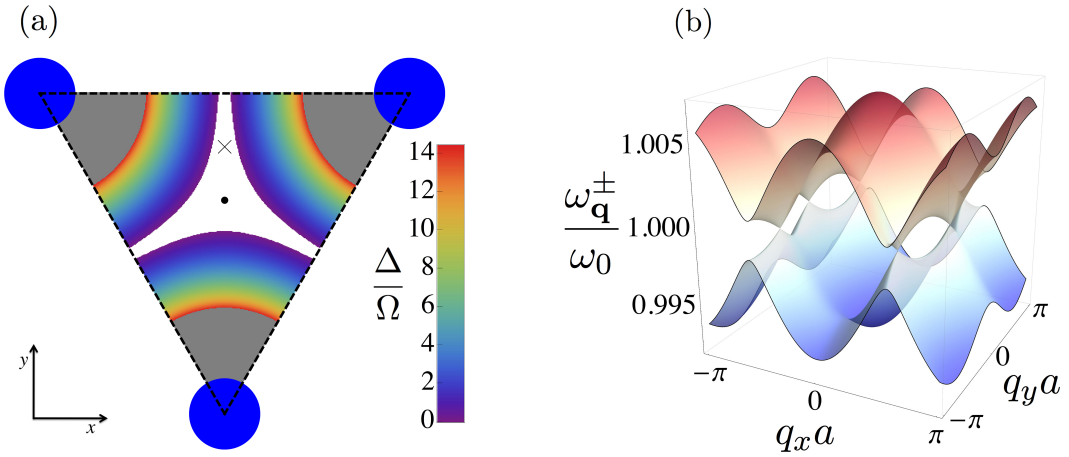


**Figure 4.16:** (a) Band gap $\Delta$ as a function of the position of the $B$ sublattice for $\theta = 0$. For a perfect honeycomb array, the $B$ sublattice is located at the center of the triangle (black dot) defined by the three neighbouring nanoparticles in sublattice $A$ (depicted as blue circles in the figure). The white region indicates the absence of a gap, while the colour scale gives the size of the gap in units of $\Omega$. The grey areas indicate regions for which the interparticle distance is smaller than $3r$ and where the dipole-dipole approximation breaks down. The cross, corresponding to a displacement $\boldsymbol{\ell} = (0, a/4)$, indicates a rather large sublattice deformation for which the spectrum, plotted in panel (b), is still characterised by the presence of massless Dirac quasiparticles (see text). In the figure, $a = 6r$ and $\epsilon_D = 1$. Reprinted with permission from [124]. Copyright 2015 IOP Publishing.

lines where the effects of next-nearest-neighbours become increasingly important. As can be seen from the figure, the gapless dispersion is robust in a sizeable region around the point $\boldsymbol{\ell} = (0, 0)$ (black dot in the figure). While shifting the $B$ sublattice towards the $A$ one, a non-vanishing gap forms, whose magnitude progressively increases.

To emphasise that indeed the gapless domain in Figure 4.16(a) supports Dirac CPs, we focus on the particular displacement $\boldsymbol{\ell} = (0, a/4)$ indicated by a cross in the figure. For such a bipartite hexagonal lattice, the two inequivalent Dirac points are located at $\pm\mathbf{K}_D = \pm\frac{2}{\sqrt{3}a}\arccos\left(-\frac{\sqrt{2197}}{250}\right)(1, 0)$, close to which the function $f_{\mathbf{q}}$ expands as $f'_{\mathbf{q}} = \frac{-96a}{125}\left(\pm\sqrt{\frac{20101}{2197}}k_x + ik_y\right)$. Thus, close to the Dirac points the CP dispersion describes massless Dirac CPs with an angular-dependent group velocity, as shown in Figure 4.16(b).

## 4.4 Chapter Summary

In this chapter we have studied the plasmonic response of an artificial graphene metamaterial, consisting of a honeycomb array of metallic nanoparticles. Within the space

of possible polarisations we have identified a wide class of gapless phases where the plasmonic excitations are characterised by a massless chiral Dirac Hamiltonian. The system was seen to offer a wide tunability, as one can also realise gapped phases, as well as dispersions that are translationally invariant and even flat bands. The gapped phases emerge whilst progressively tilting the polarisation, which drives the coalescence and subsequent annihilation of pairs of Dirac cones, in analogy to real graphene under significant elastic strain.

We also studied bipartite hexagonal lattices in general, obtained by a rigid shift of one sublattice from the initial honeycomb arrangement, and analysed the fate of the polarisation phase diagram. The phase diagram undergoes a series of topological transitions as one deforms the array, and shows a significant variation for displacements of a few percent. Importantly we demonstrated that a large family of bipartite arrays of metallic nanoparticles can support Dirac plasmonic modes, although with varying distributions of Dirac and gapped phases. Such information is crucial for the design of plasmonic metamaterials with Dirac-like properties.

Identifying the eigenmodes of a honeycomb array of metallic nanoparticles is an important first step in understanding the optical properties of Dirac metamaterials. The natural question to address next is the fate of the CPs of the system when coupled to a photonic environment to form plasmon polaritons. This is the subject of the next chapter.

# Chapter 5

# Dirac plasmon-polaritons in nanoplasmonic arrays

Much of the research presented in this chapter forms the substance of a paper that will shortly be submitted to Nature Physics as a letter. This work was carried out with my collaborators Charlie-Ray Mann, Guillaume Weick and my supervisors William L. Barnes and Eros Mariani.

Polaritons are hybrid states resulting from the strong-coupling between light and matter excitations, the photonic states being endowed with signatures of their matter counterpart [35, 89]. Metamaterials offer great control over these states and can be used to create photonic systems with non-trivial topological properties [132]. It is well known that entirely distinct physical systems can possess equivalent properties when the matter systems share an underlying symmetry or topology [29]. In this vein, a myriad of material constituents and geometrical arrangements have been extensively explored to reproduce and extend exciting condensed-matter phenomena. However, whilst the matter symmetries are indeed crucial in determining the polaritonic properties, we can also tailor the photonic states to produce qualitatively distinct polaritonic properties for the same matter system.

In this chapter we first demonstrate the existence of chiral massless Dirac polaritons in a cavity-embedded plasmonic array. We then show the robustness of the associated degeneracy point (properties whose origins can be traced back to the matter symmetries) and highlight a phenomenal tunability of the dispersion and eigenstates that arises from

the modulation of the photonic states of the enclosing cavity. Tuning the photonic environment allows an order-of-magnitude renormalisation of the group velocity, and the remarkable ability to invert the chirality of Dirac modes.

In section 5.1 we consider the interaction of the fundamental transverse electromagnetic (TEM) mode of a planar optical cavity with a honeycomb array of nanoparticles embedded in the centre of the cavity. We proceed to obtain the Hopfield matrix for an arbitrary number of Umklapp processes. These processes are often neglected, but for our plasmonic system with a degenerate point at the Brillouin zone edge, such an approximation leads to an unphysical breaking of the corresponding degeneracy in the polaritonic spectrum. After obtaining the spectrum with the correct symmetries we show qualitatively distinct regimes induced by changing the cavity height, and thus the strength of the light-matter coupling, suggesting a highly tunable spectrum.

Next, in section 5.2 we carry out a Schrieffer-Wolff transformation of the polaritonic Hamiltonian in order to obtain an effective Hamiltonian expanded around the degeneracy point in the polaritonic spectrum. In this case the effective Hamiltonian is analogous to the Dirac Hamiltonian of graphene with trigonal warping, aside from an additional term which induces a diagonal asymmetric term proportional to $|\mathbf{k}|^2$. Moreover, all the coefficients of the Hamiltonian can be tuned with the cavity height, which leads to some remarkable properties of the eigenstates, such as the ability to invert the chirality of Dirac modes. We discuss implications for transport phenomena, and then conclude the chapter in section 5.3.

## 5.1 Polaritonic Hamiltonian and spectrum

Recall from chapter 4 (equation 4.44) that in the limit $\Omega/\omega_0 \ll 1$ the Hamiltonian describing the CPs is

$$H_{\text{pl}} = \hbar\omega_0 \sum_{\mathbf{q}} \left( a^\dagger_{\mathbf{q}} a_{\mathbf{q}} + b^\dagger_{\mathbf{q}} b_{\mathbf{q}} \right) + \hbar\Omega \sum_{\mathbf{q}} \left( f_{\mathbf{q}} b^\dagger_{\mathbf{q}} a_{\mathbf{q}} + \text{H.c.} \right). \tag{5.1}$$

We now need to construct the Hamiltonian describing photons and their interactions with the CPs. Firstly we discuss the photonic modes of a planar optical cavity and obtain an expression for the magnetic vector potential of the fundamental cavity mode.

We then obtain the full Hamiltonian of the light-matter coupling and investigate the polaritonic dispersion whilst varying the coupling strength via the cavity height.

### 5.1.1 Quantised cavity modes

We consider a planar optical cavity that is perfectly reflecting, with the cavity walls perpendicular to the $z$ axis [133] as shown in Figure 5.1. In this case, the magnetic vector potential can be expanded over a set of orthonormal modes with polarisation $\eta \in \{1, 2\}$ and wavevector

$$\boldsymbol{\kappa}_{\mathbf{k}}^{l} = (k_x, k_y, \pi l/L). \tag{5.2}$$

The wavenumbers $k_x$ and $k_y$ are good quantum numbers as they lie in the transitionally invariant plane of the cavity, whereas the $z$-component is quantised with $l \in \mathbb{N}$. We parameterise $\boldsymbol{\kappa}$ in spherical coordinates as $\theta_{\mathbf{k}}^{l} = \arccos\left(\pi l/L|\boldsymbol{\kappa}_{\mathbf{k}}^{l}|\right)$ and $\phi_{\mathbf{k}} = \arctan\left(k_y/k_x\right)$, and denote the wavevector in the plane of the cavity (which is also the plane of the array) as $\mathbf{k} = (k_x, k_y)$. We are only interested in the value of the vector potential in the plane of the cavity where we shall embed the honeycomb array, which we choose to be the centre of the cavity at $z = L/2$ as shown in Figure 5.1. Thus, we define $\mathbf{A}(\boldsymbol{\rho}) \equiv \mathbf{A}(\boldsymbol{\rho}, L/2)$ where $\boldsymbol{\rho} = (x, y)$.

We find that even multiples of $l$ correspond to modes polarised in the $\hat{\mathbf{z}}$ direction, whereas odd multiples of $l$ correspond to modes polarised in the plane of the array. We separate $\mathbf{A}$ into these two parts

$$\mathbf{A} = \mathbf{A}^{\perp} + \mathbf{A}^{\parallel}, \tag{5.3}$$

where

$$\mathbf{A}^{\perp}(\boldsymbol{\rho}) = -\omega_0 \hat{\mathbf{z}} \sum_{l}^{\text{even}} N_l \sum_{\mathbf{k}} \sin\theta_{\mathbf{k}}^{l} \omega_{\mathbf{k}l}^{-1/2} c_{\mathbf{k}l} \mathrm{e}^{i\mathbf{k}\cdot\boldsymbol{\rho}} + \text{H.c.}, \tag{5.4}$$

is the component of $\mathbf{A}$ perpendicular to the plane of the cavity, and

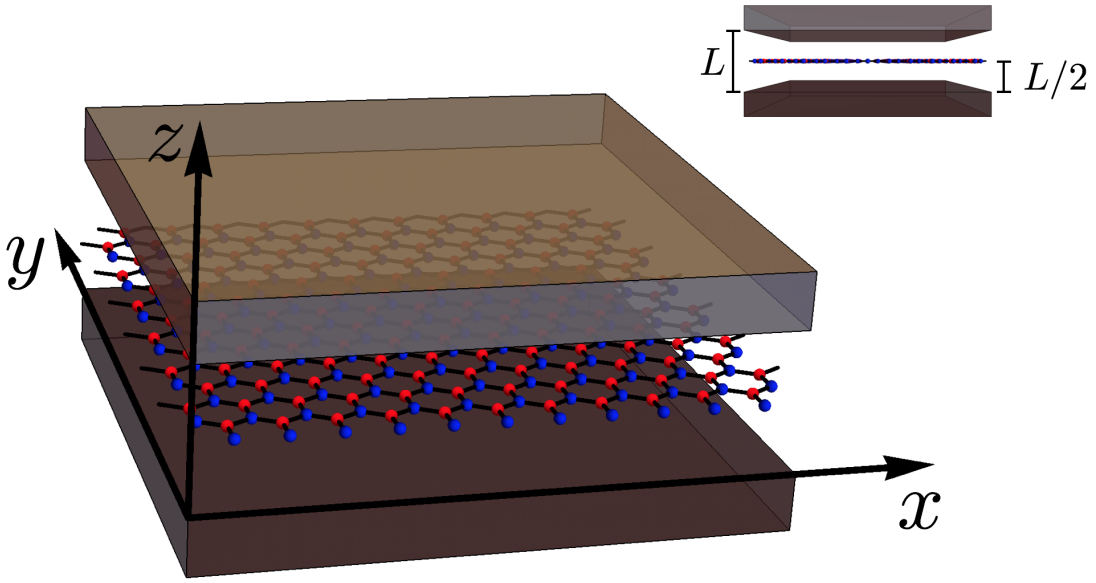


**Figure 5.1:** Schematic of (a section of) the cavity and embedded nanoparticle array. The top-right inset displays an alternative viewing angle.

$$\mathbf{A}^{\parallel}(\boldsymbol{\rho}) = \sum_{l}^{\text{odd}} N_{l-1} \sum_{\mathbf{k},\eta} \mathbf{u}_{\mathbf{k}l\eta} \omega_{\mathbf{k}l}^{-1/2} d_{\mathbf{k}l\eta} \mathrm{e}^{i\mathbf{k}\cdot\boldsymbol{\rho}} + \text{H.c.} \tag{5.5}$$

The operators $c^{\dagger}_{\mathbf{k}l}$ and $d^{\dagger}_{\mathbf{k}l\eta}$ create cavity photons with dispersion $\omega_{\mathbf{k}l} = c|\boldsymbol{\kappa}^{\boldsymbol{l}}_{\mathbf{k}}|$, polarised along the direction $\hat{\mathbf{z}}$ and $\mathbf{u}_{\mathbf{k}l\eta}$ respectively, where

$$\mathbf{u}_{\mathbf{k}l\eta} = \begin{cases} i\cos\theta^{l}_{\mathbf{k}}(\cos\phi_{\mathbf{k}}\hat{\mathbf{x}} + \sin\phi_{\mathbf{k}}\hat{\mathbf{y}}), & \eta = 1 \\ -\sin\phi_{\mathbf{k}}\hat{\mathbf{x}} + \cos\phi_{\mathbf{k}}\hat{\mathbf{y}}, & \eta = 2 \end{cases}. \tag{5.6}$$

Here $\mathcal{V}$ is the volume of the cavity and $N_l$ is a normalisation constant given by

$$N_l = \begin{cases} (\hbar/2\epsilon_0\mathcal{V})^{1/2}, & l = 0 \\ (\hbar/\epsilon_0\mathcal{V})^{1/2}(-1)^{l/2}, & l \neq 0 \end{cases}. \tag{5.7}$$

Note that for odd $l$ we sum over the two polarisations in the vector potential of equation 5.3, whereas for even $l$ only the TM polarisation has a non-vanishing field in the centre of the cavity where we embed the array. In the following section we will consider dipoles polarised in the $\hat{\mathbf{z}}$ direction, originating from nanoparticles orientated perpendicular to the cavity array with an anisotropy sufficient to decouple the transverse and longitudinal

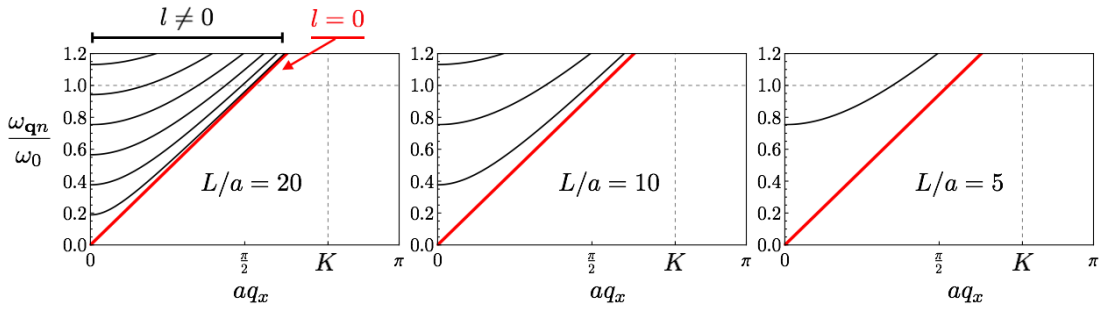


**Figure 5.2:** Plots showing the dispersion of the TEM mode $l = 0$ (red line) and the TM cavity modes $l \neq 0$ (black curves) for various cavity heights as indicated in the figures. We see that as the cavity height is decreased the dispersions of the TM modes are shifted up in frequency, whilst the dispersion of the TEM mode is independent of the cavity height. In the figure $c/\omega_0 a = 3/5$, $\epsilon_{\mathrm{D}} = 1$ and $a = 3r$.

modes within the frequency bandwidth of interest. In this case we need just consider $\mathbf{A}^{\perp}$.

There are some distinguishing features between the TEM mode $l = 0$ and the other TM cavity modes $l \neq 0$. As we see in Figure 5.2 the dispersion of the TEM mode is independent of the cavity height, whereas the TM cavity modes shift up in frequency with decreasing $L$. Therefore, the frequency of the TEM mode $\omega_{\mathbf{k}} = c|\mathbf{k}|$ is always less than the frequency of a TM cavity mode $\omega_{\mathbf{k}l}$. In addition the light-matter coupling between the CPs and the TM cavity modes vanishes as $L \to 0$. Therefore, the existence of the TEM mode is crucial as it permits tuning of the light-matter interaction without the detuning that occurs for the TM cavity modes, and maintains a non-vanishing light-matter interaction as the cavity height is decreased. In fact to capture the essential properties of the polaritons we need only consider the TEM mode, as the inclusion of the higher order $l \neq 0$ modes provides only a qualitative modification of the band structure and eigenstates. For this reason we consider just the fundamental $l = 0$ (TEM) cavity mode to highlight the key physics. Under this assumption the magnetic vector potential reads

$$\mathbf{A}(\boldsymbol{\rho}) = -\hat{\mathbf{z}} \sum_{\mathbf{k}} \left( \frac{\hbar}{2\epsilon_0 \mathcal{V} \omega_{\mathbf{k}}} \right)^{1/2} c_{\mathbf{k}} \mathrm{e}^{i\mathbf{k}\cdot\boldsymbol{\rho}} + \mathrm{H.c.} \tag{5.8}$$

Furthermore in anticipation of the following section we can express the wavevector as

$$\mathbf{k} = \mathbf{q} - \mathbf{G}_n, \tag{5.9}$$

where $\mathbf{q}$ is restricted to the first Brillouin zone of the honeycomb array, and $\mathbf{G}_n$ is an arbitrary reciprocal lattice vector labelled by $n$. Thus, we write equation 5.8 as

$$\mathbf{A}(\boldsymbol{\rho}) = -\hat{\mathbf{z}} \sum_{\mathbf{q}n} \left( \frac{\hbar}{2\epsilon_0 \mathcal{V} \omega_{\mathbf{q}n}} \right)^{1/2} c_{\mathbf{q}n} \mathrm{e}^{i(\mathbf{q}-\mathbf{G}_n)\cdot\boldsymbol{\rho}} + \mathrm{H.c.}, \tag{5.10}$$

where $\omega_{\mathbf{q}n} = c|\mathbf{q} - \mathbf{G}_n|$ and $c^\dagger_{\mathbf{q}n}$ creates a cavity photon with wavevector $\mathbf{q} - \mathbf{G}_n$. Note that in equation 5.10 we have not made any physical changes to $\mathbf{A}$ with respect to equation 5.8, and in the context of an empty cavity we can regard our transformation as just a relabelling of $\mathbf{k}$.

### 5.1.2 Light-Matter Hamiltonian

We now proceed to obtain a light-matter interaction Hamiltonian using the magnetic vector potential of 5.10. In general, the Hamiltonian which describes an array of dipoles interacting with an electromagnetic field is given by

$$H_{\mathrm{light-matter}} = \underbrace{\sum_{\mathbf{R},s} \frac{-Q}{M} \boldsymbol{\Pi}_s(\mathbf{R}_s) \cdot \mathbf{A}(\mathbf{R}_s)}_{H_{\mathrm{pl-ph}}} + \underbrace{\sum_{\mathbf{R},s} \frac{Q^2}{2M} \mathbf{A}^2(\mathbf{R}_s)}_{H_{\mathrm{se}}} \tag{5.11}$$

where $H_{\mathrm{pl-ph}}$ is the 'plasmon-photon' interaction Hamiltonian and $H_{\mathrm{se}}$ is the photonic 'self-energy' $\mathbf{A}^2$ dependent term of the Hamiltonian. For compactness we write the electronic centre of mass conjugate momentum given by equation 4.24 as

$$\boldsymbol{\Pi}_s(\mathbf{R}_s) = \hat{\mathbf{z}} \left( \frac{\hbar M \omega_0}{2\mathcal{N}} \right)^{1/2} \sum_{\mathbf{q}} i\gamma^{s\,\dagger}_{\mathbf{q}} \mathrm{e}^{i\mathbf{q}\cdot\mathbf{R}_s} + \mathrm{H.c.} \tag{5.12}$$

where $\gamma^A_{\mathbf{q}} \equiv a_{\mathbf{q}}$ and $\gamma^B_{\mathbf{q}} \equiv b_{\mathbf{q}}$. Note that there is no sum over $n$ as the CP dispersion is periodic, and so a plasmon with wavevector $\mathbf{q}$ is indistinguishable from one with wavevector $\mathbf{q} - \mathbf{G}_n$. Note also that we have assumed the LSPs to be polarised in the $\hat{\mathbf{z}}$ direction, which as we stated previously is realisable with orientated anisotropic nanoparticles. Substituting the expressions 5.10 and 5.12 into 5.11 we can rewrite $H_{\mathrm{pl-ph}}$ as

$$H_{\mathrm{pl-ph}} = \hbar\omega_0 \frac{1}{\mathcal{N}} \sum_{\mathbf{R},s} \sum_{\mathbf{q}',\mathbf{q}n} i\gamma^{s}_{\mathbf{q}'}{}^{\dagger} \mathrm{e}^{-i\mathbf{q}'\cdot\mathbf{R}_s} \xi_{\mathbf{q}n} \left[ c_{\mathbf{q}n} \mathrm{e}^{i(\mathbf{q}-\mathbf{G}_n)\cdot\mathbf{R}_s} + c^{\dagger}_{\mathbf{q}n} \mathrm{e}^{-i(\mathbf{q}-\mathbf{G}_n)\cdot\mathbf{R}_s} \right] + \mathrm{H.c.}, \tag{5.13}$$

where the coupling strength is given by

$$\xi^2_{\mathbf{q}n} = \frac{8\pi}{6\sqrt{3}} \frac{\Omega}{\omega_{\mathbf{q}n}} \frac{a}{L}. \tag{5.14}$$

The fact that the light-matter interaction scales with the cavity height as $\xi_{\mathbf{q}n} \propto 1/\sqrt{L}$ is the key to the tunable polariton dispersion and the intriguing properties we will discuss shortly.

As we will see, it is necessary to include Umklapp processes to maintain the essential symmetries of the system. Let us methodically calculate an expression for the first term in $H_{\mathrm{pl-ph}}$ of equation 5.13 so it is clear where a phase factor relating to these Umklapp processes originates. Defining

$$\chi = (1/\mathcal{N}) i\gamma^{s}_{\mathbf{q}'}{}^{\dagger} \mathrm{e}^{-i\mathbf{q}'\cdot\mathbf{R}_s} \xi_{\mathbf{q}n}, \tag{5.15}$$

where $\exp(i\mathbf{G}_n \cdot \mathbf{R}) = 1$ for all $\mathbf{G}_n$, we get

$$\sum_{\mathbf{q}'\mathbf{R}} \chi = i\xi_{\mathbf{q}n} \gamma^{s}_{\mathbf{q}}{}^{\dagger} c_{\mathbf{q}n} \mathrm{e}^{-i\mathbf{G}_n\cdot\mathbf{e}_s}, \tag{5.16}$$

leading to

$$\sum_{s} \sum_{\mathbf{q}'\mathbf{R}} \chi = i\xi_{\mathbf{q}n} \left( a^{\dagger}_{\mathbf{q}} \phi^{*}_{n} + b^{\dagger}_{\mathbf{q}} \phi_n \right) c_{\mathbf{q}n}, \tag{5.17}$$

with $\phi_n = \mathrm{e}^{i\mathbf{G}_n\cdot\mathbf{e}_A} = \left(\mathrm{e}^{i\mathbf{G}_n\cdot\mathbf{e}_B}\right)^*$. We introduced the factor

$$\phi_n = \exp(ia\mathbf{G}_n \cdot \hat{\mathbf{y}}), \tag{5.18}$$

which parametrises the phase of the light-matter interaction. Following this procedure the interaction Hamiltonian 5.13 can be written as

$$H_{\mathrm{pl-ph}} = \hbar\omega_0 \sum_{\mathbf{q}n} i\xi_{\mathbf{q}n} \left(\phi_n^* a_{\mathbf{q}}^\dagger + \phi_n b_{\mathbf{q}}^\dagger\right) \left(c_{\mathbf{q}n} + c_{-\mathbf{q}n}^\dagger\right) + \mathrm{H.c.}, \tag{5.19}$$

where the minus sign in subscripts implies that both $\mathbf{q}$ and $\mathbf{G}_n$ are multiplied by $-1$, such that $c_{-\mathbf{q}n}^\dagger$ creates a cavity photon with wavevector $-(\mathbf{q}-\mathbf{G}_n)$. We can now apply this same procedure to $H_{\mathrm{se}}$ in equation 5.11. Substituting the expansion of the vector potential 5.10 into $H_{\mathrm{se}}$ gives

$$H_{\mathrm{se}} = \frac{\hbar\omega_0}{\mathcal{N}} \sum_{s,\mathbf{R},\mathbf{q},n,\mathbf{q}',n'} \xi_{\mathbf{q}n}\xi_{\mathbf{q}'n'} c_{\mathbf{q}n} \mathrm{e}^{i(\mathbf{q}-\mathbf{G}_n)\cdot\mathbf{R}_s} \left(c_{\mathbf{q}'n'} \mathrm{e}^{i(\mathbf{q}'-\mathbf{G}_{n'})\cdot\mathbf{R}_s} + \mathrm{H.c.}\right) + \mathrm{H.c.}, \tag{5.20}$$

which following similar steps as above can be expressed as

$$H_{\mathrm{se}} = \hbar\omega_0 \sum_{\mathbf{q}nm} 2\xi_{\mathbf{q}n}^2 \alpha_{\mathbf{q}nm} c_{\mathbf{q}n} \left(c_{-\mathbf{q}m} + c_{\mathbf{q}m}^\dagger\right) + \mathrm{H.c.}, \tag{5.21}$$

where

$$\alpha_{nm} = (\omega_{\mathbf{q}n}/\omega_{\mathbf{q}m})^{1/2} \mathrm{Re}[\phi_n \phi_m^*]. \tag{5.22}$$

### 5.1.3 Exact diagonalisation

The full Hamiltonian for our system, including the purely plasmonic, photonic and coupling terms is thus

$$H = H_{\mathrm{pl}} + H_{\mathrm{ph}} + H_{\mathrm{pl-ph}} + H_{\mathrm{se}}. \tag{5.23}$$

To find the normal modes of the equation we introduce the operator

$$\beta_{\mathbf{q}} = \mathbf{C}\boldsymbol{\Psi}, \tag{5.24}$$

where $\mathbf{\Psi}$ is a vector column of superposition coefficients and $\mathbf{C}$ is a vector row of operators, defined as

$$\mathbf{\Psi} = \big(w_{\mathbf{q}}, x_{\mathbf{q}}, y_{\mathbf{q}}, z_{\mathbf{q}}, \underbrace{u_{\mathbf{q}1}, v_{\mathbf{q}1}}_{1}, \underbrace{u_{\mathbf{q}2}, v_{\mathbf{q}2}}_{2}, \underbrace{\ldots, \ldots}_{\ldots}, \underbrace{u_{\mathbf{q}n}, v_{\mathbf{q}n}}_{n}\big)^T, \tag{5.25}$$

$$\mathbf{C} = \big(a_{\mathbf{q}}, a^\dagger_{-\mathbf{q}}, b_{\mathbf{q}}, b^\dagger_{-\mathbf{q}}, \overbrace{c_{\mathbf{q}1}, c^\dagger_{-\mathbf{q}1}}^{1}, \overbrace{c_{\mathbf{q}2}, c^\dagger_{-\mathbf{q}2}}^{2}, \overbrace{\ldots, \ldots}^{\ldots} \overbrace{c_{\mathbf{q}n}, c^\dagger_{-\mathbf{q}n}}^{n}\big), \tag{5.26}$$

where the over- and under-braces numbered $n$ highlight the pairs of photonic operators in $\mathbf{C}$ (and coefficients in $\mathbf{\Psi}$) that correspond to the $n$th photonic mode. If one were to expand out the product of equation 5.24 it would have the more familiar form of equation 4.34. Diagonalising the system implies that the eigenmode operator $\beta_{\mathbf{q}}$ obeys the Heisenberg equation

$$[\beta_{\mathbf{q}}, H] = \hbar\omega^{\mathrm{pol}}_{\mathbf{q}}\beta_{\mathbf{q}}, \tag{5.27}$$

which leads to the eigenvalue equation

$$\mathbf{C}\mathbf{M}\mathbf{\Psi} = \mathbf{C}\omega^{\mathrm{pol}}_{\mathbf{q}}\mathbf{\Psi}, \tag{5.28}$$

where $\mathbf{M}_{ij}$ is the factor stemming the commutator of equation 5.27 that multiplies the $i$th operator in $\mathbf{C}$ and the $j$th coefficient in $\mathbf{\Psi}$. We split up the (infinite) Hopfield matrix $\mathbf{M}$ into those parts which arise from the commutator with each of the four subsidiary Hamiltonians of equation 5.23, such that

$$\mathbf{M} = \begin{pmatrix} \mathbf{M}_{\mathrm{pl}} & \mathbf{M}^{\mathcal{J}}_{\mathrm{pl-ph}} \\ \mathbf{M}_{\mathrm{pl-ph}} & \mathbf{M}_{\mathrm{ph}} + \mathbf{M}_{\mathrm{se}} \end{pmatrix}, \tag{5.29}$$

where the '$\mathcal{J}$-hermitian conjugate' of an arbitrary matrix $\mathbf{X}$ is defined in terms of matrix elements as

$$\left(\mathbf{X}^{\mathcal{J}}\right)_{ij} = (-1)^{i+j}\left(\mathbf{X}_{ji}\right)^*. \tag{5.30}$$

The plasmonic matrix is the same as before in equation 4.36

$$\mathbf{M}_{\mathrm{pl}} = \begin{pmatrix} \omega_0 & 0 & \Omega f_{\mathbf{q}} & -\Omega f_{\mathbf{q}} \\ 0 & -\omega_0 & \Omega f_{\mathbf{q}} & -\Omega f_{\mathbf{q}} \\ \Omega f^*_{\mathbf{q}} & -\Omega f^*_{\mathbf{q}} & \omega_0 & 0 \\ \Omega f^*_{\mathbf{q}} & -\Omega f^*_{\mathbf{q}} & 0 & -\omega_0 \end{pmatrix}, \tag{5.31}$$

and the photonic matrix is a diagonal list of frequencies

$$\mathbf{M}_{\mathrm{ph}} = \mathrm{diag}\left(\omega_{\mathbf{q}1}, -\omega_{\mathbf{q}1}, \omega_{\mathbf{q}2}, -\omega_{\mathbf{q}2}, ..., ..., \omega_{\mathbf{q}n}, -\omega_{\mathbf{q}n}\right). \tag{5.32}$$

The interaction matrix is characterised by matrix elements

$$\left(\mathbf{M}_{\mathrm{ph-pl}}\right)_{ij} = i\xi_{\mathbf{q}d(i)} \begin{cases} \phi^*_{d(i)}, & j = 1, 2 \\ \phi_{d(i)}, & j = 3, 4 \end{cases} \tag{5.33}$$

where $d(n) = (n+1)\backslash 2 \in \mathbb{Z}$ is a counting function with $n\backslash m$ the integer division of $n$ by $m$. Finally $\mathbf{M}_{\mathrm{se}}$ has matrix elements

$$\left(\mathbf{M}_{\mathrm{se}}\right)_{ij} = 4\hbar\omega_0(-1)^{j+1}\alpha_{d(j)d(i)}\xi^2_{\mathbf{q}d(j)}. \tag{5.34}$$

### 5.1.4 Polaritonic dispersion

In Figure 5.3 we plot the polariton dispersion $\omega^{\mathrm{pol}}_{\mathbf{q}}$ from equation 5.28, which corresponds to the eigenvalues of the matrix $\mathbf{M}$ given in equation 5.29. We truncate the matrix $\mathbf{M}$ by limiting the sum over the $n$ Umklapp processes such that the resulting dispersion sufficiently converges. In Figure 5.3(a) we plot the dispersion along the symmetry lines $\Gamma - K - M - \Gamma$ in the absence of coupling, that is we plot the TEM mode of the empty cavity and the CP dispersion (equation 4.41). We observe four points where the bands cross, labelled by circled numbers. One may expect that in the presence of coupling between these individual modes there will be anticrossings at all four of these band crossings.

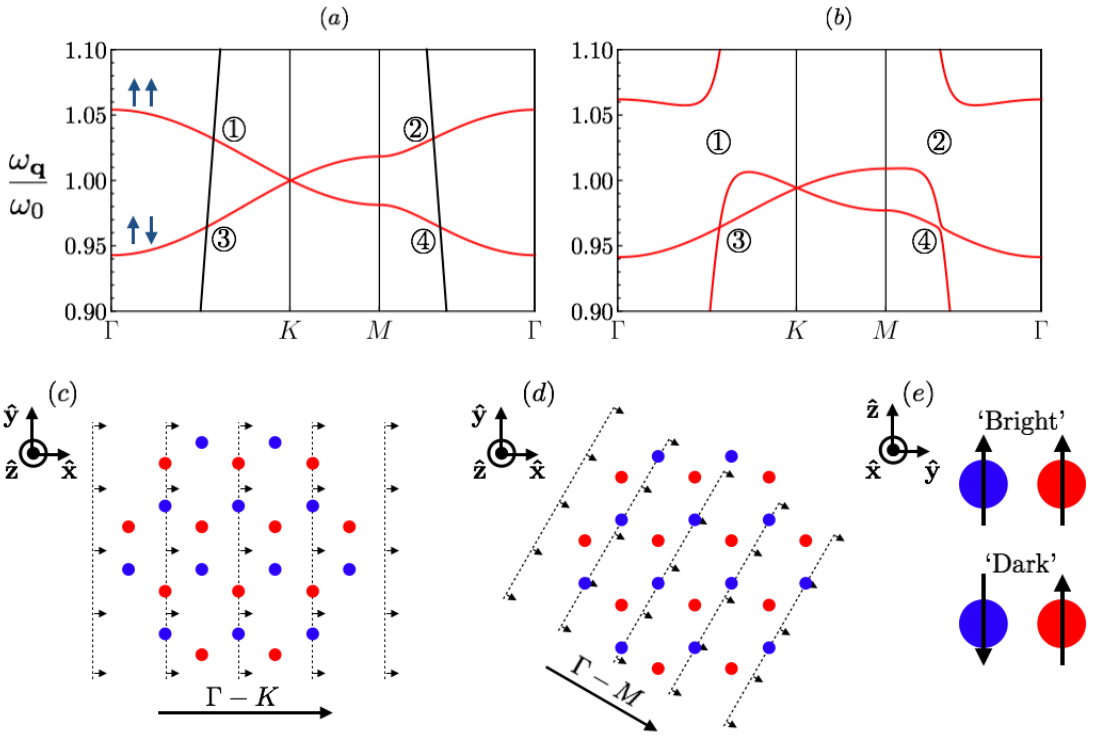


**Figure 5.3:** $(a-b)$ Plots showing $(a)$ the CP dispersion $\omega_{\mathbf{q}}^{\pm}$ (red line) of equation 4.41 and the TEM cavity mode $\omega_{\mathbf{q}n}$ (black line) in the absence of any coupling; and $(b)$ the polaritonic dispersion ($\omega_{\mathbf{q}}^{\mathrm{pol}}$ of equation 5.28) that arises from the coupling between these modes. In $(a)$ the circled numbers indicate the locations of the band crossings, and the pairs of blue arrows schematically indicate whether that CP band is 'bright' (symmetric) or 'dark' (asymmetric). In Figure $(b)$ we observe large anticrossings at ① and ② due to the strong light-matter coupling with the optically bright CP mode. There is no anticrossing at ③, and only a very small anticrossing at ④, due to the vanishing light-matter interaction with the optically dark CP mode. $(c-d)$ Schematics showing the wavefronts (dashed parallel lines) of a photonic mode with wavevector along the direction $(c)$ $\Gamma-K$, and $(d)$ $\Gamma-M$, superimposed on a schematic of the honeycomb lattice structure. $(e)$ Schematics of a bright and dark mode where the black arrows indicate the dipole moments on an $A$ site (blue circle) and $B$ site (red circle). In a bright mode the dipole moments are in-phase (parallel), whereas in a dark mode they are out-of-phase (anti-parallel). In the figure $c/\omega_0 a = 3/4$, $\epsilon_{\mathrm{D}} = 1$ and $a = 3r$.

However, in Figure 5.3(b) we observe large anticrossings at the points ① and ② in the polariton dispersion, but no anticrossing at the point ③ and only a very small anticrossing at the point ④. This can be understood as due to the different configurations of the lattice in the upper and lower CP bands. In the upper band the dipole moments in the sublattices $A$ and $B$ are in-phase with one another and so constructively interfere (see schematic in Figure 5.3(e)). This symmetric mode is optically 'bright' and couples significantly with photonic modes for any wavevector. In the lower band the dipole moments in each sublattice are out-of-phase with one another and destructively interfere, giving rise to an optically 'dark' mode that only weakly interacts with light. The largest (but still small) anticrossing for the dark mode is along the direction $\Gamma - M$, whilst the

smallest anticrossing is along the direction $\Gamma - K$ where the interaction with light completely vanishes. The schematics in Figures 5.3(c-d) help to explain this by showing the wavefronts of a plane wave with a wavevector along these two high symmetry directions, superimposed on a schematic of the honeycomb lattice. For example in (c) we observe that the direction $\Gamma - K$ is orthogonal to one of the separation vectors $\mathbf{e}_1$ and so the total field of the dipoles disappears along this direction. This gives rise to an additional degeneracy along the $\Gamma - K$ direction at ③.

Before continuing our discussion of the polaritons we need to address the crucial question of how we should truncate the infinite Hopfield matrix $\mathbf{M}$. The function $\xi_{\mathbf{q}n}$ is inversely proportional to $|\mathbf{q} - \mathbf{G}_n|$ so to capture the qualitative effects one might be tempted to consider just the $\mathbf{G} = \mathbf{0}$ mode. In fact this is the approximation taken by Hopfield in his seminal paper [35] where he treats exciton-polaritons that arise from the coupling between a single exciton band of a three-dimensional crystal and free photons. In this scenario it is acceptable to neglect Umklapp processes as there are no essential symmetries or degeneracies to preserve, and so their inclusion only qualitatively modifies the physics. Another key difference to note is that as the lattice and photonic modes are of the same dimension, there is no dependence of the light-matter interaction strength on a geometric length scale.

However, for our system of interacting CPs and cavity photons, neglecting Umklapp processes leads to a fundamentally incorrect result as shown in Figure 5.4(a), where for small enough values of the cavity height $L$ the Dirac point is destroyed. This is because at $\mathbf{q} = \mathbf{K}$ there are three degenerate photonic modes ($\mathbf{G}_1 = \mathbf{0}$, $\mathbf{G}_2 = \mathbf{b}_1$ and $\mathbf{G}_3 = \mathbf{b}_2 - \mathbf{b}_1$) with the same interaction strength $\xi_{\mathbf{K}1} = \xi_{\mathbf{K}2} = \xi_{\mathbf{K}3}$, so in selecting $\mathbf{G}_1$ but neglecting the other two we artificially break the degeneracy of the $\mathbf{K}$ point.

In Figure 5.4(b) we show that selecting sets of $\mathbf{G}_n$ which are degenerate at the $\mathbf{K}$ point keeps the associated Dirac point intact. However, we point out that in this scenario the Dirac point at the $\mathbf{K}'$ point artificially shifts or ceases to exist. Thus, in principle there is no methodical way to maintain all essential symmetries in the dispersion when truncating the Hopfield matrix. In practice, by choosing a large enough number of photonic modes the symmetries are approximately maintained at both $K$ and $K'$, as shown in Figure 5.4(c).

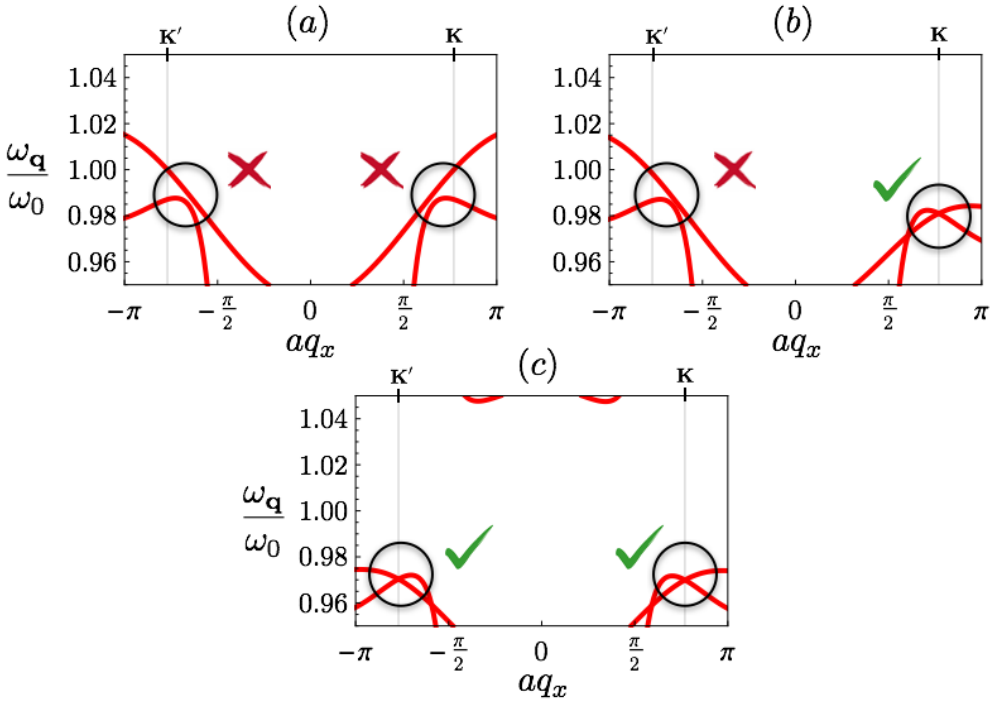


**Figure 5.4:** Comparison of the polariton dispersions $\omega_{\mathbf{q}}^{\mathrm{pol}}$ obtained from including different photonic modes in the Hopfield matrix $\mathbf{M}$ of equation 5.29. We consider (a) only the photonic mode $\mathbf{G}_n = \mathbf{0}$, (b) the three modes which are degenerate with $\mathbf{G}_n = \mathbf{0}$ at the Dirac point, and (c) 48 photonic modes centred around $\mathbf{q} = \mathbf{0}$. The green ticks and red crosses next to the black circles highlight whether the symmetries around the $K$ or $K'$ points have been artificially broken. In the figure $a = 3r$, $\epsilon_D = 1$, $c/\omega_0 a = 3/5$, and $L = 12a$.

With these considerations in mind let us examine the actual features of the dispersion $\omega_{\mathbf{q}}^{\mathrm{pol}}$ a little further. In Figure 5.5 we present the evolution of the dispersion with decreasing cavity height. Note that there is a global negative energy shift of the bands, caused by the larger anticrossing between the photonic mode and the bright CP modes as the light-matter coupling strength increases. There is a large renormalisation of the group velocity around the $K$ point, in fact in panel (d) the bands are practically flat around this point. We also observe that the additional degeneracy along the $\Gamma - K$ direction approaches and then merges with the degeneracy at $K$ at a critical cavity height $L_{\mathrm{c}}$ (in the figure $L_{\mathrm{c}} \approx 5$a). Subsequently, as the cavity height is decreased further, it appears that the bands have inverted on themselves.

The transition where the degeneracies merge at the $K(K')$ point must occur for the critical cavity height $L_{\mathrm{c}}$ when the group velocity along the $\Gamma - K(K')$ direction vanishes

$$\frac{\partial \omega_{\mathbf{q}}^{\mathrm{pol},\pm}(L_{\mathrm{c}})}{\partial q_x}\Big|_{\mathbf{q}=\mathbf{K}} = 0, \tag{5.35}$$

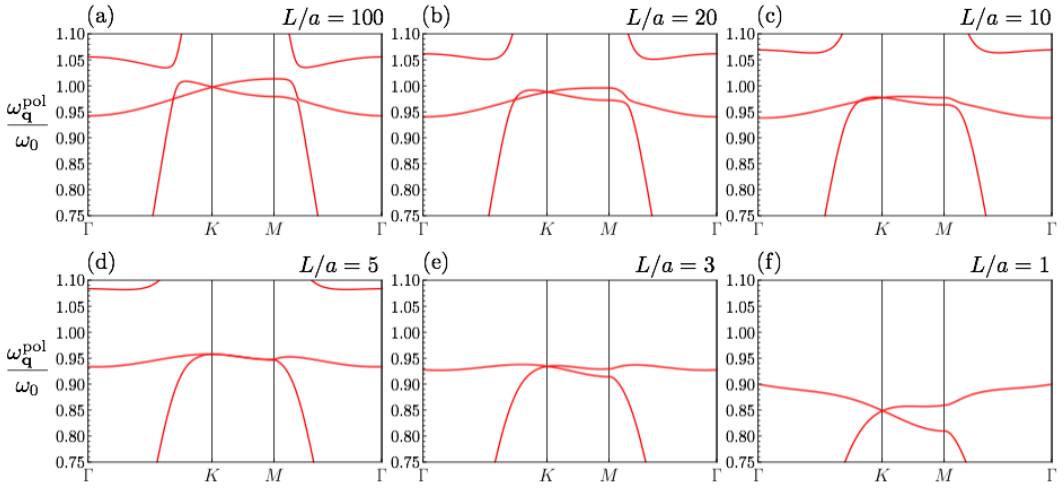


**Figure 5.5:** Evolution of the polaritonic dispersion with decreasing cavity height (indicated above each panel). With decreasing cavity height the light-matter interaction strengthens which increases the magnitude of the anticrossing with the bright CP modes. This causes a global negative energy shift of the bands degenerate at the $K$ point. Also we notice the additional degeneracy along the $\Gamma - K$ direction approach the $K$ point and merge with the degeneracy at about $L/a = 5$ as shown in panel (d). Subsequently, in panels (e-f) it appears that the bands have inverted on themselves. In the figure $a = 3r$, $c/\omega_0 a = 3/5$, $\epsilon_D = 1$, and we take 12 photonic modes centred about $\mathbf{K}$.

where $\omega_{\mathbf{q}}^{\mathrm{pol},\pm}$ indicates the upper $(+)$ and lower $(-)$ polariton bands that are degenerate at the $K(K')$ point. Equation 5.35 can be solved numerically, but later we will obtain an analytical expression for $L_{\mathrm{c}}$ accurate to second order in $\xi_{\mathbf{q}n}$.

Though we have not proved it yet, we imagine most readers are confident in the existence of a Dirac point at $K$ and $K'$ in the limit of weak light-matter coupling, which in the following we term a Conventional Dirac Point (CDP). It is perhaps less evident that the CDP should continue to exist after merging with the additional degeneracy along $\Gamma - K$, which we term a Satellite Dirac Point (SDP). To better understand this merging and the properties of the eigenstates we now perform a unitary Schrieffer-Wolff transformation [134] to obtain an effective Hamiltonian in the CP subspace, which provides an accurate description of the two bands degenerate at the $K$ and $K'$ points to second order in the light-matter coupling parameter $\xi_{\mathbf{q}n}$.

## 5.2 Dirac-like collective plasmon polaritons

We wish to develop an effective theory for the plasmon-like polaritonic dynamics of the two bands degenerate at the $K$ and $K'$ points. We thus seek a transformation of the

Hamiltonian that renders the block off diagonal terms (the light-matter coupling terms) of the Hamiltonian zero to first order in the interaction parameter $\xi_{\mathbf{q}n}$. This is accomplished in the subsequent subsection by means of a Schrieffer-Wolff (SW) transformation which we exploit to eliminate all terms linear in $\xi_{\mathbf{q}n}$. Following on we conduct an expansion around the $K$ point and investigate properties of the resulting Dirac Hamiltonian.

### 5.2.1 Effective Hamiltonian in the plasmonic subspace

Firstly we segregate the terms in the full Hamiltonian 5.23 according to whether they contain a coupling between plasmon and photon operators. Thus, we write $H = H_0 + H_1$ where

$$H_0 = H_{\mathrm{pl}} + H_{\mathrm{ph}} + H_{\mathrm{se}}, \qquad H_1 = H_{\mathrm{pl-ph}}. \tag{5.36}$$

Following this we conduct a canonical transformation of the Hamiltonian $H \to \bar{H} = \mathrm{e}^{S} H \mathrm{e}^{-S}$ where we impose that the transformation generator $S$ be first order in $\xi_{\mathbf{q}n}$. Of course we must also constrain $S$ to be anti-Hermitian to preserve the Hermicity of the Hamiltonian. The goal now is to find a final constraint which eliminates terms in $\bar{H}$ that are first order in $\xi_{\mathbf{q}n}$. The choice is obvious upon expanding $\bar{H}$ as per the Baker-Campbell-Hausdorff formula [135]

$$\bar{H} = \sum_{n=0}^{\infty} \frac{1}{n!} [S, H]_n = H + [S, H] + \frac{1}{2}[S, [S, H]] + \frac{1}{6}[S, [S, [S, H]]] + \ldots \tag{5.37}$$

$$= H_0 + \underbrace{H_1 + [S, H_0]}_{\text{linear in } \xi_{\mathbf{q}n}} + \underbrace{[S, H_1] + \sum_{n=2}^{\infty} \frac{1}{n!} [S, H]_n}_{\text{higher order terms}}. \tag{5.38}$$

A keen eye might observe that not all of $H_1 + [S, H_0]$ is linear due to the $H_{\mathrm{se}}$ term, but importantly this is the only part of the expression that contains linear terms. Thus, the essence of the SW transformation is imposing the constraint

$$[S, H_0] = -H_1, \tag{5.39}$$

which after straightforward algebra yields the effective Hamiltonian

$$\bar{H} = H_0 + \sum_{n=1}^{\infty} \frac{n}{(n+1)!} \left[S, H_1\right]_n , \tag{5.40}$$

which to first order in $H_1$ reads

$$\bar{H} = H_0 + \frac{1}{2} \left[S, H_1\right] . \tag{5.41}$$

In the following we will neglect non-resonant plasmon-plasmon terms (which only appear in $H_{\mathrm{pl}}$), due to their negligible contribution to the normal mode operator $\beta_{\mathbf{q}}$. In section 4.2.2 we have seen this to be explicitly true for the purely plasmonic Hamiltonian when $\Omega/\omega_0 \ll 1$ as the two bands $\omega^+_{\mathbf{q}}$ and $\omega^-_{\mathbf{q}}$ are near resonance. Moreover, in Figure 5.6 we numerically calculate the eigenvectors of the Hopfield matrix for the full Hamiltonian and find that non-resonant terms are indeed negligible in a wide region of reciprocal space around $K$. However, such arguments do not allow us to neglect plasmon-photon and photon-photon non-resonant terms, as in general any photonic band $n$ is not at all in resonance with another photonic band $n'$ or either of the plasmonic bands.

We write the antihermitian generator as $S = \mathcal{S} - \mathcal{S}^\dagger$ which simplifies the identification of a term that satisfies equation 5.39 to finding an $\mathcal{S}$ that satisfies

$$[H_0, \mathcal{S}] = \hbar\omega_0 \sum_{\mathbf{q}n} i\xi_{\mathbf{q}n} \left(\phi^*_n a^\dagger_{\mathbf{q}} + \phi_n b^\dagger_{\mathbf{q}}\right) \left(c_{\mathbf{q}\mathrm{n}} + c^\dagger_{-\mathbf{q}\mathrm{n}}\right) . \tag{5.42}$$

This is given by

$$\mathcal{S} = \sum_{\mathbf{q}n} i\omega_0\xi_{\mathbf{q}n} \left[\left(\chi^-_{\mathbf{q}n} a^\dagger_{\mathbf{q}} + \chi^{-*}_{\mathbf{q}n} b^\dagger_{\mathbf{q}}\right) c_{\mathbf{q}\mathrm{n}} + \left(\chi^+_{\mathbf{q}n} a^\dagger_{\mathbf{q}} + \chi^{+*}_{\mathbf{q}n} b^\dagger_{\mathbf{q}}\right) c^\dagger_{-\mathbf{q}\mathrm{n}}\right] , \tag{5.43}$$

where

$$\chi^\pm_{\mathbf{q}n} = \frac{(\omega_0 \pm \omega_{\mathbf{q}n})\phi^*_n - \Omega f^*_{\mathbf{q}}\phi_n}{(\omega_0 \pm \omega_{\mathbf{q}n})^2 - \Omega^2 |f_{\mathbf{q}}|^2} . \tag{5.44}$$

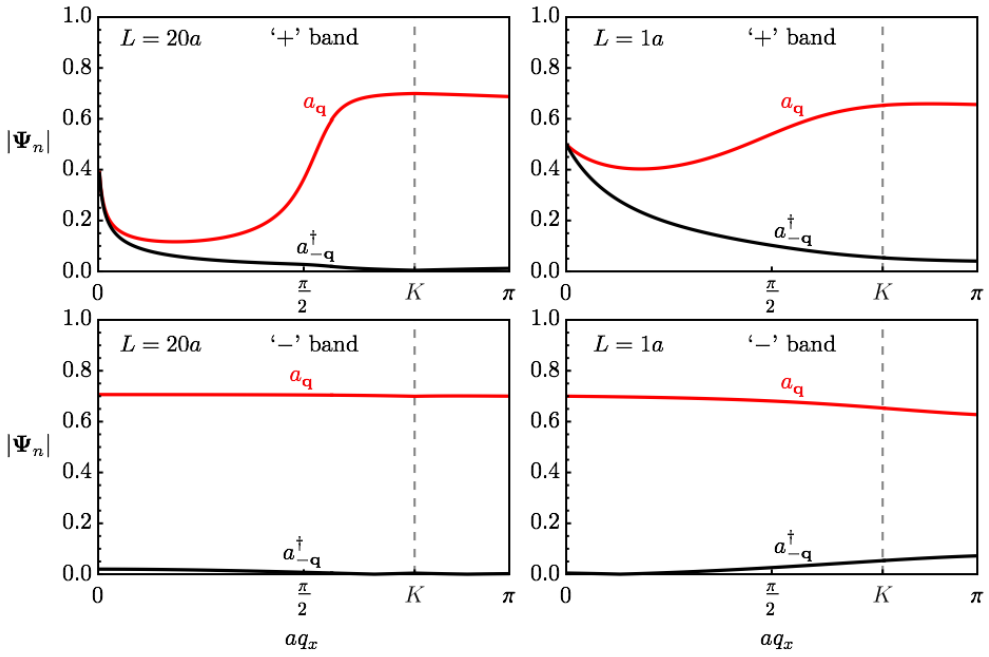


**Figure 5.6:** Comparison of resonant and non-resonant expansion coefficients $\mathbf{\Psi}_n$ of the Hopfield operator $\beta_{\mathbf{q}}$ (see equation 5.24) for the plasmonic operators $\mathbf{\Psi}_1 = a_{\mathbf{q}}$ and $\mathbf{\Psi}_2 = a^\dagger_{-\mathbf{q}}$. We plot these operators for both the upper (+) and lower (−) polariton bands which are degenerate at the $K$ point, and for two cavity heights as indicated in the figures. We observe that the non-resonant terms are significantly smaller than the resonant terms around the $K$ point. In the figure $c/\omega_0 a = 3/5$, $\epsilon_D = 1$ and $a = 3r$.

Thus, after calculation of $[S, H_1]$ we arrive at the Hamiltonian $\bar{H}$. In the full basis $\beta_{\mathbf{q}}$ the Hamiltonian is zero on the block off-diagonals, which allows us to separate the plasmonic and photonic subspaces. We can thus write the effective Hamiltonian of the plasmonic subspace in the basis $(a_{\mathbf{q}}, b_{\mathbf{q}})^T$ as

$$\bar{\mathcal{H}} = \hbar \begin{pmatrix} \omega_0 & \Omega f^*_{\mathbf{q}} \\ \Omega f_{\mathbf{q}} & \omega_0 \end{pmatrix} - \hbar\omega_0^2 \sum_n \sum_{s=\pm} s\xi^2_{\mathbf{q}n} \begin{pmatrix} \mathrm{Re}\left[\phi_n \chi^s_{\mathbf{q}n}\right] & \chi^s_{\mathbf{q}n}\phi^*_n \\ \chi^{s*}_{\mathbf{q}n}\phi_n & \mathrm{Re}\left[\phi_n \chi^s_{\mathbf{q}n}\right] \end{pmatrix}. \tag{5.45}$$

Except in extreme cases, such as when the light line passes near $\omega_0$ at the degeneracy point we can approximate $\chi^{\pm}_{\mathbf{q}n}$ in the regime $\Omega f_{\mathbf{q}} \ll \omega_0 \pm \omega_{\mathbf{q}n}$ as $\chi^{\pm}_{\mathbf{q}n} = (\omega \pm \omega_{\mathbf{q}n})^{-1}\phi^*_n$. In this case using the expression 5.14 for $\xi_{\mathbf{q}n}$ we can approximate the Hamiltonian 5.45 as

$$\bar{\mathcal{H}} = \mathcal{H}_0 - \mathcal{H}_\delta \tag{5.46}$$

where

$$\mathcal{H}_0 = \hbar \begin{pmatrix} \omega_0 & \Omega f_{\mathbf{q}}^* \\ \Omega f_{\mathbf{q}} & \omega_0 \end{pmatrix}, \tag{5.47}$$

is the Hamiltonian of the bare CPs as obtained previously in equation 4.44, and

$$\mathcal{H}_\delta = \hbar\omega_0\Delta \sum_n \delta_{\mathbf{q}n} \begin{pmatrix} 1 & (\phi_n^*)^2 \\ (\phi_n)^2 & 1 \end{pmatrix}, \tag{5.48}$$

provides corrections to the bare CP Hamiltonian $\mathcal{H}_0$ which are quadratic in the light-matter coupling parameter $\xi_{\mathbf{q}n}$. In equation 5.48

$$\Delta = \frac{8\pi}{3\sqrt{3}} \frac{\Omega}{\omega_0} \frac{a}{L}, \tag{5.49}$$

is a coupling constant dependent on the plasmon-plasmon coupling strength $\Omega$ and cavity height $L$, and $\delta_{\mathbf{q}n} = \omega_0^2/(\omega_{\mathbf{q}n}^2 - \omega_0^2)$. In the Hamiltonian 5.46 there is a wavevector dependent renormalisation of the natural frequency $\omega_0$, and the factors $\phi_n$ crucially modify the function $f_{\mathbf{q}}$ and introduce additional degeneracies in the bandstructure

$$\bar{\omega}_{\mathbf{q}}^\tau = \omega_0 \left(1 - \Delta \sum_n \delta_{\mathbf{q}n}\right) + \tau |\Omega f_{\mathbf{q}} - \omega_0 \Delta \sum_n \delta_{\mathbf{q}n} \phi_n^2|. \tag{5.50}$$

We will discuss the role of these degeneracies in the following section, where we investigate the transition at the critical cavity height $L_c$ in greater depth. However, before proceeding let us compare the dispersion of the SW and original Hamiltonian as shown in Figure 5.7. There is an excellent quantitative agreement before criticality $L > L_c$ throughout the majority of wavevector space. There is also a good qualitative agreement around the Dirac point after the critical cavity height $L < L_c$, though the quantitative agreement has diminished. It is inevitable that a second order expansion in the light-matter coupling decreases in accuracy as we increase the light-matter coupling parameter $\xi_{\mathbf{q}n}$ with decreasing cavity height. In addition whilst the non-resonant plasmonic operators are easily neglected at larger cavity heights $L > L_c$, their Hopfield expansion coefficients become appreciable (though still significantly small with respect to the resonant coefficients) at smaller cavity heights $L < L_c$, as we saw in Figure 5.6. Nonetheless the SW Hamiltonian still captures all the important qualitative effects.

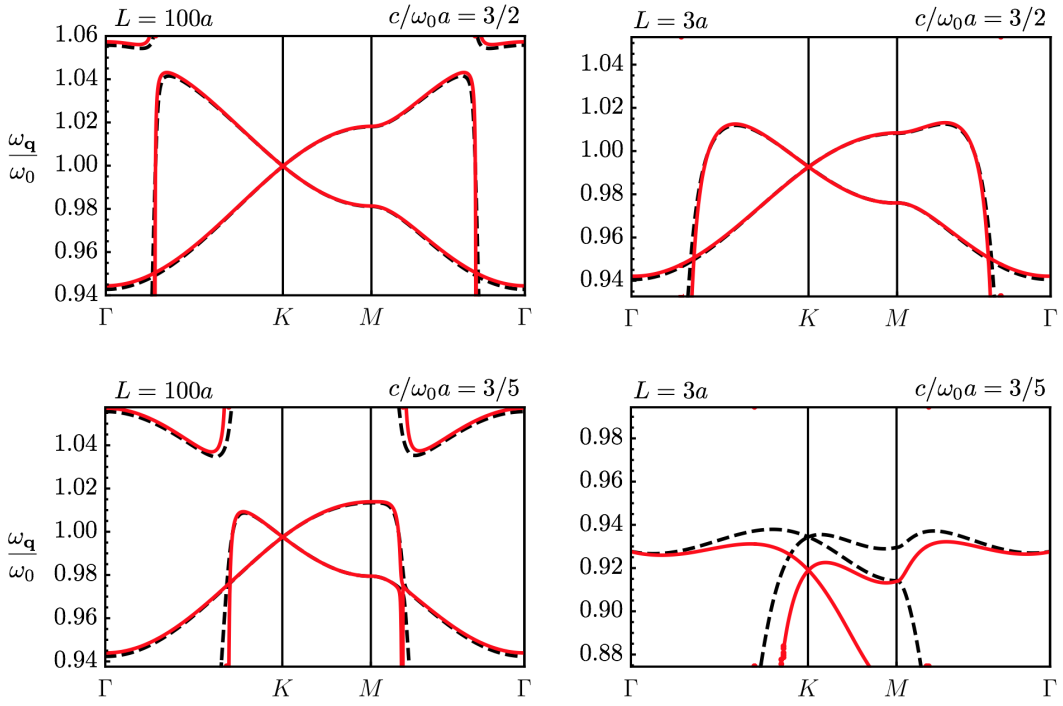


**Figure 5.7:** Comparison between the polariton dispersion of the 'full' Hamiltonian (black dashed lines corresponding to equation 5.23) and the SW Hamiltonian in the plasmonic subspace (red solid lines corresponding to equation 5.46). The left (right) plots are for a cavity height $100a$ ($3a$), and the top (bottom) plots are for a value of $c/\omega_0 a$ as 3/2 (3/5). In the figure $a = 3r$ and $\epsilon_\mathrm{D} = 1$.

### 5.2.2 Topological transition at critical cavity height

From the polariton dispersion in equation 5.50 we can see that the degeneracies occur when

$$|\Omega f_\mathbf{q} - \omega_0 \Delta \sum_n \delta_{\mathbf{q}n} \phi_n^2| = 0. \tag{5.51}$$

Equation 5.51 indicates that the CDPs at the $K(K')$ points that exist for the bare CP dispersion persist here. This can be verified by noting that at $K(K')$ the function $f_\mathbf{q}$ is zero (as we saw in chapter 4) and that the function $\delta_{\mathbf{q}n}$ is identical for photonic modes degenerate at the $K(K')$ points, and thus we have the sum $\sum_n \phi_n^2 = 0$. Equation 5.51 is satisfied at six other locations in the Brillouin zone, along the directions $\Gamma - K(K')$ where the functions $f_\mathbf{q}$ and $\sum_n \delta_{\mathbf{q}n}\phi_n^2$ are both real. These degeneracies, corresponding to SDPs, come in a pair of triplet SDPs where each triplet encircles a $K(K')$ point along the three directions $\Gamma - K(K')$ in the Brillouin zone. This situation is reminiscent of bilayer graphene [136, 137], in as much as there is a central degeneracy at $K(K')$ with

three satellite degeneracies encircling this point. However here, as we see in Figures 5.9(d-f), the SDPs are critically tilted such that the iso-frequency contours no longer form closed ellipses around these points. As discussed in section 3.1.4 a system with $\mathcal{IT}$ symmetry must have a Chern density that is a sum of Dirac delta functions that act as monopole sources of Berry flux. Referring to Figure 5.8 we see that the SDPs are such singularities in the Chern density and sources of Berry flux, and in this sense we can identify them as Dirac points.

In Figure 5.8 we show a schematic of the locations and trajectories of SDPs as the cavity height is decreased, obtained by solving equation 5.51. Before criticality each triplet of SDPs approaches a CDP along the direction $\Gamma - K(K')$, subsequently merges with the CDP when $L = L_c$, and then after criticality continues along the same trajectory (corresponding to the direction $K(K') - M$ in the Brillouin zone). Also in Figure 5.8 we show the topological charge of the Dirac points, corresponding to the number of clockwise rotations the pseudospin vector makes for a clockwise closed loop in the immediate vicinity of the Dirac point it encloses [138–140] (see Figure 5.9). The CDP at $K(K')$ has a topological charge of $+1(-1)$, surrounded by SDPs with a topological charge of $-1(+1)$. The merging of Dirac points for $L = L_c$ is not accompanied by their annihilation, as the SDPs and CDPs have distinct physical origins. As discussed earlier, the CDP arises from the two-dimensional bipartite lattice, and the time-reversal symmetric and parity invariant nature of the system [28]. Whereas the SDPs stem from the additional degeneracies in the polariton spectrum along those directions perpendicular to the nearest neighbour vectors $\mathbf{e}_j$, where the complete destructive interference between the sublattices in the asymmetric configuration leads to a vanishing light-matter interaction. However, after criticality eventually the SDPs that emerge from the $K$ point will annihilate with the SDPs of opposite topological charge that emerge from the $K'$ point.

Figures 5.9(a-c) show the evolution of the Berry curvature around the $K$ point for this transition from sub- to super-critical values of the cavity height. By observing the pseudospin vector field, which is equivalent to the unit vector of Berry curvature, we can verify the topological charge of the Dirac and hybrid points. The Dirac points act as vortices in the pseudospin vector field, as well as sources and drains of Berry curvature. For sub-critical values of the cavity height we observe that the pseudospin in the immediate vicinity of the CDP is $\mathbf{V}_\tau = -\tau\hat{\mathbf{k}}$, aligned parallel with the momentum $\mathbf{k}$

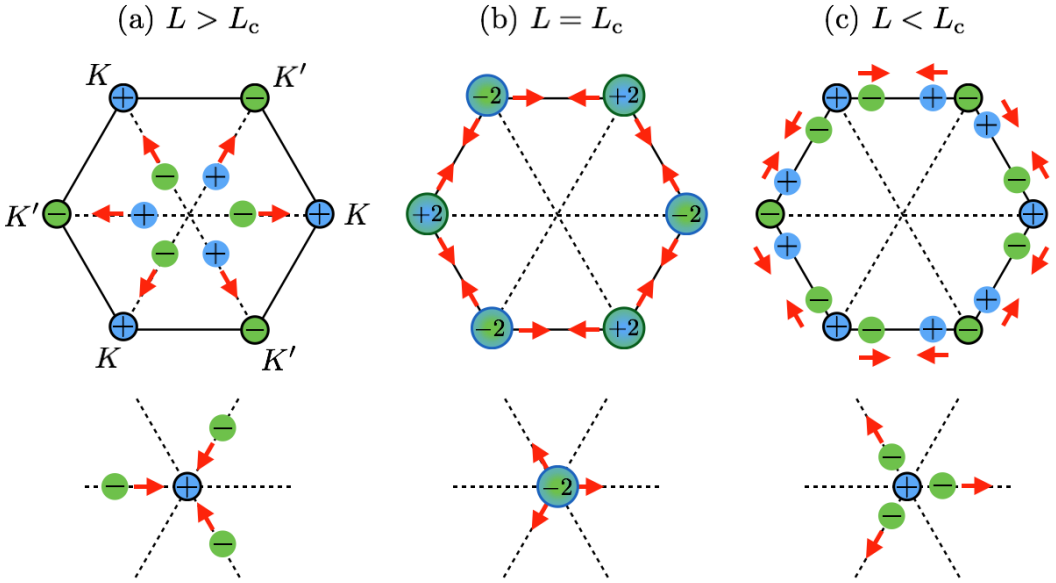


**Figure 5.8:** The location and trajectories (red arrows) of SDPs (coloured disks) shown in the Brillouin zone (top figures), and around the $K$ point in the extended zone scheme (bottom figures), as $L$ is decreased. For (a) $L > L_c$ the SDPs around the $K(K')$ point with topological charge -1(+1) approach the CDP with topological charge +1(-1) along the directions $\Gamma - K(K')$. At (b) $L = L_c$ the SDPs merge with the CDP at $K(K')$ and give rise to a hybrid point with topological charge -2(+2). Finally when (c) $L < L_c$ the SDPs reemerge along the same trajectory which corresponds to the direction $K(K')-M$ in the Brillouin zone. In the figure $c/\omega_0 a = 3/5$, $\epsilon = 1$ and $a = 3r$.

measured from **K** in the lower polariton band $\bar{\omega}_{\mathbf{q}}^{(-)}$, so undergoes one clockwise rotation for a clockwise loop around $K$. At criticality the SDPs have merged with the CDP giving rise to a hybrid point with a topological charge of -2 and thus, we see that the pseudospin rotates counter-clockwise twice as fast. After criticality the pseudospin again returns to a clockwise rotation, however we note that curiously the pseudospin is now aligned anti-parallel to **k** in the lower polariton band.

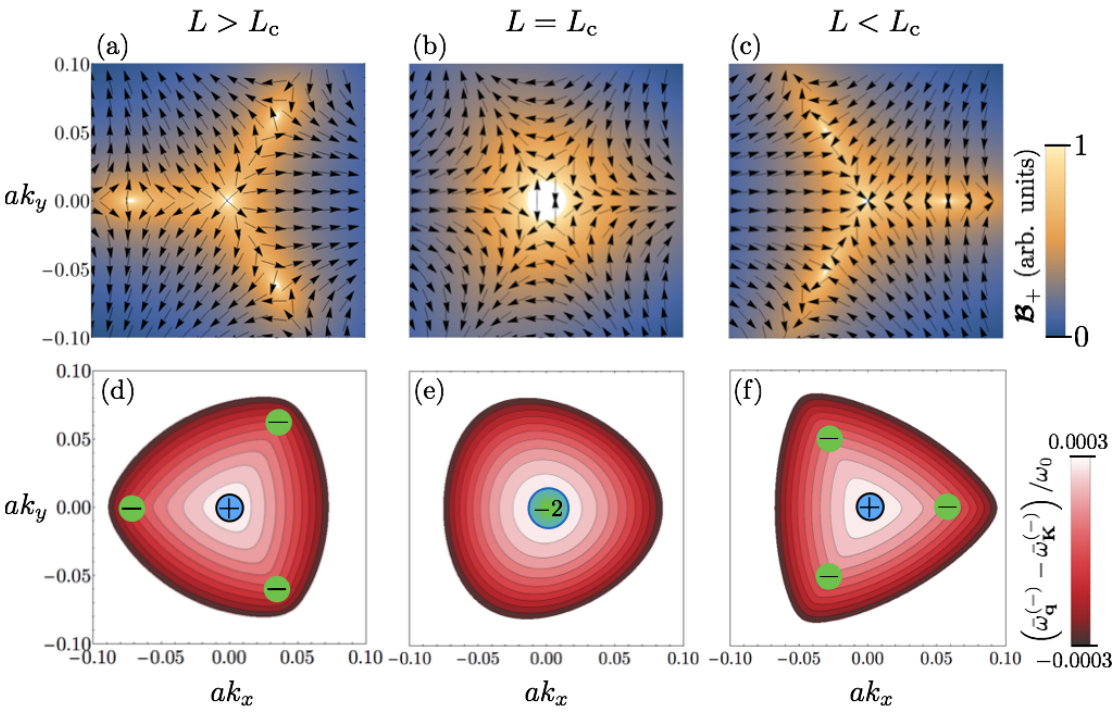


**Figure 5.9:** (a-c) Evolution of the magnitude (colour scale) and direction (black arrows) of the Berry curvature $\boldsymbol{\mathcal{B}}_{(-)}$ (see equation 3.30) around the $K$ point for the lower polariton band $\bar{\omega}^{(+)}_{\mathbf{q}}$ of equation 5.50 as we decrease the cavity height. (d-f) Isofrequency contours of the lower polariton band $\bar{\omega}^{(-)}_{\mathbf{q}}$ measured from the CDP frequency $\bar{\omega}^{(-)}_{\mathbf{K}}$, and the location in momentum space of the SDPs (green disks), CDP (blue disk) and hybrid point (multicoloured disk). We show the cavity height decreasing from being (a,d) sub-critical $L/a = 7.2$, to (b,e) critical $L/a \approx 6.9$, and (c,f) super-critical $L/a = 6.7$. Recall that the unit vector of the Berry curvature gives us the pseudospin vector $\mathbf{V}_{(-)}$ (see equation 3.32). Thus, from the plots we can visually verify the topological charge of the Dirac points by counting the number of clockwise rotations the pseudospin vector undergoes for a closed clockwise loop around the respective point. In the figure $c/\omega_0 a = 3/5$, $\epsilon = 1$ and $a = 3r$.

### 5.2.3 Second order expansion around the degeneracy point

To understand the origin of the 'flip' of the pseudospin direction, we wish to develop an effective Hamiltonian for the polaritons in the vicinity of the CDP. An expansion of the Hamiltonian 5.46 in $\mathbf{k} = \mathbf{q} - \mathbf{K}$ where $|\mathbf{k}| \ll |\mathbf{K}|$ requires us to include terms up to second order, as the linear terms vanish at criticality. In this approximation the Hamiltonian $\mathcal{H}_0$ of equation 5.47 reads

$$\mathcal{H}_0 = \hbar\omega_0 \begin{pmatrix} 1 & 0 \\ 0 & 1 \end{pmatrix} - \hbar v \begin{pmatrix} 0 & \hat{\pi}^* \\ \hat{\pi} & 1 \end{pmatrix} + \frac{\hbar a v}{4} \begin{pmatrix} 0 & (\hat{\pi})^2 \\ (\hat{\pi}^*)^2 & 0 \end{pmatrix} \tag{5.52}$$

where we have defined $\hat{\pi} = k_x + ik_y$. For the component $\mathcal{H}_\delta$ of the equation 5.48 we require the expansion of the function $\delta_{\mathbf{q}n}$ given by

$$\delta_{\mathbf{q}n} = \delta_{\mathbf{K}n} + \delta_{\mathbf{K}n,x}k_x + \delta_{\mathbf{K}n,y}k_y + \frac{1}{2}\left[\delta_{\mathbf{K}n,xx}k_x^2 + \delta_{\mathbf{K}n,yy}k_y^2 + 2\delta_{\mathbf{K}n,xy}k_xk_y\right], \tag{5.53}$$

with coefficients

$$\delta_{\mathbf{K}n,\alpha} = -2(c/\omega_0)^2\delta_{\mathbf{K}n}^2(\mathbf{K} - \mathbf{G}_n)_\alpha, \tag{5.54}$$

$$\delta_{\mathbf{K}n,\alpha\alpha} = 2(c/\omega_0)^2\delta_{\mathbf{K}n}^2\left[4(c/\omega_0)^2\delta_{\mathbf{K}n}(\mathbf{K} - \mathbf{G}_n)_\alpha^2 - 1\right], \tag{5.55}$$

$$\delta_{\mathbf{K}n,xy} = 8(c/\omega_0)^4\delta_{\mathbf{K}n}^3(\mathbf{K} - \mathbf{G}_n)_x(\mathbf{K} - \mathbf{G}_n)_y. \tag{5.56}$$

We can obtain an expression for this expanded Hamiltonian by exploiting its symmetries. For an arbitrary set of photonic modes degenerate at the $K$ point each of the factors $\delta_{\mathbf{K}n,\alpha}$, $\delta_{\mathbf{K}n,xy}$ and $\phi_n^2$ sum to zero, and $\mathcal{H}_\delta$ has the form

$$\mathcal{H}_\delta = \hbar\omega_0\delta_0\begin{pmatrix}1 & 0\\ 0 & 1\end{pmatrix} - \hbar v\delta_D\begin{pmatrix}0 & \hat{\pi}^*\\ \hat{\pi} & 0\end{pmatrix} + \frac{\hbar a v\delta_w}{4}\begin{pmatrix}0 & (\hat{\pi})^2\\ (\hat{\pi}^*)^2 & 0\end{pmatrix} - \hbar a^2\omega_0\delta_a\begin{pmatrix}|\hat{\pi}|^2 & 0\\ 0 & |\hat{\pi}|^2\end{pmatrix}. \tag{5.57}$$

The dominant photonic mode is $\mathbf{G}_0 = \mathbf{0}$ (and its rotations about $\mathbf{K}$). Truncating the sum to just this mode yields the explicit coefficients

$$\delta_0 = 3\Delta\delta_{\mathbf{K}}, \qquad \delta_D = 2\Delta|a\mathbf{K}|\frac{\omega_0}{\Omega}\left(\frac{c}{\omega_0 a}\right)^2\delta_{\mathbf{K}}^2, \tag{5.58}$$

$$\delta_w = 8\Delta|a\mathbf{K}|^2\frac{\omega_0}{\Omega}\left(\frac{c}{\omega_0 a}\right)^4\delta_{\mathbf{K}}^3, \qquad \delta_a = \Delta\left(\frac{c}{\omega_0 a}\right)^2\left[3 - 6|a\mathbf{K}|^2\left(\frac{c}{\omega_0 a}\right)^2\delta_{\mathbf{K}}\right]\delta_{\mathbf{K}}^2,$$

where $\delta_{\mathbf{K}} \equiv \delta_{\mathbf{K}0}$. From the expressions 5.58 we see that each of the terms in $\mathcal{H}_\delta$ provide corrections to the bare CP Hamiltonian $\mathcal{H}_0$ which are inversely proportional to the cavity

height $L$, due to the common factor $\Delta$ (see equation 5.49). Using equation 5.57 we can write the expansion of the full Hamiltonian 5.46 in the compact form

$$\bar{\mathcal{H}}/\hbar = \left(\tilde{\omega_0} + \tilde{\alpha}k^2\right)\mathbb{1} - \tilde{v}k\boldsymbol{\sigma}\cdot\hat{\mathbf{k}} + \tilde{\mu}k^2(\boldsymbol{\sigma}^*\cdot\hat{\mathbf{k}})^{\circ 2}, \tag{5.59}$$

where $k = |\mathbf{k}|$, $(\mathbf{X}^{\circ n})_{ij} \equiv (\mathbf{X}_{ij})^n$, and the corresponding dispersion is

$$\bar{\omega}^{\tau}_{\mathbf{k}} = \tilde{\omega}_0 + \tilde{\alpha}k^2 + \tau|\tilde{\mu}k^2 \mathrm{e}^{-i3\phi_{\mathbf{k}}} - \tilde{v}k|. \tag{5.60}$$

The coefficients $\tilde{\omega_0} = \omega_0(1-\delta_0)$, $\tilde{\alpha} = a^2\omega_0\delta_a$, $\tilde{v} = v(1-\delta_D)$ and $\tilde{\mu} = (av/4)(1-\delta_w)$ all decrease with cavity height as shown in Figure 5.10. The CDP redshifts with frequency $\tilde{\omega}_0 < \omega_0$. The term $\tilde{\alpha}k^2$ is always negative and provides another (wavevector dependent) redshift of the individual bands, and an asymmetry between them. The term weighted by $\tilde{\mu}$ creates a trigonal warping of the Dirac cones. For cavity heights close to $L = L_{\mathrm{c}}$ the terms $\tilde{\alpha}$ and $\tilde{\mu}$ are significant with respect to $\tilde{v}$ and thus, the Dirac cones are highly asymmetric and warped. In fact we see that the group velocity $\tilde{v}$ of Dirac modes can be tuned from positive to negative values, and at the critical cavity height the polaritons morph from massless Dirac polaritons into massive Dirac polaritons with an effective mass $M^*_\tau = \hbar^2/2(\tilde{\alpha} + \tau|\tilde{\mu}|)$. As discussed before, the merging of the SDPs with the CDP coincides with a vanishing group velocity around the $K$ point. Thus, from the Hamiltonian 5.59 we can obtain a simple expression for the critical cavity height, given by

$$\delta_D(L_{\mathrm{c}}) = 1. \tag{5.61}$$

We can now verify the transition of the topological charge of the $K$ point at criticality, as a Hamiltonian of the form $k^n(\boldsymbol{\sigma}\cdot\hat{\mathbf{k}})^{\circ n}$ (and its conjugate) corresponds to a degeneracy at $\mathbf{k} = 0$ with topological charge $n$ $(-n)$ [139, 140]. Thus, to leading order in $\mathbf{k}$, before and after criticality the Hamiltonian 5.59 is proportional to $k(\boldsymbol{\sigma}\cdot\hat{\mathbf{k}})$ and the topological charge at $K$ is $+1$. Whereas when $L = L_{\mathrm{c}}$ the terms linear in $\mathbf{k}$ vanish and the Hamiltonian is proportional to $k^2(\boldsymbol{\sigma}^*\cdot\hat{\mathbf{k}})^{\circ 2}$, and so the $K$ point has a topological charge of $-2$.

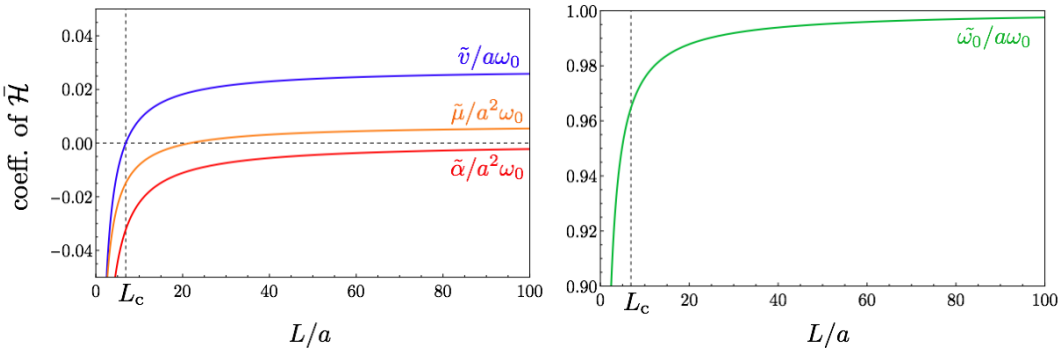


**Figure 5.10:** The two plots show the dependence of the coefficients of the Hamiltonian 5.59 on the cavity height $L$, as indicated in the figures. The CDP redshifts with the frequency $\tilde{\omega_0}$. At the critical cavity height $L_c$ the group velocity $\tilde{v}$ vanishes and the Hamiltonian contains only terms second order in $\mathbf{k}$. For cavity heights close to criticality the terms $\tilde{\alpha}$ and $\tilde{\mu}$, which are responsible for the asymmetry and trigonal warping of the bands respectively, are significant with respect to $\tilde{v}$ and thus the Dirac cones are highly asymmetric and warped. In the figure $c/\omega_0 a = 3/5$, $\epsilon = 1$ and $a = 3r$.

The approximate Hamiltonian also helps to unveil an intriguing phenomena that we alluded to earlier. For sub- and super-critical values of $L$ we can approximate the Hamiltonian to first order in $\mathbf{k}$. Thus, the eigenstates $|\psi^\tau_{\mathbf{k}}\rangle = \left(1, -\tau\mathrm{sgn}(\tilde{v})\mathrm{e}^{i\phi_{\mathbf{k}}}\right)^T$ of equation 5.59 can be described by the dimensionless Hamiltonian

$$\bar{\mathcal{H}} = -\mathrm{sgn}(\tilde{v})\boldsymbol{\sigma}\cdot\hat{\mathbf{k}}, \tag{5.62}$$

and so the pseudospin (see equation 3.32) reads

$$\mathbf{V}_\tau = -\tau\mathrm{sgn}(\tilde{v})\hat{\mathbf{k}}. \tag{5.63}$$

The group velocity $\tilde{v}$ of the Dirac modes changes sign at the critical cavity height, as we see in Figure 5.10. Thus, the parameter $\mathrm{sgn}(\tilde{v})$ drives a topological transition at criticality, 'flipping' the orientation of the pseudospin field. The flipped pseudospins coincide with an inversion of chirality (see equation 3.50)

$$\eta^\tau = \langle\psi^\tau_{\mathbf{k}}|\boldsymbol{\sigma}\cdot\hat{\mathbf{k}}|\psi^\tau_{\mathbf{k}}\rangle = -\tau\mathrm{sgn}(\tilde{v}). \tag{5.64}$$

This remarkable phenomena has no analogue in real or artificial graphene. To summarise the key results of this section, in Figure 5.11 we plot schematics of the dispersion 5.60 to

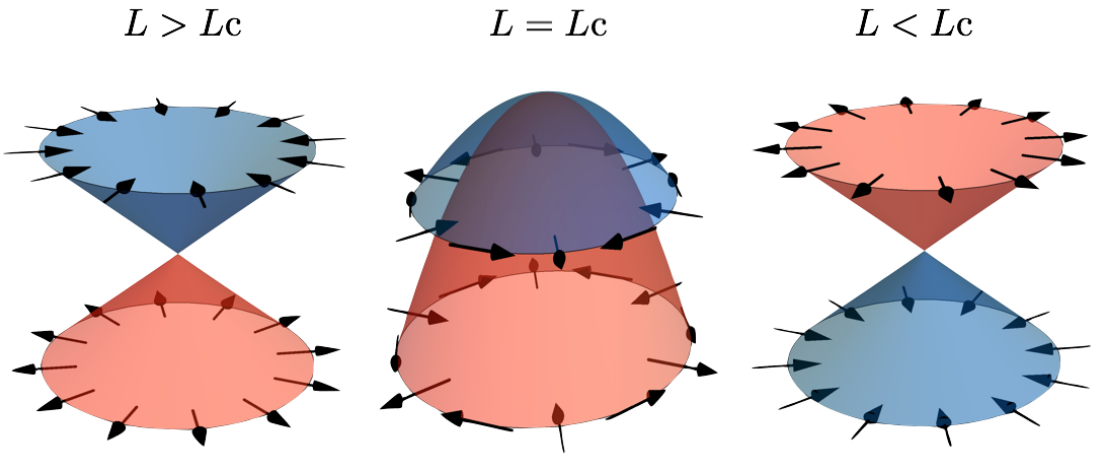


**Figure 5.11:** Schematics of the dispersion 5.60 to leading order in $\mathbf{k}$, and the corresponding pseudospin vectors (black arrows), for decreasing cavity height as indicated in the figure. The colour of the bands indicate whether the chirality is $+1$ (red) or $-1$ (blue). We clearly see that by transitioning through the critical cavity height the chirality of the bands is inverted and the pseudospin orientations are flipped.

leading order in $\mathbf{k}$, as well as the pseudospins and the chirality of the bands as indicated by their colour. Here we clearly see the topological transition driven by the sign of the group velocity. For $L > L_c$ the CDP has a topological charge of $+1$ and the massless Dirac polaritons in the upper band have a chirality $-1$ and a pseudospin $\mathbf{V}_+ = -\hat{\mathbf{k}}$ anti-aligned with the wavevector. At $L = L_c$ the quasiparticles morph into massive Dirac polaritons with a a pseudospin $\mathbf{V}_+ = (\cos 2\phi_{\mathbf{k}}, -\sin 2\phi_{\mathbf{k}})$ that rotates twice as fast around the hybrid Dirac point with a topological charge of $-2$. For $L < L_c$ the massive Dirac polaritons morph once again into massless Dirac polaritons, however they now have a chirality $+1$ and a pseudospin $\mathbf{V}_+ = +\hat{\mathbf{k}}$ that is aligned with the wavevector.

It is well known that the chiral nature of Dirac quasiparticles is responsible for many of their remarkable properties, such as the Berry phase of $\pi$, the suppression of backscattering off smooth inhomogeneities, and the Klein tunnelling phenomenon observed in real graphene [114, 116]. Here we have shown the existence of Dirac polaritons with a remarkable tunability. The renormalisation of the CDP frequency allows the exploration of conventional Klein tunnelling through regions of different cavity heights that are both sub- or super-critical, for Dirac quasiparticles with group velocities which can be tuned by orders of magnitude. This could be exploited in tunable polaritonic lenses with an effective negative refractive index and enable the realisation of Veselago lensing [141], whereby a polaritonic wave packet emitted from a point source would refocus upon transmission through such a junction. There are also exciting questions to address on

the nature of unconventional tunnelling phenomena through regions that are either side of criticality, as the inversion of chirality removes the conventional transmission channel for Dirac modes. For a smooth interface this could lead to the localisation of massless Dirac quasiparticles, as within the vicinity of the CDP there would be no states within which to transmit or reflect. Instead, this could produce a mechanism which scatters particles from within the Dirac cone to photon-like states close to the light cone, and vice versa. We emphasise that the inversion of chirality and these predicted phenomena are driven by the coupling strength to the photonic environment which preserves the symmetries of the nanoparticle array. So in addition one could combine the more conventional methods of modifying Dirac quasiparticles via their underlying symmetries with the effects induced by the cavity. For example the cavity height could be used as a parameter to tune the pseudomagnetic field and Landau Level spectrum of Dirac polaritons induced by deformations of the lattice [123].

## 5.3 Summary

A modification of the fundamental properties of Dirac quasiparticles typically involves altering the underlying symmetries of the system. This scenario was explored in chapter 4 were it was seen that breaking the inversion symmetry leads to massive Dirac plasmons with an energy dependent Berry phase, and breaking the rotational symmetry of the lattice can result in the annihilation of Dirac points. However, in this chapter we have examined an intrinsically different phenomenon, whereby we are able to drastically alter the properties of Dirac quasiparticles whilst maintaining the underlying symmetries.

Specifically we have analysed the band structure and eigenmodes of plasmon polaritons that arise from the interaction of plasmonic and photonic excitations of a honeycomb array of metallic nanoparticles embedded in an optical cavity. As with the bare collective plasmons we find a conventional Dirac point at the $K(K')$ point, characterised by a topological charge of $+1(-1)$. The polariton spectrum shows large anticrossings at the points where the dispersion of the TEM cavity mode crosses the optically bright upper CP band of the symmetric lattice configuration. This anticrossing varies with the light-matter coupling strength via the cavity height, which provides us with a highly tunable spectrum. In addition there are small anticrossings with the optically dark lower polariton band. In fact along the directions $\Gamma - K(K')$, which are orthogonal to the

nearest neighbour vectors $\mathbf{e}_j$, the light-matter interaction completely vanishes and leads to an additional triplet of satellite Dirac points that encircle the $K(K')$ point with a topological charge of $-1(+1)$.

By tuning the light-matter coupling strength we are able to induce a topological transition. As we decrease the cavity height, the group velocity of Dirac modes around $K$ can be tuned by orders of magnitude, and the SDPs approach the CDP along the directions $\Gamma - K(K')$. At the critical cavity height where the group velocity vanishes, the SDPs merge with the CDP to form a hybrid point with a topological charge of $-2(+2)$ and the massless Dirac polaritons morph into massive Dirac polaritons. Subsequently the SDPs reemerge along the direction $K(K') - M$ and the quasiparticles once again morph into massless Dirac polaritons. However, the chirality of the bands is inverted and the pseudospin orientations are flipped.

The incredible tunability of the Dirac polaritons and the effect of chirality inversion, a phenomenon which has no analogue in real or artificial graphene systems, could open up a wealth of novel Dirac physics. For example, the inversion of chirality removes the transmission channel from conventional Klein tunnelling and could lead to the localisation of massless Dirac particles, or act as a mechanism to scatter from within the Dirac cone to photon-like states near the light cone.

# Chapter 6

# Dirac plasmons in a pseudo-magnetic field

This chapter provides preliminary results on the investigation of strain-induced gauge fields for CPs in a honeycomb array of metallic nanoparticles. We will demonstrate the ability to generate a non-zero pseudo-magnetic field by application of a designed strain. Moreover, we will see that the magnitude and sign of the field can be tuned by the polarisation of the LSPs.

## 6.1 Modification of model due to strain

The essence of the physical properties of collective plasmons is encoded in the function $f_{\mathbf{q}}$ of equation 4.33, a sum of three geometrical phase factors associated with the three nearest neighbours, weighted by the polarisation-dependent function $\mathcal{C}_j$. Let us write it in a form that is more generalisable to the investigations of this chapter:

$$f_{\mathbf{q}} = \sum_{\mathbf{e}} \mathcal{C}_{\mathbf{e}} \exp(i\mathbf{q} \cdot \mathbf{e}), \tag{6.1}$$

where $\mathbf{e} \in \{\mathbf{e}_1, \mathbf{e}_2, \mathbf{e}_3\}$. In our new formulation the dependence of the interaction strength on interparticle separation is explicitly absorbed into the function

$$\mathcal{C}_{\mathbf{e}} = \frac{1 - 3(\hat{\mathbf{p}} \cdot \hat{\mathbf{e}})^2}{(|\mathbf{e}|/a)^3}. \tag{6.2}$$

Considering in-plane deformations only, to lowest order in the strain $\mathbf{u} = (u_x, u_y)$ the nearest neighbours are transformed to $\mathbf{e} \to \mathbf{e}'$ where, as we saw in section 3.4, the coordinates and lengths of $\mathbf{e}'$ are given by [122]

$$e'_\alpha = \left(\delta_{\alpha\beta} + \frac{\partial u_\alpha}{\partial x_\beta}\right) e_\beta, \qquad |\mathbf{e}'|^2 = |\mathbf{e}|^2 + 2u_{\alpha\beta} e_\alpha e_\beta, \tag{6.3}$$

where the strain tensor is

$$u_{\alpha\beta} = \frac{1}{2}\left(\frac{\partial u_\alpha}{\partial \beta} + \frac{\partial u_\beta}{\partial \alpha}\right), \tag{6.4}$$

and Einstein summation is implied over the coordinates $\alpha, \beta \in \{x, y\}$. Consider first the case of a homogeneous strain, so that there is translational invariance and we can readily repeat the quantisation procedure of previous chapters. In this case all modifications to the Hamiltonian are captured by the substitution [121, 142, 143]

$$f_{\mathbf{q}} \to f'_{\mathbf{q}} = \sum_{\mathbf{e}'} \mathcal{C}_{\mathbf{e}'} \exp(i\mathbf{q} \cdot \mathbf{e}'). \tag{6.5}$$

The interaction parameter $\mathcal{C}_{\mathbf{e}'}$ now contains the denominator $(|\mathbf{e}'|/a)^3$ and in general we have broken the rotational symmetry of the system. Expanding $f'_{\mathbf{q}}$ and retaining only those terms which are first-order in the components of the strain tensor gives $f'_{\mathbf{q}} = f_{\mathbf{q}} + L_{\mathbf{q}} + P_{\mathbf{q}} + G_{\mathbf{q}}$ where

$$\begin{cases} L_{\mathbf{q}} = & -3\sum_{\mathbf{e}} \mathcal{C}_{\mathbf{e}} u_{\alpha\beta} \hat{e}_\alpha \hat{e}_\beta \exp(i\mathbf{q} \cdot \mathbf{e}) \\ P_{\mathbf{q}} = & 6\sum_{\mathbf{e}} \hat{\mathbf{p}} \cdot \hat{\mathbf{e}} \left[u_{\alpha\beta} \hat{e}_\alpha \hat{e}_\beta \hat{\mathbf{p}} \cdot \hat{\mathbf{e}} - (\hat{\mathbf{e}} \cdot \nabla)\hat{\mathbf{p}} \cdot \mathbf{u}\right] \exp(i\mathbf{q} \cdot \mathbf{e}) \\ G_{\mathbf{q}} = & i\sum_{\mathbf{e}} \mathcal{C}_{\mathbf{e}} (\mathbf{e} \cdot \nabla)\mathbf{q} \cdot \mathbf{u} \exp(i\mathbf{q} \cdot \mathbf{e}) \end{cases} \tag{6.6}$$

We see there are three contributions to the additional terms in $f'_{\mathbf{q}}$ that arise from physically distinct effects. Changes in nearest-neighbour lengths modify the denominator

of $\mathcal{C}$ and as such $L_{\mathbf{q}}$ captures effects due to different interparticle separations. $P_{\mathbf{q}}$ contains those terms which are parametrised by the dipole orientation, originating from the expanded numerator of $\mathcal{C}$. The exponent of $f'_{\mathbf{q}}$ provides the contribution $G_{\mathbf{q}}$ which is just a geometrical term that enters the gauge field as a total derivative and so can be eliminated by a gauge transformation.

To investigate the low-energy Hamiltonian we expand $f'_{\mathbf{q}}$ around an arbitrary Dirac point $\mathbf{K}_D$ and retain only those terms linear in both the components of the strain tensor and wavevector. Thus, $f'_{\mathbf{k}} = f_{\mathbf{k}} + L_{\mathbf{k}} + P_{\mathbf{k}}$ where

$$\begin{cases} f_{\mathbf{k}} = & i\sum_{\mathbf{e}} \mathcal{C}\mathbf{k}\cdot\mathbf{e}\exp(i\mathbf{K}_D\cdot\mathbf{e}) \\ L_{\mathbf{k}} = & -3\sum_{\mathbf{e}} \mathcal{C}u_{\alpha\beta}\hat{e}_\alpha\hat{e}_\beta\exp(i\mathbf{K}_D\cdot\mathbf{e}) \\ P_{\mathbf{k}} = & 6\sum_{\mathbf{e}} \hat{\mathbf{p}}\cdot\hat{\mathbf{e}}\,[u_{\alpha\beta}\hat{e}_\alpha\hat{e}_\beta\hat{\mathbf{p}}\cdot\hat{\mathbf{e}} - (\hat{\mathbf{e}}\cdot\nabla)\hat{\mathbf{p}}\cdot\mathbf{u}]\exp(i\mathbf{K}_D\cdot\mathbf{e}) \end{cases} \tag{6.7}$$

In fact we can extend this model to the case of an inhomogeneous strain without modification [123, 144, 145]. This is because the expressions 6.7 contain all linear terms expected from symmetry analysis that enter as a gauge-field correction to the Hamiltonian [27], and the effects of inhomogeneity enter into higher order terms not considered [146].

We can now calculate the gauge field for any particular dipole orientation of interest. A natural starting point is the graphene-like orientation $\theta = 0$ as seen previously, with dipoles orientated normal to the plane.

### 6.1.1 Graphene-like case

As explored in detail in chapter 4, CPs in the honeycomb array of nanoparticles behave in much the same way as electrons in graphene, though with an additional degree of freedom originating from the tunability of the dipole moment polarisation of the LSPs. We now explore the strain-modified Hamiltonian for the graphene-like orientation $(\theta, \phi) = (0, 0)$. As this polarisation corresponds to a system with exactly the same symmetries as graphene, we know from group theoretical approaches that an invariant expansion of the Hamiltonian near the $K$ point under the application of strain will generate an additional term from the substitutions [27]

$$k_x \to k_x + \alpha(u_{yy} - u_{xx}) \qquad\qquad k_y \to k_y + 2\alpha u_{xy}, \tag{6.8}$$

where $\alpha$ is a coupling constant. Indeed, upon calculating the components of $f'_{\mathbf{q}}$ in equation 6.7 we find that the term $P_{\mathbf{k}} = 0$ and

$$L_{\mathbf{k}} = \frac{9}{4}(u_{xx} - u_{yy} \mp i2u_{xy}). \tag{6.9}$$

Note that in contrast to the strain-independent term $f_{\mathbf{k}} = -(3a/2)(\pm k_x + ik_y)$, the valley index $\tau = \pm$ operates on the real part of $f_{\mathbf{k}}$ but on the imaginary component of $L_{\mathbf{k}}$. It will be seen that this leads to the gauge field having an opposite sign in each of the two valleys, as required by the time-reversal invariance. Thus, in the conventional bases ($\hat{\Psi}^{(+)} = (a_{\mathbf{q}}, b_{\mathbf{q}})$ and $\hat{\Psi}^{(+)} = (b_{\mathbf{q}}, a_{\mathbf{q}})$) the effective Hamiltonian is

$$\mathcal{H}^{\text{eff}}_{\mathbf{k},\tau} = \hbar\omega_0 \mathbf{1} - \tau v \boldsymbol{\sigma} \cdot (\mathbf{p} + e\tau \mathbf{A}), \tag{6.10}$$

where the gauge field is

$$\mathbf{A} = -\frac{3\hbar}{2ae} \begin{pmatrix} u_{xx} - u_{yy} \\ -2u_{xy} \end{pmatrix}. \tag{6.11}$$

Aside from a global energy shift and a different constant multiplying the gauge field, one can immediately identify the effective Hamiltonian 6.10 as the direct analogue of that of strained graphene [123]. From the gauge field it is natural to define a pseudo-magnetic field $B_S = \partial_x A_y - \partial_y A_x$. To generate a non-zero $B_S$ we implement a strain profile with trigonal symmetry given by

$$\mathbf{u} = C(2xy, x^2 - y^2), \tag{6.12}$$

where $C$ is a constant, leading to a spatially uniform pseudo-magnetic field

$$B_S = \frac{12\hbar C}{ae}. \tag{6.13}$$

To specify $C$ we choose the same parameters as reference [123] where they consider a disk of diameter $D = 700a$ and a maximum strain $S_m = 0.1$ at its perimeter, which gives $C = S_m/D$. The largest energy gap between Landau levels with index 0 and 1 is then

$$\frac{\Delta_{\mathrm{LL}}}{\hbar\Omega} = 3\left(\frac{6S_m}{D/a}\right)^{1/2}, \tag{6.14}$$

with a numerical value of approximately 0.1 for this choice of parameters. The energy $\hbar\Omega$ corresponds to the bandwidth of the dispersion in the absence of strain which is approximately conical. Thus, we see that it is possible to produce an appreciable LL energy gap within this bandwidth for a realistic choice of system parameters, and of course these can be easily modified.

### 6.1.2 Arbitrary polarisation

For a general polarisation with $\theta \neq 0$ the gauge field is not restricted by symmetry to the substitutions 6.8 and can consist of a more arbitrary mix of strain tensor components. In general the Hamiltonian in the $K$ valley will be of the form

$$H_{\mathbf{k}} = \hbar\omega_0 \mathbb{1} + v\eta_\alpha \sigma_\alpha (p_\alpha + eA_\alpha). \tag{6.15}$$

The factors $\eta_\alpha$ depend on the polarisation, and also parametrise the eccentricity of the Dirac cone in the absence of strain (e.g. when $\theta = 0$ as in the previous section $\eta_x = \eta_y = 1$).

As an example we consider the polarisation $(\theta, \phi) = (\pi/2, \pi/2)$. In this case $\boldsymbol{\eta} = (\sqrt{7}/2, -1)$ and

$$\mathbf{A} = \frac{3\hbar}{20\sqrt{7}ae}\begin{pmatrix} 12(u_{xx} - u_{yy}) \\ -7(3\partial_y u_x + 11\partial_x u_y) \end{pmatrix}, \tag{6.16}$$

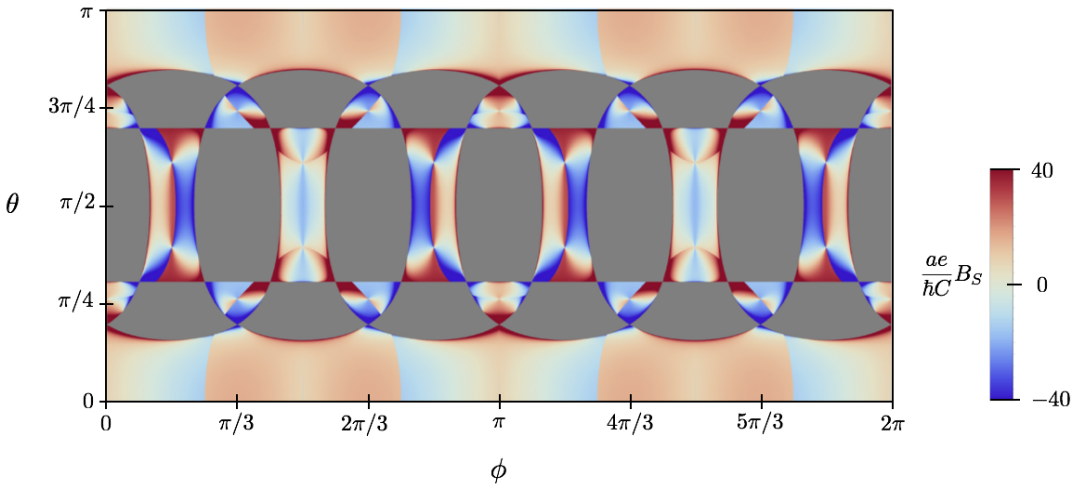


**Figure 6.1:** A plot of the pseudomagnetic field $B_S = \partial_x A_y - \partial_y A_x$ (colour scale) calculated from the Hamiltonian 6.15 obtained for an arbitrary polarisation and a strain $\mathbf{u} = C(2xy, x^2 - y^2)$. As the polarisation approaches a gapped region (grey regions) the field diverges due to the break down of the model as we approach a regime characterised by the merging of Dirac points, thus the colour scale is restricted to the range indicated in the figure.

which, for the strain profile $\mathbf{u} = C(2xy, x^2 - y^2)$ considered previously, leads to a pseudo-magnetic field

$$B_S = -\frac{183}{5\sqrt{7}}\frac{\hbar C}{ae}. \tag{6.17}$$

Comparing to the value of $B_S$ for $\theta = 0$ (equation 6.13) we see that not only is the magnitude of the field different, it is negative. In Figure 6.1 we plot a phase diagram for the values of $B_S$ as a function of polarisation $\hat{\mathbf{p}}$, obtained with the strain profile in equation 6.12, where we see a wide tunability in the field strength that is distributed in an intricate and periodic pattern.

## 6.2 Summary

In this chapter we introduced the foundations for treating strain induced gauge fields of CPs in a honeycomb array of metallic nanoparticles. We saw that for an arbitrary polarisation of the dipole moments associated with the LSPs the gauge field is not restricted by symmetry to the form $\mathbf{A} \propto (u_{yy} - u_{xx}, 2u_{xy})$, and can take on a more general combination of strain tensor components. For a strain $\mathbf{u} = C(2xy, x^2 - y^2)$

with trigonal symmetry the pseudomagnetic field $B_S$ is uniform, it depends on the polarisation, and can be tuned from positive to negative values. This could be used to design materials with a unique polarisation anisotropy, whereby not only would EM radiation of different polarisations couple to CP modes with different dispersions, but it could also experience pseudomagnetic fields of different signs. As a first step in extending this work, it could be insightful to explore different strain fields to determine whether there are configurations more experimentally realisable than trigonal strain which would produce non vanishing pseudomagnetic fields for some of the polarisations.

# Chapter 7

# Conclusion

The appeal of metamaterials is the freedom to precisely tailor the physical properties, through a fastidious selection of constituents and their geometrical arrangement. In this thesis we wished to explore novel optical properties by choice of a plasmonic metamaterial with a lattice structure that would offer such a possibility. As arrays of metallic nanoparticles are artificial materials we could have investigated any geometry imaginable; however sometimes mother nature knows best. The decision to study a honeycomb structured array of metallic nanoparticles was motivated firstly by the remarkable electronic properties of graphene, but most importantly the fact that these phenomena are due to the symmetries of the system and the honeycomb lattice, rather than any particularities of the constituents or charge carriers.

In chapter 4 we studied the purely plasmonic response of this artificial graphene system. We examined the spectrum of the collective plasmonic modes that arise from the near-field dipolar coupling between localised surface plasmons in each individual nanoparticle. This revealed a substantial tunability granted by the polarisation degree of freedom associated with the dipole orientation of the LSPs, with dispersions as varied as flat bands, translationally invariant gapped modes and a spectrum analogous to graphene. More generally we discovered a rich phase diagram as a function of the polarisation, with gapped and gapless modes, and demonstrated that every gapless phase — including those topologically disconnected from the graphene-like phase — supports collective plasmons that are effectively described by a massless Dirac Hamiltonian. The gapped phases are also of interest, particularly as they emanate from the merging and annihilation of Dirac

points as the polarisation is progressively tilted. This situation is reminiscent of Dirac point merging in real graphene under extreme elastic strain.

We also explored the properties of bipartite arrays of metallic nanoparticles beyond the artificial graphene plasmonic lattice. First we broke the inversion symmetry upon envisaging a honeycomb array comprised of inequivalent sublattices with different resonance frequencies. In this case we found that the system supports gapped chiral Dirac plasmons with an energy dependent Berry phase. Subsequently we broke the three-fold rotational symmetry and explored generic bipartite hexagonal lattices obtained by rigidly shifting one sublattice with respect to the other. Here the system still supports massless chiral modes but with a modified distribution of gapped and gapless modes in the phase diagram, as well as an altered — at times even topologically inequivalent — band structure for each polarisation. The topology of the phase diagram itself changes as one progressively shifts a sublattice away from the original honeycomb position; even for a variation in the nearest-neighbour lengths of a few percent there is a significant bulging in the phase diagram, followed by a series of topological phase transitions that split and annihilate gapless Dirac phases.

In chapter 6 we explored the effects of strain on our nanoplasmonic metamaterial. Similarly to real graphene, a strain that distorts the nanoparticle array induces a gauge field in the Hamiltonian that formally resembles a magnetic vector potential and generates a pseudomagnetic field. The magnitude and even sign of this field depends on the polarisation of the dipole moments. In addition, for an arbitrary polarisation the gauge field is not restricted to the form $\mathbf{A} \propto (u_{yy} - u_{xx}, 2u_{xy})$, as it is for real graphene and for $\theta = 0$ in the nanoparticle array, and instead can consist of a more arbitrary combination of strain tensor components. This could have interesting implications in the design of metamaterials with a unique polarisation anisotropy, whereby EM radiation of different polarisations would couple to CP modes that experience pseudomagnetic fields of different magnitudes and signs.

In summary, the analysis of chapters 4 and 6 revealed the strong analogies between the plasmonic modes of a honeycomb array of metallic nanoparticles and the electronic properties of graphene, as well as the existence of a wide class of bipartite hexagonal lattices that exhibit massless chiral Dirac modes, all of which are highly tunable from the polarisation of the dipoles. Our considerations will be important in the design of

plasmonic metamaterials that guide electromagnetic radiation via chiral modes with precisely designed features.

The mantra of metamaterials is 'function from form' [147]. However, chapter 5 exemplified that it is not sufficient to consider the form of the matter field alone when predicting even just the general optical features of a metamaterial. In fact the nature of the photonic environment and the light-matter coupling can have a significant qualitative impact. Having thoroughly examined the plasmonic modes in the preceding chapter, we then wished to address their interaction with a photonic environment, and investigate the true eigenmodes of the light-matter system. To accomplish this we developed a full analytical quantum theory of the strong coupling regime between the collective plasmons in a honeycomb array of metallic nanoparticles, and the fundamental photonic mode of an enclosing optical cavity. We identified that the polaritonic spectrum, like its purely plasmonic counterpart, persists in being characterised by the presence of massless chiral Dirac modes. The associated Dirac point is completely robust, despite an energy renormalisation the $K(K')$ point remains degenerate for any strength of the light-matter coupling and fixed in momentum space.

The conventional Dirac point at $K(K')$ arises because of the symmetries of the honeycomb lattice. However, the photonic environment generates three additional satellite Dirac points around each CDP, along the directions $\Gamma - K(K')$ where the light-matter interaction between the cavity photons and dark CP modes vanishes. By modulating the light-matter coupling strength via the cavity height we unveiled a phenomenal tunability of the Dirac polaritons. In particular, as the cavity height is decreased we observed an order-of-magnitude renormalisation of the group velocity around $K(K')$, a red-shift of the Dirac point frequency, and the approach of the SDPs towards the CDP. At the critical cavity height $L_c$ the SDPs merge with the CDP and subsequently reemerge along the directions $K(K') - M$. The CDP and SDPs around the $K(K')$ point have a topological charge of $+1(-1)$ and $-1(+1)$ respectively, however they do not annihilate at the critical cavity height due to their distinct physical origins. Instead the transition is accompanied by the morphing of massless Dirac polaritons around $K(K')$ into massive Dirac polaritons at the critical cavity height, and then back into massless Dirac polaritons as the cavity height is decreased further. Crucially after criticality the chirality of the Dirac modes is inverted and the pseudospin orientations are flipped. The inversion

of chirality is a phenomenon which has no analogue in real or artificial graphene systems. This remarkable result entails an alteration of the fundamental properties of Dirac quasiparticles, yet without changing any of the underlying symmetries. Instead the chirality inversion is driven solely by the coupling strength to a photonic environment that preserves the symmetries of the system.

One important topic to address in future studies is the transport properties of these Dirac polaritons with a tunable chirality. The inversion of chirality removes the conventional transmission channel of Klein tunnelling within the Dirac cone. This could lead to the localisation of massless Dirac polaritons at the interface between regions of different cavity heights. It could also be exploited as a mechanism to scatter between states within and outside the Dirac cone. Indeed it would be interesting to investigate any of the phenomena of Dirac quasiparticles that are intrinsically linked to the chirality. For example, by combining the effects of the cavity with strain-induced pseudomagnetic gauge fields the cavity height could act as a tunable parameter for the Landau Level spectrum.

Perhaps a more essential question that could benefit from further studies is the nature of damping that is inherent in plasmonic arrays. Certainly these chiral modes profit from a suppression of backscattering, the mechanism which is responsible for the gigantic mobilities in graphene. However, polaritons have a finite lifetime and as we saw in chapter 2 they suffer from three main dissipation channels: radiation damping — which scales as the nanoparticle volume, Landau damping — which is inversely proportional, and Ohmic damping — which is size independent. While these mechanisms are well understood in the context of single nanoparticles, interactions in nanoparticle arrays will likely modify the situation. For example theoretical studies on metallic nanoparticle dimers indicate that the dipolar interactions have a minimal impact on the Landau damping, whereas radiation damping depends greatly on the wavelength of the collective mode [125]. Additional work is required to understand the impact of interactions and different lattice structures on the plasmonic damping mechanisms.

Finally, while the analysis in this thesis has focused on arrays of metallic nanoparticles with resonances in the visible range, the mathematical model itself is generalisable to other electromagnetic systems where the response of the functional components can be

modelled as dipolar. For example this may facilitate proof-of-principle experiments in the microwave regime with helical resonators.

# Appendix A

# Derivation of dispersion relation for surface plasmon polaritons

We consider a simple geometry which gives an effective one-dimensional problem, whereby the waves propagate along the $x$-axis, and the dielectric profile depends only on one co-ordinate, $\epsilon = \epsilon(z)$, with no spatial variation along the $y$-direction.

Using the identities $\nabla \times (\nabla \times \mathbf{E}) = \nabla(\nabla \cdot \mathbf{E}) - \nabla^2\mathbf{E}$ and $\nabla \cdot \epsilon\mathbf{E} = \mathbf{E} \cdot \nabla\epsilon + \epsilon\nabla \cdot \mathbf{E}$, the wave equation can be written as

$$\nabla\left(-\frac{1}{\epsilon}\mathbf{E} \cdot \nabla\epsilon\right) - \nabla^2\mathbf{E} = -\mu_0\epsilon_0\epsilon\frac{\partial^2\mathbf{E}}{\partial t^2}, \tag{A.1}$$

which for negligible variation in $\epsilon = \epsilon(\mathbf{r})$ over the order of one optical wavelength gives the ordinary wave equation

$$\nabla^2\mathbf{E} - \frac{\epsilon}{c^2}\frac{\partial^2\mathbf{E}}{\partial t^2} = 0. \tag{A.2}$$

Due to the assumption of non-varying dielectric function, equation A.2 must be solved in separate regions of constant $\epsilon$ and matched using proper boundary conditions. We now show that for a single metal-dielectric interface, this equation give two sets of self consistent solutions with different polarisation properties of the propagating waves. It will be seen that the boundary conditions further constrain the solutions such that only one set is physical.

Assuming a plane wave form $\mathbf{E}(x,y,z,t) = \mathbf{E}(z)\mathrm{e}^{i\beta x}\mathrm{e}^{i\omega t}$, which implies propagation along the $x$-axis and homogeneity in the $y$-direction, equation A.2 reduces to

$$\frac{\partial^2 \mathbf{E}}{\partial z^2} + (k_0^2\epsilon - \beta^2)\mathbf{E} = 0, \tag{A.3}$$

where $k_0 = \omega/c$ is the wave vector of the wave in vacuum. Explicit expressions for the field components are obtained directly from Maxwell's equation and are:

$$\partial_z E_y = -i\omega\mu_0 H_x \tag{A.4a}$$
$$\partial_z E_x - i\beta E_z = i\omega\mu_0 H_y \tag{A.4b}$$
$$i\beta E_y = i\omega\mu_0 H_z \tag{A.4c}$$
$$\partial_z H_y = i\omega\epsilon_0\epsilon E_x \tag{A.4d}$$
$$\partial_z H_x - i\beta H_z = -i\omega\epsilon_0\epsilon E_y \tag{A.4e}$$
$$i\beta H_y = -i\omega\epsilon_0\epsilon E_z \tag{A.4f}$$

which have been simplified for our case of propagation along the $x$-direction ($\partial_x \to i\beta$) with translational invariance along the $y$-direction ($\partial_y \to 0$). This set can be further reduced simply by eliminating either $E_z$ or $H_z$, and performing substitutions to obtain two sets of solutions. For one set, corresponding to transverse electric (TE) modes we have:

$$H_x = i\frac{1}{\omega\mu_0}\frac{\partial E_y}{\partial z} \tag{A.5a}$$
$$H_z = \frac{\beta}{\omega\mu_0}E_y \tag{A.5b}$$
$$\frac{\partial^2 E_y}{\partial z^2} + (k_0^2\epsilon - \beta^2)E_y = 0. \tag{A.5c}$$

For the other set, corresponding to transverse magnetic (TM) modes we have:

$$E_x = -i\frac{1}{\omega\epsilon_0\epsilon}\frac{\partial H_y}{\partial z} \tag{A.6a}$$

$$E_z = -\frac{\beta}{\omega\epsilon_0\epsilon}H_y \tag{A.6b}$$

$$\frac{\partial H_y}{\partial z} + (k_0^2\epsilon - \beta^2)H_y = 0. \tag{A.6c}$$

First we will show that the transverse electric set has no solution for a propagating wave at the metal-dielectric interface. The form of $E_y$ that fulfils the TE mode set of equations A.5 with an evanescent decay in the $z$-direction is

$$E_y(z) = \begin{cases} A_d \mathrm{e}^{i\beta x}\mathrm{e}^{-k_d z}, & z > 0 \\ A_m \mathrm{e}^{i\beta x}\mathrm{e}^{+k_m z}, & z < 0 \end{cases} \tag{A.7}$$

with $H_x$ and $H_z$ given trivially also by the equation set A.5. For convenience we have defined $k_i \equiv k_{i,z}$. Continuity of $E_y$ and $H_x$ at the interface requires that $A_m(k_m + k_d) = 0$ and $A_m = A_d$. Since an evanescent confinement requires that $\mathrm{Re}(K_m) > 0$ and $\mathrm{Re}(K_d) > 0$, it is therefore the case that $A_m = A_d = 0$, and as such SPPs with a TE polarisation do not exist at a single interface.

Fortunately, SPPs with a TM polarisation do exist. The form of $H_y$ is determined by the equation set A.6, and is

$$H_y(z) = \begin{cases} A_d \mathrm{e}^{i\beta x}\mathrm{e}^{-k_d z}, & z > 0 \\ A_m \mathrm{e}^{i\beta x}\mathrm{e}^{+k_m z}, & z < 0 \end{cases} \tag{A.8}$$

Continuity of $H_y$, $\epsilon_m E_z$ and $\epsilon_d E_z$ at the interface requires that $A_d = A_m$ and

$$\frac{k_d}{k_m} = -\frac{\epsilon_d}{\epsilon_m}, \tag{A.9}$$

which reveals that an evanescent confinement only exists for an interface made from materials with real components of their permittivities with opposite sign. Substituting $H_y$ of equation A.8 into the TM wave equation A.6c gives

$$k_i^2 = \beta^2 - k_0^2 \epsilon_i, \tag{A.10}$$

which from condition A.9 gives an expression for the dispersion as

$$\beta = k_0 \sqrt{\frac{\epsilon_m \epsilon_d}{\epsilon_m + \epsilon_d}}. \tag{A.11}$$

# Appendix B

# Arbitrarily orientated dipoles: Anisotropic nanoparticles

In this section we demonstrate that for a dimer of arbitrarily orientated spheroidical nanoparticles (though aligned with one another) with suitably chosen eccentricities we can approximate the eigenmodes in a wide range of frequencies as being aligned to the principal axis. To introduce the formalism and provide a comparison we first treat the case of a dimer of spherical nanoparticles.

## B.1 Eigenmodes of a dimer of spherical nanoparticles

We repeat the calculations of section 4.1 to determine the eigenmodes of a dimer of spherical nanoparticles, as shown in Figure B.1. Previously we assumed *a priori* that the dipoles in each nanoparticle were polarised in the same direction as one another. Here we will show this to be true, but begin by explicitly considering the three degrees of freedom for each dipole. The non-interacting part of the Hamiltonian is

$$H_0 = \sum_n \left( \frac{\Pi_{n\sigma}^2}{2M} + \frac{1}{2} M \omega_0 h_{n\sigma}^2 \right), \tag{B.1}$$

where $n \in \{1, 2\}$ labels the two nanoparticles, $\sigma \in \{x, y, z\}$ and $h_{n\sigma}$ ($\Pi_{n\sigma}$) denote the displacement of the electronic centre of mass (and its conjugate momentum) in the $n$th

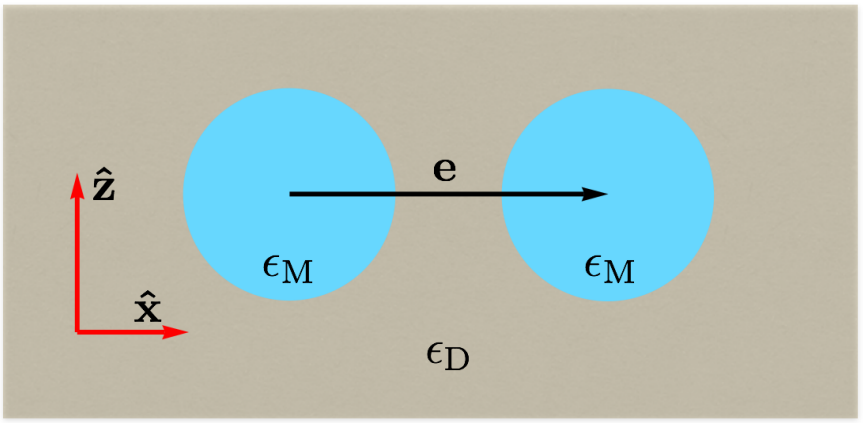


**Figure B.1:** Schematic of a dimer of metallic nanospheres with a separation vector $\mathbf{e} = a\hat{\mathbf{x}}$ and relative permittivity $\epsilon_{\mathrm{M}}$, embedded in a dielectric with relative permittivity $\epsilon_{\mathrm{D}}$.

particle along the direction $\sigma$. Thus referring to equation 4.7 the interaction Hamiltonian is

$$H_{\mathrm{int}} = \frac{N^2 e^2}{4\pi\epsilon_0\epsilon_{\mathrm{D}} a^3} \sum_{\sigma} \eta_\sigma h_{1\sigma} h_{2\sigma}, \tag{B.2}$$

where $\eta_x = 1$ and $\eta_y = \eta_z = -2$ parameterise the interaction strength between the same components of the two dipoles. The interaction between different components for each dipole is zero. Solving for the time-harmonic solutions $h_{n\sigma} \propto \exp(-i\omega t)$, the full Hamiltonian $H = H_0 + H_{\mathrm{int}}$ along with the corresponding equations of motion $\dot{h}_{n\sigma} = \partial H/\partial \Pi_{n\sigma}$ and $\dot{\Pi}_{n\sigma} = -\partial H/\partial h_{n\sigma}$ give the eigenvalue equations

$$\begin{pmatrix} \omega_0^2 - \omega^2 & 2\omega_0\Omega\eta_\sigma \\ 2\omega_0\Omega\eta_\sigma & \omega_0^2 - \omega^2 \end{pmatrix} \begin{pmatrix} h_{1\sigma} \\ h_{2\sigma} \end{pmatrix} = 0. \tag{B.3}$$

The solutions are a set of parallel and anti-parallel eigenmodes aligned along each direction $\sigma$, i.e. $h_{1\sigma} = \pm h_{2\sigma}$ where $\sigma = x$ is a longitudinal mode and $\sigma = y$ and $\sigma = z$ are transverse modes. The corresponding eigenfrequencies are

$$\omega_\sigma = \omega_0 \sqrt{1 \pm 2\frac{\Omega}{\omega_0}\eta_\sigma}. \tag{B.4}$$

To achieve eigenmodes of a nanoparticle dimer that are arbitrarily orientated we need to break the spherical symmetry. Let us do that now.

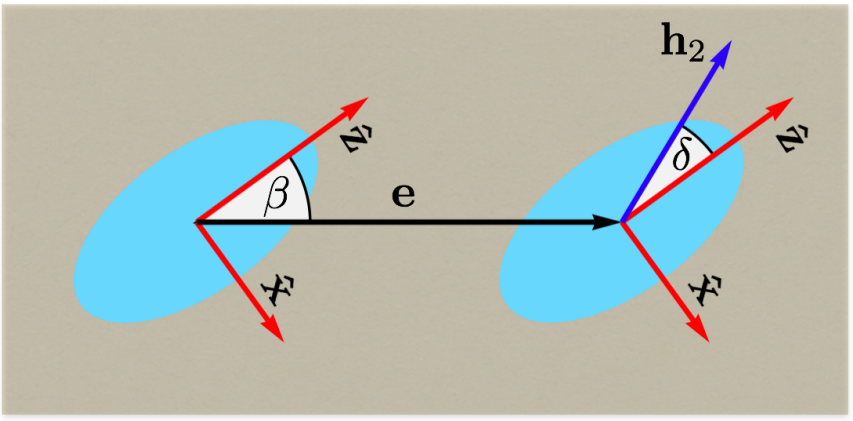


**Figure B.2:** Schematic of a dimer of metallic nanospheroids with a separation vector $\mathbf{e} = a\,(\sin\beta\hat{\mathbf{x}} + \cos\beta\hat{\mathbf{z}})$. The tilt of the particles is described by $\beta$, the angle between the principal axis (along the $\hat{\mathbf{z}}$ direction) and the separation vector $\mathbf{e}$. Also shown is one of the eigenmodes $\mathbf{h}_2 = (h_{2x}, h_{2z})$ which is misaligned from the principal axis by an angle $\delta$.

## B.2 Eigenmodes of a dimer of spheroidical nanoparticles

Now we consider the interaction between two spheroidical nanoparticles as shown in Figure B.2. The semi-axis along the direction $\sigma$ is denoted $r_\sigma$, where the principal semi-axis $r_z$ is different to $r_x = r_y$. We investigate the effect of eccentricity on the eigenmodes by restricting all spheroids to have the same volume $V = \frac{4}{3}\pi r^3$ where $r$ is the radius of a sphere with the same volume. Eccentricity is defined as

$$E = \begin{cases} \left(1 - \rho_z^2/\rho_x^2\right)^{1/2} & \text{, oblate i.e. } r_z < r_x \\ \left(1 - \rho_x^2/\rho_z^2\right)^{1/2} & \text{, prolate i.e. } r_x < r_z \end{cases}, \tag{B.5}$$

where we have introduced the dimensionless quantities

$$\rho_\sigma = \frac{r_\sigma}{r}. \tag{B.6}$$

As we have broken the spherical symmetry of each nanoparticle there will be different resonant frequencies along different axes given by

$$\tilde{\omega}_\sigma = \omega_{\mathrm{pl}}\sqrt{G_\sigma}, \tag{B.7}$$

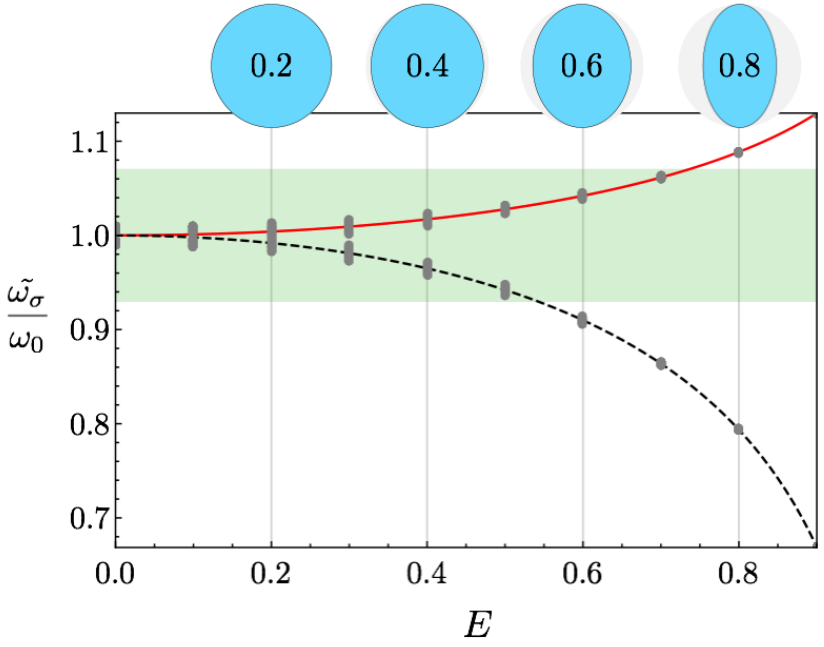


**Figure B.3:** The resonant frequency along the major-axis ($\hat{\mathbf{z}}$) and minor-axes ($\hat{\mathbf{x}}$ and $\hat{\mathbf{y}}$) as a function of eccentricity is given by the solid red and dashed black line respectively. The grey bars (that appear as dots for larger $E$) indicate the range of eigenfrequencies of the dimer for all $\beta$. Along the top of the plot we overlay blue circles with the corresponding eccentricity. The horizontal green band corresponds to the bandwidth of the green portion of the visible spectrum, assuming that $\omega_0 = 566\text{THz}$, which we present to give a sense of scale to the differences in frequencies. Recall that $\omega_0$ is equal to all the frequencies $\tilde{\omega}_\sigma$ when $E = 0$. In the figure $\Omega = 0.01$, $\epsilon_\text{D} = 1$ and $\epsilon_\text{M} = -20$.

where the depolarisation factor is given by [7]

$$G_\sigma = \rho_x\rho_y\rho_z \int_0^\infty \frac{ds}{(s+\rho_\sigma^2)\sqrt{(s+\rho_x^2)(s+\rho_y^2)(s+\rho_z^2)}}. \tag{B.8}$$

In Figure B.3 we plot the resonant frequencies of the principal axis and a minor axis as a function of eccentricity. We see that for a modest eccentricity of about 0.6 or more the difference in frequencies is large enough such that the resonances correspond to different colours in the visible spectrum. Thus it should be quite possible to choose a nanoparticle with a resonance along the principal axis in a frequency range of interest, with the resonances of the minor-axes outside that frequency range.

Thus the non-interaction part of the Hamiltonian is

$$H_0 = \sum_n \left( \frac{\Pi_{n\sigma}^2}{2M_\sigma} + \frac{1}{2} M_\sigma \tilde{\omega}_\sigma h_{n\sigma}^2 \right), \tag{B.9}$$

and the interaction Hamiltonian is given by

$$H_{\text{int}} = \sum_{\sigma,\sigma'} 2M_\sigma \omega_0 \Omega_{\sigma\sigma'} \eta_{\sigma\sigma'} h_{1\sigma} h_{2\sigma'}, \tag{B.10}$$

where $\eta_{\sigma\sigma'}$ parameterises the effect of the nanoparticle orientation $\beta$ on the interaction between the dipole component $\sigma$ in nanoparticle 1 and component $\sigma'$ in nanoparticle 2, given by

$$\eta_{xy} = \eta_{yx} = \eta_{yz} = \eta_{zy} = 0 \qquad \eta_{xz} = \eta_{zx} = -3\sin\beta\cos\beta \tag{B.11}$$

$$\eta_{xx} = 1 - 3\sin^2\beta \qquad \eta_{yy} = 1 \qquad \eta_{zz} = 1 - 3\cos^2\beta. \tag{B.12}$$

In addition we have introduced the factors $\Omega_{\sigma\sigma'} = \Omega\alpha_\sigma\alpha_{\sigma'}$, where $\alpha_\sigma$ is the polarisability of the spheroid along direction $\sigma$ relative to the sphere with the same volume, and $\Omega$ is the interaction strength between a dimer of such spheres. The relative polarisability is given by [7]

$$\alpha_\sigma = \rho_x\rho_y\rho_z \frac{2\epsilon_{\text{D}} + \epsilon_{\text{M}}}{3\epsilon_{\text{D}} + 3G_\sigma(\epsilon_{\text{M}} - \epsilon_{\text{D}})}. \tag{B.13}$$

Thus the full Hamiltonian $H = H_0 + H_{\text{int}}$ leads to the system of equations

$$\begin{pmatrix} \tilde{\omega}_x^2 - \omega^2 & 2\omega_0\Omega_{xx}\eta_{xx} & 0 & 2\omega_0\Omega_{xz}\eta_{xz} \\ 2\omega_0\Omega_{xx}\eta_{xx} & \tilde{\omega}_x^2 - \omega^2 & 2\omega_0\Omega_{xz}\eta_{xz} & 0 \\ 0 & 2\omega_0\Omega_{zx}\eta_{zx} & \tilde{\omega}_z^2 - \omega^2 & 2\omega_0\Omega_{zz}\eta_{zz} \\ 2\omega_0\Omega_{zx}\eta_{zx} & 0 & 2\omega_0\Omega_{zz}\eta_{zz} & \tilde{\omega}_z^2 - \omega^2 \end{pmatrix} \begin{pmatrix} h_{1x} \\ h_{2x} \\ h_{1z} \\ h_{2z} \end{pmatrix} = 0, \tag{B.14}$$

and

$$\begin{pmatrix} \tilde{\omega}_y^2 - \omega^2 & 2\omega_0\Omega\eta_{yy} \\ 2\omega_0\Omega\eta_{yy} & \tilde{\omega}_y^2 - \omega^2 \end{pmatrix} \begin{pmatrix} h_{1y} \\ h_{2y} \end{pmatrix} = 0, \tag{B.15}$$

where we are able to decouple the second matrix from the first as the mode $\sigma = y$ is always perpendicular to the separation vector $\mathbf{e}$. We numerically solve equation B.14 to

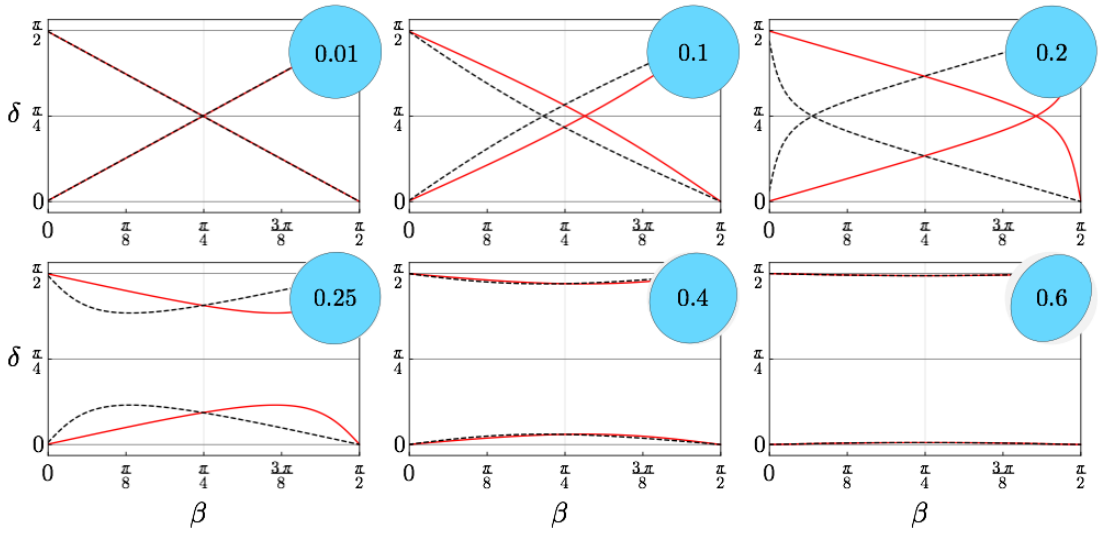


**Figure B.4:** Several plots showing how the eigenmode misalignment angle $\delta$ changes with the nanoparticle tilt angle $\beta$ for different eccentricities (represented by blue circles with the value of $E$ overlaid). The parallel and anti-parallel modes are given by the solid red and dashed black lines respectively. In the figure $\Omega = 0.01$, $\epsilon_{\mathrm{D}} = 1$ and $\epsilon_{\mathrm{M}} = -20$.

obtain the orientation of the eigenmodes, and in Figure B.4 we plot $\delta$, the 'misalignment' angle of an eigenmode from the nanoparticle principal axis, as a function of the tilt angle $\beta$. Let us be clear about what $\delta$ represents. We are only interested in the eigenmodes of equation B.14 as the eigenmodes of B.15 are independent of $\beta$ and are trivially $h_{1y} = \pm h_{2y}$ as with the dimer of spheres. There are two sets of eigenmodes $\mathbf{h}_1 = (h_{1x}, h_{1z}) = \pm\mathbf{h}_2$ for equation B.14, and for any eigenmode $\delta$ is the smallest angle between $\mathbf{h}_1$ (or equally $\mathbf{h}_2$) and the principal axis i.e. either the axis $\hat{\mathbf{y}}$ or $-\hat{\mathbf{y}}$, whichever is smaller.

For a sphere, with $E = 0$, these modes start at $\beta = 0$ with $\delta = 0$ and $\delta = \pi/4$, corresponding to the longitudinal and transverse mode respectively. As $\beta$ is varied the orientations $\delta$ change by exactly the same proportion, highlighting the fact that the eigenmodes for a sphere are fixed to the directions parallel and perpendicular to the separation axis. As soon as we introduce an eccentricity, there is a competition of sorts between the original symmetry directions of the separation axis, and the new symmetry direction of the nanoparticle semi-axes. This introduces an asymmetry between the parallel and anti-parallel modes, which no longer perfectly track the tilt angle $\beta$. As we increase the eccentricity the modes increasingly tend to align with the semi-axes, and for a modest eccentricity $E = 0.6$ the dipole orientations are almost perfectly aligned with the nanoparticles semi-axes.

We have shown that for a dimer of spheroids with a moderate eccentricity the eigenmodes are almost completely aligned with the semi-axes of the spheroids and there is a significant difference in the resonant frequencies along the major-axis and minor-axes. Therefore it is possible to choose a dimer of spheroids with a sufficient eccentricity such that we can model the eigenmodes in a frequency region of interest as aligned to the principal axis. Whilst we have not demonstrated it here, it is not unreasonable to expect these results to extend to arbitrary arrays of spheroids or indeed arrays of other anisotropic particles.

# Appendix C

# Videos

**Figure C.1:** Scan the QR code with your mobile device or visit:
http://www.ipcms.unistra.fr/wp-content/uploads/2014/11/tunable_CP_dispersion.mp4.
($a$) Phase diagram for the perfect honeycomb lattice showing at which polarisation angles $(\theta, \phi)$ the collective plasmon spectrum is gapless (white regions) or gapped (coloured regions). The black lines indicate where one of the interaction parameters $\mathcal{C}_j$ is zero ($\mathcal{C}_1 = 0$, $\mathcal{C}_2 = 0$ and $\mathcal{C}_3 = 0$ along the solid, dashed and dotted lines, respectively). ($b$) Collective plasmon dispersion corresponding to the LSP polarisation $(\theta, \phi)$ indicated by a red dot in panel ($a$). The latter spans the following polarisation angles:
($i$) $(0 \leq \theta \leq \pi/2, \phi = \pi/4)$,
($ii$) $(\theta = \pi/2, \pi/4 \leq \phi \leq \pi/2)$,
($iii$) $(\arcsin(\sqrt{1/3}) \leq \theta \leq \pi/2, \phi = \pi/2)$,
($iv$) $(\theta = \arcsin(\sqrt{1/3}), \pi/4 \leq \phi \leq \pi/2)$.
Coupling parameter used in the video: $\Omega/\omega_0 = 0.01$.

**Figure C.2:** Scan the QR code with your mobile device or visit:
http://www.ipcms.unistra.fr/wp-content/uploads/2014/11/broken_inversion_symmetry.mp4 Collective plasmon dispersions from equation 4.64 with LSP polarisation normal to the plane ($\theta = 0$), for increasing values of $\delta$, as indicated by the red arrow. Coupling parameter used in the video: $\tilde{\Omega}/\bar{\omega} = 0.01$.

**Figure C.3:** Scan the QR code with your mobile device or visit:
http://www.ipcms.unistra.fr/wp-content/uploads/2014/11/deformed_bipartite_lattice.mp4.
($a$) Phase diagram showing the polarisation angles $(\theta, \phi)$ at which the collective plasmon spectrum is gapped or gapless (orange and cream regions, respectively) for different positions of the $B$ sublattice, parametrised by the vector $\boldsymbol{\ell}$ as indicated in the video. The corresponding deformed structure is shown in panel ($e$), where the $A$ (immobile) sublattice corresponds to the blue dots, while the $B$ (moving) sublattice corresponds to the red dots. Panels ($b$) and ($c$) display the same phase diagram as in panel ($a$) on the $(\theta, \phi)$ unit sphere, viewed from ($b$) $(\theta = \pi/2, \phi = 0)$ and ($c$) from the north pole $\theta = 0$. ($d$) Corresponding collective plasmon dispersion for $\theta = 0$. In the video $\Omega/\omega_0 = 0.01$ and we are considering bipartite hexagonal lattices of identical nanoparticles.

# Bibliography


[1]M. Born and W. E., *Principles of Optics* (Pergamon Press, Oxford, 1961).

[2]W. L. Barnes, A. Dereux, and T. W. Ebbesen, "Surface Plasmon Sub-wavelength Optics", Nature **424**, 824–830 (2003).

[3]S. A. Maier, *Plasmonics: Fundamentals and Applications* (Springer, New York City, 2007).

[4]T. Klar, M. Perner, S. Grosse, G. von Plessen, W. Spirkl, and J. Feldmann, "Surface-Plasmon Resonances in Single Metallic Nanoparticles", Phys. Rev. Lett. **80**, 4249–4252 (1998).

[5]K. Kneipp, Y. Wang, H. Kneipp, L. T. Perelman, I. Itzkan, R. R. Dasari, and M. S. Feld, "Single Molecule Detection Using Surface-Enhanced Raman Scattering (SERS)", Phys. Rev. Lett. **78**, 1667–1670 (1997).

[6]U. Kreibig and M. Vollmer, *Optical Properties of Metal Clusters* (Springer Series in Materials Science, Berlin Heidelberg, 1994).

[7]C. F. Bohren and D. R. Huffman, *Absorption and scattering of light by small particles* (John Wiley & Sons, Weinheim, 1983).

[8]U. Leonhardt, "Optical Conformal Mapping", Science **312**, 1777–1780 (2006).

[9]J. B. Pendry, "Controlling Electromagnetic Fields", Science **312**, 1780–1782 (2006).

[10]D. Schurig, J. J. Mock, B. J. Justice, S. A. Cummer, J. B. Pendry, A. F. Starr, and D. R. Smith, "Metamaterial Electromagnetic Cloak at Microwave Frequencies", Science **314**, 977–980 (2006).

[11]J. B. Pendry, "Negative refraction makes a perfect lense", Phys. Rev. Lett. **85**, 3966–3969 (2000).

[12]N. Fang, "Sub-Diffraction-Limited Optical Imaging with a Silver Superlens", Science **308**, 534–537 (2005).

[13]O. Hess and K. L. Tsakmakidis, "Trapped Rainbow Storage of Light in Metamaterials", Adv. Sci. Tech. **75**, 256–265 (2010).

[14]J. R. Krenn, A. Dereux, J. C. Weeber, E. Bourillot, Y. Lacroute, J. P. Goudonnet, G. Schider, W. Gotschy, A. Leitner, F. R. Aussenegg, and C. Girard, "Squeezing the Optical Near-Field Zone by Plasmon Coupling of Metallic Nanoparticles", Phys. Rev. Lett. **82**, 2590–2593 (1999).

[15]S. A. Maier, M. L. Brongersma, P. G. Kik, and H. A. Atwater, "Observation of near-field coupling in metal nanoparticle chains using far-field polarization spectroscopy", Phys. Rev. B **65**, 193408 (2002).

[16]S. A. Maier, P. G. Kik, and H. A. Atwater, "Observation of coupled plasmon-polariton modes in Au nanoparticle chain waveguides of different lengths: Estimation of waveguide loss", Appl. Phys. Lett. **81**, 1714–1716 (2002).

[17]L. Zhao, K. L. Kelly, and G. C. Schatz, "The Extinction Spectra of Silver Nanoparticle Arrays: Influence of Array Structure on Plasmon Resonance Wavelength and Width", J. Phys. Chem. B **107**, 7343–7350 (2003).

[18]M. L. Brongersma, J. W. Hartman, and H. A. Atwater, "Electromagnetic energy transfer and switching in nanoparticle chain arrays below the diffraction limit", Phys. Rev. B **62**, 16356 (2000).

[19]X. Wang, P. Gogol, E. Cambril, and B. Palpant, "Near- and Far-Field Effects on the Plasmon Coupling in Gold Nanoparticle Arrays", J. Phys. Chem. C **116**, 24741–24747 (2012).

[20]K. S. Novoselov, A. K. Geim, S. V. Morozov, D. Jiang, Y. Zhang, S. V. Dubonos, I. V. Grigorieva, and A. A. Firsov, "Electric Field Effect in Atomically Thin Carbon Films", Science **22**, 666–669 (2004).

[21]P. R. Wallace, "The Band Theory of Graphite", Phys. Rev. **71**, 622–634 (1947).

[22]K. S. Novoselov, A. K. Geim, S. V. Morozov, D. Jiang, M. I. Katsnelson, I. V. Grigorieva, S. V. Dubonos, and A. A. Firsov, "Two-dimensional gas of massless Dirac fermions in graphene", Nature **438**, 197–200 (2005).

[23]Y. Zhang, Y. W. Tan, H. L. Stormer, and P. Kim, "Experimental observation of the quantum Hall effect and Berry's phase in graphene", Nature **438**, 201–204 (2005).

[24]A. H. C. Neto, F. Guinea, N. M. R. Peres, K. S. Novoselov, and A. K. Geim, "The electronic properties of graphene", Rev. Mod. Phys. **81**, 109–162 (2009).

[25]T. Ando, T. Nakanishi, and R. Saito, "Berry's Phase and Absence of Back Scattering in Carbon Nanotubes", J. Phys. Soc. Jpn. **67**, 2857–2862 (1998).

[26]V. V. Cheianov and V. I. Fal'ko, "Selective transmission of Dirac electrons and ballistic magnetoresistance of n-p junctions in graphene", Phys. Rev. B **74**, 041403 (2006).

[27]R. Winkler and U. Zülicke, "Invariant expansion for the trigonal band structure of graphene", Phys. Rev. B **82**, 245313 (2010).

[28]J. L. Mañes, F. Guinea, and M. A. H. Vozmediano, "Existence and topological stability of Fermi points in multilayered graphene", Phys. Rev. B **75**, 155424 (2007).

[29]M. Polini, F. Guinea, M. Lewenstein, H. C. Manoharan, and V. Pellegrini, "Artificial honeycomb lattices for electrons, atoms and photons", Nat. Nanotechnol. **8**, 625–633 (2013).

[30]P. Soltan-Panahi, J. Struck, P. Hauke, A. Bick, W. Plenkers, G. Meineke, C. Becker, P. Windpassinger, M. Lewenstein, and K. Sengstock, "Multi-Component Quantum Gases in Spin-Dependent Hexagonal Lattices", Nat. Phys. **7**, 434–440 (2011).

[31]L. Tarruell, D. Greif, T. Uehlinger, G. Jotzu, and T. Esslinger, "Creating, moving and merging Dirac points with a Fermi gas in a tunable honeycomb lattice", Nature **483**, 302–305 (2012).

[32]S. Bittner, B. Dietz, M. Miski-Oglu, P. Oria Iriarte, A. Richter, and F. Schäfer, "Observation of a Dirac point in microwave experiments with a photonic crystal modeling graphene", Phys. Rev. B **82**, 014301 (2010).

[33]M. C. Rechtsman, J. M. Zeuner, A. Tünnermann, S. Nolte, M. Segev, and A. Szameit, "Strain-induced pseudomagnetic field and photonic Landau levels in dielectric structures", Nat. Photon. **7**, 153–158 (2013).

[34]S. Y. Park and D. Stroud, "Surface Plasmon Dispersion Relations in Chains of Metallic Nanoparticles: Exact Quasistatic Calculation", Phys. Rev. B **69**, 125418 (2004).

[35]J. J. Hopfield, "Theory of the Contribution of Excitions to the Complex Dielectric Constants of Crystals", Phys. Rev. **112**, 1555–1567 (1958).

[36]U. Fano, "Atomic theory of electromagnetic intreractions in dense materials", Phys. Rev. **103**, 1202–1218 (1956).

[37]C. Kittel, *Solid State Physics* (Holt, Rinehart and Winston, Austin, 2005).

[38]A. Taflove, *Computational Electrodynamics: The Finite-Difference Time-Domain Method* (Artech House, London, 1995).

[39]A. Vial, A.-S. Grimault, D. Macıas, D. Barchiesi, and M. L. de la Chapelle, "Improved analytical fit of gold dispersion: application to the modeling of extinction spectra with a finite-difference time-domain method", Phys. Rev. B **71**, 085416 (2005).

[40]R. W. Christy, "Optical constants of the noble metals", Phys. Rev. B **6**, 4370–4379 (1972).

[41]H. Ibach and D. L. Mills, *Electron energy loss spectroscopy and surface vibrations* (Academic Press, New York City, 2013).

[42]L. D. Landau, "On the vibrations of the electronic plasma", J. Phys. **X**, 25–34 (1946).

[43]D. Bohm and E. P. Gross, "Theory of plasma oscillations. B. Excitation and damping of oscillations", Phys. Rev. **75**, 1864–1876 (1949).

[44]J. Dawson, "On Landau damping", Phys. Fluids **4**, 869–874 (1961).

[45]K. Höflich, U. Gösele, and S. Christiansen, "Are volume plasmons excitable by classical light?", Phys. Rev. Lett. **103**, 087404 (2009).

[46]K. V. Sreekanth, A. De Luca, and G. Strangi, "Excitation of volume plasmon polaritons in metal-dielectric metamaterials using 1D and 2D diffraction gratings", J. Opt. **16**, 105103 (2014).

[47]S. V. Zhukovsky, O. Kidwai, and J. E. Sipe, "Physical nature of volume plasmon polaritons in hyperbolic metamaterials", Opt. Express **21**, 14982–14987 (2013).

[48]D. J. Griffiths and C. Inglefield, *Introduction to Electrodynamics* (Prentice Hall, London, 2005).

[49]G. Shvets and I. Tsukerman, *Plasmonics and Plasmonic Metamaterials: Analysis and Applications* (World Scientific Publishing, Toh Tuck, 2012).

[50]E. Kretschmann and H. Raether, "Radiative decay of non-radiative surface plasmons excited by light", Z. Naturforsch. A **23**, 2135–2136 (1968).

[51]A. Otto, "Excitation of nonradiative surface plasma waves in silver by the method of frustrated total reflection", Z. Physik **216**, 398–410 (1968).

[52]R. W. Wood, "On a Remarkable Case of Uneven Distribution of Light in a Diffraction Grating Spectrum", Proc. Phys. Soc. London **18**, 269–275 (1902).

[53]U. Fano, "The Theory of Anomalous Diffraction Gratings and of Quasi-Stationary Waves on Metallic Surfaces (Sommerfeld's Waves)", J. Opt. Soc. Am. **31**, 213–222 (1941).

[54]R. H. Ritchie, E. T. Arakawa, J. J. Cowan, and R. N. Hamm, "Surface-plasmon resonance effect in grating diffraction", Phys. Rev. Lett. **21**, 1530–1533 (1968).

[55]W. L. Barnes, "Fluorescence near interfaces: the role of photonic mode density", J. Mod. Opt. **45**, 661–699 (1997).

[56]G. W. Ford and A. Arbor, "Electromagnetic Interactions of Molecules With Metal Surfaces", Phys. Rep. **113**, 195–287 (1984).

[57]A. Zayats and I. Smolyaninov, "Nano-optics of surface plasmon polaritons", Phys. Rep. **408**, 131–314 (2005).

[58]W. L. Barnes, "Surface plasmon–polariton length scales: a route to sub-wavelength optics", J. Opt. A **8**, S87–S93 (2006).

[59]K. Saha, S. S. Agasti, C. Kim, X. Li, and V. M. Rotello, "Gold nanoparticles in chemical and biological sensing", Chem. Rev. **112**, 2739–2779 (2012).

[60]K. L. Kelly, E. Coronado, L. L. Zhao, and G. C. Schatz, "The Optical Properties of Metal Nanoparticles: The Influence of Size, Shape, and Dielectric Environment", J. Phys. Chem. B **107**, 668–677 (2003).

[61]M. Brack, "The physics of simple metal clusters: Self-consistent jellium model and semiclassical approaches", Rev. Mod. Phys. **65**, 677–732 (1993).

[62]G. Weick, G. L. Ingold, R. A. Jalabert, and D. Weinmann, "Surface plasmon in metallic nanoparticles: Renormalization effects due to electron-hole excitations", Phys. Rev. B **74**, 165421 (2006).

[63]G. Weick, R. A. Molina, D. Weinmann, and R. A. Jalabert, "Lifetime of the first and second collective excitations in metallic nanoparticles", Phys. Rev. B **72**, 115410 (2005).

[64]L. G. Gerchikov, C. Guet, and A. N. Ipatov, "Multiple plasmons and anharmonic effects in small metallic clusters", Phys. Rev. A **66**, 053202 (2002).

[65]V. V. Kresin, "Collective resonances and response properties of electrons in metal clusters", Phys. Rep. **220**, 1–52 (1992).

[66]S. Link and M. A. El-Sayed, "Size and Temperature Dependence of the Plasmon Absorption of Colloidal Gold Nanoparticles", J. Phys. Chem. B **103**, 4212–4217 (1999).

[67]U. Kreibig, "Electronic properties of small silver particles: the optical constants and their temperature dependence", J. Phys. F **4**, 999–1014 (1974).

[68]R. Garcia, A. W. Knoll, and E. Riedo, "Advanced scanning probe lithography", Nat. Nanotechnol. **9**, 577–587 (2014).

[69]W. F. van Dorp et al., "Approaching the resolution limit of nanometer scale electron beam indiced deposition", Nano Lett. **5**, 1303–1307 (2005).

[70]W. F. van Dorp, C. W. Hagen, P. A. Crozier, and P. Kruit, "Growth behavior near the ultimate resolution of nanometer-scale focused electron beam-induced deposition", Nanotechnology **19**, 225305 (2008).

[71]J. C. van Oven, F. Berwald, K. K. Berggren, P. Kruit, and C. W. Hagen, "Electron-beam-induced deposition of 3-nm-half-pitch patterns on bulk Si", J. Vac. Sci. Technol. **29**, 06F305 (2011).

[72]H. Nakao, H. Shiigi, Y. Yamamoto, S. Tokonami, T. Nagaoka, S. Sugiyama, and T. Ohtani, "Highly Ordered Assemblies of Au Nanoparticles Organized on DNA", Nano Letters **3**, 1391–1394 (2003).

[73]U. Kreibig, "Optical absorption of small metallic particles", Surf. Sci. **156**, 678–700 (1985).

[74]J. J. Mock, M. Barbic, D. R. Smith, D. A. Schultz, and S. Schultz, "Shape effects in plasmon resonance of individual colloidal silver nanoparticles", J. Chem. Phys. **116**, 6755–6759 (2002).

[75]J. Crowell and R. H. Ritchie, "Radiative decay of coulomb-stimulated plasmons in spheres", Phys. Rev. **172**, 436–440 (1968).

[76]U. Kreibig and C. v. Fragstein, "The limitation of electron mean free path in small silver particles", Z. Phys. **224**, 307–323 (1969).

[77]W. A. Murray and W. L. Barnes, "Plasmonic materials", Adv. Mater. **19**, 3771–3782 (2007).

[78]R. Jin, Y. Cao, C. A. Mirkin, K. L. Kelly, G. C. Schatz, and J. G. Zheng, "Photoinduced conversion of silver nanospheres to nanoprisms", Science **294**, 1901–1903 (2001).

[79]V. Myroshnychenko, J. Rodríguez-Fernández, I. Pastoriza-Santos, A. M. Funston, C. Novo, P. Mulvaney, L. M. Liz-Marzán, and F. J. García de Abajo, "Modelling the optical response of gold nanoparticles", Chem. Soc. Rev. **37**, 1792–1805 (2008).

[80]F. Zhou, Z. Y. Li, Y. Liu, and Y. Xia, "Quantitative Analysis of Dipole and Quadrupole Excitation in the Surface Plasmon Resonance of Metal Nanoparticles", J. Phys. Chem. C **112**, 20233–20240 (2008).

[81]A. Wokaun, J. Gordon, and P. Liao, "Radiation Damping in Surface-Enhanced Raman Scattering.", Phys. Rev. Lett. **48**, 1574–1574 (1982).

[82]S. Link and M. A. El-Sayed, "Shape and size dependence of radiative, non-radiative and photothermal properties of gold nanocrystals", Int. Rev. Phys. Chem. **19**, 409–453 (2000).

[83]C. Sönnichsen, T. Franzl, T. Wilk, G. von Plessen, J. Feldmann, O. Wilson, and P. Mulvaney, "Drastic reduction of plasmon damping in gold nanorods", Phys. Rev. Lett. **88**, 077402 (2002).

[84]W. Rechberger, A. Hohenau, A. Leitner, J. R. Krenn, B. Lamprecht, and F. R. Aussenegg, "Optical properties of two interacting gold nanoparticles", Opt. Commun. **220**, 137–141 (2003).

[85]V. Markel, "Coupled-dipole Approach to Scattering of Light from a One-dimensional Periodic Dipole Structure", J. Mod. Opt. **40**, 2281–2291 (1993).

[86]C. L. Haynes, A. D. McFarland, L. Zhao, R. P. Van Duyne, G. C. Schatz, L. Gunnarsson, J. Prikulis, B. Kasemo, and M. Käll, "Nanoparticle Optics: The Importance of Radiative Dipole Coupling in Two-Dimensional Nanoparticle Arrays", J. Phys. Chem. B **107**, 7337–7342 (2003).

[87]A. V. Kavokin, *Microcavities* (Oxford University Press, Oxford, 2007).

[88]E. M. Purcell, H. C. Torrey, and R. V. Pound, "Resonance Absorption by Nuclear Magnetic Moments in a Solid", Phys. Rev. **69**, 37–38 (1946).

[89]G. Weick and E. Mariani, "Tunable plasmon polaritons in arrays of interacting metallic nanoparticles", Eur. Phys. J. B **88**, 7 (2015).

[90]N. Meinzer, W. L. Barnes, and I. R. Hooper, "Plasmonic meta-atoms and metasurfaces", Nat. Photon. **8**, 889–898 (2014).

[91]C. A. Downing and G. Weick, "Topological collective plasmons in bipartite chains of metallic nanoparticles", Phys. Rev. B **95**, 125426 (2017).

[92]A. Poddubny, A. Miroshnichenko, A. Slobozhanyuk, and Y. Kivshar, "Topological majorana states in zigzag chains of plasmonic nanoparticles", ACS Photonics **1**, 101–105 (2014).

[93]M. S. Tame, K. R. McEnery, S. K. Ozdemir, J. Lee, S. A. Maier, and M. S. Kim, "Quantum plasmonics", Nat. Phys. **9**, 329–340 (2013).

[94]M. C. Rechtsman, J. M. Zeuner, Y. Plotnik, Y. Lumer, D. Podolsky, F. Dreisow, S. Nolte, M. Segev, and A. Szameit, "Photonic floquet topological insulators", Nature **496**, 196–200 (2013).

[95]M. C. Rechtsman, J. M. Zeuner, A. Tunnermann, S. Nolte, M. Segev, and A. Szameit, "Strain-induced pseudomagnetic field and photonic landau levels in dielectric structures", Nat. Photon. **7**, 153–158 (2013).

[96]M. C. Rechtsman, Y. Plotnik, J. M. Zeuner, D. Song, Z. Chen, A. Szameit, and M. Segev, "Topological creation and destruction of edge states in photonic graphene", Phys. Rev. Lett. **111**, 103901 (2013).

[97]M. Bellec, U. Kuhl, G. Montambaux, and F. Mortessagne, "Topological transition of Dirac points in a microwave experiment", Phys. Rev. Lett. **110**, 033902 (2013).

[98]J. C. Meyer, A. K. Geim, M. I. Katsnelson, K. S. Novoselov, T. J. Booth, and S. Roth, "The structure of suspended graphene sheets", Nature **446**, 60–63 (2007).

[99]J. C. Slonczewski and P. R. Weiss, "Band structure of graphite", Phys. Rev. **109**, 272–279 (1958).

[100]J. McClure, "Diamagnetism of Graphite", Phys. Rev. **104**, 666–671 (1956).

[101]F. D. M. Haldane, "Model for a quantum Hall effect without Landau levels: Condensed-matter realization of the parity anomaly", Phys. Rev. Lett. **61**, 2015–2018 (1988).

[102]G. W. Semenoff, "Condensed-Matter Simulation of a Three-Dimensional Anomaly", Phys. Rev. Lett. **53**, 2449–2452 (1984).

[103]M. V. Berry, "Quantal Phase Factors Accompanying Adiabatic Changes", Proc. R. Soc. A **392**, 45–57 (1984).

[104]M. Berry, "Anticipations of the Geometric Phase", Physics Today **43**, 34–40 (1990).

[105]C. A. Mead and D. G. Truhlar, "On the determination of Born–Oppenheimer nuclear motion wave functions including complications due to conical intersections and identical nuclei", J. Chem. Phys. **70**, 2284–2296 (1979).

[106]D. Griffiths, *Introduction to quantum mechanics* (Prentice Hall, London, 2005).

[107]A. Bohm, A. Mostafazadeh, H. Koizumi, Q. Niu, and J. Zwanziger, *The Geometric Phase in Quantum Systems* (Springer, Berlin Heidelberg, 2003).

[108]G. Montambaux, F. Piéchon, J. N. Fuchs, and M. O. Goerbig, "A universal Hamiltonian for motion and merging of Dirac points in a two-dimensional crystal", Eur. Phys. J. B **72**, 509–520 (2009).

[109]G. Montambaux, F. Piéchon, J.-N. Fuchs, and M. O. Goerbig, "Merging of Dirac points in a two-dimensional crystal", Phys. Rev. B **80**, 153412 (2009).

[110]M. I. Katsnelson, *Graphene: carbon in two dimensions* (Cambridge University Press, Cambridge, 2007).

[111]R. Saito, G. Dresselhaus, and M. Dresselhaus, *Physical properties of carbon nanotubes* (Imperial College Press, London, 1998).

[112]J. C. Slater and G. F. Koster, "Simplified LCAO Method for the Periodic Potential Problem", Phys. Rev. **94**, 1498–1524 (1954).

[113]S. Reich, J. Maultzsch, C. Thomsen, and P. Ordejón, "Tight-binding description of graphene", Phys. Rev. B **66**, 0354121 (2002).

[114]J. R. Schrieffer and P. A. Wolff, "Relation between the Anderson and Kondo Hamiltonians", Phys. Rev. **149**, 491–492 (1966).

[115]H. Georgi, *The quantum theory of fields* (Cambridge University Press, Cambridge, 1995).

[116]M. I. Katsnelson, K. S. Novoselov, and A. K. Geim, "Chiral tunneling and the Klein paradox in graphene", Nat. Phys. **2**, 620–625 (2006).

[117]N. Singh, *Quantum transport in mesoscopic systems* (Oxford University Press, Oxford, 2010).

[118]S. V. Morozov, K. S. Novoselov, M. I. Katsnelson, F. Schedin, L. A. Ponomarenko, D. Jiang, and A. K. Geim, "Strong suppression of weak localization in graphene", Phys. Rev. Lett. **97**, 16801 (2006).

[119]X. Wu, X. Li, Z. Song, C. Berger, and W. A. De Heer, "Weak antilocalization in epitaxial graphene: Evidence for chiral electrons", Phys. Rev. Lett. **98**, 136801 (2007).

[120]Z. Jiang, Y. Zhang, Y. Tan, H. L. Stormer, and P. Kim, "Quantum Hall effect in graphene", Science **143**, 14–19 (2007).

[121]K.-i. Sasaki, Y. Kawazoe, and R. Saito, "Local energy gap in deformed carbon nanotubes", Prog. Theor. Phys. **113**, 463 (2005).

[122]L. D. Landau, *Theory of Elasticity* (Pergamon Press, Oxford, 1960).

[123]F. Guinea, M. I. Katsnelson, and A. K. Geim, "Energy gaps and a zero-field quantum Hall effect in graphene by strain engineering", Nat. Phys. **6**, 30–33 (2010).

[124]T. J. Sturges, C. Woollacott, G. Weick, and E. Mariani, "Dirac plasmons in bipartite lattices of metallic nanoparticles", 2D Mater. **2**, 014008 (2015).

[125]A. Brandstetter-Kunc, G. Weick, D. Weinmann, and R. A. Jalabert, "Decay of dark and bright plasmonic modes in a metallic nanoparticle dimer", Phys. Rev. B **91**, 035431 (2015).

[126]M. Bellec, U. Kuhl, G. Montambaux, and F. Mortessagne, "Topological transition of Dirac points in a microwave experiment", Phys. Rev. Lett. **110**, 033902 (2013).

[127]M. Bellec, U. Kuhl, G. Montambaux, and F. Mortessagne, "Tight-binding couplings in microwave artificial graphene", Phys. Rev. B **88**, 115437 (2013).

[128]I. M. Lifshitz, "Anomalies of electron characteristics of a metal in the high pressure region", J. Exp. Theor. Phys. **11**, 1130–1135 (1960).

[129]F. Xia, D. B. Farmer, Y. M. Lin, and P. Avouris, "Graphene Field-Effect Transistors with High On/Off Current Ratio and Large Transport Band Gap at Room Temperature", Nano Lett. **10**, 715–718 (2010).

[130]M. Y. Han, B. Özyilmaz, Y. Zhang, and P. Kim, "Energy band-gap engineering of graphene nanoribbons", Phys. Rev. Lett. **98**, 206805 (2007).

[131]V. M. Pereira, A. H. Castro Neto, and N. M. R. Peres, "Tight-binding approach to uniaxial strain in graphene", Phys. Rev. B **80**, 045401 (2009).

[132]L. Lu, J. D. Joannopoulos, and M. Soljacić, "Topological Photonics", Nat. Photon. **8**, 821–829 (2014).

[133]K. Kakazu and Y. S. Kim, "Quantization of electromagnetic fields in cavities and spontaneous emission", Phys. Rev. A **50**, 1830–1839 (1994).

[134]A. H. Castro Neto, F. Guinea, N. M. R. Peres, K. S. Novoselov, and A. K. Geim, "The electronic properties of graphene", Rev. Mod. Phys. **81**, 109–162 (2009).

[135]B. C. Hall, *The Baker—Campbell—Hausdorff formula* (Springer New York, New York, 2003).

[136]E. Mariani, A. J. Pearce, and F. Von Oppen, "Fictitious gauge fields in bilayer graphene", Phys. Rev. B **86**, 165448 (2012).

[137]A. J. Pearce, F. Cavaliere, and E. Mariani, "Conductance and shot noise in strained bilayer graphene.", J. Phys. Condens. Matter **25**, 375301 (2013).

[138]J. N. Fuchs, F. Piechon, M. O. Goerbig, and G. Montambaux, "Topological Berry phase and semiclassical quantization of cyclotron orbits for two dimensional electrons in coupled band models", Eur. Phys. J. B **77**, 351–362 (2010).

[139]C. H. Park and N. Marzari, "Berry phase and pseudospin winding number in bilayer graphene", Phys. Rev. B **84**, 205440 (2011).

[140]H. Min and A. H. MacDonald, "Chiral decomposition in the electronic structure of graphene multilayers", Phys. Rev. B **77**, 155416 (2008).

[141]V. V. Cheianov, V. Fal'ko, and B. L. Altshuler, "The Focusing of Electron Flow and a Veselago Lens in Graphene p-n Junctions", Science **315**, 1252–1255 (2007).

[142]M. A. Vozmediano, M. I. Katsnelson, and F. Guinea, "Gauge fields in graphene", Phys. Rep. **496**, 109–148 (2010).

[143]H. Suzuura and T. Ando, "Phonons and electron-phonon scattering in carbon nanotubes", Phys. Rev. B **65**, 235412 (2002).

[144]T. L. Linnik, "Effective hamiltonian of strained graphene", J. Phys. Condens. Matter **24**, 205302 (2012).

[145]Y. Zhang, "Motion of electrons in semiconductors under inhomogeneous strain with application to laterally confined quantum wells", Phys. Rev. B **49**, 14352–14366 (1994).

[146]F. De Juan, M. Sturla, and M. A. H. Vozmediano, "Space dependent Fermi velocity in strained graphene", Phys. Rev. Lett. **108**, 227205 (2012).

[147]A. Demetriadou and O. Hess, "Analytic theory of optical nanoplasmonic metamaterials", Phys. Rev. B **87**, 161101 (2013).